Plasticity-Induced Fatigue Crack Closure: An Investigation Using Digital Image Correlation



Samuel O'Connor

Christ Church

University of Oxford

A thesis submitted for the degree of

MSc by Research

Trinity 2015

Acknowledgements

I would like to express my gratitude to my supervisor, Professor David Nowell, whose patience, expertise and understanding added considerably to my experience at Oxford. The time and effort put in to teach, advise and make corrections to my work is sincerely appreciated. I was lucky enough to have the opportunity to be part of the Oxford University Boat Club during my time in Oxford, which proved to be a very meaningful and unique experience. This would not have been possible without the support provided by Professor Nowell, for which I will always be extremely grateful for.

Furthermore, the support and advice provided by staff in the Engineering Department was appreciated and I learnt a lot being surrounded by very experienced and helpful people. In particular, Kalin Dragnevski, who taught me how to use the SEM and Robert Paynter, who was extremely helpful with the experimental setup and advice on analysis. These two were immensely helpful in conducting the experimental work in this thesis and I am very thankful for their assistance.

Abstract

The present work demonstrates the practical application of digital image correlation (DIC) in measuring near tip displacement fields of fatigue cracks in 6082 T6 aluminium alloy. The experimental work is focused on building from recent work done by de Matos and Nowell to directly measure fatigue crack closure with surface displacements obtained through DIC analysis. In this work, similar experiments are reproduced with extended DIC analysis and further work is performed using images obtained through in-situ SEM testing. MATLAB codes based on an existing open source program have been developed to fit images together for crack length measurements and efficiently obtain surface displacement data for a large number of points around the crack tip. In this work, near tip displacement data is used for comparison with two crack tip deformation models. The first assumes simple elastic deformation and a reasonable agreement is obtained during constant amplitude loading, although a residual stress intensity caused by the plastic wake exists, giving rise to crack closure. The other model analysed is a basic elastic-plastic assumption, proposed by Pommier and colleagues. The results during constant amplitude loading are similar, but with a slightly improved fit from the elastic model. However, a single overload cycle applied to a specimen produces significant plasticity at the crack tip and the variation in crack tip plastic displacement, represented by the second term in Pommier's model, becomes significant. Effects of load history are captured by the values of this term and the determined stress intensity factor. The relationship between these parameters and crack growth behaviour before and after an overload is investigated and related to the levels of crack closure observed. The in-situ SEM testing produced images with high resolution and magnification allowing for detailed displacement analysis and further work using this imaging method is discussed.

Contents

List of Figures **iv**

1 Introduction **1**

2 Background and Literature Review **3**

2.1 Linear Elastic Fracture Mechanics 3

2.1.1 Crack Tip Stress Analysis 4

2.1.2 Crack Tip Plasticity 6

2.1.2.1 Irwin's Plastic Zone Size 7

2.1.2.2 Strip-Yield Model 9

2.1.2.3 Plastic Zone Shape 10

2.1.2.4 Small Scale Yielding 11

2.2 Fatigue Crack Propagation 12

2.2.1 Similitude of K 12

2.2.2 Crack Closure 15

2.2.2.1 Plasticity-induced Crack Closure 17

2.2.3 Variable Amplitude Loading and Retardation 20

2.2.3.1 Reverse Plasticity at Crack Tip 20

2.2.3.2 Overload Effects 22

2.2.4 Pommier's analysis 24

2.3 Measurement of fatigue crack closure 26

2.3.1 Interferometric Strain/Displacement Gauge 27

2.3.2 Moiré interferometry 28

2.3.3 Digital image correlation 30

2.3.3.1 MATLAB DIC procedure 32

3 Fatigue Crack Analysis Under Constant Amplitude Loading 34
3.1 Testing Methodology . . . 35
3.1.1 Material and specimen characterization . . . 35
3.1.2 Experimental Set-up . . . 36
3.1.3 Specimen Loading . . . 40
3.1.3.1 Plastic Zone Size . . . 47
3.2 Image Analysis . . . 49
3.2.1 Crack Length Calculations . . . 53
3.2.2 Displacement Along Crack Flanks . . . 54
3.3 Elastic Model . . . 56
3.3.1 Calculating the Stress Intensity Factor . . . 62
3.4 Elastic-plastic Model . . . 73
3.4.1 Calculating K During Loading . . . 73
3.4.2 $K - \rho$ space . . . 76
3.5 Modelling with Full Displacement Field . . . 84
3.6 Results from All Specimens . . . 87
3.7 Pre-Cracked Specimen Comparison . . . 91
3.8 Conclusions . . . 95

4 Fatigue Crack Analysis Under Variable Amplitude Loading 96
4.1 DIC tracking of points . . . 97
4.2 Displacement Analysis . . . 99
4.2.1 Overload Cycle . . . 100
4.2.2 Post Overload . . . 103
4.3 Crack Growth . . . 110
4.4 Elastic Model Analysis . . . 112
4.4.1 Single Overload Cycle . . . 112
4.4.2 Post Overload Analysis . . . 114
4.5 Elastic Plastic Model Analysis . . . 121
4.5.1 Single Overload Cycle . . . 121
4.5.2 Post Overload Analysis . . . 122
4.6 Conclusions . . . 127

5 Imaging with a Scanning Electron Microscope **129**
5.1 Testing Methodology 130
5.1.1 Experimental Set-up 130
5.1.2 Specimen Loading 131
5.1.2.1 Plastic Zone Size 136
5.2 Data Collection & Processing 137
5.3 Constant Amplitude Loading 139
5.3.1 Displacement Along Crack Flanks 139
5.3.2 Elastic Model Analysis 141
5.3.3 Elastic-plastic Model 145
5.4 Variable Amplitude Loading 146
5.4.1 Displacement Along Crack Flanks 149
5.4.1.1 Overload Cycle 149
5.4.1.2 Post Overload Cycles 150
5.4.2 Elastic Model Analysis 152
5.4.3 Elastic-plastic Model 158
5.5 Conclusions 161

6 Conclusions and Future Work **163**
6.1 Conclusions 163
6.2 Future Work 166

Bibliography **167**

References **168**

List of Figures

2.1 Three basic modes of applying a force to enable crack propagation . . 4
2.2 Definition of the coordinate axis ahead of a crack tip. The z direction is normal to the page [1] 5
2.3 An initial approximation of the crack tip plastic zone [2] 6
2.4 Irwin's analysis schematic [2] 7
2.5 The plastic zone size defined by Irwin [2] 9
2.6 The strip-yield model. The plastic zone if modeled by yield magnitude compressive stresses at each brack tip (b) [1]. 9
2.7 Dimensionless plastic zone shapes using von Mises criterion with Poisson's ratio of $\nu = 1/3$ [3] 11
2.8 Small scale yielding concept showing various regions ahead of the crack tip [3] 12
2.9 Typical fatigue crack growth behaviour in metals [1] 14
2.10 Typical stresses along crack during a loading cycle [3] 15
2.11 A variety of different fatigue crack closure mechanisms [3] 17
2.12 Three-dimensional crack highlighting the regions where plane stress and plane strain modes are dominant with a curved crack front [3] . . 18
2.13 Various deformation modes at the crack tip of cracks under predominantly: a) Plane strain; b) Plane stress [2] 19
2.14 Planes of maximum shear stress ahead of the crack front of cracks predominantly under: a) Plane stress; b) Plane strain [3] 19
2.15 Superposition model for the relative sizes of monotonic and cyclic plastic zones at the tip of a fatigue crack [4] 21
2.16 Deformation at the crack tip during a single loading cycle. (a) crack in a virgin material. (b) plastic zone formation and crack blunting resulting from an applied tensile load, and (c) residual compressive stresses at the crack tip after unloading [1]. 22

2.17 Typical crack growth behaviour following the application of a single overload [1]. 23
2.18 The nominal stress intensity factor K_I^∞ plotted against the plastic flow intensity factor ρ as calculated using the finite element results for a cyclically increasing load sequence [5]. 26
2.19 Diffraction by the specimen grating produces beams with plane wave fronts for the no-load condition. Warped wave fronts result from inhomogeneous deformation of the specimen [6] 29
2.20 Foundations of DIC: a) Mapping from the un-deformed to the deformed space; b) Correlation function, r_{ij} plotted against in-plane displacements [7] 30
2.21 Two-dimensional digital image correlation, basic principle ($WCor = 3$) [3] 31

3.1 Tensile tests on aluminium alloy 6082 T6, the same material used for work in this chapter, performed by Paulo de Matos [3]. 36
3.2 Schematic representation of the experimental setup. 37
3.3 Images taken of the experimental setup during testing. 38
3.4 Specimen with fitted crack mouth opening displacement (CMOD) gauge [3]. 39
3.5 Drawing of grips used to apply load to specimen. Grips feature flat bottom holes and comply with ASTM E647-11 standards [3, 8]. Dimensions in mm. 40
3.6 Arrangement of components around the specimen used for fatigue testing [8]. 41
3.7 Recommended Compact Tension specimen dimensions from ASTM E647 - 11 Standard Test Method for Measurement of Fatigue Crack Growth Rates [8]. 42
3.8 CT Specimen dimensions in mm. 42
3.9 Image of a fatigue crack propagating from the tip of the notch cut in the specimen. This image is 1280×1024 pixels and the area captured is 1414×1131 µm and was taken with a load of 2 kN applied to the specimen. 43
3.10 Force data from loading the CT specimen at 5 Hz. 44
3.11 Force data from loading the CT specimen during image capture at 0.025 Hz. 44

3.12 Image capture process showing captured of image ahead of the crack tip before and after the crack has grown into this region. 46
3.13 Plastic zone shapes according to von Mises criterion with $a/W = 0.25$ and a maximum load of 2 kN. The coordinate point (0,0) represents the crack tip and axis values are distance (μm) around the crack tip. For plane strain $\nu = 0.33$. 48
3.14 Plane stress plastic zone shape according to von Mises criterion superimposed on image of the crack tip. This crack has a length of 8.9 mm (a =20.9 mm and $a/W = 0.348$) and the load is 2 kN. Points where displacement was measured with Digital Image Correlation are included for reference. 48
3.15 Plane stress plastic zone shape according to von Mises criterion superimposed on full image of a crack with length of 8.9 mm (a =20.9 mm and $a/W = 0.348$). The load is 2 kN. 48
3.16 Images of the crack tip taken during a complete loading cycle. Images are aligned after being captured to keep the crack in a similar position on each image. 50
3.17 Scale attached to surface of specimen used to convert pixels to units of length. The lines of this scale are spaced 0.25 mm. 51
3.18 A typical image of a crack with a grid of points where displacements are measured using DIC. Displacement is analysed at 2400 points on either side of the crack. 52
3.19 Collection of 10 images along a crack face aligned together to give an image of the full crack from the tip of the specimen notch. The specimen was loaded at 2 kN in this image and had been subjected to 32,600 loading cycles. This image was used to determine crack length. 54
3.20 Typical variation of relative displacement at points 50 µm and 940 µm from the crack tip. The sinusoidal applied load (P) and measurements from the CMOD gauge are plotted along with these displacements for comparison. 55
3.21 Relative load plotted against displacement, for three different sets of points located 50 µm, 475 µm and 900 µm from the crack tip. 56
3.22 Calculated vertical displacement field around a crack tip according to Equation (3.4). Crack has length of 8.9 mm (a =20.9 mm and $a/W = 0.348$) and $P = 2$kN. 58

3.23 Vertical displacement of points at various distances from the crack tip. The load applied to the specimen varies with the image number as shown in Figure 3.20. 59
3.24 Displacement of points located (a) 50 µm and (b) 900 µm from crack tip. The calculated displacement is found with Equation (3.6) but is normalised with the displacement measured using DIC at the minimum load to account for the DIC measurements all being measured relative to the displacement at 0.25 kN. 59
3.25 Calculated value of u_y at 2 kN using Equation (3.4) at locations of the grid points as shown in Figure 3.18 compared with calculated displacements using Equation (3.6) of points along the crack flank. 60
3.26 DIC measured displacement of points at load of 2 kN plotted with calculated displacement along crack faces according to Equation (3.6). In (b) the calculated displacement for all points at load 0.25 kN is subtracted from the calculated displacements shown in (a). 61
3.27 DIC measured displacement of points at load of 2 kN plotted with calculated displacement at measured points according to Equation (3.4). In (b) the calculated displacement for all points at load 0.25 kN is subtracted from the calculated displacements shown in (a). 61
3.28 (a)$\mu_y/\sqrt{r}$ vs r graph for various loads (P/P_{max}) during a single loading cycle. (b) Gradient of linear regression line from $\mu_y/\sqrt{r}$ vs r plot for all points (P/P_{max}) during a full loading cycle. 63
3.29 (a)$\mu_y/\sqrt{r}$ vs r graph for various loads (P/P_{max}) during a single loading cycle with the points within 200 µm of the visually located crack tip excluded. (b) Gradient of linear regression line from $\mu_y/\sqrt{r}$ vs r plot for all loads (P/P_{max}) during a full loading cycle. 64
3.30 (a)$\mu_y/\sqrt{r}$ vs r graph for various loads (P/P_{max}) during a single loading cycle with the crack tip location displaced by 65 µm and therefore all r values increased by this amount. (b) Gradient of linear regression line from $\mu_y/\sqrt{r}$ vs r plot for all loads (P/P_{max}) during a full loading cycle. 65
3.31 Calculated plastic zone size (r_p), according to Equation (2.4), in relation to load applied to specimen (P/P_{max}). 68
3.32 $\mu_y/\sqrt{r}$ vs r graph for various loads (P/P_{max}) during a single loading cycle with the crack tip location displaced by the plastic zone radius (Equation (2.4)) determined at each given load. 69

3.33 Calculated plastic zone size (r_p), according to Equation (2.4), in relation to load applied to specimen (P/P_{max} [grey]. 'Optimum' crack tip displacement distances are plotted for selected loads. 70
3.34 Comparison of K values calculated from the y intercept of best fit linear regression lines of $\mu_y/\sqrt{r}$ vs r plots (Equation (3.7)) and those predicted with an analytical equation based on the specimen geometry and load (Equation (3.1)). 72
3.35 Variations of relative displacement (u_y) with distance from the crack tip (r) at eight different values of load (P/P_{max}) during the loading phase of a single cycle. 74
3.36 Coefficient of determination (R^2) values of regression line fitted to u_y vs $\sqrt{r}$ plotted data (Figure 3.35) for $P/P_{max} > 0.4$. 74
3.37 Variations of relative displacement (u_y) with distance from the crack tip (r) at four different values of load (P/P_{max}) during the loading phase of a single cycle. 75
3.38 Predicted K value at crack tip during loading cycle (Equation (3.1)) plotted with typical calculated K values from experimentally obtained displacement data. Displacements from loading and unloading phases are used to calculate K by fitting linear regression lines to u_y vs $\sqrt{r}$ plots. 77
3.39 K vs ρ plots of points with various adjustments to the collected data 78
3.40 K vs ρ plot for loads $P/P_{max} > 0.4$. 79
3.41 Plots of u_y vs $\sqrt{r}$ at low loads with the best fit regression lines potted over data points. The y intercept of these fitted lines is the measure of ρ. 80
3.42 Plots of u_y vs $\sqrt{r}$ at low loads for points near the crack tip with the best fit regression lines potted over data points. The y intercept of these fitted lines is the measure of $/rho$. 81
3.43 (a) K vs Load and (b) K vs ρ plots for a single loading cycle. K and ρ are calculated from the gradients and y-intercepts of fitted regression lines to u_y vs $\sqrt{r}$ plots for points within 140 µm of the crack tip. . . . 83
3.44 Smoothed K vs ρ graph calculated from points within 140 µm of the crack tip. This graph is the same data as in Figure 3.43b but smoothed using a moving average. 83
3.45 Typical u_y vs $\sqrt{\frac{r}{2\pi}}\sin\frac{\theta}{2}\left(1+\sin^2\frac{\theta}{2}-\nu\cos^2\frac{\theta}{2}\right)$ plot for various loads (P/P_{max}) during a single loading cycle. 85

3.46 K vs Load and K vs ρ plots calculated from linear regression lines fitted to data on u_y vs $\sqrt{\frac{r}{2\pi}}\sin\frac{\theta}{2}\left(1+\sin^2\frac{\theta}{2}-\nu\cos^2\frac{\theta}{2}\right)$ plots. 86
3.47 K vs Load and K vs ρ plots calculated from linear regression lines fitted to data on u_y vs $\sqrt{\frac{r}{2\pi}}\sin\frac{\theta}{2}\left(1+\sin^2\frac{\theta}{2}-\nu\cos^2\frac{\theta}{2}\right)$ plots with the crack tip location displaced 55.5 µm ahead of where it was visually located. 86
3.48 Crack growth data for all specimen analysed during constant amplitude loading. 88
3.49 Selection of K vs ρ plots for a number of specimen at various crack lengths with the crack tip position offset. Crack length is a from the specimen geometry (Figure 3.7). 89
3.50 ΔK vs Crack Length for all specimen during constant amplitude loading. Analytical K calculated from specimen geometry and experimental K calculated from displacement data. 89
3.51 $\Delta\rho$ vs Crack Length for each loading cycle analysed over a number of specimen. Displacements were added to the crack tip position for each set of images and $\Delta\rho$ was determined for $P/P_{max} > 0.4$ kN. 90
3.52 91
3.53 92
3.54 Typical u_y vs $\sqrt{\frac{r}{2\pi}}\sin\frac{\theta}{2}\left(1+\sin^2\frac{\theta}{2}-\nu\cos^2\frac{\theta}{2}\right)$ plot for various loads during a single loading cycle using an uncracked specimen image as the base image for displacement measurements. 92
3.55 K vs Load and K vs ρ plots using an uncracked specimen image as the base image for displacement measurements. Calculated from linear regression lines fitted to data on u_y vs $\sqrt{\frac{r}{2\pi}}\sin\frac{\theta}{2}\left(1+\sin^2\frac{\theta}{2}-\nu\cos^2\frac{\theta}{2}\right)$ plots. 93
3.56 K vs Load and K vs ρ plots using an uncracked specimen image as the base image for displacement measurements. Calculated from linear regression lines fitted to data on u_y vs $\sqrt{\frac{r}{2\pi}}\sin\frac{\theta}{2}\left(1+\sin^2\frac{\theta}{2}-\nu\cos^2\frac{\theta}{2}\right)$ plots with the crack tip location displaced 55.5 µm ahead of where it was visually located. 93
3.57 DIC measured displacement of points plotted with calculated displacement at measured points according to Equation (3.4). This uses the uncracked specimen image as the base image for displacement measurements. 94

4.1 Force data from loading the CT specimen before, during and after a single overload cycle at 0.25 Hz. 97
4.2 DIC calculated displacement data showing the badly tracked points (a) during an overload cycle. These points are removed from further analysis and the resulting points used (b). 98
4.3 Points to be tracked with DIC analysis (a) and points that remain after those that are poorly tracked have been removed (b). 98
4.4 Close up images of the crack tip during the maximum load of a regular cycle (a) and the maximum load of an overload cycle (b). 99
4.5 Displacement (u_y) vs Image Number for a point 250 µm from the crack tip directly before, during and after an overload cycle. 99
4.6 Applied Load (P) vs Displacement (u_y) for a point 250 µm from the crack tip directly before, during and after an overload cycle. 100
4.7 Typical variation of relative displacement at points 50 µm and 790 µm from the crack tip during an overload cycle with a maximum load of 3 kN. The sinusoidal applied load (P) and measurements from the CMOD gauge are plotted along with these displacements for comparison. 101
4.8 Typical residual displacements of points along a crack when the load is returned to a minimum (0.25 kN) after an overload of 3 kN. 102
4.9 Relative load plotted against displacement, for three different sets of points located 50 µm, 500 µm and 790 µm from the crack tip. These displacements are from an overload cycle with a maximum load of 3 kN. 102
4.10 DIC measured displacement of points at 2 kN (a) and at an overload of 3 kN (b) plotted with calculated displacement at measured points according to Equation (3.4). 103
4.11 Typical variation of relative displacement at points 50 µm and 790 µm from the crack tip directly after an overload cycle with a maximum load of 3 kN. The sinusoidal applied load (P) and measurements from the CMOD gauge are plotted along with these displacements for comparison. 104
4.12 Relative load plotted against displacement, for three different sets of points located 50 µm, 500 µm and 790 µm from the crack tip. These displacements are analysed for the same points before an overload (a) and after an overload (b). 104
4.13 DIC measured displacement of points at 2 kN during constant amplitude loading directly after an overload plotted with calculated displacement at measured points according to Equation (3.4). 105

4.14 Relative load plotted against displacement, for three different sets of points located at various distances from the crack tip. These displacements are analysed between 1 and 8000 cycles after a single overload cycle. 106
4.15 Image of crack tip at 2000 cycles post overload. The crack tip position at the overload cycle is shown with the blue arrow. The region that was present during (and prior to) the overload cycle (to the right of the blue arrow) was measured to have higher displacements and less closure. 106
4.16 DIC measured displacement of points at 2 kN during constant amplitude loading between 1 and 8000 cycles after a single overload cycle plotted with calculated displacement at measured points according to Equation (3.4). 107
4.17 Opening Load vs Crack Length determined at a point 250 µm from the crack tip. The opening load is defined as the lowest load where the displacement is above 0.2 µm and displacement at the average of points at the next 10 load values is above 0.5 µm. 109
4.18 Opening Load vs Crack Length for multiple specimen. The plane stress plastic zone size is calculated and doubled. This distance is added to the crack tip position during the overload cycle and shown in light blue shading on each figure. 110
4.19 Rate of crack growth (per cycle) vs ΔK calculated from displacement data for a single specimen before (blue) and after (red) a single overload cycle plotted with a log scale. 111
4.20 u_y vs $\sqrt{\frac{r}{2\pi}}\sin\frac{\theta}{2}\left(1+\sin^2\frac{\theta}{2}-\nu\cos^2\frac{\theta}{2}\right)$ plot for various loads (P/P_{max}) during a single overload cycle. 112
4.21 K vs Load plot calculated from linear regression lines fitted to data on u_y vs $\sqrt{\frac{r}{2\pi}}\sin\frac{\theta}{2}\left(1+\sin^2\frac{\theta}{2}-\nu\cos^2\frac{\theta}{2}\right)$ plots for a single overload cycle. 113
4.22 u_y vs $\sqrt{\frac{r}{2\pi}}\sin\frac{\theta}{2}\left(1+\sin^2\frac{\theta}{2}-\nu\cos^2\frac{\theta}{2}\right)$ plot for various loads (P/P_{max}) for a cycle directly after a single overload cycle. 114
4.23 K vs Load plots calculated from linear regression lines fitted to data on u_y vs $\sqrt{\frac{r}{2\pi}}\sin\frac{\theta}{2}\left(1+\sin^2\frac{\theta}{2}-\nu\cos^2\frac{\theta}{2}\right)$ plots for a cycle directly after a single overload cycle. 115

4.24 K vs Load plot calculated from linear regression lines fitted to data on u_y vs $\sqrt{\frac{r}{2\pi}}\sin\frac{\theta}{2}\left(1+\sin^2\frac{\theta}{2}-\nu\cos^2\frac{\theta}{2}\right)$ plots for a cycle directly after a single overload cycle. The K value calculated from the specimen geometry is adjusted by subtracting the value of K at a load of 0.25 kN. 116
4.25 u_y vs $\sqrt{\frac{r}{2\pi}}\sin\frac{\theta}{2}\left(1+\sin^2\frac{\theta}{2}-\nu\cos^2\frac{\theta}{2}\right)$ plot for various loads (P/P_{max}) of a cycle 1000 cycles after a single overload cycle. 116
4.26 K vs Load plot calculated from linear regression lines fitted to data on u_y vs $\sqrt{\frac{r}{2\pi}}\sin\frac{\theta}{2}\left(1+\sin^2\frac{\theta}{2}-\nu\cos^2\frac{\theta}{2}\right)$ plots for a cycle 1000 cycles after a single overload cycle. 117
4.27 K vs Load plots at various stages before and after a single overload cycle for points within 300 µm of the crack tip position. 119
4.28 ΔK_{eff} vs (a) crack length and (b) number of cycles applied. Analytical calculation of K based on specimen geometry is plotted in (a)(grey). Calculated ΔK_{eff} based on experimental displacement data before (blue) and after (red) an overload cycle. 120
4.29 Rate of crack growth vs ΔK_{eff} plotted with a log scale. Data points are displayed from before (blue) and after (red) an overload cycle. ΔK_{eff} is calculated from the analysis of experimental displacement data presented in Figure 4.27 120
4.30 K vs ρ plot during a single overload cycle with maximum 3 kN. . . . 122
4.31 K vs ρ plots at various stages before (a) and after a single overload cycle for points within 300 µm of the crack tip. Crack length is a from the specimen geometry (Figure 3.7). 123
4.32 $\Delta\rho$ (as shown in Figure 4.31) vs Crack Length. Cycles before (blue) and after (red) an overload cycle are displayed. 126
4.33 Crack growth rate vs $\Delta\rho$ (as shown in Figure 4.31) with a log scale and linear regression line. Cycles before (blue) and after (red) an overload cycle are displayed. 126

5.1 Carl Zeiss Scanning Electron Microscope similar to that used at Oxford University [9] 130
5.2 Deben In-Situ Microtest tensile & compression stage with a 2 kN load cell [10]. 130
5.3 Dimensions (in mm) of specimens used for in-situ SEM testing. Specimens were cut from a sheet of aluminium alloy 6082-T6 132

5.4 Recommended Compact Tension specimen dimensions from ASTM E647 - 11 Standard Test Method for Measurement of Fatigue Crack Growth Rates [8]. (repeated from page page 42) 132
5.5 Recommended clevis and pin assembly geometry for gripping CT specimens [8]. Tolerance dimensions are in mm (inches). 133
5.6 Dimensions of constructed clevis used to pre crack the CT specimen before loading in the SEM. Dimensions in mm. 134
5.7 Pre cracking the specimen before loading on the Deben testing stage. Adapters for the smaller specimen size are fitted to make use of the experimental set-up used in Chapter 3 134
5.8 Force applied to the specimen during constant amplitude loading. . . 135
5.9 Force applied to the specimen during SEM image capture. 135
5.10 Loading applied to the specimen before, during and after an overload cycle. 136
5.11 Typical image collected from the experiment at a load of 1.25 kN. Sets of points are selected on either side of the crack to measure displacements 138
5.12 Series of images aligned to give an image of the full crack length at a load of 1.25 kN. Crack length is 7.123 mm. 139
5.13 Typical variation of relative displacement u_y vs time (image number) compared to the applied load (P/P_{max}). Relative displacement between points located at 10 µm, 50 µm and 150 µm from the crack tip is shown. 140
5.14 Relative load plotted against displacement, for three different sets of points located 10 µm, 50 µm and 150 µm from the crack tip. 140
5.15 Measured displacement vs r for various stages in a loading cycle. The displacement calculated from the elastic displacement field (Equation (3.4)) is plotted for comparison. 142
5.16 Measured displacement vs r at maximum load of 1.25 kN. The calculated displacement is reduced from Figure 5.15a by the calculated displacement at $P = 0.5$kN (Figure 5.15g) to account for crack closure. 143
5.17 Variations of relative displacement (u_y) with distance from the crack tip (r) at eight different values of load (P/P_{max}) during the loading phase of a single cycle. 144
5.18 Calculated K value at crack tip during loading cycle (Equation (3.1)) plotted with typical calculated K values from experimentally obtained displacement data. 144

5.19 Image of the crack tip with the visually determined crack tip location marked (dark blue 'x') and the crack tip offset by 25 µm (light blue 'x'). 144
5.20 K vs ρ plot for 2 consecutive cycles during constant amplitude loading. 145
5.21 K vs ρ plots calculated using only specific ranges of points near the crack tip. 146
5.22 Series of images of a crack tip captured with the SEM during a single overload cycle 147
5.23 u_y plots of points around the crack tip for an overload cycle. This shows the poorly tracked points and the remaining points after most of these were removed. 148
5.24 Grids of points around the crack tip that were tracked using DIC. Figure (b) shows the remaining points after those that were poorly tracked (Figure 5.23) were removed from analysis. 148
5.25 Displacement of points around the crack flanks at various distances from the crack tip during a single overload cycle.. 149
5.26 Residual displacement along the crack flanks once the load has been returned to the minimum (0.125 kN) at the end of a single overload cycle. 151
5.27 Extension data collected from the Deben testing stage before, during and after a single overload cycle is applied to the specimen. 151
5.28 Measured displacement vs r for various stages in a loading cycle 50 cycles after a single overload cycle has been applied to the specimen. The displacement calculated from the elastic displacement field (Equation (3.4)) is plotted for comparison. 153
5.29 Relative load vs displacement at various points along the crack flank. Graphs shown are for cycles during (a) and after (b-e) a single overload cycle. 154
5.30 u_y vs $\sqrt{\frac{r}{2\pi}}\sin\frac{\theta}{2}\left(1+\sin^2\frac{\theta}{2}-\nu\cos^2\frac{\theta}{2}\right)$ during loading for a single overload cycle. 155
5.31 K vs Load plots for calculated from the displacement around the crack flanks during cycles before (a), during (b) and after (c-e) a single overload cycle. 156
5.32 K vs Load plot for a cycle directly after a single overload cycle. The K value determined by displacement of points around the crack flanks is increased by the calculated K at 0.125 kN and the crack tip is offset by 25 µm. 157

5.33 K vs ρ plots for calculated from the displacement around the crack flanks during cycles before (a), during (b) and after (c-e) a single overload cycle. All displacements are measured from the first image (at minimum load) in each cycle. 159
5.34 K vs ρ plot for cycles before, during and after an overload cycle. All displacements are based off the first image in the cycle before the overload. 160

Chapter 1

Introduction

The most common process in which engineering structures fail under cyclic loading is through fatigue. Fractures develop in materials after a large quantity (often thousands or millions) of load applications that cause progressive and localised damage. In some cases the damage is caused with nominal maximum stress values much lower than the yield strength of the material.

The number of cycles it takes for a fatigue crack to propagate before fracture is important to know as from this data the maintenance and inspection intervals can be made for components. During constant amplitude loading, a very good prediction of this can be made by analysing test specimens to obtain data for the stress intensity factor and crack growth rate. Due to the similitude of the stress intensity factor, K, this experimental data can be applied to a component of the same material under similar conditions and the Paris Law can be applied with constants found from testing. The length of a crack and number of cycles to fracture data can be obtained through integration of a da/dN vs ΔK plot to identify the time (in cycles) required for a crack to grow. This analysis does have limitations and modifications to the Paris Law can be made in order to better incorporate the effects of crack tip plasticity and crack closure. However, this analysis does not incorporate load history effects, which may severely alter the propagation rate of a crack. While constant amplitude

loading does sometimes occur in practice, the vast majority of dynamically loaded structures actually experience variable amplitude loading that is often quite random. This loading is not as simple to analyse and estimation of component life from experimentally observed crack growth rates is much more difficult since precise component conditions are seldom replicated in the available test data. Periodic overloads are a simple example of disturbances to an otherwise constant amplitude loading regime in many practical components. These overloads inhibit crack growth and existing growth prediction techniques, which do not take such events into account, will therefore underestimate the fatigue life of a component and indicate a requirement for premature replacement. Other events in the loading history may have also occurred that lead to crack growth at higher rates than predicted in current models. Therefore, it is important to develop improved methods of life prediction from fatigue cracking which will both reduce the level of conservatism and reduce the risk of over-estimating life. Several models have been proposed to characterise crack growth under variable loading conditions, however, there is no general consensus as to the most accurate method of modelling this phenomenon.

Plasticity-induced crack closure, first investigated and reported by Elber in 1970 [11], is thought to be an important phenomenon that may explain the change in growth rate after changes in the loading cycle. The aim of this research is to investigate plasticity-induced fatigue crack closure and models that predict the amount of closure for a given loading history in an effort to better understand fatigue life. This will be done by using digital image correlation methods to analyse displacements along a growing crack that is subjected to variable loading and comparing experimental results with existing models. Experiments are performed on aluminium alloy 6082 T6, which is widely used in structural applications in the aerospace industry and DIC methods are employed using MATLAB.

Chapter 2

Background and Literature Review

2.1 Linear Elastic Fracture Mechanics

One of the primary aims of Fracture Mechanics is to establish local stress and strain fields around a crack tip by using parameters including loading conditions and the geometry of a structure. By assuming that the material is isotropic and linear elastic, Linear Elastic Fracture Mechanics calculates the stress field near the crack tip using the theory of elasticity. A crack will grow when the material fracture toughness is exceeded. There are three basic modes of loadings on a cracked body as shown in Figure 2.1: opening, sliding and tearing modes. In Linear Elastic Fracture Mechanics, many of the formulas are derived for either plane strain or plane stress associated with these three basic modes of loadings.

The limitation of Linear Elastic Fracture Mechanics is that it is only valid when the conditions for small scale yielding are satisfied. If large plastic deformation zones develop, Elastic Plastic Fracture Mechanics are more suitable.

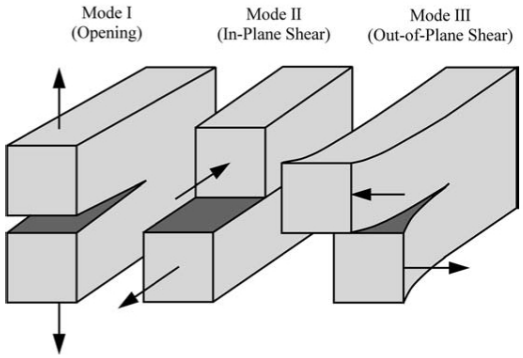


Figure 2.1: Three basic modes of applying a force to enable crack propagation

2.1.1 Crack Tip Stress Analysis

The stress intensity approach to analysing cracks was developed by Irwin in the 1950's. Assuming isotropic linear elastic material behaviour, Irwin showed that the stresses close to the crack tip have the form:

$$\sigma_{ij}(r,\theta) = \frac{K}{\sqrt{2\pi r}} f_{ij}(\theta) + ... \tag{2.1}$$

where r and θ are the cylindrical polar co-ordinates of a point with respect to the crack tip as shown in Figure 2.2. K is called the stress intensity factor, which gives the magnitude of the elastic stress field, while f_{ij} is a dimensionless quantity that depends on load and geometry. The higher-order terms of equation (2.1) depend on geometry, however as $r \to 0$, the leading terms approach infinity while the higher terms remain constant or approach zero. Therefore, the region close to the crack tip is dominated by the singularity and stress varies with $1/\sqrt{r}$ regardless of the cracked body geometry. Displacement near the crack tip varies with $\sqrt{r}$.

The following equations [4] give the stress field ahead of a crack tip for Mode I

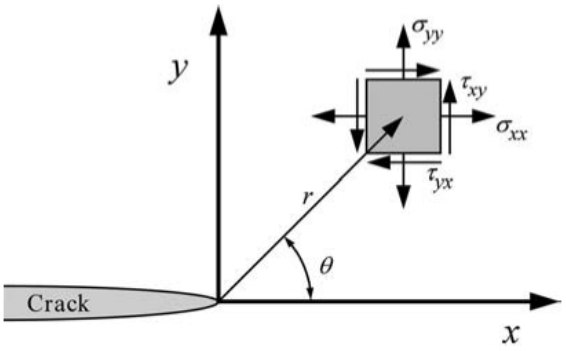


Figure 2.2: Definition of the coordinate axis ahead of a crack tip. The z direction is normal to the page [1]

loading in a linear elastic, isotropic material:

$$\begin{aligned}
\sigma_{xx} &= \frac{K_I}{\sqrt{2\pi r}} \cos\left(\frac{\theta}{2}\right)\left[1 - \sin\left(\frac{\theta}{2}\right)\sin\left(\frac{3\theta}{2}\right)\right] \\
\sigma_{yy} &= \frac{K_I}{\sqrt{2\pi r}} \cos\left(\frac{\theta}{2}\right)\left[1 + \sin\left(\frac{\theta}{2}\right)\sin\left(\frac{3\theta}{2}\right)\right] \\
\tau_{xy} &= \frac{K_I}{\sqrt{2\pi r}} \cos\left(\frac{\theta}{2}\right)\sin\left(\frac{\theta}{2}\right)\cos\left(\frac{3\theta}{2}\right)
\end{aligned} \tag{2.2}$$

From these equations it can be seen that when $\theta = 0$, the near tip stress of a crack subjected to Mode I loading has equal stresses in the x and y directions:

$$\sigma_{xx} = \sigma_{yy} = \frac{K_I}{\sqrt{2\pi r}} \tag{2.3}$$

Equation (2.3) is valid close to the crack tip where the $1/\sqrt{r}$ singularity dominates the stress field. Outside this region the stresses are instead governed by remote boundary conditions. From these equations it can also be seen that the stress intensity factor completely defines the crack tip conditions. If K is known, it is possible to solve for all components of stess, strain and displacement close to the crack tip as a function of r and θ.

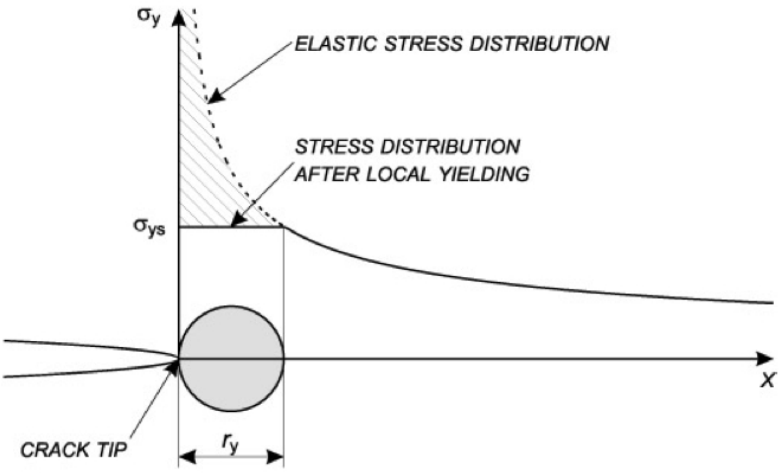


Figure 2.3: An initial approximation of the crack tip plastic zone [2]

2.1.2 Crack Tip Plasticity

At the tip of a crack the elastic field stress is singular and therefore the predicted stress is higher than the yield stress of the material. This results in a zone of plastic deformation ahead of the crack tip. The approximate size of the plastic zone ahead of the crack tip ($\theta = 0°$) can be estimated by calculating the elastic stress field ahead of the crack tip to yield stress [3].

$$\sigma_y = \frac{K_I}{\sqrt{2\pi r}} \iff r_y = \frac{1}{2\pi}\left(\frac{K_I}{\sigma_{ys}}\right)^2 \tag{2.4}$$

The value r_y corresponds to the diameter of a circular plastic zone while σ_{ys} represents the yield strength of the material. As shown in Figure 2.3, part of the stress distribution is simply cut off above the σ_{ys} value (displayed hatched in the figure), which is why this is only an initial approximation. The shape of the plastic zone is also an approximation and in this case it is simply assumed that the plastic zone is circular. A better approximation for the shape can be obtained by looking at the region in the elastic solution where the yield criterion is exceeded as shown in section 2.1.2.3.

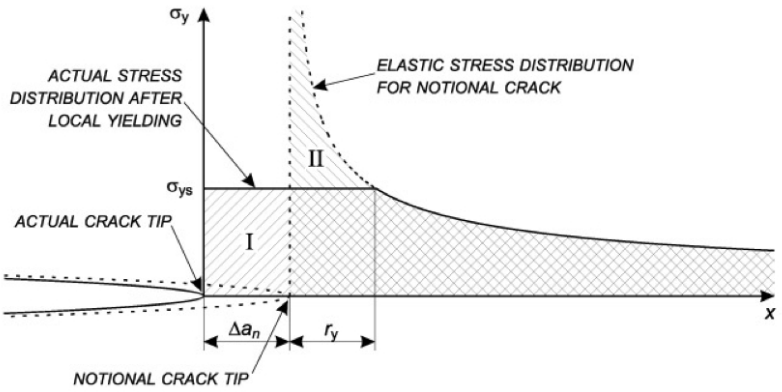


Figure 2.4: Irwin's analysis schematic [2]

2.1.2.1 Irwin's Plastic Zone Size

In 1957 a group working under G. R. Irwin [12] at the United States Naval Research Laboratory noted that plasticity plays a crucial role in the fracture of ductile materials. In these materials, a plastic zone develops at the tip of a crack as described earlier. The plastic zone size increases as the load is increased until the crack grows and the material behind the crack tip is unloaded. Irwin's analysis takes into account the stress distribution ahead of the crack tip and attempts to account for the deficiency in the initial approximation of the stress distribution simply being cut off above σ_{ys} (Figure 2.3). For his analysis to be straightforward he considers: 1) The plastic zone is a circular shape; 2) Only the situation along the x-axis is analysed; 3) The material behaviour is assumed to be elastic-perfectly plastic; 4) A plane stress state is considered.

Irwin's analysis argues that due to the occurrence of plasticity at the crack tip; the crack behaves as if it were actually longer than its physical size. This means that the displacements are larger and the stiffness is lower than in the elastic case. The effective length of the crack a_{eff} can be defined as:

$$a_{eff} = a + \Delta a_n \tag{2.5}$$

where Δa_n is the notional crack increment as shown in Figure 2.4. This crack increment accounts for the redistribution of stresses that are above σ_{ys} in the elastic case. In Figure 2.4 the σ_y distribution from the elastic solution for a crack length of $a + \Delta a_n$ is shown along with the actual σ_y distribution after local yielding. If the stresses transmitted by these two distributions are equal then area I will be equal to area II:

$$\begin{aligned} \sigma_{ys} \cdot \Delta a_n &= \int_0^{r_y} \frac{\sigma\sqrt{\pi(a+\Delta a_n)}}{\sqrt{2\pi r}}\, dr - \sigma_{ys} \cdot r_y \quad \text{or} \\ \sigma_{ys}(\Delta a_n + r_y) &= \int_0^{r_y} \frac{\sigma\sqrt{\pi(a+\Delta a_n)}}{\sqrt{2\pi r}}\, \frac{dr}{\sqrt{r}} = \frac{2\sigma\sqrt{a+\Delta a_n}}{\sqrt{2}}\sqrt{r_y} \end{aligned} \tag{2.6}$$

For a crack with length of $a + \Delta a_n$

$$r_y = \frac{1}{2\pi}\left(\frac{K_I}{\sigma_{ys}}\right)^2 = \frac{\sigma^2}{2\sigma_{ys}^2}(a + \Delta a_n) \tag{2.7}$$

Which can be used to substitute for $\sigma\sqrt{a+\Delta a_n}$ in Equation 2.6 to give

$$\sigma_{ys}(\Delta a_n + r_y) = \frac{2\sigma\sqrt{2r_y}\sqrt{r_y}}{\sqrt{2}} \tag{2.8}$$

And

$$\Delta a_n + r_y = 2r_y \tag{2.9}$$

Therefore the first approximation for the plastic zone size, r_y, is equal to the notional crack increment and the plastic zone diameter is twice that obtained as a first approximation. The notional crack tip extends to the centre of a circular plastic zone as shown clearly in Figure 2.5. At a distance $2r_y$ ahead of the actual crack tip, the elastic stress distribution $\sigma_y = \frac{K_I}{\sqrt{2\pi r}}$ takes over from σ_{ys} and therefore K_I determines the plastic zone size (Equation 2.4) along with the stresses and strains outside the plastic zone.

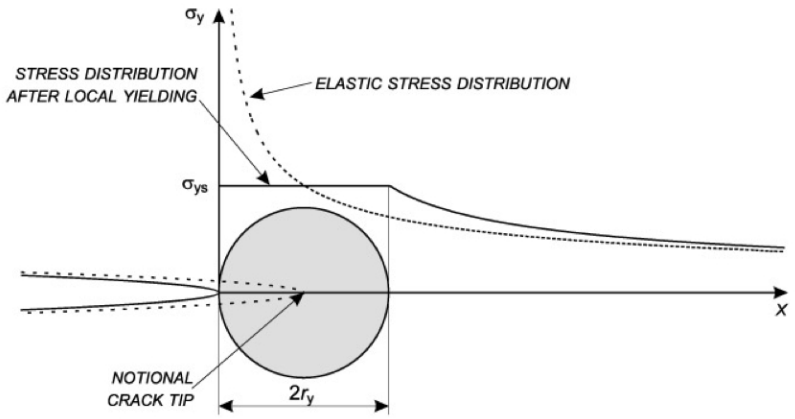


Figure 2.5: The plastic zone size defined by Irwin [2]

2.1.2.2 Strip-Yield Model

The strip-yield model was first developed by Dugdale [13] and Barenblattt [14]. In this analysis it is assumed that all plastic deformation concentrates in a long, slender strip in front of a crack tip. The material behaviour is assumed to be elastic-perfectly plastic and in a plane stress state. As in Irwin's analysis, Dugdale argued that the effective crack length is longer than the physical length. The first case considered in early analysis was that of a through crack in an infinite plane as shown in Figure 2.6. In this case the crack is modelled with a length of $2a + 2\rho$, where ρ is the length of the plastic zone. The plastic zone is considered to carry the yield stress σ_{ys} (Figure 2.6 (b)). The derivation of the Dugdale formula can be made in two ways: 1) Superimposing two elastic solutions of a through crack under remote tension and another with closure stresses at the tip; 2) formally using complex stress functions.

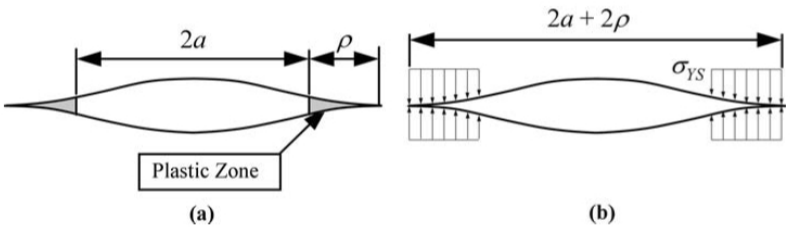


Figure 2.6: The strip-yield model. The plastic zone if modeled by yield magnitude compressive stresses at each brack tip (b) [1].

In the strip-yield zone the stresses are finite and therefore a stress singularity does not exist at the crack tip as it does in basic elastic analysis (section 2.1.1). This means that the leading term of equation (2.1) is equal to zero. When using the singularity derivation, the plastic zone length ρ is chosen so that the stress intensity factors from the remote tension and closure stress will balance and cancel each other. Using superposition to derive the size of the plastic zone will give:

$$\rho = \frac{\pi^2 \sigma^2 a}{8\sigma y s^2} = \frac{\pi}{8}\left(\frac{K_I}{\sigma_{ys}}\right)^2 \tag{2.10}$$

for $\sigma << \sigma_{ys}$. Because Irwin's analysis gives a plastic zone of diameter $2r_y$, it can be seen from equation (2.4) that this diameter is equal to $\frac{1}{\pi}\left(\frac{K_I}{\sigma_{ys}}\right)^2 = 0.318\left(\frac{K_I}{\sigma_{ys}}\right)^2$. The Dugdale plastic zone is similar but slightly larger as $\rho = \frac{\pi}{8}\left(\frac{K_I}{\sigma_{ys}}\right)^2 = 0.393\left(\frac{K_I}{\sigma_{ys}}\right)^2$.

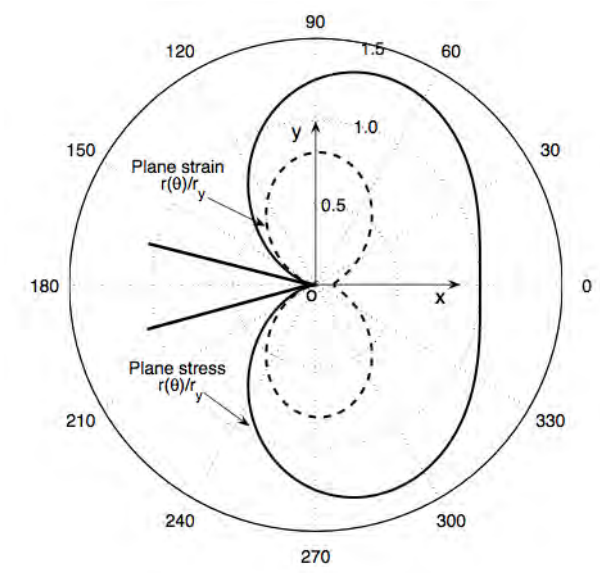
2.1.2.3 Plastic Zone Shape

The approaches by Irwin and Dugdale give an approximation for the plastic zone size, however they use a selected shape of a circle. The shape of the plastic zone can be determined from a first order approximation to the size. Estimates can be made using classical yielding criteria such as Tresca or von Mises which both give similar results. The von Mises criterion states that yielding will occur when:

$$(\sigma_1 - \sigma_2)^2 + (\sigma_2 - \sigma_3)^2 + (\sigma_3 - \sigma_1)^2 = 2\sigma_{ys}^2 \tag{2.11}$$

The plastic zone shapes for plane stress and plane strain conditions are quite different and are given by the following equations [4]:

$$\frac{r(\theta)_{PlaneStress}}{r_y} = \frac{1}{2} + \frac{3}{4}\sin^2(\theta) + \frac{1}{2}\cos(\theta) \tag{2.12}$$



[t]

Figure 2.7: Dimensionless plastic zone shapes using von Mises criterion with Poisson's ratio of $\nu = 1/3$ [3]

$$\frac{r(\theta)_{PlaneStrain}}{r_y} = \frac{3}{4}\sin^2(\theta) + \frac{1}{2}(1-2\nu)^2(1+\cos(\theta)) \tag{2.13}$$

A plot of these equations is shown in Figure 2.7 with the shapes calculated using a Poisson's ratio of $\nu = 1/3$.

2.1.2.4 Small Scale Yielding

The small scale yielding condition requires the stresses being evaluated to be within the region in which K_I is accurate but outside the plastic zone at the crack tip. The K_I dominant zone is shown in Figure 2.8 and is sometimes referred to as the singularity-dominated zone [1] due to the $1/\sqrt{r}$ singularity dominating the stress field in this region. In region 2 of Figure 2.8, higher order terms become more significant when looking for an accurate solution (equation (2.1)) and K does not uniquely characterise the magnitude of these higher order terms. Outside both of these regions, the stresses are essentially the remote applied stress.

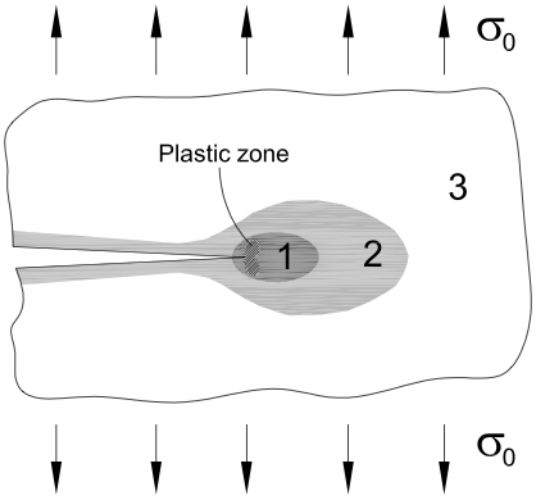
[h]


Figure 2.8: Small scale yielding concept showing various regions ahead of the crack tip [3]

2.2 Fatigue Crack Propagation

Fatigue cracks form due to the weakening of a material caused by repeatedly applied loads. With loads above a certain threshold, microscopic cracks will form and gradually propagate as the cyclic loading is continued. Eventually a crack will reach a critical length and the structure will fracture as the crack suddenly propagates further.

2.2.1 Similitude of K

The main idea behind the similitude principle is related to the fact that the size of an object is relative and physical phenomena within an object can be reduced to size independent relations [15]. Another way of describing the approach is that "similar conditions applied to the same system will have similar consequences" [4]. An example of this approach being used is with Hooke's Law, which uses the size independent similitude parameters of stress and strain to relate the force-deflection behaviour in a structure. With these similitude parameters, a size independent material constant called the elastic modulus can be defined.

This approach can be applied to fatigue crack growth. In this case the crack growth behaviour is reduced to material behaviour that is independent of crack length. In order to do this a similitude parameter is defined, which relates the conditions for similitude between the various ranges of crack geometries that may exist. The stress intensity factor, K, is used in metals and becomes the similitude in crack growth analysis. The linear elastic K is a simplification of the stress state in front of a crack and is examined because the driving force for growth of a crack is related to the stress state ahead of the crack tip. Similitude implies that a similar K cycle applied to a crack in a standard test specimen will induce the same crack growth increments in a structure with an arbitrary geometry consisting of the same material.

Static and fatigue crack growth can be differentiated with K defined as a similitude parameter. Static crack propagation occurs when a critical value of K is reached, as static crack growth is related to a critical stress state in front of the crack tip. This critical stress intensity factor is often referred to as the fracture toughness of a solid. With fatigue crack growth, the similitude parameter can be defined as $\Delta K = K_{max} - K_{min}$ due to growth being related to the cyclic stress state ahead of the crack tip.

The relationship between ΔK and da/dN for constant amplitude loading was an important discovery as the stress intensity - crack length relationship for components can be found from standard tests. With this the da/dN for various crack lengths can be found and integrating the $da/dN - \Delta K$ data from a standard test over a range of crack lengths will produce an $a - n$ curve that displays the growth of a fatigue crack by the number of cycles. The number of cycles required for a crack to grow to a maximum permissible length before failure can be estimated from this data.

The similitude approach seems to be physically sound and logical, however, close examination is needed to ensure that similar conditions do apply. Besides ΔK in fatigue crack growth, the growth rate also depends on the stress ratio (R), load

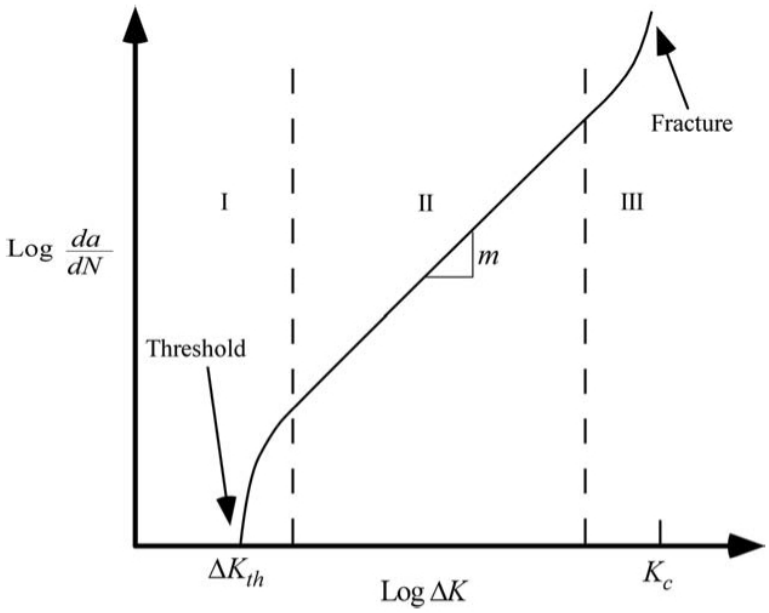


Figure 2.9: Typical fatigue crack growth behaviour in metals [1]

frequency, environment, shape of the load cycle, temperature and the load history.

Fatigue crack growth can be divided into three regions on a $da/dN - \Delta K$ curve. In region I a threshold stress intensity factor ΔK_{th} exists and below this value a crack will either not propagate or propagate at an extremely low rate. By knowing this value the range of stresses applied to a crack or crack lengths can be calculated in order to avoid crack growth. Region II is characterised by a linear fit between $\log(da/dN)$ and $\log(\Delta K)$ which is defined by the Paris Law:

$$\frac{da}{dN} = C(\Delta K)^m \tag{2.14}$$

In region III, prior to failure, the crack growth rate rises sharply. In this region the K_{max} in the fatigue stress cycle becomes equal to the critical stress intensity factor, K_c, and failure occurs.

2.2.2 Crack Closure

The phenomenon of fatigue crack closure was first studied and reported by Elber in 1970 [11]. It was found that during a stress cycle, a fatigue crack is partly or fully closed rather than always open from the tip as one might first think. The nature of the crack opening and closing was dependent on position in the loading cycle. This is shown in Figure 2.10 where the opening stress (σ_{op}) and closing stress (σ_{cl}) are marked. The opening stress is the stress level where the crack becomes fully open and free of compressive stresses during loading while the closing stress is the level at which contact between the crack faces first occurs during unloading. The behaviour shown in Figure 2.10 was attributed to residual plastic deformation left along the crack faces during crack propagation including significant compressive stresses in this region.

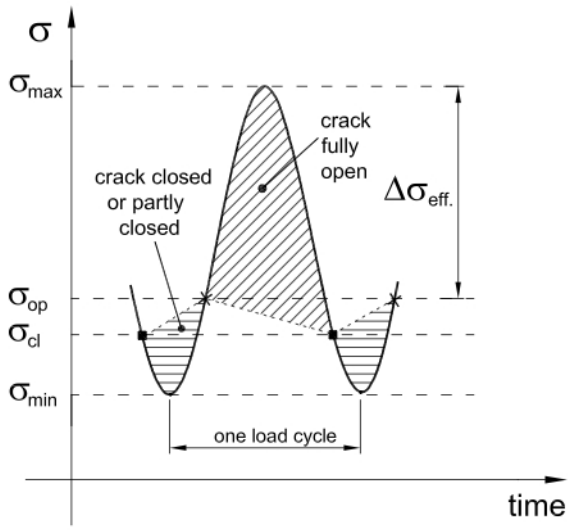


Figure 2.10: Typical stresses along crack during a loading cycle [3]

Elber proposed the following equation for crack opening stresses based on experiments on 2024-T3 Al alloy:

$$\frac{\sigma_{op}}{\sigma_{max}} = 0.5 + 0.1R + 0.4R^2 \qquad -0.1 \leq R \leq 0.7 \tag{2.15}$$

In this equation σ_{max} is the maximum applied stress during a loading cycle as shown in Figure 2.10. It was suggested by Elber that stress variation contributes to the crack extension if $\sigma > \sigma_{op}$ and stress singularity occurs at the crack tip. This led to a definition of an effective stress range $\Delta\sigma_{eff}$ as

$$\Delta\sigma_{eff} = \sigma_{max} - \sigma_{op} \tag{2.16}$$

The corresponding effective stress intensity factor range is then

$$\Delta K_{eff} = (\sigma_{max} - \sigma_{op}) \cdot \sqrt{\pi a} = \Delta\sigma\sqrt{\pi a} \tag{2.17}$$

Elber went on to propose a modified version of the Paris Law, which can be expressed as

$$\frac{da}{dN} = C(U \cdot \Delta K)^m \quad \text{or} \quad \frac{da}{dN} = C(\Delta K_{eff})^m \tag{2.18}$$

Where

$$U = \frac{K_{max} - K_{op}}{K_{max} - K_{min}} = \frac{\Delta K_{eff}}{\Delta K} \tag{2.19}$$

Fatigue crack closure has subsequently been extensively investigated given the relevance on Elber's findings. It has been found that there are various different phenomena that lead to numerous distinctive forms of crack closure as shown in Figure 2.11. In general, it is thought that fatigue crack closure is an intrinsic feature of growing fatigue cracks that can have an influence on many different aspects of crack growth. Incorporation of closure effects in calculations allows for more accurate predictions in crack growth rates for both long and short fatigue cracks [16, 17] in many applications under both constant and variable amplitude loading. Given the extensive research carried out since Elber's work, it is not surprising that there have also been a number of controversial or contradictory findings reported. Included in these findings are measurements of different magnitudes of closure that have been

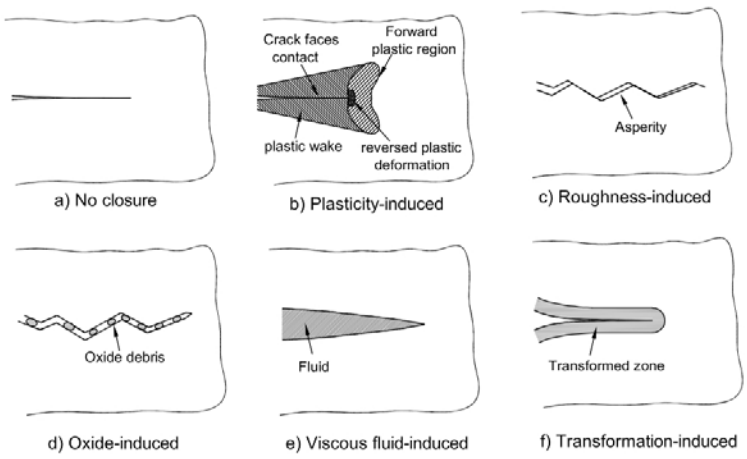


Figure 2.11: A variety of different fatigue crack closure mechanisms [3]

found with different measurement techniques, the presence of crack closure under plane strain conditions and the ability of load history effects to be accounted for by crack closure. These issues are discussed comprehensively in work by de Matos [3].

2.2.2.1 Plasticity-induced Crack Closure

Crack closure has been experimentally investigated by various techniques over many years. These techniques include acoustic emission [18] and compliance methods [11, 18] among others. These studies have generally proven the importance on crack closure in fatigue and that plasticity-induced closure is the dominant mechanism under many conditions [19]. Plasticity-induced crack closure results from the near-tip plastic strains under cyclic loading which causes the premature contact of crack surfaces. As a fatigue crack propagates through plastically deformed material at the crack tip, residual plastic displacements are left in the wake of the crack tip, which can be seen in Figure 2.11 b). These displacements press together the fracture surfaces, which transmit residual compressive stresses across the plastic wake causing the crack to be partly or fully closed at points in a loading cycle.

In thin sheet materials, the plasticity induced crack closure is seen clearly as plane stress conditions prevail with the dominant effect of plastic deformation. However,

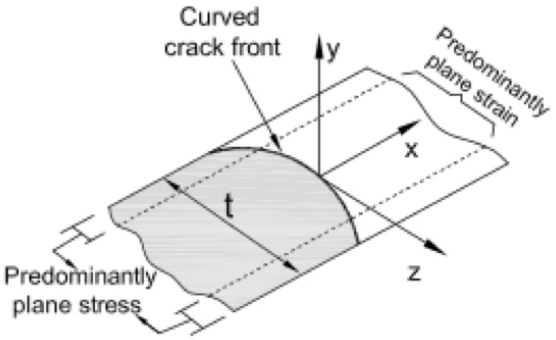


Figure 2.12: Three-dimensional crack highlighting the regions where plane stress and plane strain modes are dominant with a curved crack front [3]

in thicker materials with fatigue cracks the problem is more three-dimensional rather than a plane problem, which is more complicated, and it is hard to pinpoint exactly where the crack tip is located. At the surface the condition is similar to plane stress although there is a stress gradient along the crack front in the through-thickness direction to the approximately plane strain on the interior of the material. The crack front is also generally not straight but usually curved which may cause different growth rates and plastic flow in the surface layers. This curved nature of the crack front is displayed in Figure 2.12 along with plane stress shown at the surface along the crack and plain strains on the material interior.

It is the thickness of material and loading conditions that determine whether the stress state within the crack is predominantly plane stress or plane strain. No exact model exists for determining this transition from plane stress like state to plane strain like state. It is sometimes suggested in literature that a plane stress situation through the full material thickness will be obtained if the plane stress formula calculated value, r_y, of the estimated plastic zone size is equal or larger than half the material thickness [20].

Different deformation modes lead to different positions of the planes to maximum shear stress at the crack front. It is important to distinguish between the plane stress

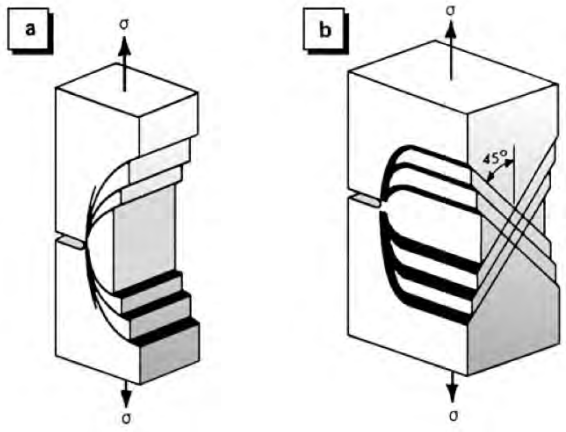


Figure 2.13: Various deformation modes at the crack tip of cracks under predominantly: a) Plane strain; b) Plane stress [2]

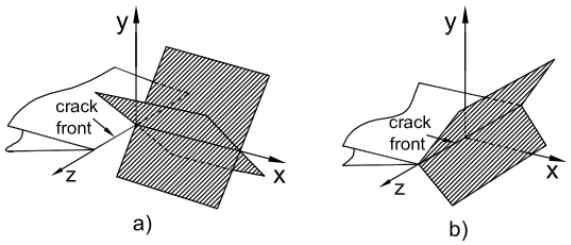


Figure 2.14: Planes of maximum shear stress ahead of the crack front of cracks predominantly under: a) Plane stress; b) Plane strain [3]

and plane strain as they each lead to these different deformation modes and therefore different orientation of stress at the crack front. The different deformation modes are displayed schematically in Figure 2.13. Under plane strain, the planes of maximum shear stress are inclined about 70° to the crack plane (Figure 2.14 a) while under plane stress, the maximum shear stress planes cross in front of the crack front at a 45° angle (Figure 2.14 b). In a three-dimensional case both of these stresses are present in different regions of the crack front and therefore the situation is significantly more complex.

The mechanism of plasticity induced fatigue crack closure under plane stress conditions has been examined thoroughly and there is some understanding of the phenomenon. When the load is applied, flow of material can occur and a residual wedge develops on the flanks of an advancing fatigue crack. This wedge results from material

coming from the side faces of the specimen and leaves a wake of plastic deformation along the crack flanks. With plane strain conditions however, it is difficult to imagine the origin of this plastic wedge as plastic flow does not change the volume of a material except in other cases where deformation induced phase transformation or void growth are present [21]. There is no general consensus amongst the scientific community concerning the physical mechanism of crack closure occurrence during plane strain conditions. A significant number of experimental studies and mechanical analysis have been carried out over the last 30 years. These include models proposed to explain the possibility of crack closure under plane strain conditions. Some of this work includes that performed by Ewalds and Forne [22], Pitoniak et al. [23], McClung et al. [24], Sehitoglu and Sun [25]. Even with this analysis, some still question whether or not crack closure occurs under plane strain conditions.

2.2.3 Variable Amplitude Loading and Retardation

The simple Paris relationship between ΔK, da/dN and R, is only valid in situations of constant amplitude loading. Real structures, however, very rarely conform to this ideal and the fatigue analysis of variable amplitude conditions that accounts for prior loading history are considerably more cumbersome than simple analyses that assume similitude and constant loading.

2.2.3.1 Reverse Plasticity at Crack Tip

At the tip of a growing fatigue crack, a monotonic plastic zone is created during the loading phase of each cycle and a much smaller reversed (cyclic) plastic zone during unloading. The cyclic zone is approximately one-quarter of the size of the monotonic plastic zone although this varies slightly with R. This creates residual plastic deformation consisting of monotonically stretched material. A superposition model can be used to show the relative sizes of each plastic zone and is shown in

Figure 2.15.

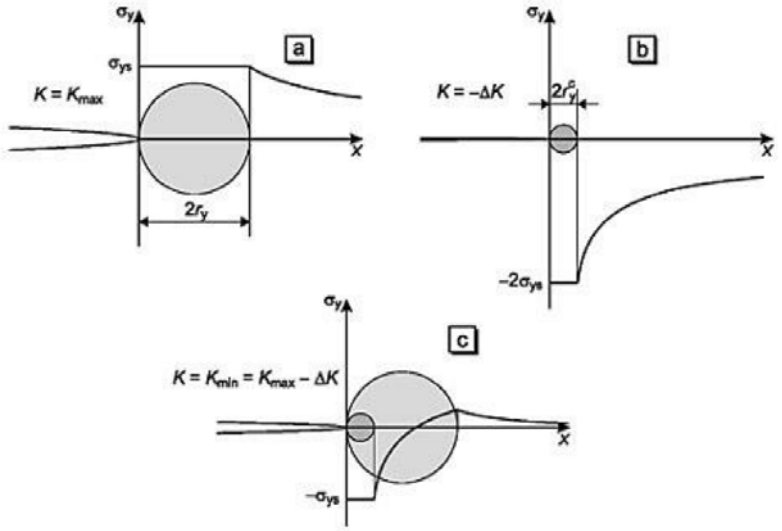


Figure 2.15: Superposition model for the relative sizes of monotonic and cyclic plastic zones at the tip of a fatigue crack [4]

During the loading cycle σ_y changes from $+\sigma_{ys}$ to $-\sigma_{ys}$ on unloading. To obtain the solution for a zone of reversed plastic flow, the solution in Figure 2.15 b) is subtracted from that in Figure 2.15 a). The solution in Figure 2.15 b) shows the yield stress doubled due to it changing from $+\sigma_{ys}$ to $-\sigma_{ys}$, therefore the size of the cyclic plastic zone, $2r_y^c$, depends on ΔK and twice the yield strength, *i.e.*

$$2r_y^c = \frac{1}{\pi}\left(\frac{\Delta K}{2\sigma_{ys}}\right)^2 \tag{2.20}$$

With $R = 0$, $\Delta K = K_{max}$ and the monotonic plastic zone is 4 times larger than the cyclic zone. Formation of these plastic zones is clearly shown in Figure 2.16.

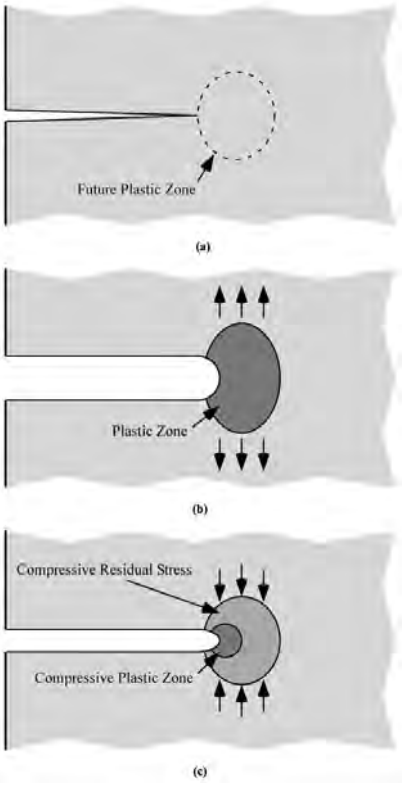


Figure 2.16: Deformation at the crack tip during a single loading cycle. (a) crack in a virgin material. (b) plastic zone formation and crack blunting resulting from an applied tensile load, and (c) residual compressive stresses at the crack tip after unloading [1].

2.2.3.2 Overload Effects

When constant amplitude loading is applied to a crack, the plastic zone will reach a steady-state size. If a single overload cycle is introduced into the loading pattern, this one cycle will produce a significantly larger plastic zone. As the load is then returned to the original constant amplitude, the residual stresses that result from the overload plastic zone are likely to influence subsequent fatigue behaviour. The effects of a single overload are shown in Figure 2.17. Typically a period of retardation, where crack growth decelerates by an order of magnitude or more, is experienced after the overload. This may be preceded by a shorter period of acceleration, however, the general effect is that of retardation. As the crack grows the growth rate eventually speeds up and reaches the rate of growth expected during constant amplitude loading.

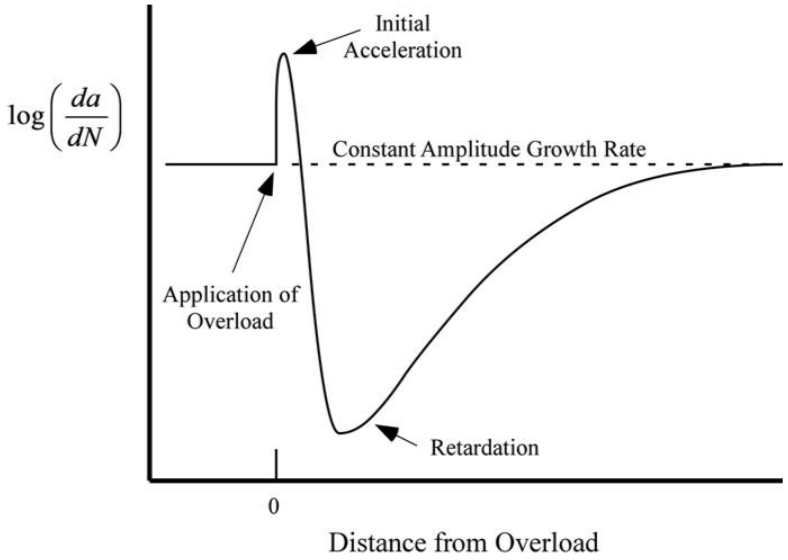


Figure 2.17: Typical crack growth behaviour following the application of a single overload [1].

Some possible mechanisms proposed to explain retardation following an overload are listed below:

1. The crack tip is blunted during an overload and then growth is delayed as the crack tip resharpens.

2. The large compressive residual stresses caused by the overload retard the crack growth rate.

3. Plasticity-induced closure is experienced as a result of residual stresses behind the crack tip while the crack grows into the overload zone.

A common opinion among fatigue specialists is that plasticity-induced closure is responsible for retardation effects [1]. The phenomenon of delayed retardation, where the crack growth rate retardation has a delay before taking effect, is one of the most compelling pieces of evidence for this argument. The slowing of the crack growth rate would be expected to be immediate if the retardation were driven by a reduction of K_{max} due to compressive stresses in front of the crack tip. After an overload, closure does not occur and therefore there may be an acceleration in crack growth

rate. When more loading cycles are applied, the crack grows a short distance into the plastically deformed overload zone. The large compressive residual stresses cause plasticity-induced closure where $\Delta K_{eff} < \Delta K$ and retardation occurs.

2.2.4 Pommier's analysis

The prediction of history effects induced by plasticity is a difficult task faced when variable loading conditions are encountered. Pommier attempts to model the growth of a fatigue crack under complex loading conditions by using a finite element method to analyse the effects of crack tip plasticity. An issue faced with the simulation of mode I fatigue growth by elastic-plastic finite element computations is the very large computation cost. In practical applications where components have fatigue lives in the order of millions of cycles, and cracks do not generally remain planar, this issue becomes even more significant. This model attempts to use a global and fast approach rather than a local and time consuming one [5].

The model relies on partitioning the displacement field ahead of the crack into both elastic and plastic components. The elastic component, u^{el}, is the normalised elastic displacement field that is associated with $\tilde{K}$. For plane stress this is given by the following equations:

$$\begin{aligned} u_x^{el} &= \frac{2}{E}\sqrt{\frac{r}{2\pi}}\cos\frac{\theta}{2}\left(1+\sin^2\frac{\theta}{2}-\nu\cos^2\frac{\theta}{2}\right) \\ u_y^{el} &= \frac{2}{E}\sqrt{\frac{r}{2\pi}}\sin\frac{\theta}{2}\left(1+\sin^2\frac{\theta}{2}-\nu\cos^2\frac{\theta}{2}\right) \end{aligned} \tag{2.21}$$

The plastic field, u^{pl}, is associated with crack tip opening. This can be obtained to a first approximation by the displacement field that results from a unit dislocation at the crack tip. The branch of this unit dislocation is cut along the crack, which means

constant displacement along the crack. The reference plastic field is as follows [5]:

$$\begin{aligned} u_x^{pl}(r,\theta) &= \frac{1}{\pi(\kappa+1)}[(\kappa-1)\log r - 2\cos^2\theta], \\ u_y^{pl}(r,\theta) &= \frac{1}{\pi(\kappa+1)}[(\kappa+1)\log r - 2\cos\theta\sin\theta] \end{aligned} \tag{2.22}$$

with $\kappa = 3 - 4\nu$ in plane strain, $r^2 = x^2 + y^2$ and $-\pi \leq \theta \leq \pi$. By including the plastic flow intensity factor ρ, a global measure of plastic deformation in the crack tip region, the displacement field associated with a very small variation around the crack, u, can be approximated as follows:

$$u \approx \tilde{K} u^{el} + \rho u^{pl} \tag{2.23}$$

$\tilde{K}$, the resultant stress intensity factor, and ρ can be found using a 2D finite element model. Once known, the estimated field as calculated using equation (2.23) can be determined at any point (r, θ) lying in the K-dominant area. During each step of a finite element computation, the approximation in equation (2.23) is performed using a post-treatment routine. This can be employed to generate evolutions of $\rho_I(t)$ under various loading conditions. These generated evolutions can be done for various cases of loading and employed like an experimental database to identify an empirical model for crack tip plasticity.

Figure 2.18 displays predicted crack behaviour in crack K/ρ space. Below the closure point marked in this figure, the approximation in equation (2.23) does not apply so both ρ and K remain constant. The domains that are marked C represent periods when the variation of ρ is negligible and the cracked structure is assumed to behave elastically. This occurs after each load reversal and the domain varies both in dimension and position. Above the point D, the monotonic plastic zone size increases and D is therefore a threshold for the development of plasticity within the crack tip monotonic zone. The model attempts to predict fatigue crack propagation

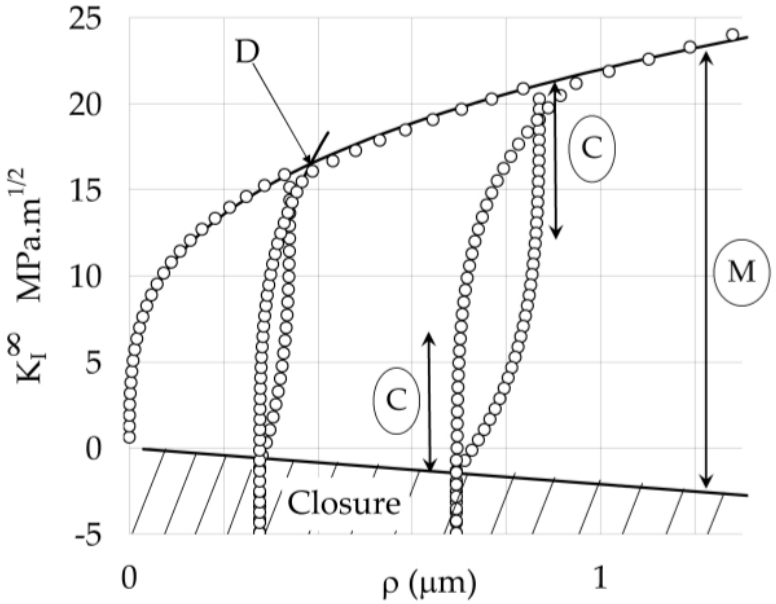


Figure 2.18: The nominal stress intensity factor K_I^∞ plotted against the plastic flow intensity factor ρ as calculated using the finite element results for a cyclically increasing load sequence [5].

by analysing the hysteresis within the K/ρ space.

2.3 Measurement of fatigue crack closure

One of the main challenges faced by engineers when analysing displacement and strain of materials during deformation is accurate measurement. This is certainly the case when dealing with experimental set-ups that have confining space restrictions or miniature material samples are being tested. In these cases conventional extensometers and resistance foil gauges are impractical as they could be damaging, cumbersome, or even impossible to fit. In particular, when looking at cracks, displacements are often relatively small and it is usually a challenge to measure them directly with sufficient sensitivity and accuracy. As a consequence, Gianola identified the following features as being highly desirable for precise measurements of displacement and strain:

i) no contact with the specimen required, ii) sufficient spatial resolution to measure locally at the region of interest, iii) the ability to capture non-uniform full-field deformations, and iv) a direct measurement that does not require recourse to a numerical or analytical model [7].

Optical methods of measuring strain and displacement can meet all of these requirements and have a high sensitivity and accuracy required analysing small displacements. A few optical techniques of measuring displacement are outlined below.

2.3.1 Interferometric Strain/Displacement Gauge

One optical measurement approach is a laboratory tool developed by Sharpe [26] that measures relative displacements using a laser that is reflected off small reflecting surface markers on a specimen. This Interferometric Strain/Displacement Gauge (ISDG) can measure displacements over gauge lengths as short as 100 µm with a resolution as low as 5 µm [27]. The ISDG involves a single coherent laser beam illuminating and being reflected from two tiny indentations, usually photolithography deposited gold lines, Vickers micro-hardness indents, or focused ion bean (FIB) deposited platinum lines, that are placed perpendicular to the direction of strain. The reflected and diffracted light produces interference fringes that are similar to Young's two slit experiment but in reflection rather than transmission. Monitoring the changes and shift of the fringe pattern allows direct strain measurement in the gauge section of the specimen.

This method was developed further by Li [28] with an interferometric strain/slope rosette (ISSR) to measure three derivatives of in-plane displacements in addition to three derivatives of out-of-plane displacements. With these six displacement derivatives, components of a strain tensor and rotation can be determined at certain points on a specimen. The frequency response of this system can be sufficient to enable dy-

namic measurements, which could be useful when looking at strain without slowing the loading of a specimen.

These techniques could be used at many points in order to get strain readings across a specimen, however, in order to measure full-field deformations techniques such as moiré interferometry or Digital Image Correlation (DIC) could be more effective.

2.3.2 Moiré interferometry

Practiced extensively in the microelectronics industry to measure thermally induced deformation of electronic packages, Moiré Interferometry is used to measure tiny deformations of solid bodies and has become an important tool in academic, research and industrial institutions. According to Walker [29] in his paper "A Historical Review of Moiré Interferometry," the initial foundation of the developments that have produced modern moiré interferometry may be found in a book written by Guild [30] of the National Physical Laboratory in 1954 called "The Interference System of Crossed Diffraction Gratings." Developments in Japan by Kato and his colleagues [31] were thought to have been the first modern developments before Post [32, 33] and Sciammarella [34] made further progress in the United States. At around the same time McKelvie and Walker [35] made significant contributions at Strathclyde University.

This technique consists of using an interference pattern created when two grids are overlaid and displaced relative to another. Moiré interferometry is very similar to geometric moiré where fringe patterns are created from the occlusion of light between two superimposed gratings. Instead of using two gratings, the simplicity of geometric moiré is combined with the high sensitivity of optical interferometry and a pattern is produced due to the interference between a physical grating attached to a specimen and a virtual grating created by interference of two incident beams of coherent

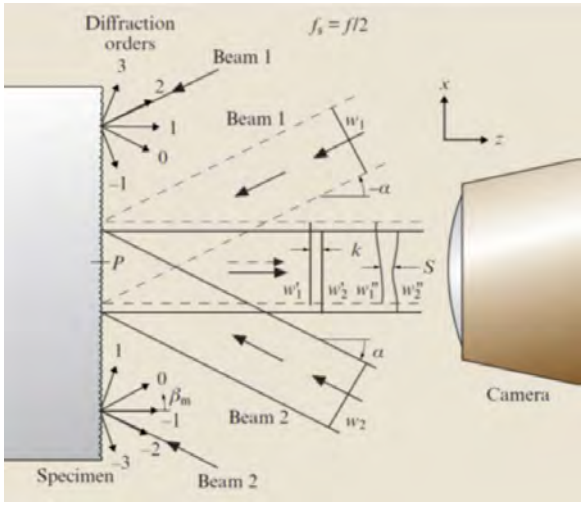


Figure 2.19: Diffraction by the specimen grating produces beams with plane wave fronts for the no-load condition. Warped wave fronts result from inhomogeneous deformation of the specimen [6]

light. Figure 2.19 shows the basic experimental set-up with the two beams of light illuminating the grating and the pattern being captured by a camera. The frequency of the physical grating is f_s and the angle of the beams of light α are defined by the equation $\sin\alpha = \lambda f_s$. This means the beams are diffracted such that their first orders emerge normal to the specimen as w_1' and w_2', in the direction of the camera. When the beams intersect with the half-angle α, interference fringes are generated with a frequency f, where $f \equiv 2f_s$. Small specimens of complex geometry can be tested and as the directions of diffracted rays change continuously, the beams emerge as warped wave fronts w_1'' and w_2''. Interference between these wave fronts occurs and contours of their separation S are generated. By having camera focused on the plane of the specimen, the image captured is the moiré pattern.

This allows in-plane displacements to be measured with very high sensitivity. With the large amounts of displacement data that this technique produces, reliable normal and shear strain distributions can be extracted from the patterns. When using moiré interferometry with fatigue specimens, the specimen must be either be tested in an interferometer or a dedicated interferometer assembled to the fatigue testing rig.

2.3.3 Digital image correlation

Digital Image Correlation (DIC) is an optical method of tracking and measuring changes between images. It is especially useful when looking at strain in samples where non-contact techniques are needed for various reasons such as size, location or temperature. In current experiments, DIC is useful in analysing the displacement at multiple points across a surface when a force is being applied to deform the test specimen. Points can be selected anywhere on the surface, so once a crack or area of interest has been identified, close analysis of that area can be carried out. DIC techniques are common and have been increasing in popularity due to their relative ease and implementation of use. A great appeal of DIC is the minimal cost, accurate results and readily available software. It can be as simple as using just a USB webcam and an open source MATLAB package to undertake basic DIC strain measurements. First conceived and developed at the University of South Carolina in the early 1980s [36–39], DIC has been continually optimised and improved since [40–45]. The technique works by maximizing a correlation coefficient that is determined by looking at pixel intensity array subsets on at least two corresponding images.

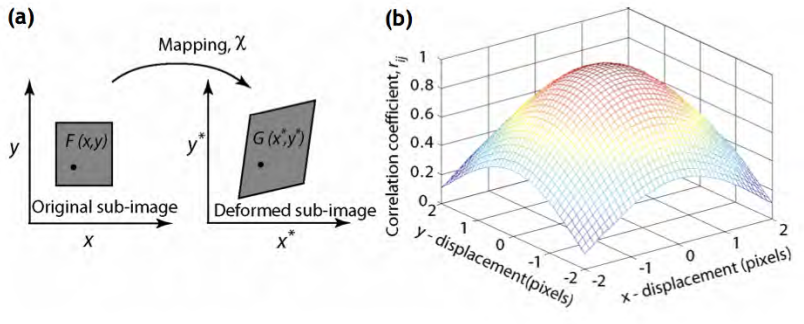


Figure 2.20: Foundations of DIC: a) Mapping from the un-deformed to the deformed space; b) Correlation function, r_{ij} plotted against in-plane displacements [7]

The deformation mapping function that relates the images is extracted (Figure 2.20) and used to show displacements within the images. Put simply, points are first selected on a reference image and then, on subsequent images, an area around

each point is searched in order to find the location that has a maximum similarity (highest correlation) to the selected reference point. The change in location between the reference area and the area of maximum similarity is used to determine the displacement value. This can be seen in Figure 2.21. A point is selected on a reference image (Figure 2.21 a)) and a reference cross-correlation area is defined, in this case it is $(4 \times WCor + 1) \times (4 \times WCor + 1)$. On the next image (Figure 2.21 b)), a search area of approximately half the size is defined containing the point that needs to be tracked. This example uses a displacement of $\Delta x = \Delta y = 2$. By running the image cross correlation technique, the point is found within the search area and matched up with the original point location as shown in Figure 2.21 c). The distance between the centre of the search area and the centre of the reference cross-correlation area is found (Δx and Δy) and the search area is then re-positioned with its centre at the location of the point just found. This re-positioning allows for the tracking of points that are continuously moving away from the reference point.

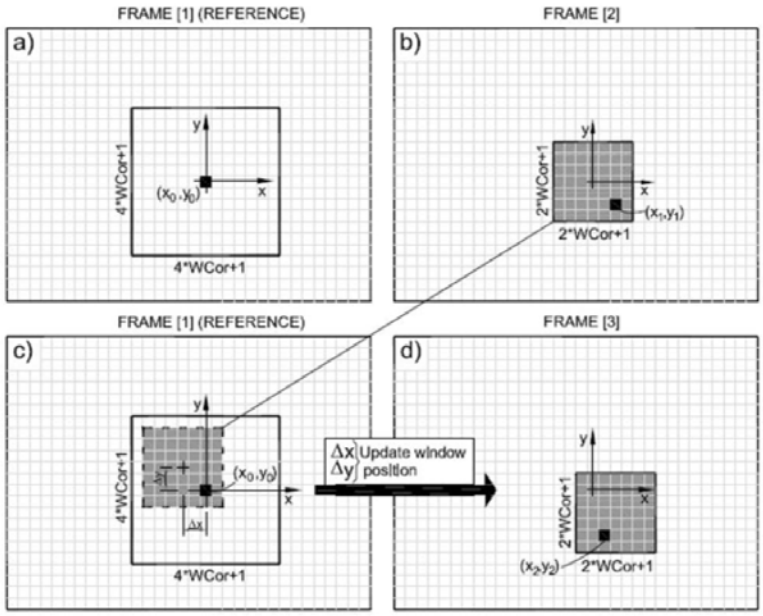


Figure 2.21: Two-dimensional digital image correlation, basic principle ($WCor = 3$) [3]

According to experiments done by Sutton [46], it is important that the two subsets

have the same level of light intensity or contrast in order for image matching to be performed accurately. This could prove difficult if the specimen is moving between images, causing light to be reflected from different areas of the specimen face. With this in mind, experiments are designed to limit the movement of a specimen to simply the deformation around an area of interest. The points selected to track are usually from a random speckle pattern applied to the specimen. Jin [47] found that generating a speckle pattern by spray painting or etching is an effective method.

2.3.3.1 MATLAB DIC procedure

The experimentally obtained images in this work were analysed using MATLAB with DIC code based on that produced by Eberl et al. [48]. While the inputs were adjusted to select specific points to be tracked, the script used to calculate displacements (named *automate_image.m*) was unchanged from that produced by Eberl. This script utilises the MATLAB function *cpcorr.m* that is part of the Image Processing Toolbox. The function *cpcorr* uses pairs of points with one identified on a base image (the first image in a series of images) and the other on an input image (in the order defined by the series). The displacement between the base image control point and the input image control point is determined with the function using the following general procedure:

1. An 11-by-11 template (default size that was adjusted in this work) is extracted around the input control point and a 21-by-21 search region is identified around the base control point.

2. The normalized cross-correlation of the template area with the search region on the base image is calculated using the function *normxcorr2.m*.

3. The absolute peak of the cross-correlation matrix is found using the function *findpeak.m*. This function was adjusted to increase the resolution of the marker positions to 1/1000th pixel.

4. Finally, the position of the peak is used to adjust the coordinates of the input control point for the next image.

This procedure is used on all defined points to obtain displacements over a series of images. The size of the template area was increased above the default value in each experiment and the region around the base control point remained at roughly double the size of the template area (e.g. a template area of 31×31 pixels and search region of 61×61 pixels was used in Chapter 3).

Chapter 3

Fatigue Crack Analysis Under Constant Amplitude Loading

This chapter explores how simple DIC techniques can be used to analyse the displacements around a crack tip under constant amplitude loading. Displacements normal to the crack are analysed and compared to basic models to analyse plasticity and the Stress Intensity factor at the crack tip. A conventional elastic model for a sharp crack and a recent two-parameter model for crack tip stress proposed by Pommier and co-workers [5] were used to analyse displacements around the crack flanks.

3.1 Testing Methodology

3.1.1 Material and specimen characterization

The material used in this experimental work was aluminium alloy 6082 T6. This is a medium strength alloy with excellent corrosion resistance and is widely used in airframe structural applications. Compact tension (CT) specimens were formed from this material with dimensions determined by recommendations in ASTM standards as described in 3.1.3.

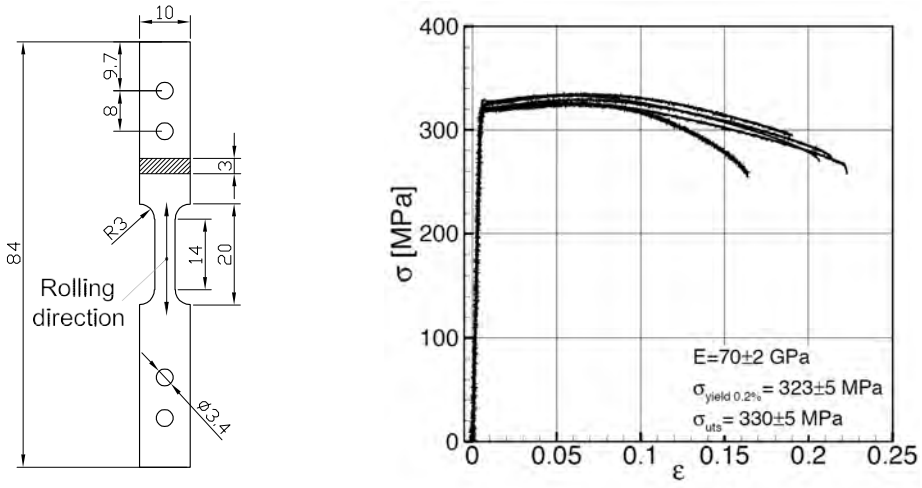
Tests were not performed to determine yield stress, ultimate stress or Young's modulus prior to specimen fatigue testing. However, Paulo de Matos [3] performed testing on the same material and the results are presented here in Figure 3.1. Tensile test specimens were machined from 1 in thick 6082 T6 aluminium alloy that was heat treated and artificially aged. This was the same material used to machine the CT test specimens used throughout this work. The direction of loading on the tensile test specimen was the same as the rolling direction of the material. Dimensions of a test specimen and stress/strain data is presented in Figure 3.1 with the Young's modulus, yield stress and ultimate tensile strength shown in Figure 3.1b.

The chemical composition of the aluminium alloy 6082 T6 was not analysed, however typical chemical composition values obtained from Aalco Metals Limited [49] are presented below in Table 3.1.

Alloy	Mn	Fe	Mg	Si	Cu	Zn	Ti	Cr	Al
6082	0.4-1.0%	0.5%	0.6-1.2%	0.7-1.3%	0.1%	0.2%	0.1%	0.25%	Balance

Table 3.1: Typical chemical composition for aluminium alloy 6082 [49]

De Matos performed further testing on aluminium alloy 6082 T6, including metallographic analysis. In this analysis the grain size of three small samples, each with dimensions $10 \times 10 \times 3$mm, was measured by etching them with Keller's reagent. The grains were elongated along the rolling direction and had an estimated length



(a) End view (b) side view

Figure 3.1: Tensile tests on aluminium alloy 6082 T6, the same material used for work in this chapter, performed by Paulo de Matos [3].

of 600 µm and width (dimension across rolling direction) of 100 µm. De Matos mentioned difficulties in obtaining an accurate measure for grain size from the chemical etching process, however he believed these determined values were reasonable. It was noted that using a Scanning Electron Microscope in backscatter diffraction (EBSD) mode could be used as a more precise way of characterising the microstructure of the material [3]. This was not performed in experimental work done by de Matos and nor was it done for this experimental work due to its relative complexity and insufficient need for an accurate measure in the current analysis.

3.1.2 Experimental Set-up

The aim of this experimental procedure was to examine the crack closure behaviour of CT specimens under constant amplitude loading. The experimental set-up and procedure was based on experiments performed previously by de Matos [3] with the same loads, specimen geometry and testing rig used. Rather than using specimens of various thicknesses, as de Matos did, only thin specimens of t =3 mm were used. This thickness of specimen is expected to be 'plane stress' like when loaded. The

specimens were loaded in a servohydraulic testing machine fitted with a 15 kN load cell and controlled by a Kelsey Instruments K7500 servocontroller. The specimen was held in grips (Figures 3.5 and 3.6) with the upper grip fixed on a frame. The bottom grip was controlled by an actuator, which together with the top grip, could apply mode I loading on the specimen. This configuration can be seen in Figure 3.3a. A schematic of the experimental set-up is shown in Figure 3.2 while Figure 3.3 displays a series of images showing the placement of various components within the set-up.

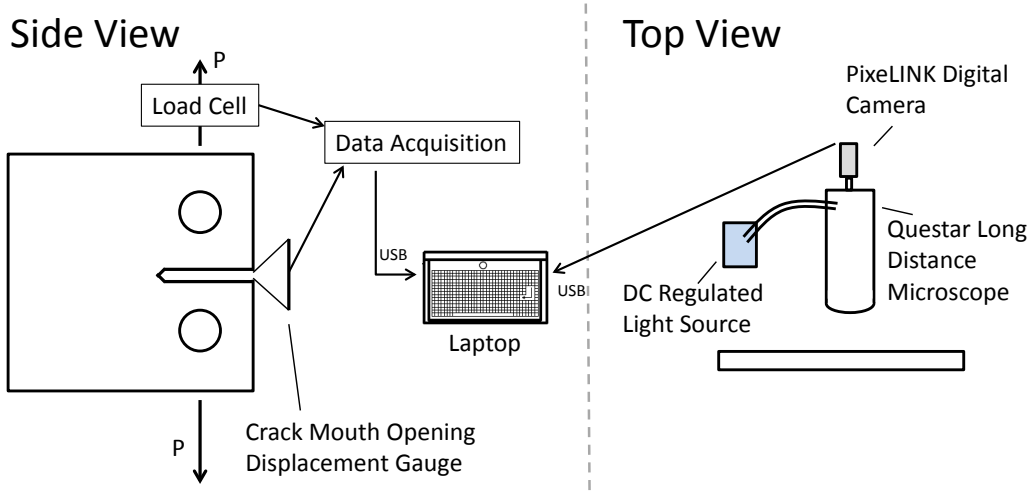


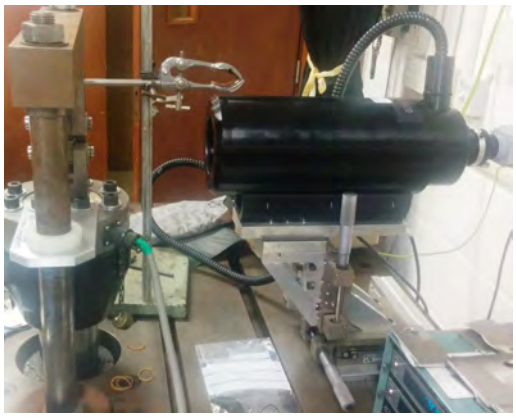
Figure 3.2: Schematic representation of the experimental setup.

Experimental data was acquired using a National Instruments USB Data Acquisition (DAQ) device attached to a laptop running LabVIEW software. A LabVIEW Virtual Instrument was written to plot the acquired data from the load cell in real time and record the data to a file when the testing cycle had concluded. During image recording, the specimen loading cycle frequency was 0.025 Hz and loading data was recorded at a rate of 20 points per second, giving a total 800 data points over a full cycle. A trigger initiated images to be captured every second data point resulting in 400 images taken over a full cycle at a rate of 10 per second. This allowed each image to have an associated applied load from the captured load cell data.

In addition to capturing load data and activating the camera trigger, the DAQ device also collected data from a crack mouth opening displacement (CMOD) gauge



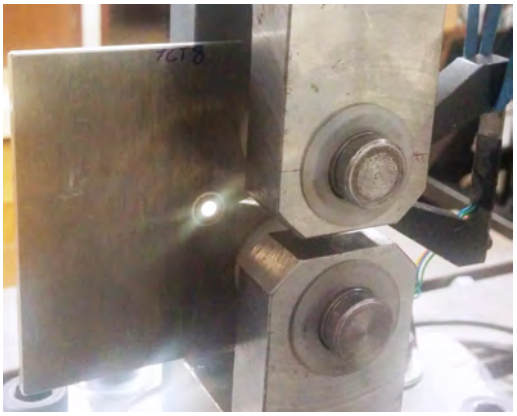
(a) End view



(b) Side view



(c) Camera used to capture images



(d) Imaging area on specimen

Figure 3.3: Images taken of the experimental setup during testing.

placed on the specimen. Positioning of the CMOD on the specimen can be seen in Figure 3.4. Readings from the CMOD were given by measurement through a strain gauge on the bar attaching the two arms that lead into the crack mouth. The strain gauge voltage measurements are received in the DAQ device after passing through a strain gauge bridge box and Fylde FE-351-UA universal amplifier.

A PixeLINK PL-B741U CMOS camera (Figure 3.3c) was used to capture images. This high performance 1.3 megapixel monochrome camera captured images at a resolution of 1280×1024 pixels and connected to the laptop through a USB 2.0 interface. PixeLINK Capture OEM software running on a laptop saved a 50 second AVI video comprising 500 images (slightly longer than a single cycle to ensure the full cycle is captured) for each loading cycle that image capturing was required.

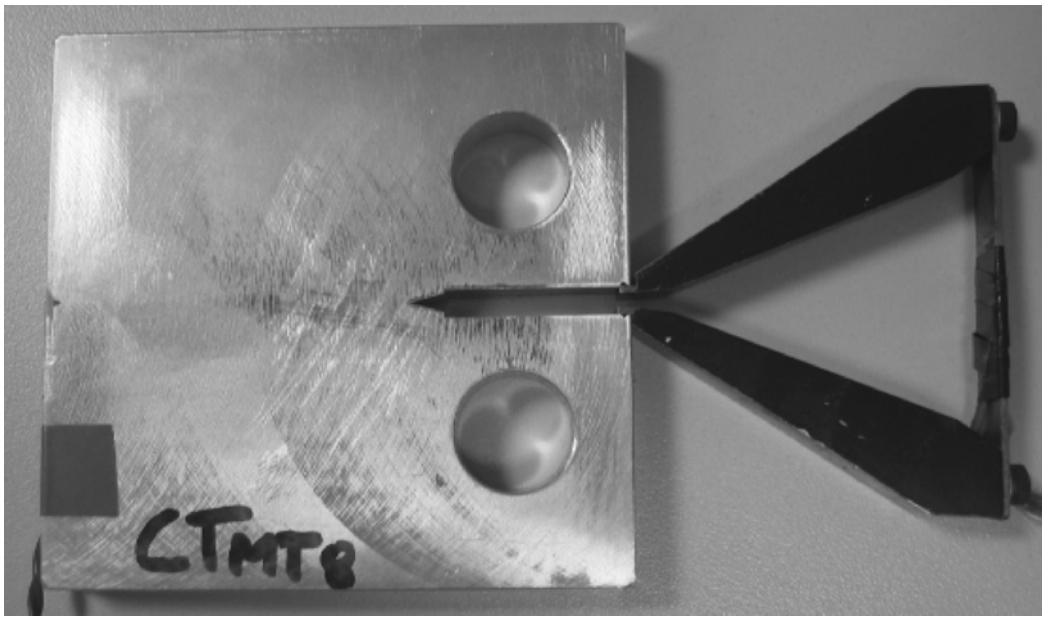


Figure 3.4: Specimen with fitted crack mouth opening displacement (CMOD) gauge [3].

The PixeLINK camera was mounted on a Questar QM-100 photo-visual long distance microscope (shown in Figure 3.3b) to capture images of the crack tip region. This lens has a focus range between $15 - 35$cm and the lens position was determined by finding a point within this range where the lens could be focused easily and the crack tip would stay within the image frame during a full loading cycle. Mounted too close and the crack tip would move out of the image frame as the load increased on the specimen. A DC Regulated Fibre Optic light source with linear light guide was used through the Questar lens to provide illumination of the crack tip region. This illuminated imaging region can be seen clearly on the specimen in Figure 3.3d. The lens and camera were mounted on a precision translational stage with an ACU-RITE Qwikcount digital readout system. This allowed for precise movement of the imaging devices and was initially intended to be used in calculating precise measurements of crack length.

Fixtures were manufactured to hold the specimen and apply mode I loading forces to the specimen. A clevis and pin assembly for gripping the specimens was made according to the ASTM E647-11 [8] standard that included the recommended geometry,

dimensions and features. A drawing showing the dimensions of the clevis grips produced for this testing is shown in Figure 3.5. One particular feature to note is the flat bottom of the oversized holes. With a pin placed through these holes to hold the specimen, this feature is designed to reduce nonlinear force vs displacement behaviour caused by the rotation of the specimen and pin.

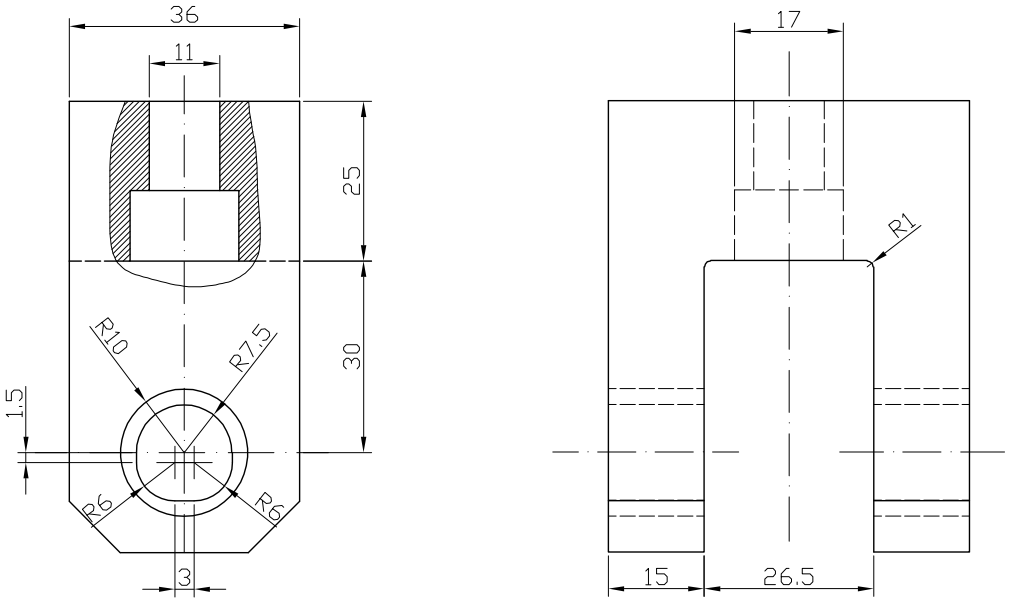


Figure 3.5: Drawing of grips used to apply load to specimen. Grips feature flat bottom holes and comply with ASTM E647-11 standards [3, 8]. Dimensions in mm.

Spacers and pins held the specimen in place during testing. A diagram of the complete clevis and pin assembly with a specimen in place is shown in Figure 3.6.

3.1.3 Specimen Loading

The specimen size and shape was the same as the specimens tested by de Matos [3]. This specimen geometry was designed to comply with recommendations made in ASTM E647-11 Standard Test Method for Measurement of Fatigue Crack Growth Rates [8]. Figure 3.7 shows the geometry specifications provided in ASTM E647-11. The specimen thickness of 3 mm is at the lower limit but still within the recommended thickness range. The detailed dimensions of the CT specimens tested is displayed in

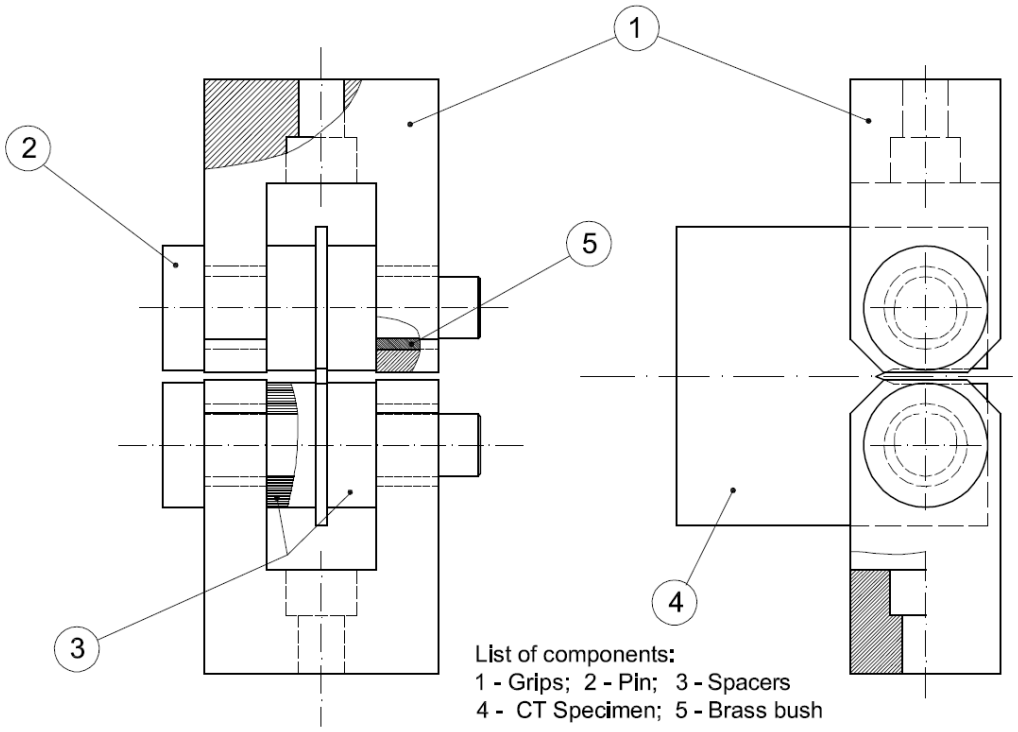


Figure 3.6: Arrangement of components around the specimen used for fatigue testing [8].

Figure 3.8. The specimens were machined so that the notch, where the crack will propagate from when loaded was perpendicular to the rolling direction. The notches were manufactured using a sharp cutter. A typical notch cut into the specimen is shown in Figure 3.9 with a crack propagating from the notch after loading the specimen for 20,000 cycles.

A corresponding Stress Intensity Factor, K, can be calculated from this geometry according to the crack length with Equation (3.1) [8]. This equation assumes that the test material is linear-elastic, isotropic and homogeneous. This computed K value also disregards potential effects of residual stress or crack closure. With these limitations in mind this calculation will be used as a comparison of an analytical K

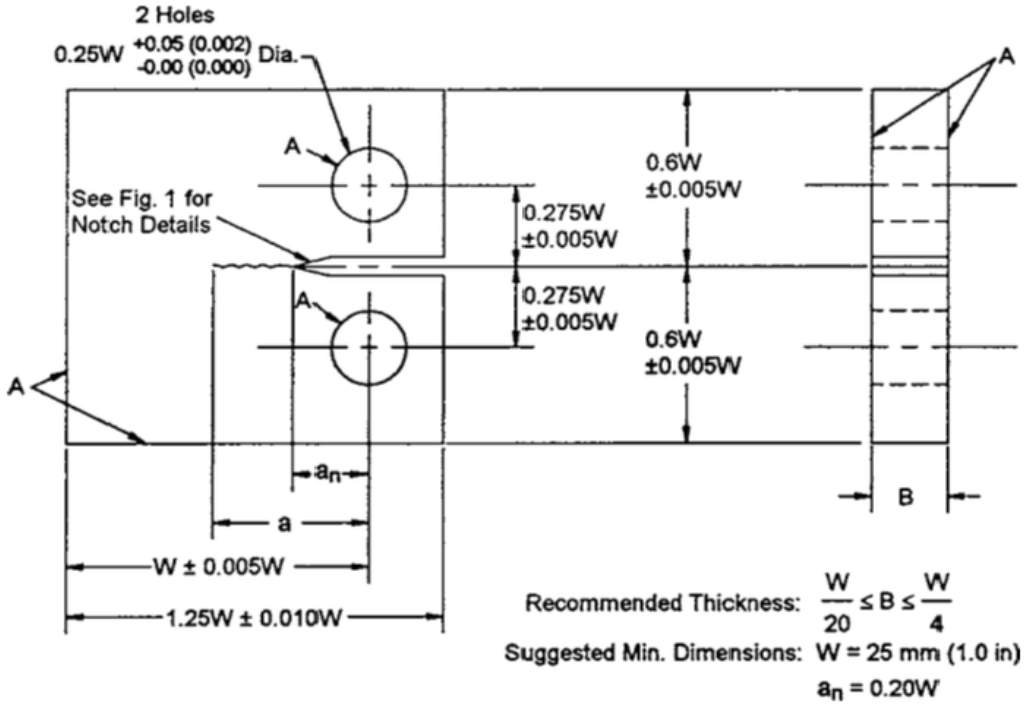


Figure 3.7: Recommended Compact Tension specimen dimensions from ASTM E647 - 11 Standard Test Method for Measurement of Fatigue Crack Growth Rates [8].

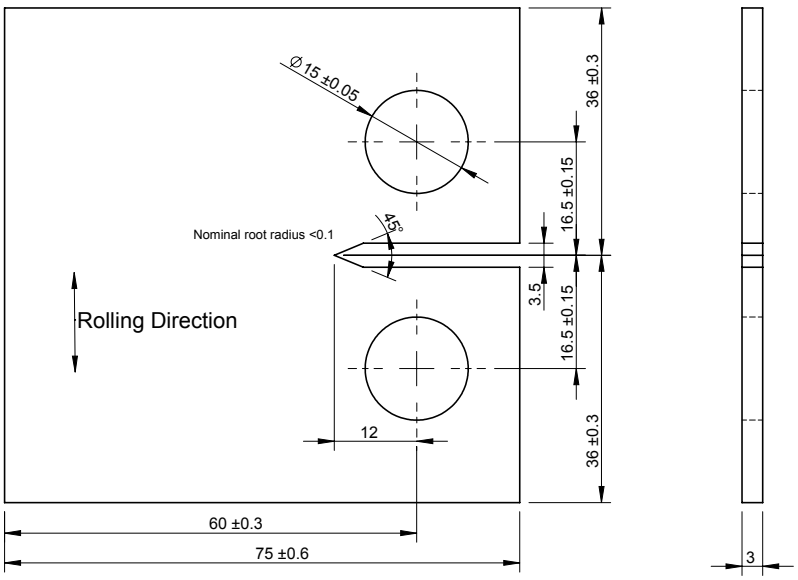


Figure 3.8: CT Specimen dimensions in mm.

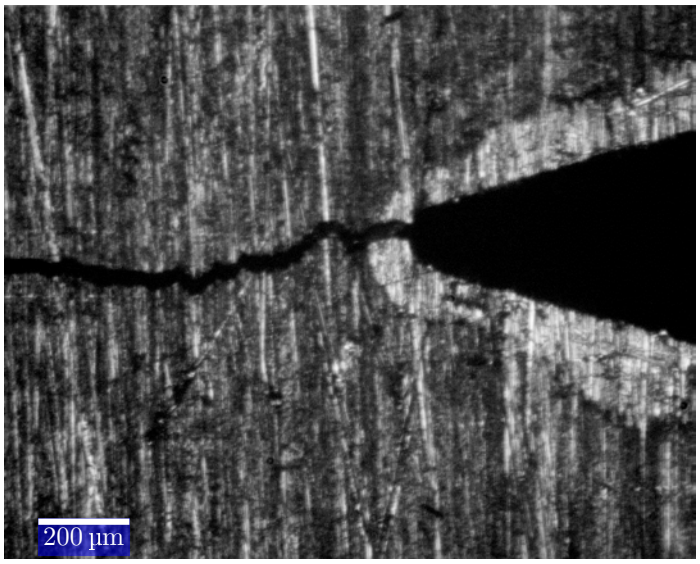


Figure 3.9: Image of a fatigue crack propagating from the tip of the notch cut in the specimen. This image is 1280×1024 pixels and the area captured is 1414×1131 µm and was taken with a load of 2 kN applied to the specimen.

value to the experimental data in this analysis.

$$K_I = \frac{P}{B\sqrt{W}} f\left(\frac{a}{W}\right) \quad \textit{where } B \textit{ is specimen thickness}$$
$$f\left(\frac{a}{W}\right) = \frac{2+\frac{a}{W}}{\left(1-\frac{a}{W}\right)^{3/2}}\left[0.886 + 4.64\left(\frac{a}{W}\right) - 13.32\left(\frac{a}{W}\right)^2 + 14.72\left(\frac{a}{W}\right)^3 - 5.60\left(\frac{a}{W}\right)^4\right] \tag{3.1}$$

Specimens were initially loaded at a frequency of 5 Hz for 30,000 cycles. This loading had a maximum load of 2 kN and a minimum of 0.25 kN giving an R-ratio of 0.125. Figure 3.10 displays data obtained during this initial loading phase. The K7500 servocontroller produced the sinusoidal load to the testing rig, however the sinusoidal pattern is not observed clearly with the relatively slow rate of data capture compared to this frequency of loading. During image capture the loading frequency was reduced from 5 Hz to 0.025 Hz in order to allow time for a large number of images to be captured in a single loading cycle. At this frequency the sinusoidal pattern of loading can be seen clearly (Figure 3.11).

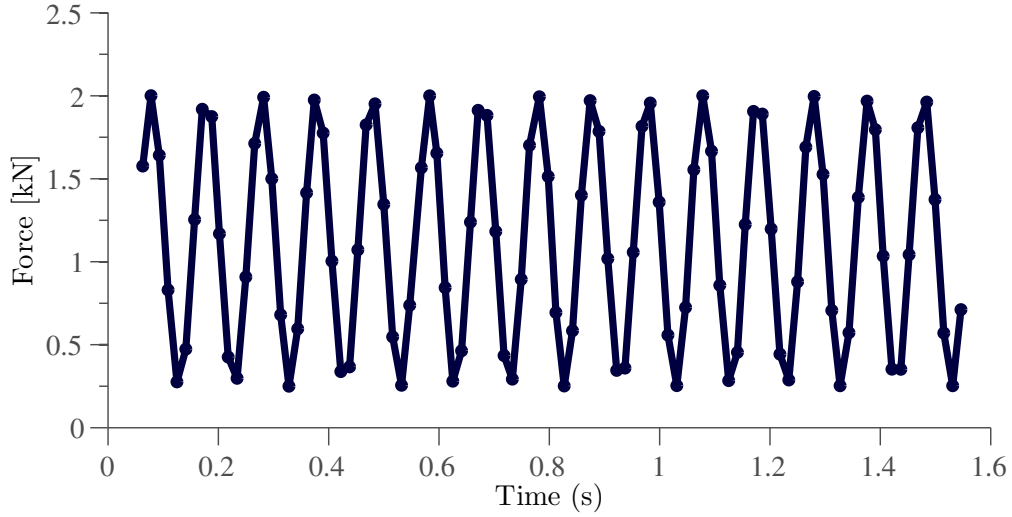


Figure 3.10: Force data from loading the CT specimen at 5 Hz.

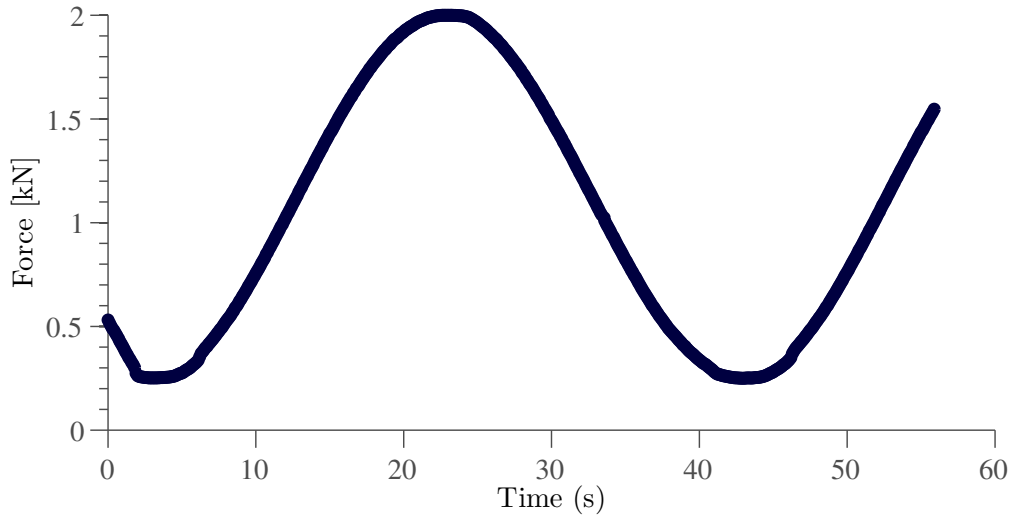


Figure 3.11: Force data from loading the CT specimen during image capture at 0.025 Hz.

In each case a crack propagated between 6–8 mm during the first 30,000 cycles of loading. After this initial period of crack growth, images were taken at various stages of crack elongation before and after a single overload cycle was applied. A full list of the timing of each set of images is in Table 3.2. Specimen CT5 was not included as an accidental large load was applied resulting in the specimen breaking in half.

Reference Name	Cycles Applied	Crack Length [mm]
CT1	20000	14.94
	25000	16.14
	30000	17.42
	35000	19.03
	40000	**21.05**
	41000	21.35
	42000	21.47
CT2	35000	19.26
	40000	**21.85**
	41000	22.02
	45000	22.75
	50000	25.16
CT3	30000	17.86
	35000	19.66
	40000	**22.03**
	41000	22.19
	42000	22.35
	45000	22.97
	50000	26.29
CT4	30000	17.43
	35000	19.04
	40000	**20.95**
	41000	21.33
	42000	21.45
	45000	21.80
	50000	24.48
CT6	32700	19.66
	35600	21.24
	37700	22.51
	39300	**23.76**
	42000	24.31
	43000	24.53
	44000	24.91
CT7	32600	20.90
	34900	22.34
	36300	23.84
	37260	**24.98**
	38000	25.70
	39000	25.90
	40000	26.63
	41000	27.79
CT8	32600	20.59
	35000	22.19
	36700	23.67
	37800	**24.20**
	39000	24.86
	42000	25.97
	43000	27.21
CT9	33000	19.83
	35300	21.10
	37500	22.40
	39000	23.54
	40000	**24.47**
	41000	25.07
	42000	25.17
	43000	25.41
	44000	25.49
	45000	25.82
	46000	26.81
	47000	28.41
	48000	32.46
CT10	33500	21.10
	36000	22.75
	38000	**24.43**
	39000	25.02
	40000	25.12
	41000	25.32
	42000	25.67
	43000	26.04
	44000	27.07
	45000	28.52

Table 3.2: Details of cycles applied to the specimen at points of image capture. Overload cycles are highlighted in bold and crack length is a from the specimen geometry (Figure 3.7).

Often the timing of image capture was determined by trying to match up the images taken with images previously captured ahead of the crack tip. This was done in an effort to compare images of the crack tip during a loading cycle to those of the same area of the uncracked specimen as shown in Figure 3.12. The result of this was that images were captured with varying distances of crack growth between each set of images.

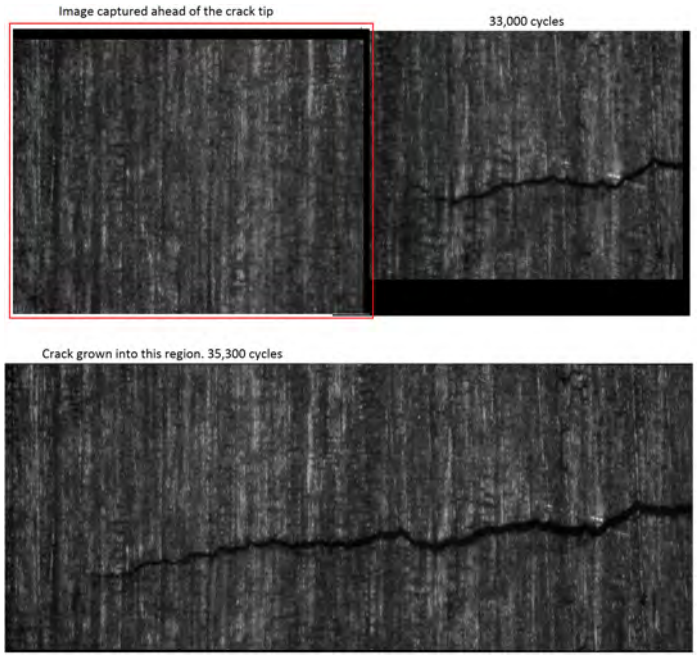


Figure 3.12: Image capture process showing captured of image ahead of the crack tip before and after the crack has grown into this region.

In this chapter results are presented primarily from the specimen labelled CT7 (Table 3.2) due to the consistent good fit of images taken prior to cracking and images of the crack tip. With some other specimens, the crack path deviated slightly from what was expected and a good match of pre cracking and crack tip images was not obtained. This was desired for analysis shown in Section 3.7. Although only results from one specimen are predominantly shown here, the same digital image correlation was performed and plots produced for all specimen with only features consistent across multiple specimens presented in this chapter.

3.1.3.1 Plastic Zone Size

The forward plastic zone size calculations are listed in Table 3.3. These are estimated by calculating the elastic stress field ahead of the crack tip to yield stress according to Equation (2.4). The shape of the plastic zone can be approximated using the von Mises criterion for yielding as explained in section 2.1.2.3. Equations (3.2) and (3.3) are used to calculate values of the plastic zone area and the results of these equations of a crack with $a/W = 0.25$ is shown with Figure 3.13. As the crack grows, the plastic zone size is expected to grow. To get an idea of the scale of this calculated plastic zone size compared to the crack tip imaging area, the calculated plastic zone size is superimposed on a crack in Figure 3.14. This is a specimen that has been loaded for $32,600$ cycles and has a length of 8.9 mm ($a/W = 0.348$). The same plastic zone size is displayed on the full image of this crack from the notch (Figure 3.15) to show how it compares to the overall length of the growing crack. It should be noted, however, that it may be the cyclic plastic zone size that matters more than the forward plastic zone when looking at a growing fatigue crack. The cyclic plastic zone size is 1/4 of the forward plastic zone, as described in Section 2.2.3.1.

		$r_y = \frac{1}{2\pi}\left(\frac{K}{\sigma_{yield}}\right)^2$[µm]		$r_y = \frac{1}{6\pi}\left(\frac{K}{\sigma_{yield}}\right)^2$[µm]	
t[mm]	P_{max}[kN]	$a/W = 0.25$	$a/W = 0.5$	$a/W = 0.25$	$a/W = 0.5$
3	2	274.0	1054.3	91.4	351.4

Table 3.3: Size of the plane stress and plane strain plastic zones at $a/W = 0.25$ and $a/W = 0.5$. The corresponding crack length are 3 mm and 18 mm from the specimen notch.

$$r(\theta)_{plane\,stress} = \frac{1}{4\pi}\left(\frac{K_I}{\sigma_{ys}}\right)^2\left(1 + \frac{3}{2}\sin^2\theta + \cos\theta\right) \tag{3.2}$$

$$r(\theta)_{plane\,strain} = \frac{1}{4\pi}\left(\frac{K_I}{\sigma_{ys}}\right)^2\left((1-2\nu)^2(1+\cos\theta) + \frac{3}{2}\sin\theta\right) \tag{3.3}$$

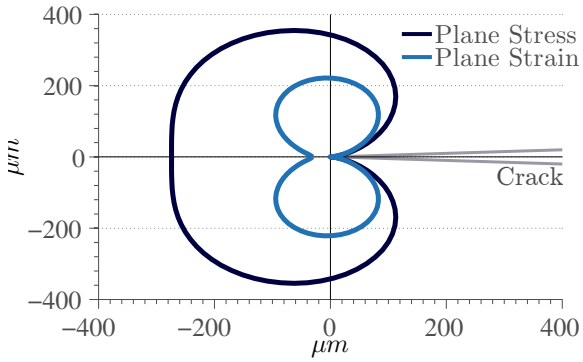


Figure 3.13: Plastic zone shapes according to von Mises criterion with $a/W = 0.25$ and a maximum load of 2 kN. The coordinate point (0,0) represents the crack tip and axis values are distance (μm) around the crack tip. For plane strain $\nu = 0.33$.

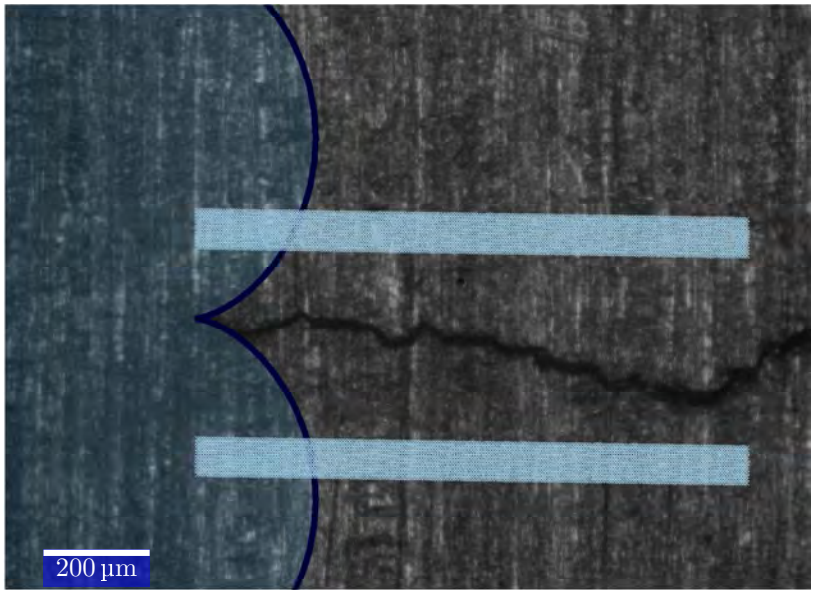


Figure 3.14: Plane stress plastic zone shape according to von Mises criterion superimposed on image of the crack tip. This crack has a length of 8.9 mm (a =20.9 mm and $a/W = 0.348$) and the load is 2 kN. Points where displacement was measured with Digital Image Correlation are included for reference.

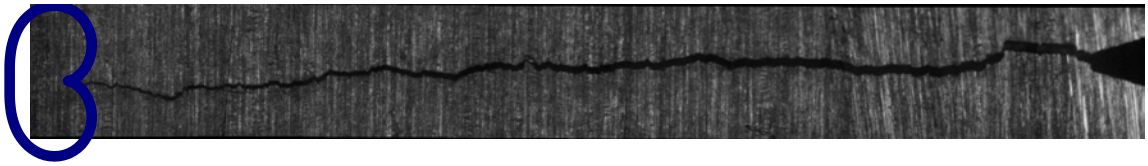
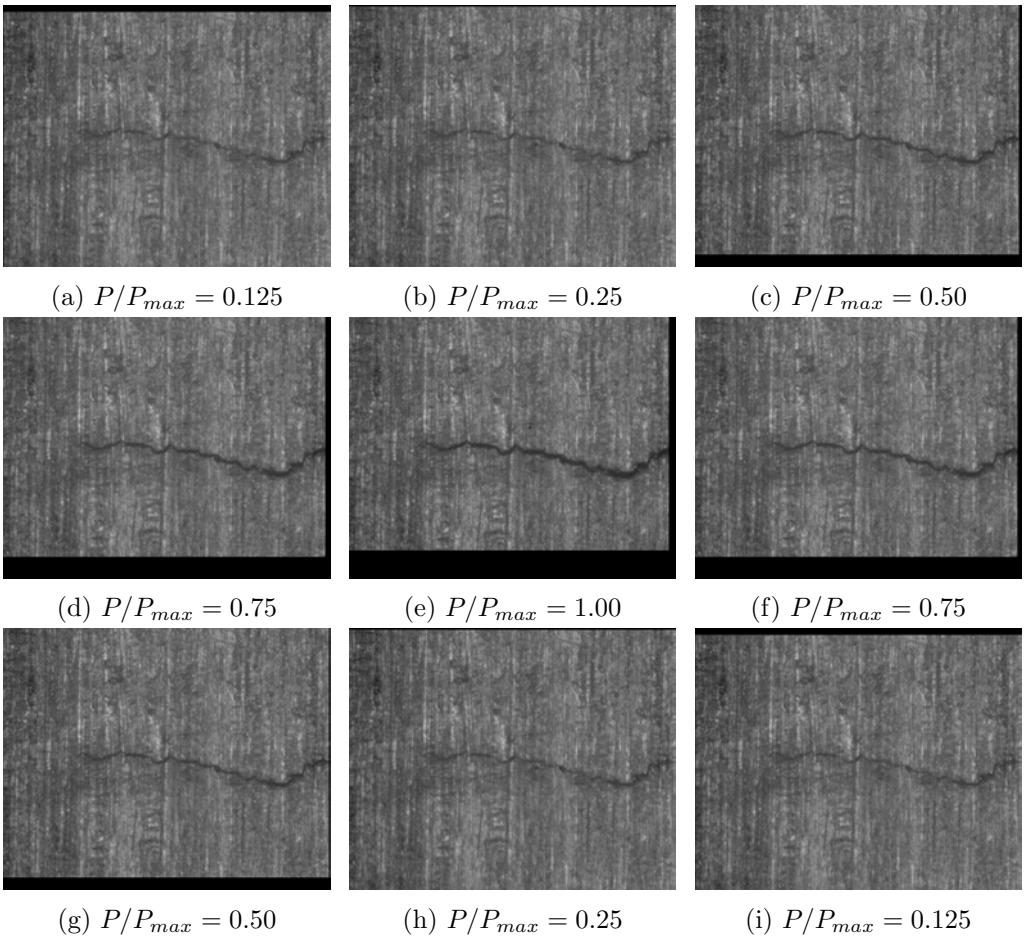


Figure 3.15: Plane stress plastic zone shape according to von Mises criterion superimposed on full image of a crack with length of 8.9 mm (a =20.9 mm and $a/W = 0.348$). The load is 2 kN.

3.2 Image Analysis

Images were captured and saved as an AVI file with the PixeLINK Capture OEM software. From this video file, the individual frames were extracted and saved as TIFF image files for analysis. To improve the accuracy of the Digital Image Correlation, the images were aligned using a function in the MATLAB Image Processing Toolbox. This reduced the translational movement of the specimen within the image series as load was applied to the specimen and allowed the Digital Image Correlation algorithm to search a smaller area to find the tracked point. To align the images a base image was chosen as an image where the load was low and the crack closed. From this, the normalized 2-D cross-correlation (using the *normxcorr2* function) between a section of each image and this base image was calculated. The peak of the cross-correlation matrix indicated the offset (in pixels) each image had from the base image. The images were then moved by this offset within their original frames and black pixels were added to fill the gaps. Figure 3.16 displays a series of images during a complete loading cycle between 0.25 kN and 2 kN. The crack is located in a similar position in each image due to the alignment of the images and the extra blank space is especially prominent at the maximum load (Figure 3.16d). This is due to the movement of the specimen in relation to the fixed position of the camera. The size of this area indicates the magnitude of the translational movement of the specimen in relation to the camera as the load is increased.

The images were captured at 1280×1024 pixels and a scale was needed to convert the measurement of pixels to length. A very thin scale with each marker spaced 0.25 mm was attached to a specimen loaded on the testing rig and images captured of some areas on the scale. An example image of the scale used for unit conversion is presented in Figure 3.17. A number of measurements were taken in pixels between markers on the scale of a series of scale images and averaged to produce a factor to convert from pixels to length. This worked out to be 1.104 μm/pixel and gives the



(a) $P/P_{max} = 0.125$ (b) $P/P_{max} = 0.25$ (c) $P/P_{max} = 0.50$

(d) $P/P_{max} = 0.75$ (e) $P/P_{max} = 1.00$ (f) $P/P_{max} = 0.75$

(g) $P/P_{max} = 0.50$ (h) $P/P_{max} = 0.25$ (i) $P/P_{max} = 0.125$

Figure 3.16: Images of the crack tip taken during a complete loading cycle. Images are aligned after being captured to keep the crack in a similar position on each image.

area of each full image to be 1414×1131 µm. This area however is reduced in some way on most images due to the alignment techniques used. Tracking the movement of each point with Digital Image Correlation is carried out in pixels, and this conversion is used throughout the experimental calculations to convert the displacement of points to units of length.

To calculate displacement in the y direction along the crack, sets of points are tracked on either side of the crack with Digital Image Correlation. In this experiment a mirroring grid of points was produced on either side of the crack with displacement measured between each point and its mirrored partner point. A grid of many points was used, as opposed to a few individual points (as used by Nowell and de Matos

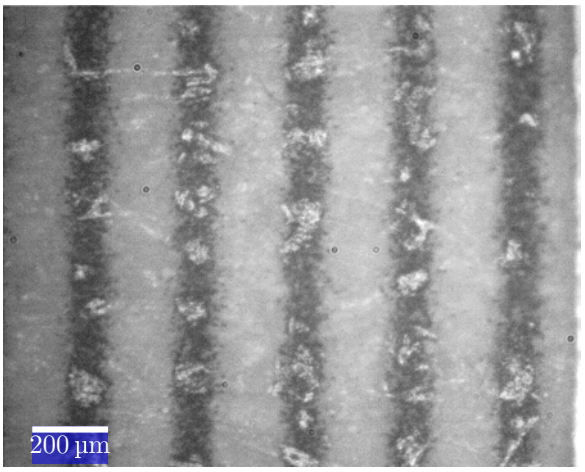


Figure 3.17: Scale attached to surface of specimen used to convert pixels to units of length. The lines of this scale are spaced 0.25 mm.

[50]), in order to minimise errors from the tracking of points. Initial attempts using a small number of points (<20) allowed for quick calculations, however using a grid of points produced more consistent results, with poorly tracked points having less effect on the analysed displacement data.

The two grids were produced by first selecting the best visual determination of the crack tip location on the image of maximum load. This was set as the initially determined crack tip location for the series of loading cycle images for all further analysis. Another point was selected on the crack towards the crack mouth so that a straight line between the two points will be roughly parallel to the crack faces. It was not always possible to get a good fit due to the crack not being straight so sufficient space between sets of points was given to ensure points were located on either side of the crack. A line between these two visually determined points served as the mirror line and points were spaced out on either side of this line. In the horizontal x direction, 200 points on each side were spaced evenly between the 2 visually selected points. In the y direction, 12 points were spaced with a distance of 5 pixels between them. The closest points to the crack were located 150 pixels in the y direction on either side of the determined mirror line. This gave two grids with a total of 4800 tracked points between them and 2400 pairs of points used to determine displacement along

the crack faces. An example of the location of the two grids of points around the crack is displayed in Figure 3.18. This grid of points analysed is also seen with the calculated plastic zone in Figure 3.14. As seen here, the crack is not always mid way between the two grids due to the mirroring line selected not following the exact path of the crack but rather just doing a best fit between two points; one at the crack tip and another near the crack mouth on the image. This is not expected to significantly effect the displacement results due to the y direction displacement field having little change with distance normal to the crack, as shown in Figure 3.22a.

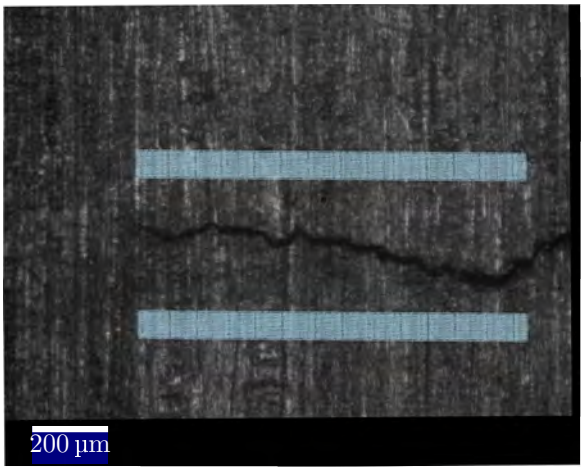


Figure 3.18: A typical image of a crack with a grid of points where displacements are measured using DIC. Displacement is analysed at 2400 points on either side of the crack.

3.2.1 Crack Length Calculations

In order to calculate a predicted value of K using the geometry of the specimen, the crack length needed to be specified. The length from crack tip to the notch cut in the specimen was added to the distance from the tip of the notch to the centre of the loading holes (12 mm) to give a value of a used in Equation (3.1). To measure the length of the crack a series of images were captured of the full crack from tip to the tip of the notch. This was performed directly after the images and data of a complete loading cycle had been captured and the load was held at the maximum 2 kN for the duration of the process. This ensured that the crack could be easily seen and the crack tip position could be located visually with a higher level of accuracy than if the load was less than the maximum. The initial crack tip imaging location was used as the first image, before the lens was then moved approximately half an image frame closer to the crack mouth for each subsequent image. This collection of images were aligned together using normalized 2-D cross-correlation in a similar process to that performed on crack tip images. The overall image size of the resulting image was expanded with each additional image and the full resolution of each initial image was preserved. Figure 3.19 is an example of a resulting image of the full crack length after 32,600 loading cycles. In this example the resulting image has a size of 8760×1024 and is made from 10 1280×1024 pixel images. The crack tip and notch tip positions were visually determined and the resulting measure of pixels between them were used to calculate the length of the crack. In Figure 3.19 the crack tip was determined to be 8061.8 pixels from the tip of the notch, which was converted to units of length giving 8.834 mm and $a = 20.834$mm.

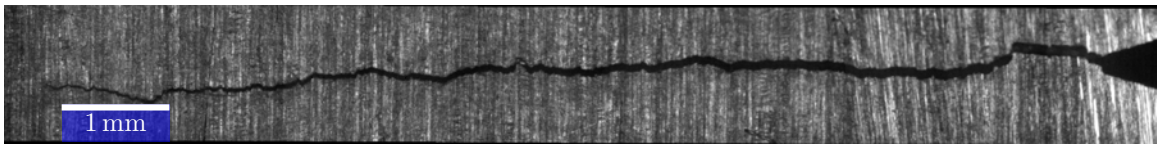


Figure 3.19: Collection of 10 images along a crack face aligned together to give an image of the full crack from the tip of the specimen notch. The specimen was loaded at 2 kN in this image and had been subjected to 32,600 loading cycles. This image was used to determine crack length.

3.2.2 Displacement Along Crack Flanks

The total change in vertical distance between each set of points is calculated giving a measure of the displacement along the crack flanks at each given load (P) and distance from the crack tip (r). The relative displacement of a typical crack (the same crack shown in Section 3.2) at points near the crack tip (50 µm) and close to the image edge (940 µm) is plotted along with the relative load during a single loading cycle in Figure 3.20. The effect of crack closure is quite clear in this plot during the initial loading and final unloading phases. In these periods there is very little change in relative displacement until $P/P_{max} > 0.3$ during loading and then again as $P/P_{max} < 0.3$ during unloading. This causes the graph of point displacements to have an overall narrower shape than that of the load, due to the portions at low loads when there is very little change in displacements while the force is increasing. While generally a very similar shape, points near the crack tip follow a slightly different path during loading than points further from the tip. Near the tip, there is a longer period of time before the displacements along the crack flanks increase (higher opening load) than further from the tip. Compared with measurements from the CMOD gauge (measurements of crack mouth displacement), all points measured along the crack flanks experience a greater period of time (and therefore a greater load) before displacements increase during initial loading. This shows that while the crack mouth displacement is increasing at low loads, it is not until the load reaches a certain opening load that the crack will be fully open right to the crack tip. This opening load

rises as proximity to the crack tip increases. All points appear to reach their maximum relative displacements when the load is at the maximum point of a cycle as expected. Figure 3.21 shows again the difference in load required for points near and far from the crack tip to begin to show crack opening by increases in displacement. Points at 900 µm from the crack tip will begin to displace in the y direction when $P/P_{max} > 0.25$ while points 50 µm from the tip will still have barely no displacement at this load. Those points located 50 µm from the crack tip will instead not start to increase in displacement until $P/P_{max} > 0.30$. This figure also clearly shows the difference in magnitude of the total displacement of points as P rises, with displacements of points further from the crack tip being much higher than those near the tip.

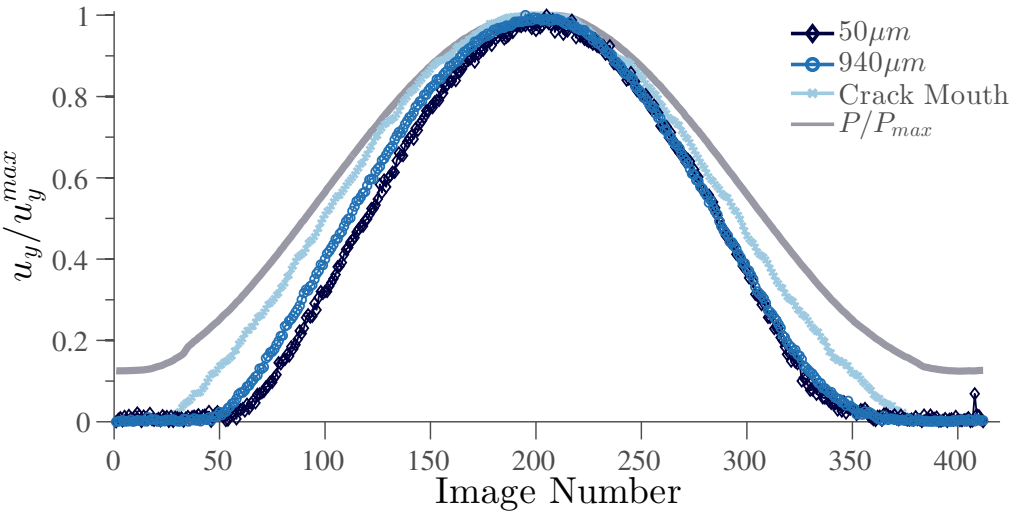


Figure 3.20: Typical variation of relative displacement at points 50 µm and 940 µm from the crack tip. The sinusoidal applied load (P) and measurements from the CMOD gauge are plotted along with these displacements for comparison.

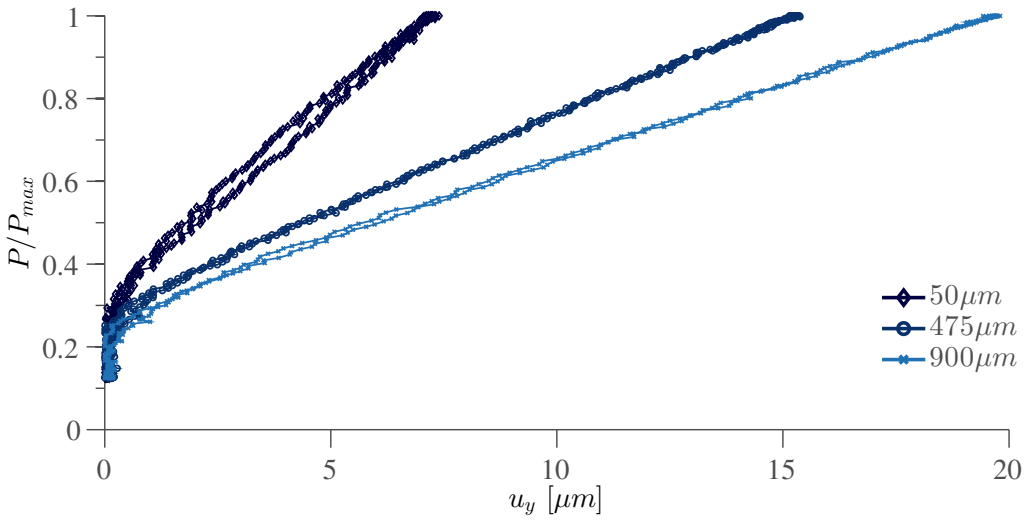


Figure 3.21: Relative load plotted against displacement, for three different sets of points located 50 µm, 475 µm and 900 µm from the crack tip.

3.3 Elastic Model

The experiment is setup to capture images of the crack tip in a position to analyse displacements along the crack flanks. This is due to the most significant displacements occurring along the crack flanks and limited displacement information would be obtained ahead of the crack tip (Figure 3.22). These measured displacements (u_y) along the crack flanks are used to compare different models of crack tip deformation, while also experimentally obtaining parameters which characterise crack loading.

The plane stress solution for vertical displacement, u_y, of points around the crack tip of an elastic crack is shown below in Equation (3.4) [4]:

$$u_y = 2\frac{K}{E}\sqrt{\frac{r}{2\pi}}\sin\frac{\theta}{2}\left(1+\sin^2\frac{\theta}{2}-\nu\cos^2\frac{\theta}{2}\right) \tag{3.4}$$

Where E is Youngs Modulus (estimated to be 70 GPa for the material being examined), r and θ are the cooridnates of points with respect to the crack tip as shown in Figure 2.2 (page 5), ν is the Poisson's ratio of the material (estimated to be 0.33) and K_I is the mode I stress intensity factor. Results from this solution are plotted in a contour plot in Figure 3.22a, which shows how the displacements

around the crack tip change with r. There is generally very little expected change in u_y in the y direction at each given value of r (given as x in Figure 3.22) along the crack flanks except for very near the crack tip. This is important, as it means that it is not expected to matter that the grids are not precisely along the crack faces, as mentioned earlier. This plot is slightly modified for the straightness of the crack and superimposed on an image of a crack in Figure 3.22b to show the expected displacement field around a typical growing crack.

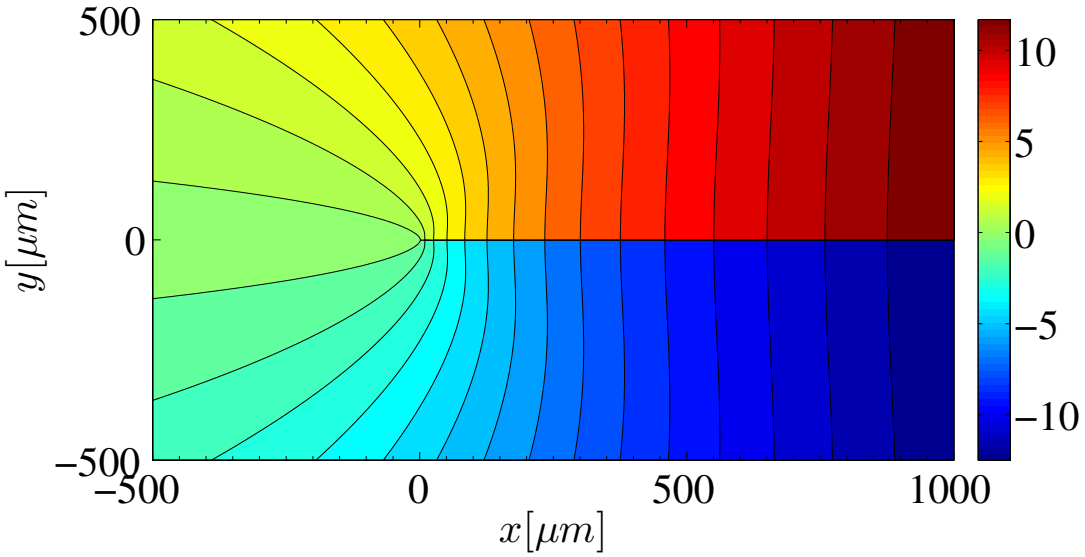
Looking simply at points along the crack flanks, Equation (3.4) can be used with $\theta = \pi$. This gives an equation for the displacement along the crack flanks according to the conventional elastic model for a sharp crack [4]:

$$u_y = \pm \frac{4K_I}{E} \sqrt{\frac{r}{2\pi}} \tag{3.5}$$

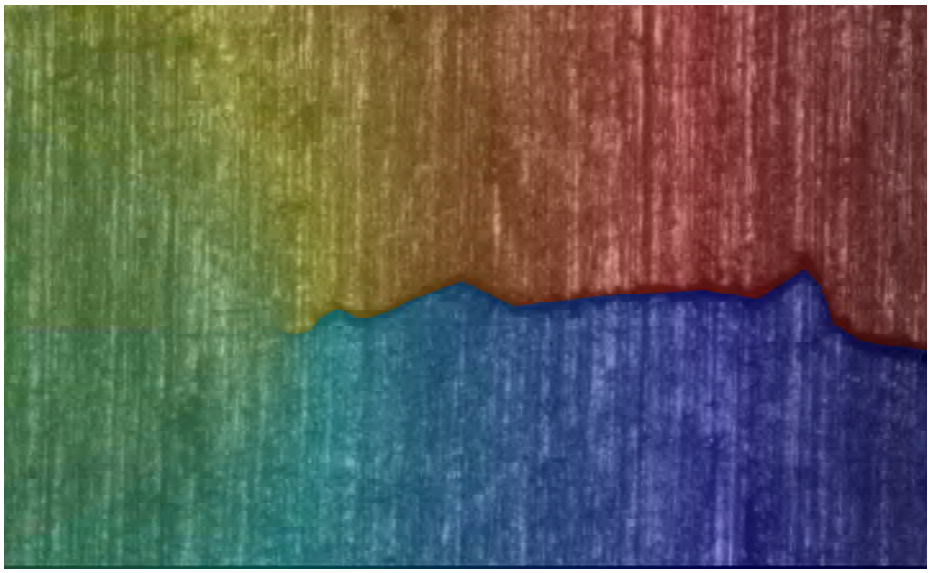
The plus-minus sign is used to account for both the upper (positive) and lower (negative) crack faces. Therefore the relative displacement between a set of two points along the crack can be given by:

$$u_y = \frac{8K_I}{E} \sqrt{\frac{r}{2\pi}} \tag{3.6}$$

Using Equation (3.6) with K calculated from Equation (3.1), an expected value of u_y can be obtained for a given load at a distance r from the crack tip. This calculated value is plotted alongside the displacements obtained from DIC analysis over a single loading cycle in Figure 3.23. Near the crack tip the calculated value of u_y is significantly lower than that measured from captured images, while at a distance of 900 µm from the crack the calculated value is higher for the duration of the loading cycle. Although the calculated displacement is higher at a distance of 900 µm from the crack tip, the shape and magnitude of the two curves are rather close. Due to the Digital Image correlation being based on displacements measured from an initial



(a) Calculated vertical displacement field around crack tip (located at [0,0]). All units including displacements are in µm.

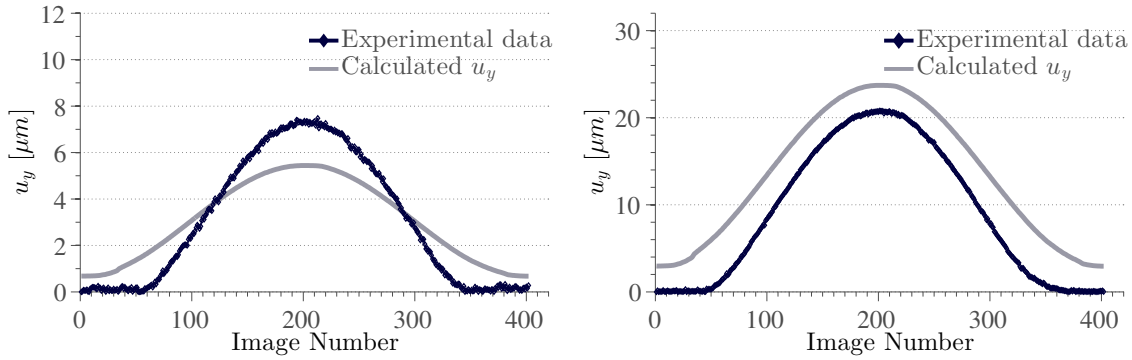


(b) Figure 3.22a adjusted and superimposed on a typical image of a crack.

Figure 3.22: Calculated vertical displacement field around a crack tip according to Equation (3.4). Crack has length of 8.9 mm (a =20.9 mm and $a/W = 0.348$) and $P = 2$kN.

image captured at 0.25 kN, the displacement will always be 0 at this load, even if there is some displacement between $0 < P < 0.25$ kN. This means the calculated value of u_y can be normalised with the experimental data at this point, so that there is not an initial offset. With the calculated displacement adjusted by removing this initial offset, the calculated value matches rather well with DIC measurements at a

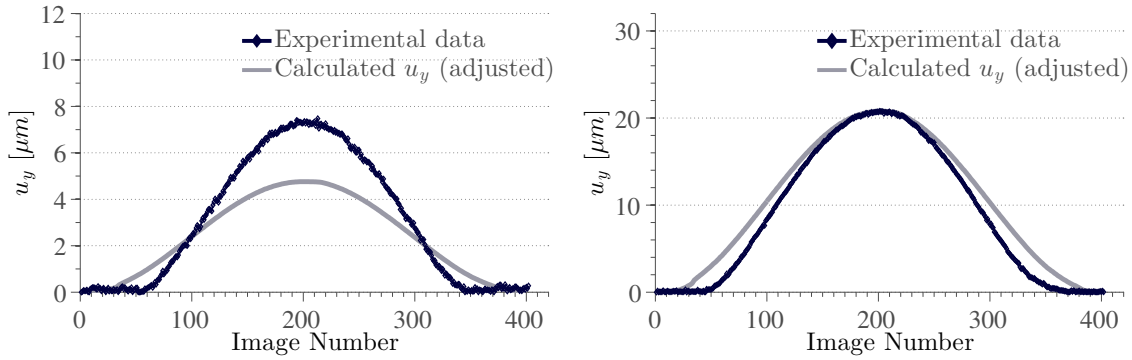
distance of 900 µm from the crack tip. The adjusted calculated displacement values are plotted in Figure 3.24b. Near the crack tip, the measured displacements are still higher than the calculated values using Equation (3.6) and, in fact, have a worse fit when adjusted for the offset at 0.25 kN (Figure 3.24b).



(a) Displacement of points located 50 µm from crack tip

(b) Displacement of points located 900 µm from crack tip

Figure 3.23: Vertical displacement of points at various distances from the crack tip. The load applied to the specimen varies with the image number as shown in Figure 3.20.



(a) Displacement during loading at 50 µm from the crack tip

(b) Displacement during loading at 900 µm from the crack tip

Figure 3.24: Displacement of points located (a) 50 µm and (b) 900 µm from crack tip. The calculated displacement is found with Equation (3.6) but is normalised with the displacement measured using DIC at the minimum load to account for the DIC measurements all being measured relative to the displacement at 0.25 kN.

By using Equation (3.6), the calculated value of u_y when r is small is the value when $y = 0$. In the experimental calculations there is an offset in the y direction from the crack that may cause the experimental data to differ from calculations. This offset comes from selecting grid points some distance from the crack (Figure 3.18). Equa-

tion (3.4) could be used instead to calculate the displacement at the locations of the analysed points. The difference between the two methods of calculating displacement can be seen in Figure 3.25 (which shows only points within 200 µm from the crack tip) where there is a significant difference in displacement values with $r < 100$µm. When calculated at the locations of the DIC tracked points, the displacement is calculated to have some positive displacement value rather than going to 0 as r reduces.

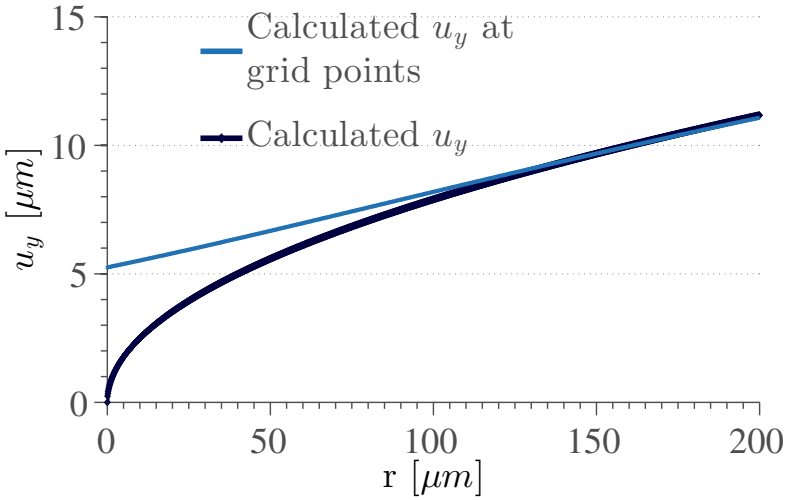
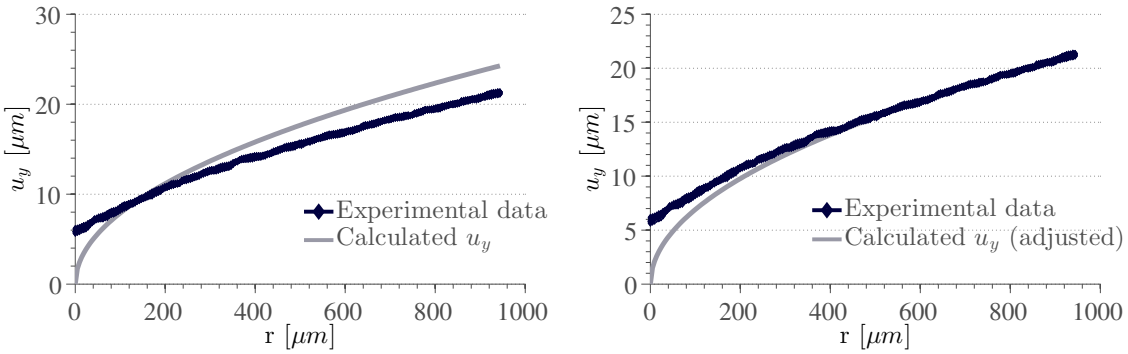


Figure 3.25: Calculated value of u_y at 2 kN using Equation (3.4) at locations of the grid points as shown in Figure 3.18 compared with calculated displacements using Equation (3.6) of points along the crack flank.

Calculating displacement in this way produces expected values closer to that measured with DIC analysis. Figure 3.26 shows DIC collected data and calculations of u_y using Equation (3.6) for points along the crack flanks at 2 kN. Near the crack tip the calculations do not fit well with the measured data, however when an adjustment is made to account for the offset at 0.25 kN (Figure 3.26), the calculations fit very well with the measured data at points over 400 µm from the crack tip.

Using Equation (3.4) to calculate the y-direction displacements at the location of the measured grid points gives a significantly improved fit with the measured data at points near the crack tip (Figure 3.27). As was the case when using the equation for points at the crack flanks, setting the calculated value of displacement to 0 at a load

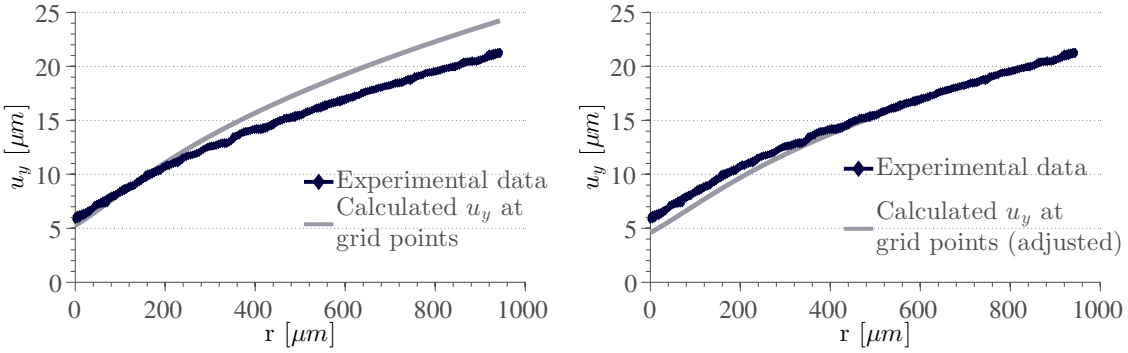


(a) DIC measured points and calculated displacement using Equation (3.6)

(b) Displacement using Equation (3.6) normalised to 0 at 0.25 kN

Figure 3.26: DIC measured displacement of points at load of 2 kN plotted with calculated displacement along crack faces according to Equation (3.6). In (b) the calculated displacement for all points at load 0.25 kN is subtracted from the calculated displacements shown in (a).

of 0.25 kN improves the fit with points further (over 400 µm) from the crack tip.



(a) DIC measured points and calculated displacement using Equation (3.4)

(b) Displacement using Equation (3.4) normalised to 0 at 0.25 kN

Figure 3.27: DIC measured displacement of points at load of 2 kN plotted with calculated displacement at measured points according to Equation (3.4). In (b) the calculated displacement for all points at load 0.25 kN is subtracted from the calculated displacements shown in (a).

3.3.1 Calculating the Stress Intensity Factor

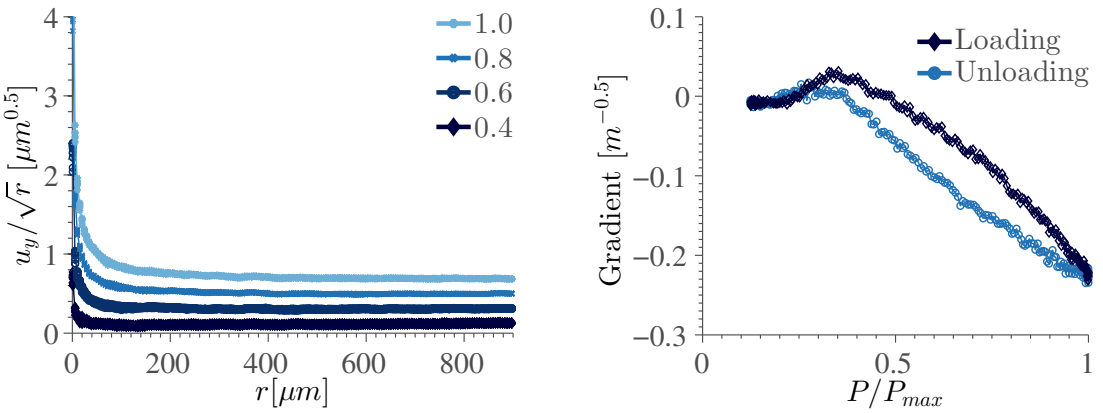
Using the displacement along the crack flanks and Equation (3.6), a plot of $\mu_y/\sqrt{r}$ vs r should be expected to give a straight line with a gradient of 0. This can then be used to obtain an experimental measurement of K from the y intercept of a line of best fit on the data points (Equation (3.7)). The K value calculated from experimental data can be compared with that expected from the specimen geometry (Figure 3.8, Equation (3.1)).

$$K_I = \frac{cE\sqrt{2\pi}}{8} \tag{3.7}$$

Where c is the y intercept.

A typical plot of $\mu_y/\sqrt{r}$ vs r is presented in Figure 3.28a. This plot is made from the displacement data of all points at P/P_{max} values of 0.4, 0.6, 0.8 and 1.0 during the loading phase of a single cycle. The resulting plot does not produce straight lines as expected, and instead there are much higher values of $\mu_y/\sqrt{r}$ near the crack tip than further along the crack length. At the visual crack tip location, the values of $\mu_y/\sqrt{r}$ are rather high, before decreasing quickly and settling on a more consistent value as r increases. The distance from the crack tip before $\mu_y/\sqrt{r}$ settles to a consistent value increases with an increase in the applied load. At $P/P_{max} = 0.4$ only approximately the closest 50 µm of points near the crack tip do not fit the rest of the calculated points, while at $P/P_{max} = 1.0$ this increases to the first 200 µm of points.

Linear regression lines were fitted to $\mu_y/\sqrt{r}$ vs r data at each point of the loading cycle where images were obtained. The gradient at each load was calculated (Figure 3.28b) to examine how closely it matched the expected value of 0. At low loads, there is very little displacement along the crack flanks and the crack remains closed, as shown earlier in Figure 3.21. During this phase the gradient remains close to zero as expected, however, as the crack opens the gradient of a regression line decreases



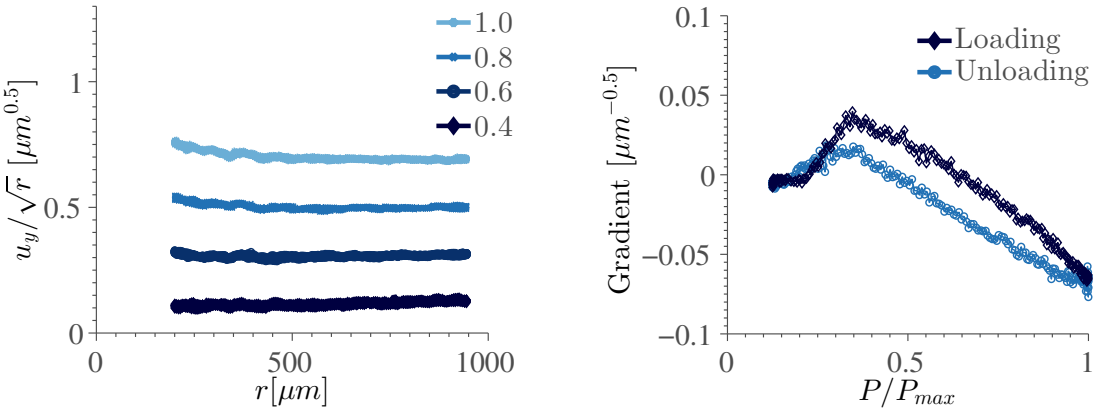
(a) All points at first measured positions (b) Gradient of regression lines from plot in (a)

Figure 3.28: (a)$\mu_y/\sqrt{r}$ vs r graph for various loads (P/P_{max}) during a single loading cycle. (b) Gradient of linear regression line from $\mu_y/\sqrt{r}$ vs r plot for all points (P/P_{max}) during a full loading cycle.

due to the $\mu_y/\sqrt{r}$ values near the crack tip being significantly higher than points further along the crack flanks. This figure shows again how this data has an increasingly poor fit with the model as the load is increased.

Looking at Figure 3.28a, it seems that excluding all data points within 200 µm of the crack tip will leave a figure with plotted points in generally flat lines with gradients close to 0. Figure 3.29a shows the resulting graph with points near the crack tip excluded and indeed the data forms significantly straighter lines. The average absolute gradient of the linear regression lines fitted to all loading points captured during a loading cycle has a value of 0.0268, which is significantly closer to the expected value of 0 than without points removed (gradient = 0.2057). Without removing any points the average R^2 during a loading cycle was 0.0927, which is a rather poor fit and indicates that the regression line approximates the data points with very little accuracy. However, a measure of variance (σ^2) of $\mu_y/\sqrt{r}$ may be a better indicator to assess the spread of the data from a mean value as a linear relationship is not expected. Without removing points the mean σ^2 for $P/P_{max} > 0.4$ is 8.486×10^{-7}, which decreases to 4.733×10^{-7} with the exclusion of points within 200 µm of the crack tip. This indicates an improved fit and shows that points some distance from

the crack tip have a closer fit to the suggested equation. The gradients of regression lines decrease as the load is increased, as was the case when analysing all points. This suggests that maybe not enough points were excluded, and at higher loads the displacements of points near the crack tip that are higher than expected for their location are producing negative gradients of best fitted lines. At lower loads, the positive gradients of a fitted line could be due to the crack being closed and points further from the crack tip opening first.



(a) Points within $200\mu m$ of crack tip excluded (b) Gradient of regression lines from plot in (a)

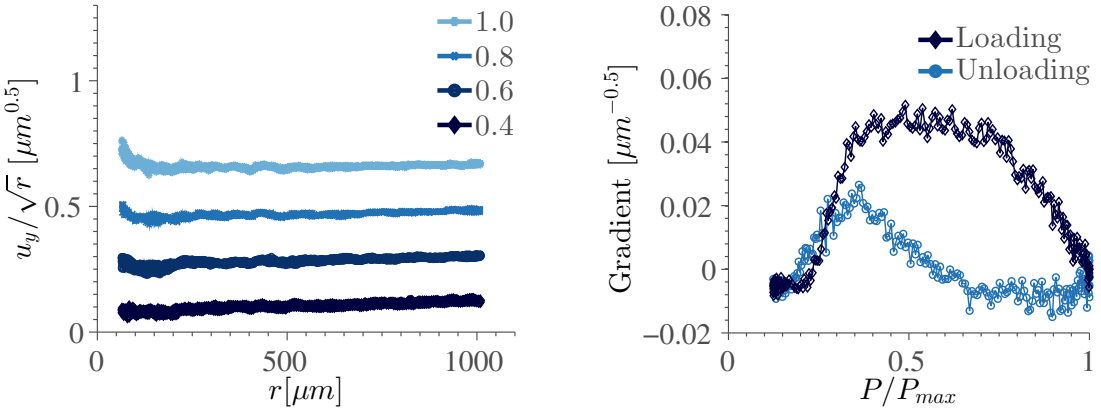
Figure 3.29: (a)$\mu_y/\sqrt{r}$ vs r graph for various loads (P/P_{max}) during a single loading cycle with the points within 200 µm of the visually located crack tip excluded. (b) Gradient of linear regression line from $\mu_y/\sqrt{r}$ vs r plot for all loads (P/P_{max}) during a full loading cycle.

In order to improve the fit of the experimental data an offset of the crack tip location could be added with the following justification:

- Visually locating the crack tip is a rather imprecise practice due to the resolution of the captured images. There is a good chance that the actual crack tip position is in fact ahead of what can be visually identified in the images.
- Even if a precise visual surface location is obtained, the crack tip is 3D and therefore the actual crack tip position could be ahead of that seen visually on the surface.

- Irwin (Section 2.1.2.1) suggests that the behaviour of the crack tip could be characterised with a 'virtual' crack tip position located ahead of the physical crack tip location due to the occurrence of plasticity.

Therefore, an offset is added to the values of r to examine how it effects the fit of the experimental data to the elastic model. Looking at the average gradients of regressions lines fitted to all points captured during of a loading cycle, the average gradient is closest to 0 when a crack tip displacement of 65 µm is added to all r values. Figure 3.30 shows a plot of the resulting data from adding a displacement of 65 µm to the crack tip location. The average absolute gradient of regression lines is 0.0150, which again is notably closer to 0, while the mean σ^2 of $\mu_y/\sqrt{r}$ for $P/P_{max} > 0.4$ is 7.524×10^{-7}, which is higher than only excluding points. The gradients are generally slightly positive throughout the loading cycle, and with a displaced crack tip location the different response between the loading and unloading sections of the loading cycle can be seen in Figure 3.30b.



(a) Crack tip location displaced 65 µm

(b) Gradient of regression lines from plot in (a)

Figure 3.30: (a)$\mu_y/\sqrt{r}$ vs r graph for various loads (P/P_{max}) during a single loading cycle with the crack tip location displaced by 65 µm and therefore all r values increased by this amount. (b) Gradient of linear regression line from $\mu_y/\sqrt{r}$ vs r plot for all loads (P/P_{max}) during a full loading cycle.

Both displacing the crack tip location away from the crack mouth, from that which is visually located, and excluding points close to the crack tip, improve the fit of the

Added r (μm)	Excluded points (μm from crack tip) 0	100	200	300	400	500
0	0.2057	0.0424	0.0268	0.0178	0.0145	0.0126
20	0.0722	0.0293	0.0192	0.0137	0.0130	0.0141
40	0.0336	0.0184	0.0132	0.0117	0.0136	0.0177
60	0.0162	0.0142	0.0143	0.0167	0.0195	0.0225
80	0.0264	0.0280	0.0252	0.0238	0.0258	0.0288
100	0.0419	0.0419	0.0357	0.0310	0.0313	0.0340

Table 3.4: Mean (absolute) gradients of lines of best fit from $\mu_y/\sqrt{r}$ vs r plot during a single loading cycle. Distance to the crack tip (added r) was adjusted to simulate the crack tip being ahead of where it was visually located. Points were excluded at different distances depending on their proximity to the crack tip.

collected data to that which is expected from Equation (3.6). A table (Table 3.4) is presented with the average gradients of lines of best fits over analysed points during a complete loading cycle. This shows the resulting effects these adjustments have on the gradients of linear lines fitted to $\mu_y/\sqrt{r}$ vs r data. As expected from looking at the plots in Figure 3.30, adding a displacement to the crack tip location and excluding points near the crack tip both result in the average gradient of fitted lines being closer to 0. It is interesting to note that as the number of excluded points is increased, the value of added displacement to the crack tip location needed to produce an average absolute gradient closest to 0 decreases. The mean σ^2 of $\mu_y/\sqrt{r}$ also significantly decreases by excluding points near the crack tip (Table 3.5) and, like the gradient, the decrease is more prominent than by adding an offset to the crack tip location. Therefore it is determined that the points near the crack tip do not fit well with this model when analysed in this way. Position of these points in relation to the crack tip and the cyclic plastic zone at the crack tip may be factors in this poor fit.

The cyclic plastic zone at the crack tip is likely to be a contributing factor in the difference in calculated data of points near the crack tip and those some distance from the tip. Figures 3.14 and 3.15 show an approximation of the calculated forward plastic zone size using the theoretical K values. While the cyclic plastic zone is expected to

Added r (μm)	Excluded points (μm from crack tip) 0	100	200	300	400	500
1	8.4863	6.1235	4.7330	3.4867	2.4823	1.6573
20	7.8760	6.3689	4.9645	3.6931	2.6591	1.8006
40	7.6892	6.6140	5.1996	3.9561	2.8908	1.9897
60	7.5699	6.8600	5.4360	4.1740	3.0775	2.1465
80	7.4822	7.0988	5.6700	4.3947	3.2683	2.3070
100	7.4132	7.3394	5.9062	4.6187	3.4659	2.4744

Table 3.5: Mean σ^2 ($\times 10^{-7}$) for $P/P_{max} > 0.4$ of $u_y/\sqrt{r}$ during a single loading cycle. Distance to the crack tip (added r) was adjusted to simulate the crack tip being ahead of where it was visually located. Points were excluded at different distances depending on their proximity to the crack tip.

be smaller than this, there is likely to still be some overlap of the plastic zone and points that are being analysed. This could account for the pattern that is seen of the displacements of points near the tip differing from expectations obtained from looking at other points some distance from the tip. As the load increases, so does K and therefore the plastic zone size increases. The increase in the size of the plastic zone could explain the effect of the increase in the selection of points near the crack displacing more than expected as the P approaches P_{max}.

The approximate plastic zone size at the crack tip can be estimated by calculating the elastic stress field ahead of the crack tip to yield stress, as explained in Section 2.1.2. The radius of this plastic zone, r_p, is found from Equation (2.4):

$$\sigma_y = \frac{K_I}{\sqrt{2\pi r}} \iff r_p = \frac{1}{2\pi}\left(\frac{K_I}{\sigma_{ys}}\right)^2 \qquad \text{(2.4 revisited)}$$

However, Irwin in his analysis (Section 2.1.2.1) argues that due to the occurrence of plasticity at the crack tip; the crack behaves as if it were actually longer than its physical size. This means that the displacements are larger and the stiffness is lower than in the elastic case. The effective length of the crack a_{eff} can be defined as:

$$a_{eff} = a + \Delta a_n \qquad \text{(2.5 revisited)}$$

Where

$$\Delta a_n + r_p = 2r_p \qquad \text{(2.9 revisited)}$$

And therefore

$$a_{eff} = a + r_p \qquad (3.8)$$

This gives the notional crack tip location a distance r_p ahead of the crack tip location determined to be a and a plastic zone size of $2r_p$. Using Equation (2.4) to calculate the forward plastic zone radius, r_p, with the value of K obtained from the specimen geometry (Equation (3.1)), the values of r_p increase as the load applied to the specimen increases. With a growing crack, the cyclic plastic zone size is present at the crack tip, which is 1/4 of the forward plastic zone size calculated with Equation (2.4). The calculated values of the forward and cyclic plastic zone radiuses during a complete loading cycle are shown in Figure 3.31.

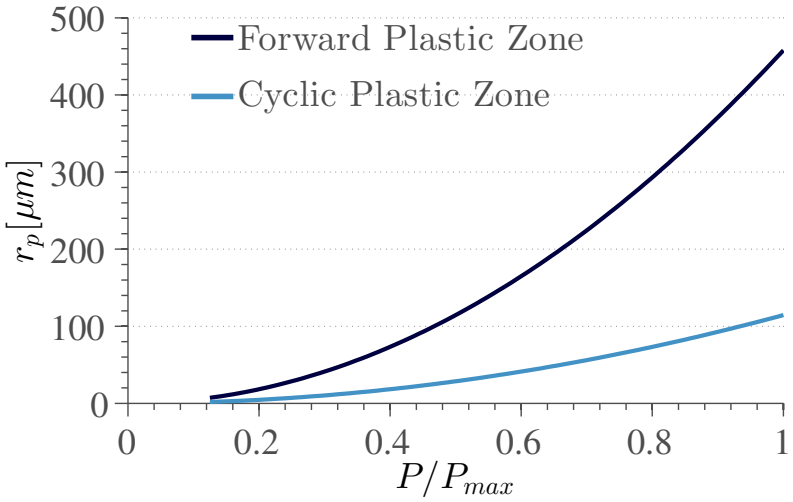


Figure 3.31: Calculated plastic zone size (r_p), according to Equation (2.4), in relation to load applied to specimen (P/P_{max}).

To examine Irwin's theory of a notional crack tip located ahead of the visually determined crack tip location, an offset is added to all measured points along the crack (r). For each load this offset is adjusted according to the cyclic plastic zone in Figure 3.31. The resulting plot of $\mu_y/\sqrt{r}$ vs r is shown in Figure 3.32. The resulting plots have a mean gradient of fitted linear regression lines of 0.0469 for $P/P_{max} < 0.4$. It appears the fit is reasonable at lower loads, other than at points close to the crack tip, and then the added offset is slightly too high at higher loads, leading to a positive gradient of a fitted regression line. The crack tip offset required to produce a linear regression line with a gradient closest to 0 can be found for each load (described as the 'optimum' displacement) and the displacements are plotted in relation to the plastic zone size in Figure 3.33. This figure shows that the cyclic plastic zone is close to, but slightly above the offset that produces the closest fit to the elastic model. Using the value of K calculated from the specimen geometry, which does not take into account crack closure, may be a reason for the calculated plastic zone size offset being slightly larger than the offset producing the best fit to the model.

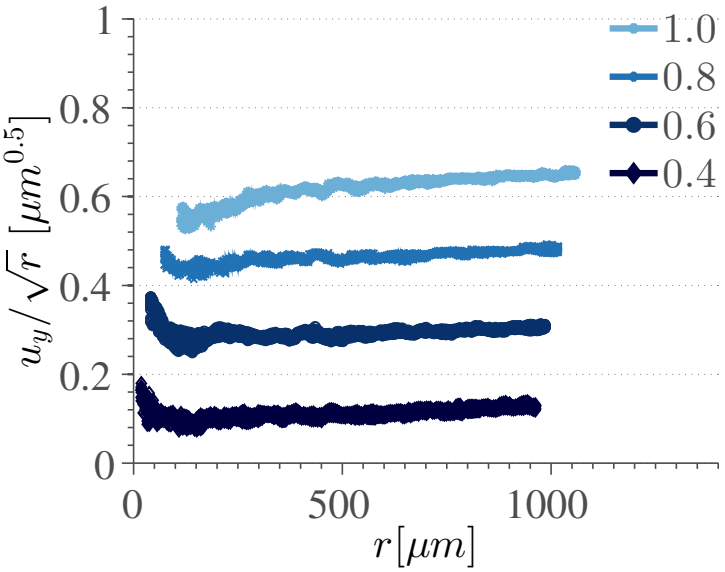


Figure 3.32: $\mu_y/\sqrt{r}$ vs r graph for various loads (P/P_{max}) during a single loading cycle with the crack tip location displaced by the plastic zone radius (Equation (2.4)) determined at each given load.

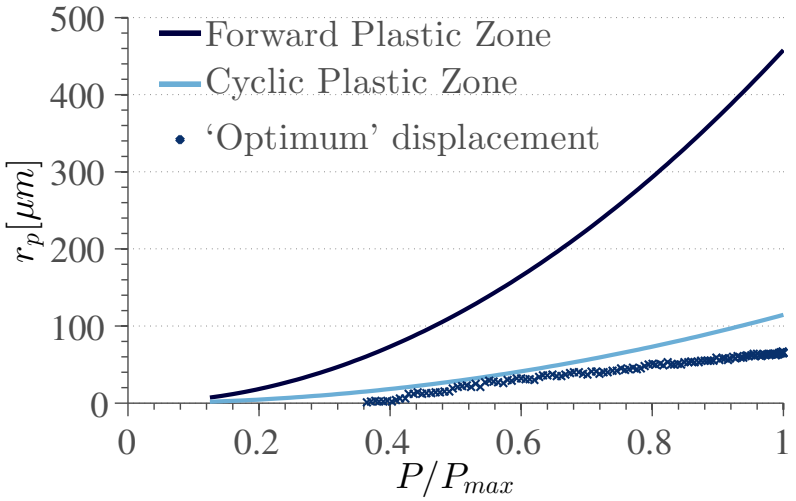
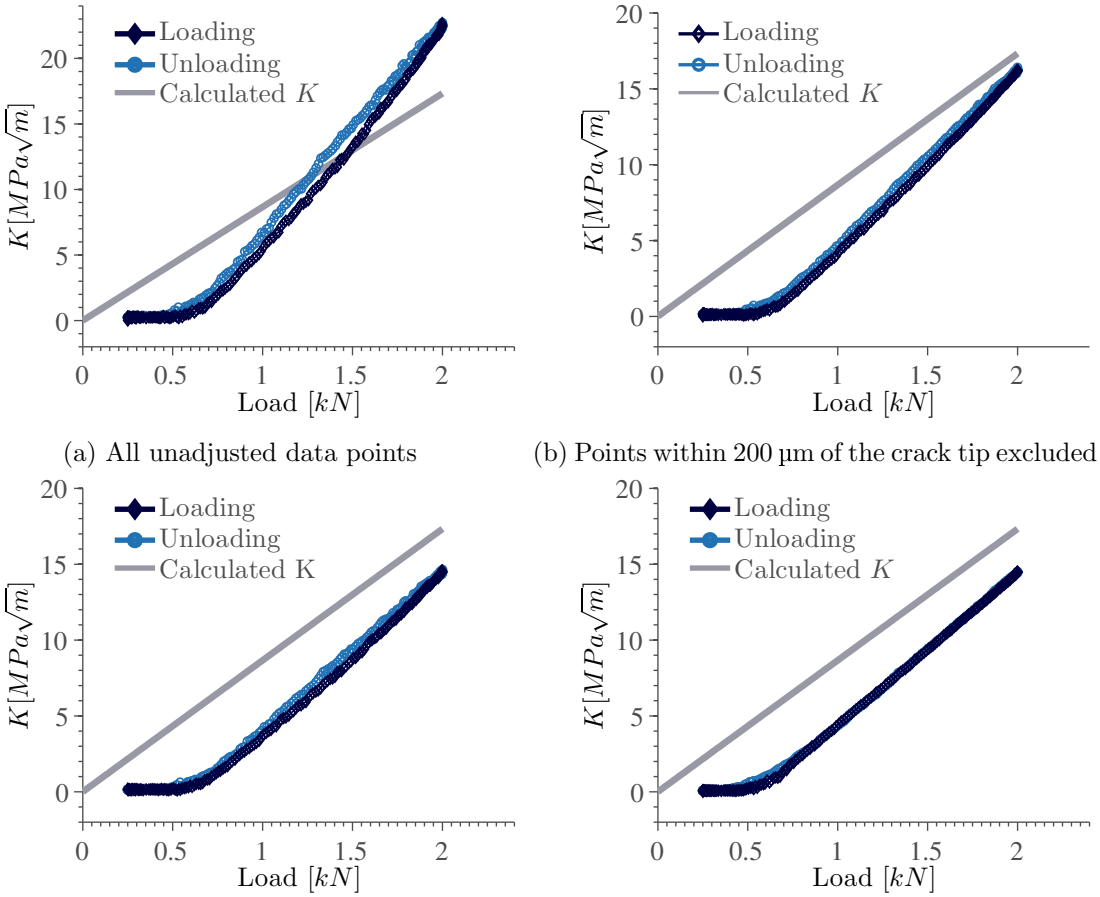


Figure 3.33: Calculated plastic zone size (r_p), according to Equation (2.4), in relation to load applied to specimen (P/P_{max} [grey]. 'Optimum' crack tip displacement distances are plotted for selected loads.

The data from these $\mu_y/\sqrt{r}$ vs r plots can be used, as described earlier, to obtain a value for the stress intensity factor, K (Equation (3.7)). This may be compared to the calculated value of K for the geometry of the specimen and load applied (Equation (3.1)). With the original unadjusted data points, the value of K calculated from the experimentally obtained displacement data does not match up well with that predicted from the specimen geometry (Figure 3.34a). Initially there is a delay in the rise of the Stress Intensity Factor as the load increases due to the crack being closed and displacement around the crack not increasing until the crack starts to open. After the load surpasses approximately 0.6 kN ($P/P_{max} = 0.3$) the experimentally determined value of K increases linearly and rapidly, at a faster rate than the theoretical K, up to a maximum of 22.72 $MPa\sqrt{m}$. This sharp rise in K with a maximum above the theoretical value is a reflection of the poor fit of the displacement data with Equation (3.6) and the resulting large negative gradient of a linear regression line fitted to the plotted data points in Figure 3.28. The significant negative gradient caused by high displacements of points near the crack tip results in the fitted line having a larger than expected y intercept value and therefore a high K value especially as the

load increases. As discussed earlier, adjusting the data obtained by either excluding points or adding a displacement to the crack tip location provides an improved fit and the plot of K vs Load (Figures 3.34b and 3.34c) shows a closer match to the theoretical value of K. The best fit is obtained by adjusting the data with an 'optimum' displacement that is found by selecting the crack tip offset that produces a linear regression line closest to 0 on a $\mu_y/\sqrt{r}$ vs r plot. This 'optimum' displacement is also the one closest to the cyclic plastic zone size.

In all cases the crack closure at lower loads results in an offset from the theoretical calculation due to the measure of displacement around the crack not increasing until the load rises above a certain opening load. Another way of explaining this is if the section of the graph with similar gradient to the theoretical K value was traced back to a load of 0, there would be a residual K of approximately 4 $MPa\sqrt{m}$. This residual K is caused by crack closure and the associated residual compressive stresses around the crack tip which exist as the load decreases to 0. This negative K has no physical meaning on its own but it is a convenient concept in a superposition argument (Section 2.2.3.1) when combined with the applied value, provided that the total $K > 0$ [50]. The displacement field around the crack tip does not match the predicted K field due to the residual stresses, however the crack shape is predominantly elastic after opening and the residual stresses produce an offset. This is a convenient means of estimating the crack opening load and therefore the effective Stress Intensity Factor at the crack tip.



(a) All unadjusted data points

(b) Points within 200 µm of the crack tip excluded

(c) Crack tip location displaced 65 µm from visually determined location

(d) Crack tip location displaced various 'optimum' distances as shown in Figure 3.33

Figure 3.34: Comparison of K values calculated from the y intercept of best fit linear regression lines of $\mu_y/\sqrt{r}$ vs r plots (Equation (3.7)) and those predicted with an analytical equation based on the specimen geometry and load (Equation (3.1)).

3.4 Elastic-plastic Model

The background and detailed description of the elastic-plastic model proposed by Pommier [5] is given in Section 2.2.4. The model relies on partitioning the displacement field around the crack into both elastic and plastic normalised components. The model leads to a similar equation as the linear model represented by Equation (3.6), however there is the addition of a plasticity factor, ρ:

$$u_i(r) = \frac{8K_I}{E}\sqrt{\frac{r}{2\pi}} + \rho \tag{3.9}$$

The plasticity factor, ρ, has units of length and a plot of u_y against $\sqrt{r}$ should yield a straight line that has a gradient of $8K/(E\sqrt{2\pi})$ and a y intercept of ρ. These values can be found by plotting the vertical displacements, u_y, against $\sqrt{r}$ for different values of P/P_{max}. From this plot, a linear regression line of best fit can be found for each P/P_{max} value with the gradient and y intercept being used to find K and ρ respectively.

3.4.1 Calculating K During Loading

An experimental measure of K was calculated by plotting u_y against $\sqrt{r}$ and taking the gradient as $8K/(E\sqrt{2\pi})$. The displacement of all analysed points was plotted in this fashion and a linear regression line of best fit through all points was used in this calculation.

Figure 3.35 shows a typical set of results obtained with a crack length of approximately 20.9 mm (the same crack shown in Figures 3.14 and 3.15). It can be seen that the displacement data does give rather straight lines when plotted this way. Linear regression lines are fitted to the data points for a complete loading cycle and the coefficient of determination (R^2) values obtained for $P/P_{max} > 0.4$ lie in the range $0.9561 < R^2 < 0.9904$ with a mean R^2 of 0.9851, indicating a good fit with a linear

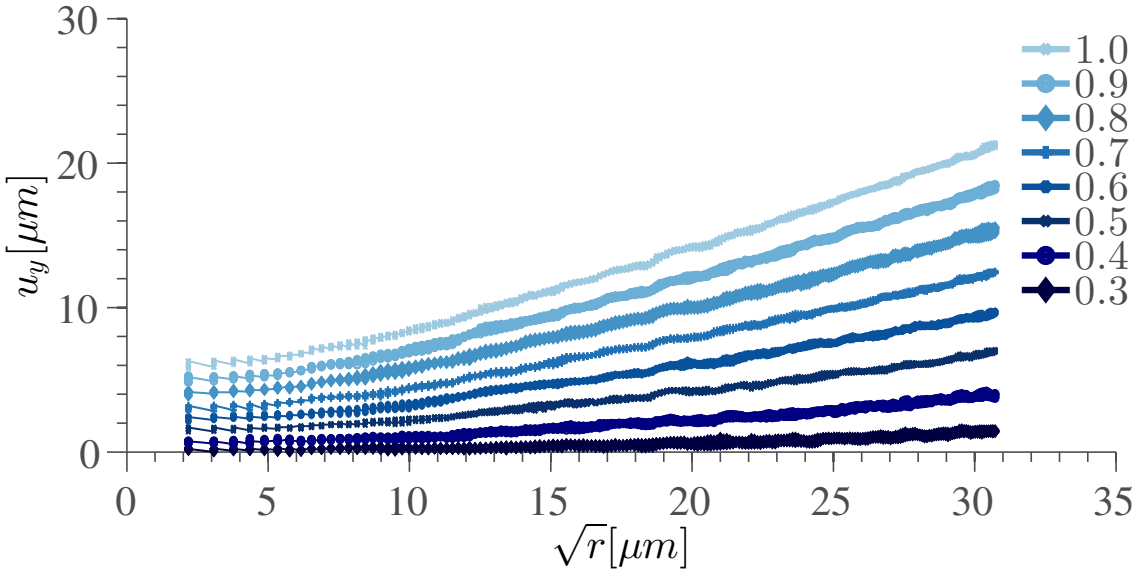


Figure 3.35: Variations of relative displacement (u_y) with distance from the crack tip (r) at eight different values of load (P/P_{max}) during the loading phase of a single cycle.

regression line. At loads below this, when the crack is closed and just opening, there is a significant drop of in the quality of fit of a regression line. As the load increases, the quality of fit of a linear regression line increases up to the maximum of 0.9904 and is displayed in Figure 3.36.

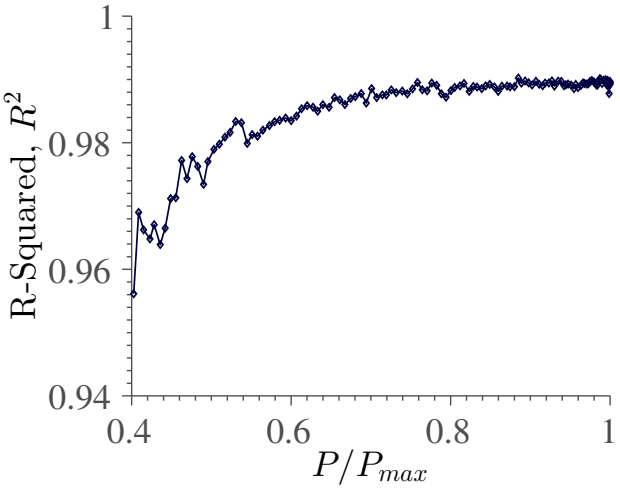
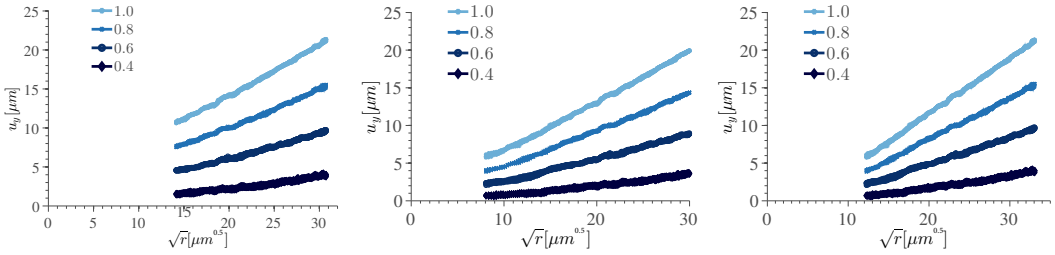


Figure 3.36: Coefficient of determination (R^2) values of regression line fitted to u_y vs $\sqrt{r}$ plotted data (Figure 3.35) for $P/P_{max} > 0.4$.

The collected data can be adjusted in a similar fashion to that done for the elastic model (Section 3.3) to see if adding an offset or excluding points near the crack tip will improve the fit with a linear regression line. The resulting plots are displayed in Section 3.4.1 and all improve the R^2 values of fitted lines for loads above $P/P_{max} > 0.4$. Excluding all points within 200 µm of the crack tip (Figure 3.37a)increases the mean R^2 value over a full loading cycle to 0.9931 with a range of $0.9674 < R^2 < 0.9982$. Adding a displacement of 65 µm (Figure 3.37b) produces a further increased mean R^2 of 0.9955 with range $0.9767 < R^2 < 0.9988$ while a larger displacement of 150 µm (Figure 3.37c) gives $0.9810 < R^2 < 0.9993$ with a mean R^2 of 0.9971. The goodness of fit of a linear regression line keeps increasing slightly as the displacement of the crack tip location increases, even to a point that is physically impossible (past the end of the specimen) and so this is probably not a suitable indicator to be used for identifying the actual crack tip location.



(a) Excluding points within 200 µm of crack tip

(b) Displacement of 65 µm added to crack tip location

(c) Displacement of 150 µm added to crack tip location

Figure 3.37: Variations of relative displacement (u_y) with distance from the crack tip (r) at four different values of load (P/P_{max}) during the loading phase of a single cycle.

As mentioned previously, the gradient of a line of best fitted to this data is $8K/(E\sqrt{2\pi})$. Therefore:

$$K_I = \frac{mE\sqrt{2\pi}}{8} \tag{3.10}$$

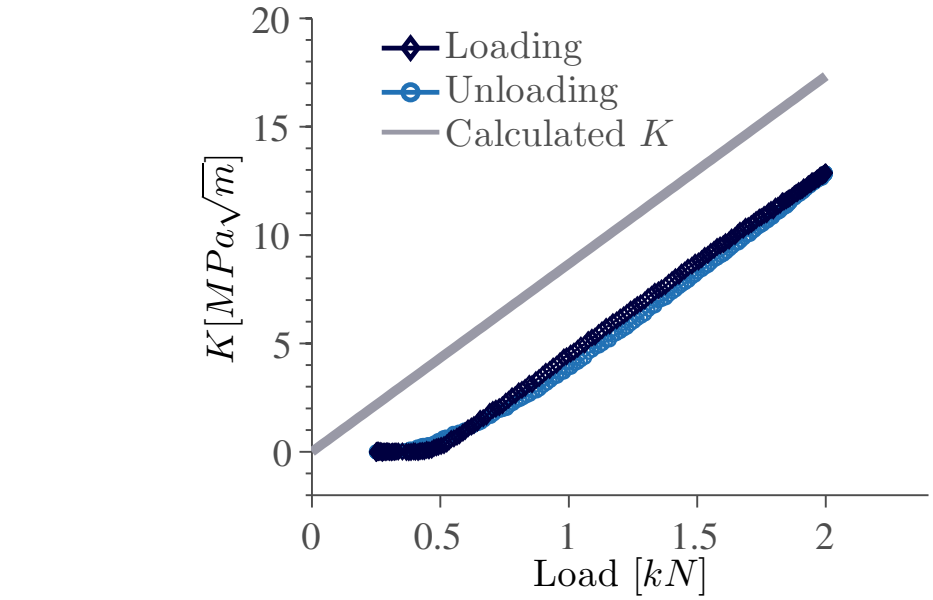
Where m is the gradient.

A value of K can be found from the experimentally obtained displacement data using this equation. Graphs showing typical calculated K values from experimental

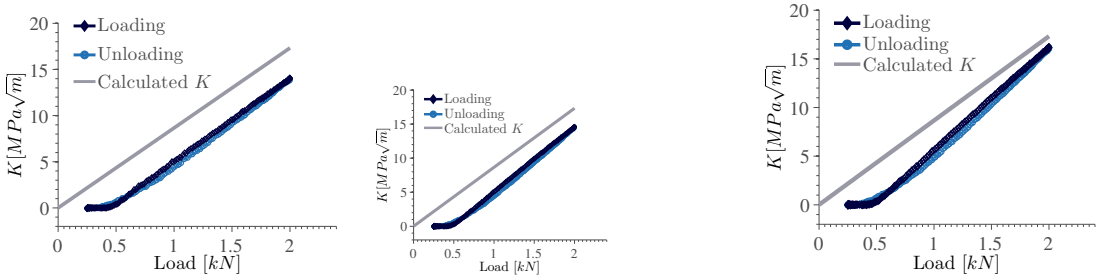
displacement data during a complete loading cycle are displayed in Figure 3.37. The analytical value of K calculated from the specimen geometry and loading is displayed alongside for comparison. As with the elastic model, the crack closure creates an offset due to residual stresses at the crack tip when the load is low. After this initial period of closure, the value of K calculated from the experimental displacement data increases linearly with load at a very similar rate to the predicted K value. The gradients of these two lines very closely match once the crack has opened at loads above approximately 0.6 kN ($P/P_{max} = 0.3$). Excluding points near the crack tip (Figure 3.38b) and adding a displacement of 65 µm (Figure 3.38c) do not significantly alter the shape and fit of the experimentally determined K value compared with the analytically calculated K. However, as the crack tip displacement increases, the gradient of the experimental K values increase and no longer match that of the predicted K calculated from the specimen geometry (Figure 3.38d). With larger displacements above 150 µm the value of K rises even higher at a maximum load as the plotted points on a u_y vs $\sqrt{r}$ span smaller $\Delta\sqrt{r}$ ranges and the gradients of fitted lines become steeper.

3.4.2 $K - \rho$ space

The model produced by Pommier and Hamam [5] predicts some phases of loading within a load cycle to be largely elastic, with a change in K and very little variation in ρ. These periods are specifically when loading from zero and the initial unloading phase (directly after the maximum load is applied in a cycle). Figure 2.18 shows a schematic of the estimated crack behaviour in $K-\rho$ space. The K vs ρ plots produced from calculations to the gradients and y intercept values of u_y vs $\sqrt{r}$ graphs are shown in Figure 3.39. A rather different shape of the $K - \rho$ space can be seen as the data is adjusted in different ways as done previously. In general, as more displacement is added to the crack tip location, the ρ values decrease. This is due to the y-intercept



(a) All points, unadjusted



(b) Excluding points within 200 µm of crack tip

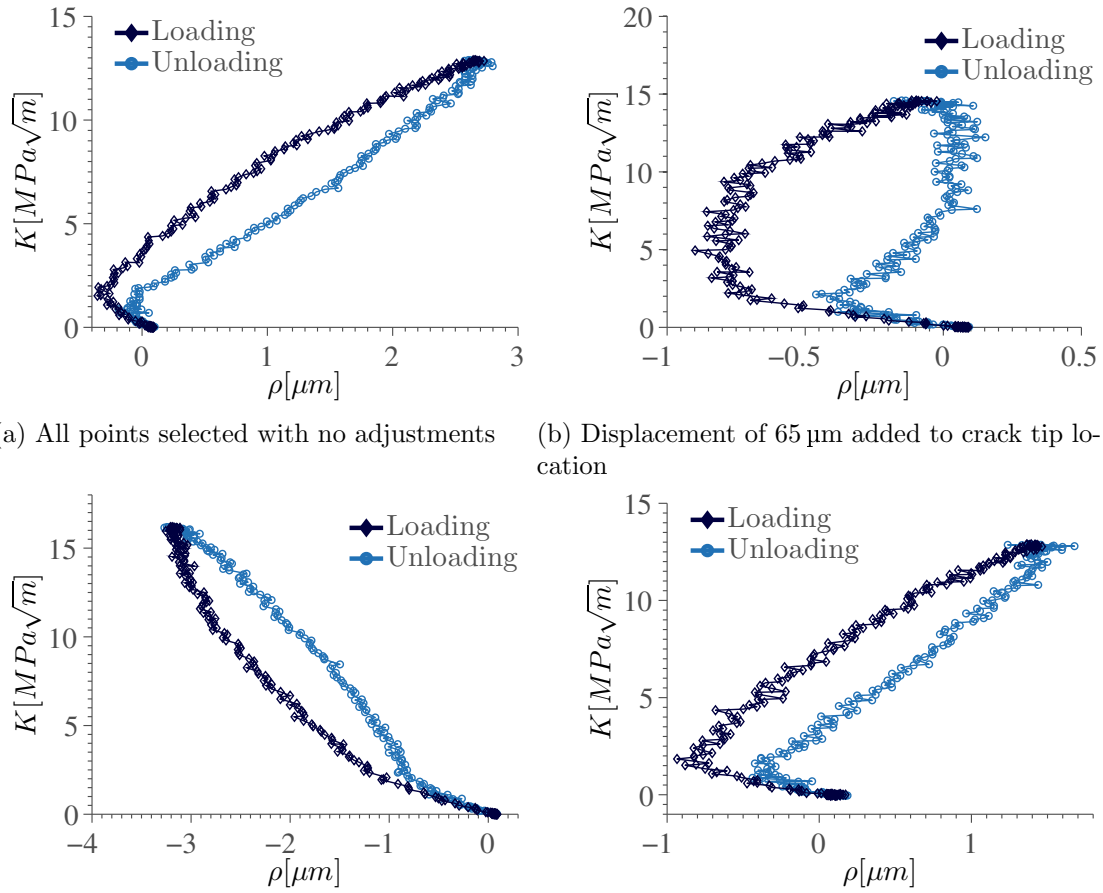
(c) Displacement of 65 µm added to crack tip location

(d) Displacement of 150 µm added to crack tip location

Figure 3.38: Predicted K value at crack tip during loading cycle (Equation (3.1)) plotted with typical calculated K values from experimentally obtained displacement data. Displacements from loading and unloading phases are used to calculate K by fitting linear regression lines to u_y vs $\sqrt{r}$ plots.

of the regression line having a lower value as the points form a steeper line (higher K) with a lower $\sqrt{r}$ range. This causes the graph points to be shifted to the left as the K value increases as can be seen in the difference between Figure 3.39a and Figure 3.39d. The magnitude of this shift left (reduction of ρ) is proportional to the load with higher loads having a greater reduction in ρ when an offset is added. In all cases the loading and unloading portions of a cycle follow different paths and the hysteresis type behaviour that is predicted can be clearly seen.

One feature that is common in all graphs of Figure 3.39 is the negative ρ values



(a) All points selected with no adjustments

(b) Displacement of 65 µm added to crack tip location

(c) Displacement of 150 µm added to crack tip location

(d) Excluding points within 200 µm of the crack tip

Figure 3.39: K vs ρ plots of points with various adjustments to the collected data

especially during the initial loading phase. It is likely that the fit of a regression line to the displacement points before the crack is open will be poor due to the very small displacements. With such small displacements the size of any small error tracking the points is magnified. Looking at Figure 3.39b for points with $P > 0.3P/P_{max}$ in Figure 3.40, some of the features in Pommier's model can be seen. During the initial opening phase there is very little change in ρ as K increases until K is approximately 3/4 of K_{max}. Above this load, K increases but there is also a significant increase in ρ until $K = K_{max}$. The unloading portion of the cycle is the reverse of the loading with the initial unloading having very little change in ρ with the reduction in K. The last phase of the unloading is a linear reduction in ρ with K back towards, but not

looking as though it will be equal to if the graph continued, the value of ρ at initial loading. Although the shape of the graph is similar to what is expected, the values of ρ are negative throughout which does not make physical sense.

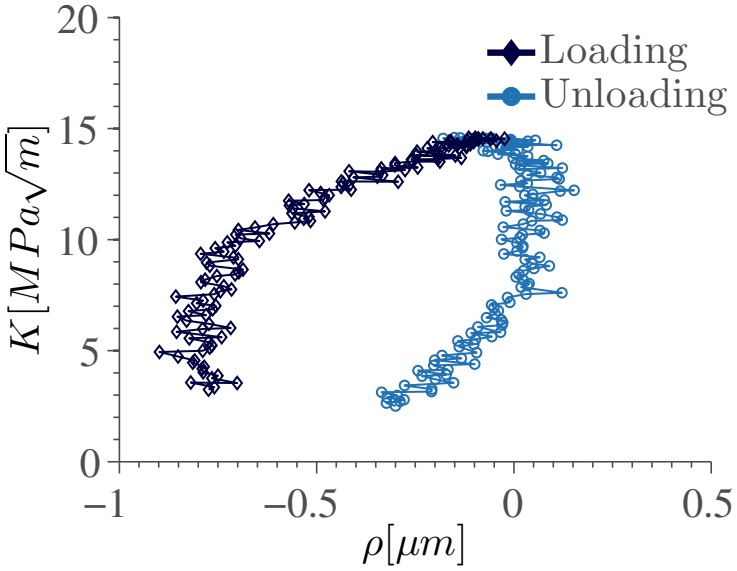
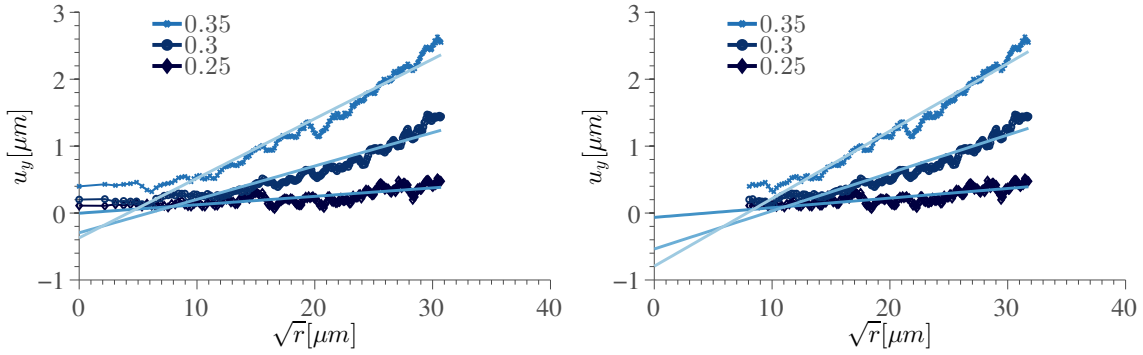


Figure 3.40: K vs ρ plot for loads $P/P_{max} > 0.4$.

The prevalence to negative ρ values in all K vs ρ plots of Figure 3.39 suggests that there may be some error in fitting a linear regression line to the data points. Looking closer at plots of u_y vs $\sqrt{r}$ at lower loads shows where this effect comes from. Figure 3.41 shows these graphs with loads $P < 0.35P/P_{max}$. A linear regression line is fitted to each set of points and the y-intercept of that line is what determines ρ. In each case the y-intercept of a regression line is negative, even though the displacements of points very close to the crack tip are actually increasing and are certainly not negative. This poor fit of a linear regression line at points near the crack tip at low loads is likely due to plasticity at the crack tip and crack closure. As the crack opens, points further from the crack tip have greater displacements than those near the tip and the displacements of those points fit well with a straight line as expected in Equation (3.9). However, the displacement of these points is not as high as expected for their position from the crack tip and therefore a fitted line has a poor fit with the points near the crack tip. Adding an offset to the crack

tip location improves the fit of the regression lines for points close to the crack tip, although again the displacements are lower than expected to produce a straight line with positive y-intercept. Adding an offset to the crack tip location actually reduces the y-intercept of a linear regression line due to increasing the gradient and moving the points further from the y axis. Looking at only the points in close vicinity of the crack tip location (Figure 3.42) shows clearly that the displacement of points near the crack tip are all increasing as the load increases up to $P/P_{max} = 0.35$. A fitted line to only these points results in positive ρ values as the load and K increases. Tables showing the gradient, y-intercept and R^2 goodness of fit of regression lines for all points and then only the closest 30 point locations (140 µm) to the crack tip are displayed in Tables 3.6 and 3.7. These tables show how low the R^2 values are at low loads and that only looking at points near the crack tip changes the y-intercept from predominantly negative values to positive numbers that make physical sense. The R^2 values of fitted lines are significantly higher with $P/P_{max} > 0.35$ than below this value.

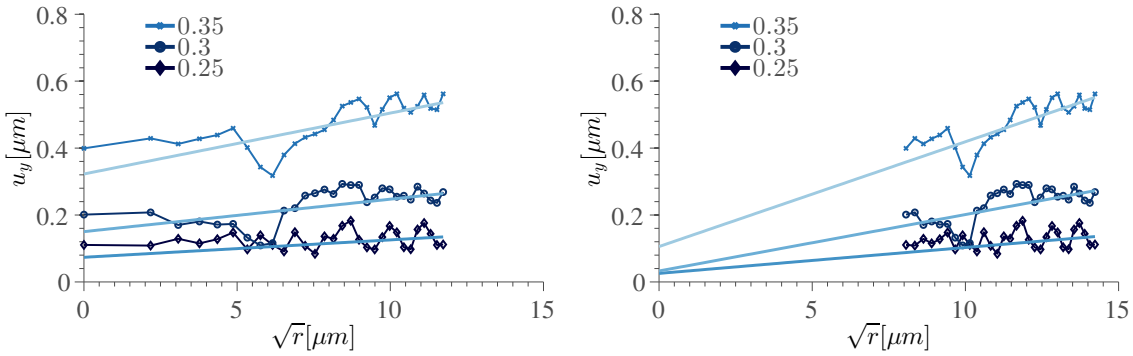


(a) All points, unadjusted

(b) Displacement of 65 µm added to crack tip location

Figure 3.41: Plots of u_y vs $\sqrt{r}$ at low loads with the best fit regression lines potted over data points. The y intercept of these fitted lines is the measure of ρ.

Although fitting regression lines to only a select number of points near the crack tip produces lower R^2 values than fitting lines to all the points, the positive ρ values make more physical sense and are a closer match to what points near the crack tip



(a) All points, unadjusted

(b) Displacement of 65 µm added to crack tip location

Figure 3.42: Plots of u_y vs $\sqrt{r}$ at low loads for points near the crack tip with the best fit regression lines potted over data points. The y intercept of these fitted lines is the measure of $/rho$.

	Unadjusted points			Displacement of 65 µm added		
P/P_{max}	Gradient	y-intercept	R^2	Gradient	y-intercept	R^2
0.15	-0.0004	0.0724	0.0053	-0.0003	0.0713	0.0026
0.20	0.0004	0.0612	0.0060	0.0005	0.0580	0.0076
0.25	0.0127	-0.0142	0.5765	0.0147	-0.0796	0.5949
0.30	0.0489	-0.2790	0.8779	0.0562	-0.5312	0.9080
0.35	0.0875	-0.3448	0.9431	0.1002	-0.7853	0.9656
0.40	0.1263	-0.2138	0.9598	0.1443	-0.8410	0.9774
0.45	0.1677	0.0180	0.9734	0.1913	-0.8086	0.9885
0.50	0.2054	0.2348	0.9807	0.2340	-0.7709	0.9934

Table 3.6: Gradient, y-intercept and R^2 values of fitted linear regression lines to u_y vs $\sqrt{r}$ data at various loads. The right columns are the same measures but from lines fitted to data that has had the crack tip position offset by adding 65 µm to the visually located position.

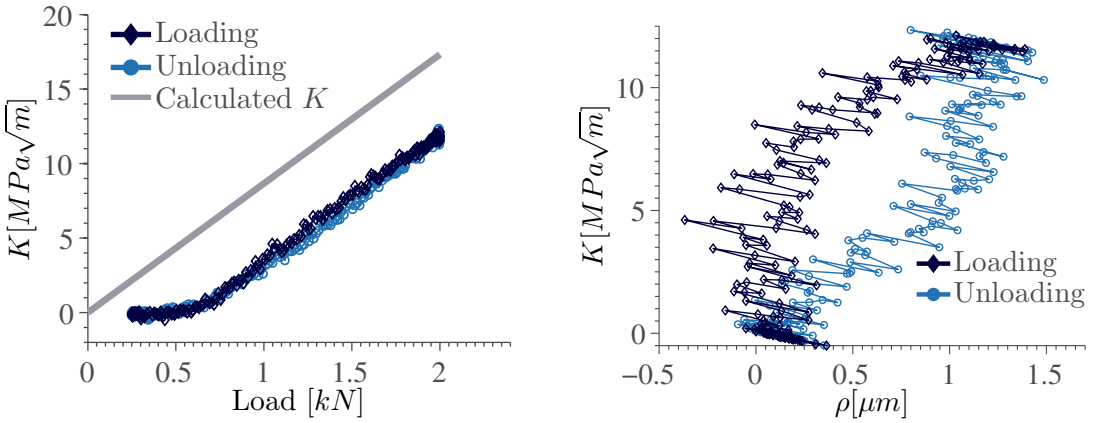
are actually doing (i.e. not having a negative displacement). As carried out earlier, plots of K vs Load and K vs ρ are produced (Figure 3.43). The K vs Load (P) is very similar to that seen previously in Figure 3.37, although there is a greater offset leading to $K_{max} = 12.34MPa\sqrt{m}$, whereas previously, when looking at all points, $K_{max} = 14.60MPa\sqrt{m}$. This is caused by a longer period of no change in K during initial loading, representing the higher opening load at points close to the crack tip. This effect was also clearly seen in Figure 3.21, where the displacement of points was unchanged until a higher load was reached for points near the crack tip compared with those some distance away. Due to the small number of points sampled that

	Unadjusted points			Displacement of 65 µm added		
P/P_{max}	Gradient	y-intercept	R^2	Gradient	y-intercept	R^2
0.15	-0.0130	0.1665	0.4961	-0.0205	0.2999	0.4619
0.20	-0.0048	0.1045	0.1993	-0.0087	0.1660	0.2377
0.25	0.0052	0.0735	0.1183	0.0077	0.0254	0.0978
0.30	0.0097	0.1502	0.2553	0.0169	0.0326	0.2885
0.35	0.0182	0.3225	0.4493	0.0313	0.1056	0.4970
0.40	0.0440	0.5661	0.8686	0.0738	0.0636	0.9116
0.45	0.0625	0.9737	0.8589	0.1071	0.2344	0.9416
0.50	0.0964	1.2470	0.9063	0.1629	0.1327	0.9662

Table 3.7: Gradient, y-intercept and R^2 values of fitted linear regression lines to u_y vs $\sqrt{r}$ data of points within 140 µm of the crack tip at various loads. The right columns are the same measures but from lines fitted to data that has had the crack tip position offset by adding 65 µm to the visually located position.

are in close proximity to the crack tip and the $\sqrt{r}$ values being rather low, small errors in tracking the points with Digital Image Correlation have greater effects on the fitted lines and therefore the K and ρ values. This can be seen in Figure 3.43b where very small changes in K and in particular ρ create significant noise in the K vs ρ plot. While there was certainly some roughness in the K vs ρ plots of Figures 3.39 and 3.40, it wasn't significant and the general shape and features of the graph could be determined. This is because a large number of data points are analysed to reduce the effects of any tracking errors, resulting in a better and more consistent fit for the linear regression lines. This graph in Figure 3.43b can be smoothed however, and the resulting plot of smoothing the ρ data using a moving average over 20 points is shown in Figure 3.44. This plot has similar characteristics to Figure 3.39b and also the model proposed by Pommier [5]. The major differences to Figure 3.39b include the positive values of ρ and the characterisation of the complete loading cycle rather than just values above $P/P_{max} > 0.3$. In this case the value ρ remains relatively unchanged from $K = 0$ up to K 7.5 (63% of K_{max}) before increasing relatively linearly up to K_{max}. The initial unloading phase has relatively little reduction in ρ as K lowers before another relatively linear phase of ρ reducing as K reduces to 0. The gradients

of the linear periods of change in K and ρ are very similar in the loading and unloading phases. In addition to this, the elastic phases where ρ has very little change during initial loading and unloading are also very similar in size in terms of ΔK.



(a) K vs Load (b) K vs ρ

Figure 3.43: (a) K vs Load and (b) K vs ρ plots for a single loading cycle. K and ρ are calculated from the gradients and y-intercepts of fitted regression lines to u_y vs $\sqrt{r}$ plots for points within 140 µm of the crack tip.

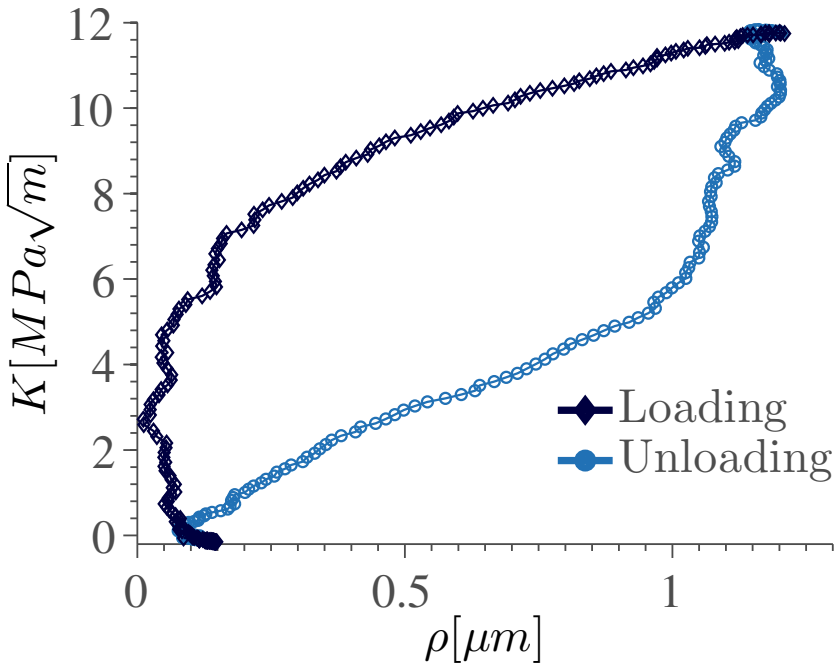


Figure 3.44: Smoothed K vs ρ graph calculated from points within 140 µm of the crack tip. This graph is the same data as in Figure 3.43b but smoothed using a moving average.

3.5 Modelling with Full Displacement Field

The full y direction displacement field around the crack tip can be calculated by:

$$u_y = 2\frac{K}{E}\sqrt{\frac{r}{2\pi}}\sin\frac{\theta}{2}\left(1+\sin^2\frac{\theta}{2}-\nu\cos^2\frac{\theta}{2}\right) \qquad \text{(3.4 revisited)}$$

As shown previously when looking at the predicted and actual displacement data, this equation can be used to adjust for the position of the grid points, which is especially significant at locations very near the crack tip.

A plot of u_y vs $\sqrt{\frac{r}{2\pi}}\sin\frac{\theta}{2}\left(1+\sin^2\frac{\theta}{2}-\nu\cos^2\frac{\theta}{2}\right)$ can be used to calculate K from the gradient. The calculation to do this is shown below in Equation (3.11).

$$K = \frac{mE}{2} \qquad (3.11)$$

Where m is the gradient.

An example of this plot is shown in Figure 3.45 with loads $P/P_{max} > 0.3$. The points form very straight lines with increasing gradients as the load is increased. It is a very similar plot to that seen previously with a u_y vs $\sqrt{r}$ graph in Figure 3.35 although in this case the points near the crack tip fit well with the linear trend of all the points analysed. The fit of a linear regression line is also improved from that obtained by adjusting the data in Section 3.4.1 to having a mean $R^2 = 0.9960$ and a range of $0.9750 < R^2 < 0.9991$.

This fitted regression line is used to calculate a value of K from the experimentally obtained displacement data. Shown in Figure 3.46a this is very similar to that seen in prior analysis, with a clear offset from the analytically calculated K due to crack closure. With $P/P_{max} > 0.4$ the gradients of both lines are similar with the experimentally determined K having a gradient of 8.1075 vs 8.6622 $MPa\sqrt{m}/kN$ for the K calculated from the specimen geometry.

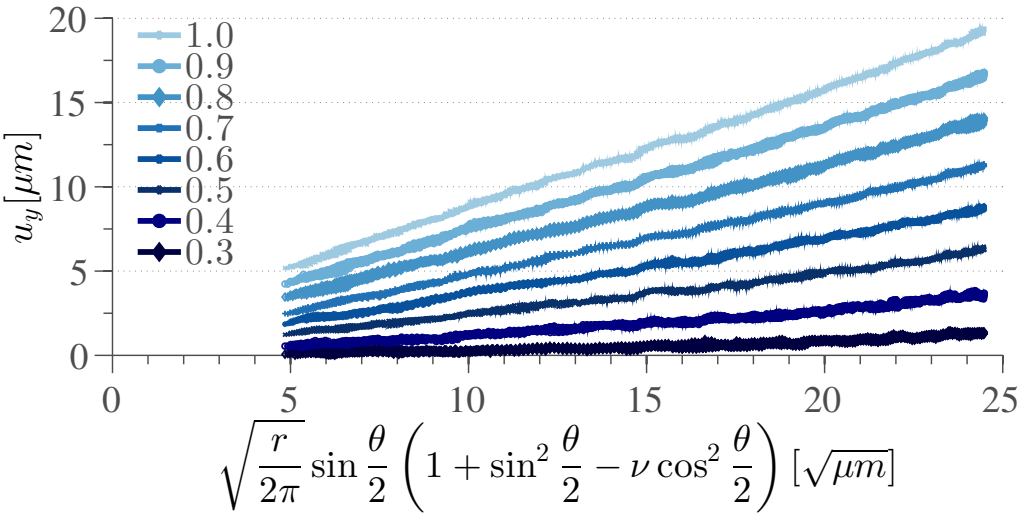


Figure 3.45: Typical u_y vs $\sqrt{\frac{r}{2\pi}}\sin\frac{\theta}{2}\left(1+\sin^2\frac{\theta}{2}-\nu\cos^2\frac{\theta}{2}\right)$ plot for various loads (P/P_{max}) during a single loading cycle.

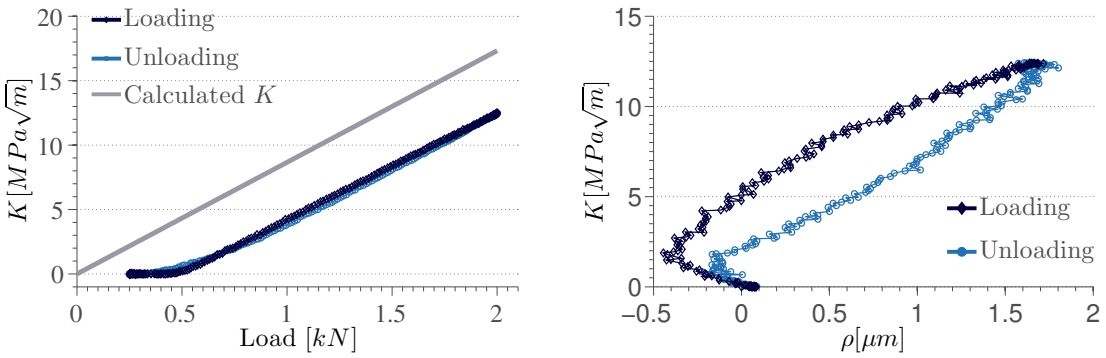
Adding a displacement to the crack tip location, so that the actual crack tip is ahead of that visually located on the surface, increases the gradient of the experimental K value. A displacement of 61 µm gives a gradient of 8.667 $MPa\sqrt{m}/kN$, which is very similar to that of the analytically calculated value of K ($8.662MPa\sqrt{m}/kN$). This displacement is also a similar amount to that which produced a good fit previously. There was again an improved fit of regression lines on a u_y vs $\sqrt{\frac{r}{2\pi}}\sin\frac{\theta}{2}\left(1+\sin^2\frac{\theta}{2}-\nu\cos^2\frac{\theta}{2}\right)$ plot with the mean $R^2 = 0.9966$ and range of $0.9765 < R^2 < 0.9994$. This plot of K vs P is shown in Figure 3.47a.

The elastic-plastic model can also be adjusted by adding a plasticity factor, ρ as follows:

$$u_y = 2\frac{K}{E}\sqrt{\frac{r}{2\pi}}\sin\frac{\theta}{2}\left(1+\sin^2\frac{\theta}{2}-\nu\cos^2\frac{\theta}{2}\right)+\rho \tag{3.12}$$

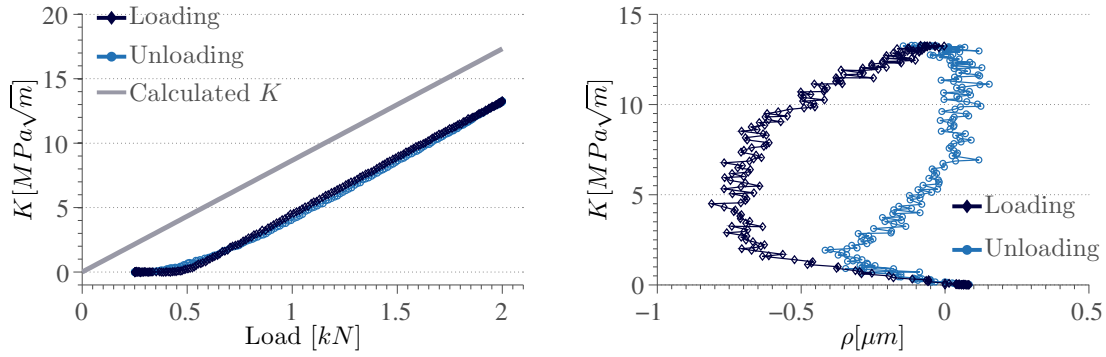
The value of ρ at each load is obtained by calculating the y-intercept of a linear regression line fitted to data on a u_y vs $\sqrt{\frac{r}{2\pi}}\sin\frac{\theta}{2}\left(1+\sin^2\frac{\theta}{2}-\nu\cos^2\frac{\theta}{2}\right)$ plot. The plots shown in Figures 3.46b and 3.47b show a very similar shape to those seen in Section 3.4.2 although the values of ρ are slightly smaller. This is due to a change in

the calculation of ρ from the equation proposed by Pommier, which looks at points along the crack flanks, to that produced for the position of analysed grid points in Equation (3.12). In general, the fit of regression lines to the experimental data is improved, the calculated value of K from the experimental data is slightly closer to the theoretical calculation of K and the change in ρ over a single cycle is calculated to be lower when using Equation (3.12) rather than Equation (3.9). These differences in typical calculated values of K and ρ are shown in Table 3.8.



(a) K vs Load (b) K vs ρ

Figure 3.46: K vs Load and K vs ρ plots calculated from linear regression lines fitted to data on u_y vs $\sqrt{\frac{r}{2\pi}}\sin\frac{\theta}{2}\left(1+\sin^2\frac{\theta}{2}-\nu\cos^2\frac{\theta}{2}\right)$ plots.



(a) K vs Load (b) K vs ρ

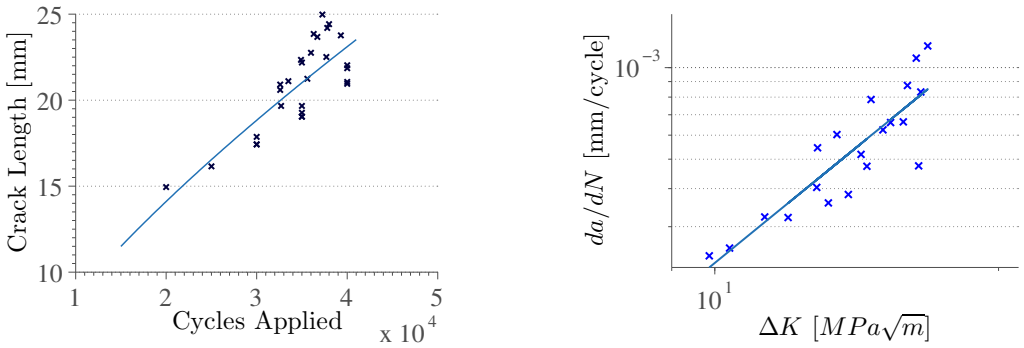
Figure 3.47: K vs Load and K vs ρ plots calculated from linear regression lines fitted to data on u_y vs $\sqrt{\frac{r}{2\pi}}\sin\frac{\theta}{2}\left(1+\sin^2\frac{\theta}{2}-\nu\cos^2\frac{\theta}{2}\right)$ plots with the crack tip location displaced 55.5 µm ahead of where it was visually located.

	Equation (3.9)		Equation (3.12)	
	K	ρ	K	ρ
Unadjusted data	11.6209	2.9172	12.4242	2.2466
Crack tip offset 61 µm	13.1347	0.9650	13.2824	1.0210

Table 3.8: Differences in K $[MPa\sqrt{m}]$ and ρ [µm] for typical experimental data over a single loading cycle according to the equation used. Equation (3.9) assumes all points are along the crack flank while Equation (3.12) accounts for the position of the points that are analysed in relation to the crack tip.

3.6 Results from All Specimens

The experiments described in this chapter were repeated on 10 specimens of the same geometry. Analysis was carried out on all the specimen at each loading cycle where images were captured. It was not the purpose of this experiment to examine closely the growth of a fatigue crack during constant amplitude loading and so not many points or crack length were recorded. What was recorded is shown in Figure 3.48, with power law (Figure 3.48a) and linear (Figure 3.48b) regression lines showing a general trend. Figure 3.48b shows a reasonable linear fit on a log-log scale as expected by the Paris' law. This plot uses values of da/dN calculated numerically from crack growth between sets of images. In this case the fitted line has a gradient of 2.5289 and $R^2 = 0.7643$. An offset was added to the crack tip location from where it was visually located in each case. To determine this offset, the gradient of a K vs Load plot was used and the offset adjusted so that it would best match that of the theoretical K vs Load plot. This was used in earlier analysis (Figure 3.47) and seemed a reasonable way to improve the fit of the data with analytical models by accounting for the likely scenario that the crack tip is actually not exactly where it is visually located on the surface. A selection of the resulting K vs ρ graphs made from fitting regression line to u_y vs $\sqrt{\frac{r}{2\pi}}\sin\frac{\theta}{2}\left(1+\sin^2\frac{\theta}{2}-\nu\cos^2\frac{\theta}{2}\right)$ of the adjusted data points is shown in Figure 3.49. These graphs have generally similar shapes and features when an offset is added to the crack tip location. The graphs of K vs Load are very similar to those seen in prior analysis in this chapter (Figure 3.47).



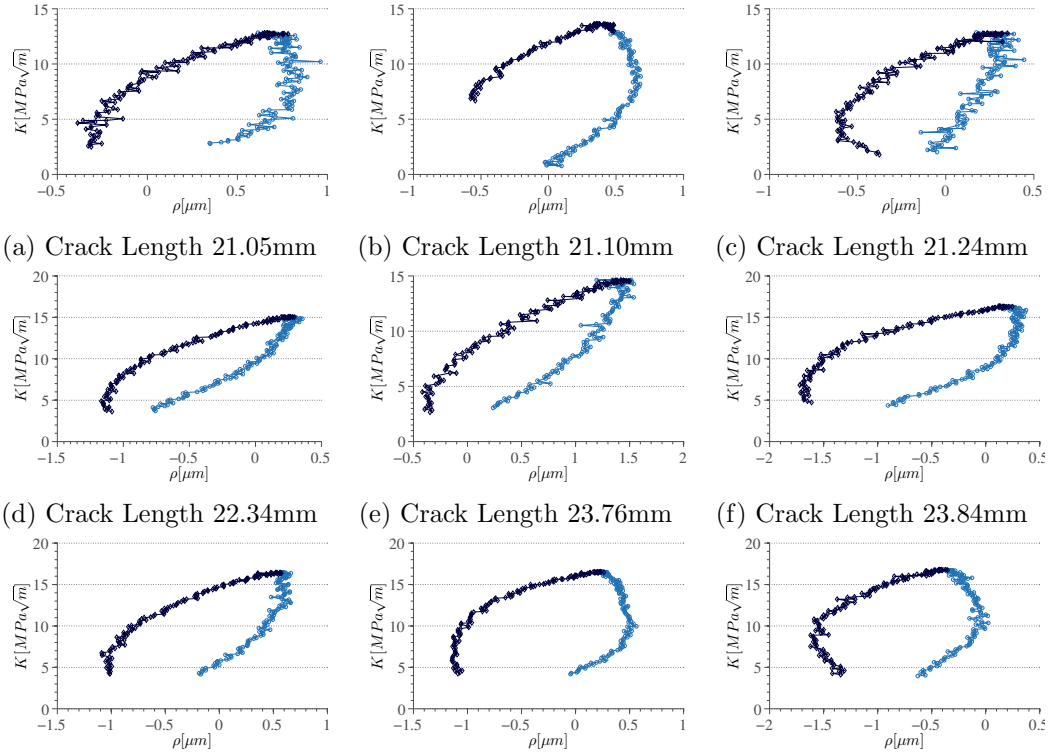
(a) Crack Length vs Cycles Applied for all specimens during constant amplitude loading.

(b) Rate of crack growth (per cycle) vs ΔK calculated from displacement data

Figure 3.48: Crack growth data for all specimen analysed during constant amplitude loading.

The ΔK value from this analysis can be compared with the analytical calculation for ΔK based off the specimen geometry and loading applied. As expected this ΔK from displacement data is lower than that calculated analytically due to crack closure. This reduction in ΔK is consistent over multiple specimen and crack lengths as seen in Figure 3.50.

As the crack grows in length, the plastic zone size, rate of crack growth and Stress Intensity Factor all increase. Looking at $\Delta\rho$ vs Crack Length (Figure 3.51), there appears to be some relationship, although not a terribly strong one. A power law regression line has an R^2 value of 0.5775. With a greater amount of data this relationship could be examined more closely although, as previously mentioned, the shape of the K vs ρ plot that this value is determined from is quite sensitive to the crack tip location. Accurately locating the crack tip position is important when determining the ρ value in this way. Although it was used in this case, simply choosing the location by fitting data to a theoretical model of K may not be the most accurate solution for looking at the magnitude of ρ. Nevertheless it is expected that the magnitude of the ρ value is related to the rate of crack growth



(a) Crack Length 21.05mm (b) Crack Length 21.10mm (c) Crack Length 21.24mm

(d) Crack Length 22.34mm (e) Crack Length 23.76mm (f) Crack Length 23.84mm

(g) Crack Length 24.20mm (h) Crack Length 24.43mm (i) Crack Length 24.98mm

Figure 3.49: Selection of K vs ρ plots for a number of specimen at various crack lengths with the crack tip position offset. Crack length is a from the specimen geometry (Figure 3.7).

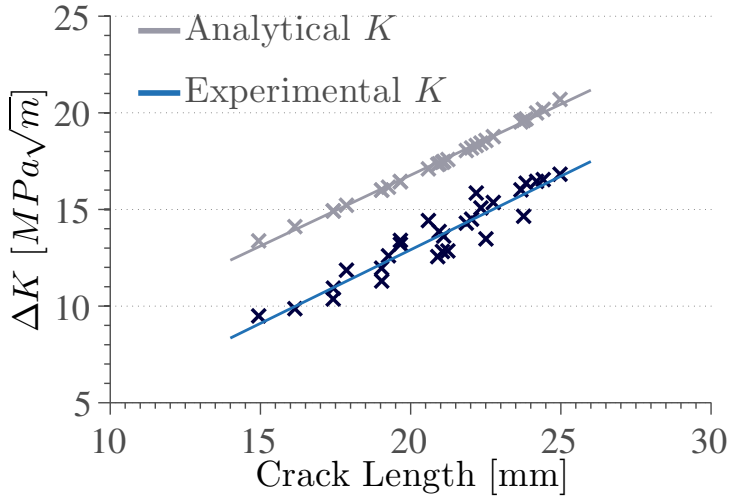


Figure 3.50: ΔK vs Crack Length for all specimen during constant amplitude loading. Analytical K calculated from specimen geometry and experimental K calculated from displacement data.

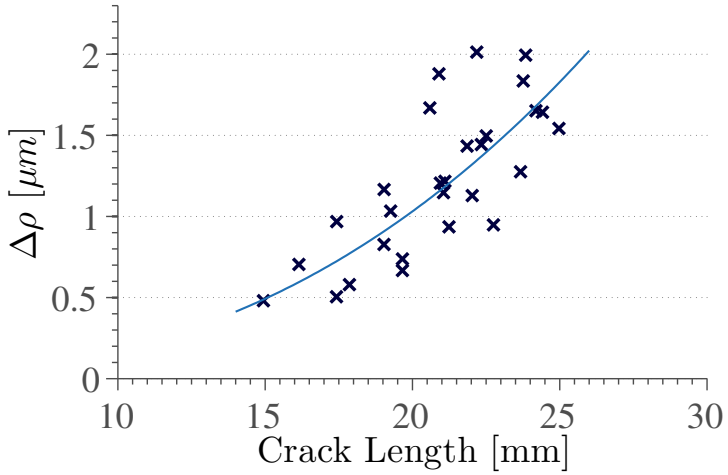


Figure 3.51: $\Delta\rho$ vs Crack Length for each loading cycle analysed over a number of specimen. Displacements were added to the crack tip position for each set of images and $\Delta\rho$ was determined for $P/P_{max} > 0.4$ kN.

3.7 Pre-Cracked Specimen Comparison

Images were captured ahead of the crack tip in an effort to provide a base image for displacements around a crack to be determined. This was done by taking a number of images ahead of a growing crack, applying a load to the specimen to grow the crack into this region and then aligning the pre crack images with those of the current crack. This proved successful in a number of cases, however for some samples the crack did not grow into the expected region or not enough images were captured. Looking again at displacement plots during a single loading cycle, the crack closure is still very clear although there is as offset in displacement for when the crack is closed. This displacement from an uncracked area indicates that there is some material within the crack that causes this extra displacement around the crack while the crack is closed. Plots of relative displacement during a single loading cycle and relative load vs displacement for points various distances from the crack tip are shown in Figures 3.52 and 3.53. Near the crack tip the displacement when the crack is closed is just over 1/3 of the maximum displacement for those points giving quite a high relative displacement when the crack is closed as seen in Figure 3.52.

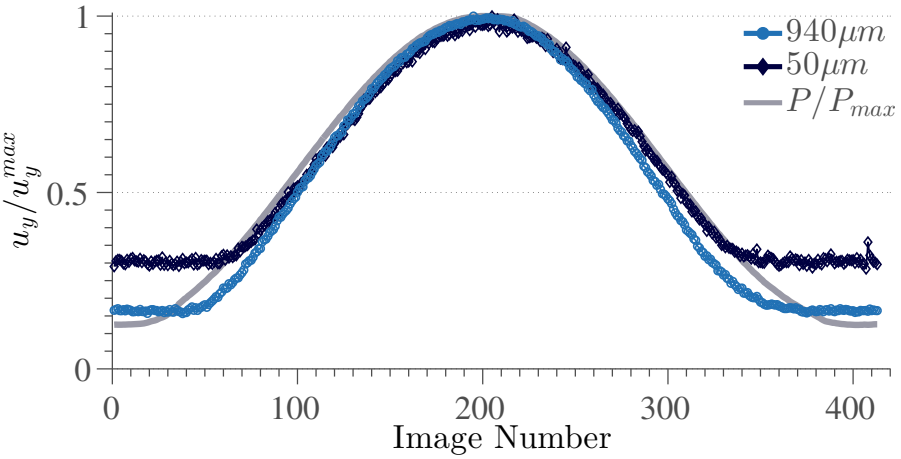


Figure 3.52

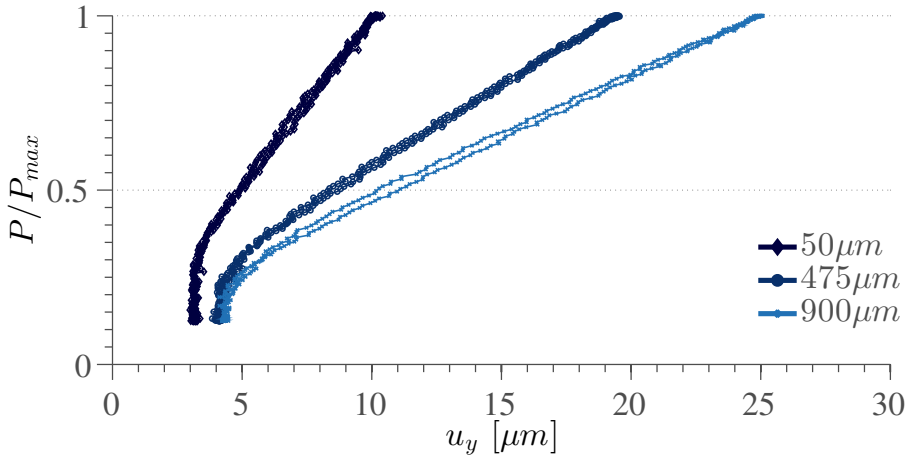


Figure 3.53

The offset of points when the crack is closed is added to the displacements throughout the loading cycle. Looking at a plot of u_y vs $\sqrt{\frac{r}{2\pi}}\sin\frac{\theta}{2}\left(1+\sin^2\frac{\theta}{2}-\nu\cos^2\frac{\theta}{2}\right)$ (Figure 3.54), the lines of points are not as straight as they were in earlier analysis due to this offset. Linear regression lines therefore do not fit as well as before with the mean $R^2 = 0.9776$ and the range being $0.8760 < R^2 < 0.9943$ for loads $P/P_{max} > 0.4$.

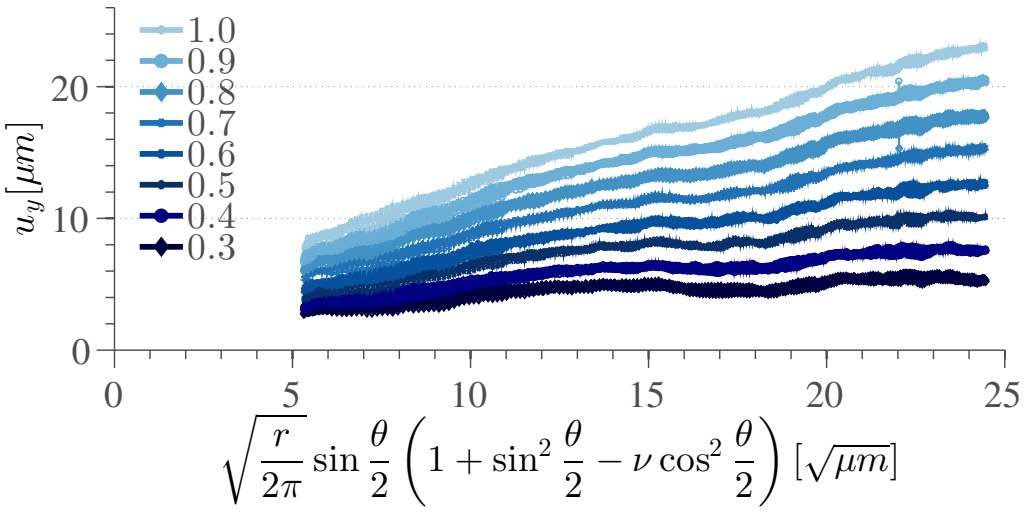
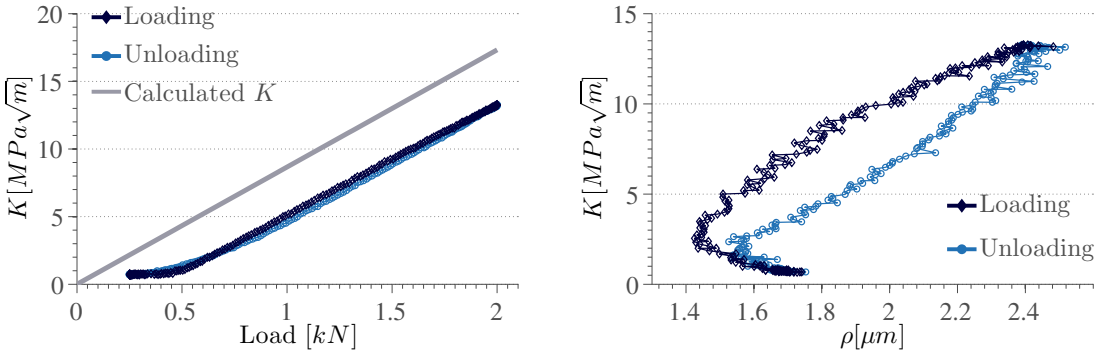


Figure 3.54: Typical u_y vs $\sqrt{\frac{r}{2\pi}}\sin\frac{\theta}{2}\left(1+\sin^2\frac{\theta}{2}-\nu\cos^2\frac{\theta}{2}\right)$ plot for various loads during a single loading cycle using an uncracked specimen image as the base image for displacement measurements.

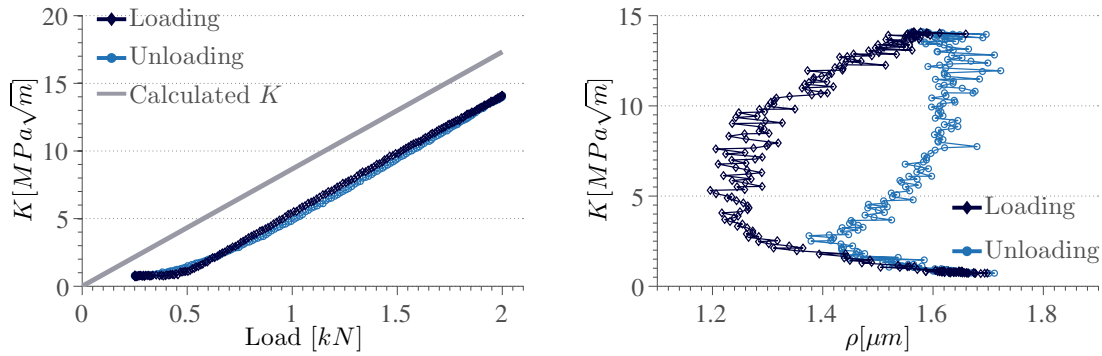
Plots of K vs Load are consistent with those seen earlier in this chapter, as is the shape of the K vs ρ plot (Section 3.7). Adding a displacement to the crack tip location also has a very similar effect to when only analysing images based on the

closed crack (Figure 3.56). One big difference however is the value of ρ. Due to the added displacement of the points around the closed crack from the uncracked specimen, the values of ρ are now not zero at the minimum load of 0.25 kN. This means the reduction in ρ during initial loading no longer results in a negative ρ that was thought not to make much physical sense.



(a) K vs Load (b) K vs ρ

Figure 3.55: K vs Load and K vs ρ plots using an uncracked specimen image as the base image for displacement measurements. Calculated from linear regression lines fitted to data on u_y vs $\sqrt{\frac{r}{2\pi}}\sin\frac{\theta}{2}\left(1+\sin^2\frac{\theta}{2}-\nu\cos^2\frac{\theta}{2}\right)$ plots.

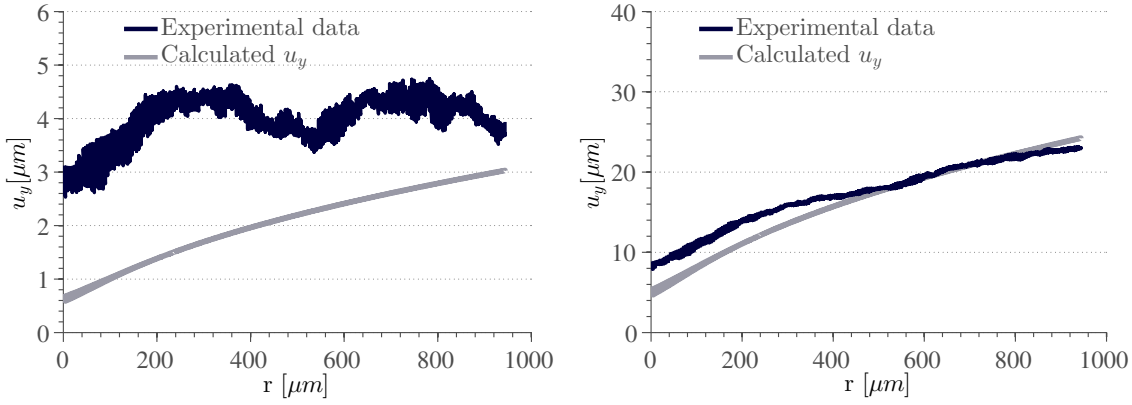


(a) K vs Load (b) K vs ρ

Figure 3.56: K vs Load and K vs ρ plots using an uncracked specimen image as the base image for displacement measurements. Calculated from linear regression lines fitted to data on u_y vs $\sqrt{\frac{r}{2\pi}}\sin\frac{\theta}{2}\left(1+\sin^2\frac{\theta}{2}-\nu\cos^2\frac{\theta}{2}\right)$ plots with the crack tip location displaced 55.5 µm ahead of where it was visually located.

The displacement of points around the crack at the minimum load of 0.25 kN is shown in Figure 3.57a along with the theoretical calculation of displacement according to Equation (3.4). In previous cases, when the image at 0.25 kN was used to base the

DIC displacement measurements, this experimental displacement is zero at all points. This displacement around the closed crack is more than the theoretical calculation for all points along the crack and significantly more than the analytical value right near the crack tip location. This is the displacement of points around the closed crack and is what is added to all displacement points leading to the diminished fit of straight lines in Figure 3.54. At higher loads the fit of displacement data from the DIC analysis is quite similar to the theoretical calculation (Figure 3.57b). There is no need to make any adjustments to normalise the analytical calculation with the experimental data in this case as was done in Figures 3.26 and 3.27 because the experimental displacements are calculated from an uncracked specimen rather than a cracked specimen at 0.25 kN. This good fit suggests that it is reasonable to make the adjustment of normalising the analytical data when looking at the displacements, as was done earlier in this chapter.



(a) Load = 0.25kN (b) Load = 2kN

Figure 3.57: DIC measured displacement of points plotted with calculated displacement at measured points according to Equation (3.4). This uses the uncracked specimen image as the base image for displacement measurements.

3.8 Conclusions

This chapter showed that experimentally obtained displacement data from along the crack flanks produced a reasonable fit with an elastic model during constant amplitude loading, particularly at points some distance away from the crack tip. An offset of the crack tip location improved the fit of the experimental data to the model and the best fit was obtained when this offset was near to the size of the calculated cyclic plastic zone. This is expected when using Irwin's analysis of a 'virtual' crack tip location that is ahead of the physical crack tip due to the presence of plasticity.

Using an elastic-plastic model produced an improved fit with the experimental data. The experimentally determined K values were lower than those calculated analytically due to the presence of closure, however, once the crack opened the change in K with P was very much as expected. Hysteresis type behaviour in a $K - \rho$ space was shown, as Pommier's model suggested. However, due to crack closure and points further from the crack tip opening before those near the crack tip, a prominent negative ρ value was found during initial loading. This value was shown to be no negative when using the uncracked area as the base image form displacement measurements, yet the behaviour still showed a reduction in ρ due to regression lines not fitting well with points close to the crack tip. Disregarding points at low loads when the crack is closed and adding a small offset to the crack tip location produced behaviour similar to that predicted in Pommier's model, as did only analysing points close to the crack tip.

Capturing multiple sets of images over many samples allowed for analysis on crack growth behaviour. Growth occurred with a relationship between growth rate and K expected from the Paris law. In addition to this there appears to be some relationship between values of $\Delta\rho$ and the crack length although the experimentally obtained values of ρ are very sensitive to the crack tip location, which was rather difficult to determine accurately.

Chapter 4

Fatigue Crack Analysis Under Variable Amplitude Loading

After a period of crack growth under constant amplitude loading, as described in Chapter 3, a single overload cycle was applied to each CT specimen. This cycle was at 3 kN (150% of maximum constant amplitude load) and the loading profile for this cycle is shown in Figure 4.1. Images were collected during the overload cycle and then at selected periods after the overload had been applied, including the cycle directly following the overload. This chapter investigates the effects a single overload cycle has on the analysed parameters at the crack tip. This chapter uses the specimen labelled CT9 for detailed analysis, due to this specimen having the largest amount of data collected post overload. As in the previous chapter, the same analysis was performed on all specimens and only features consistent across multiple specimen are presented here.

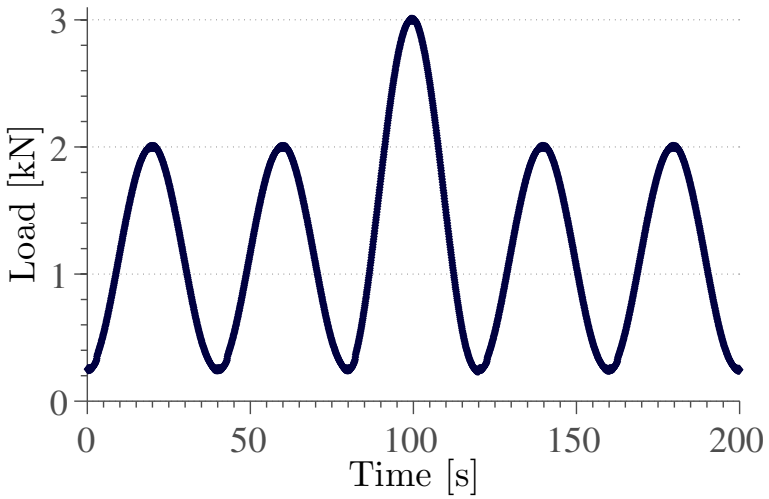
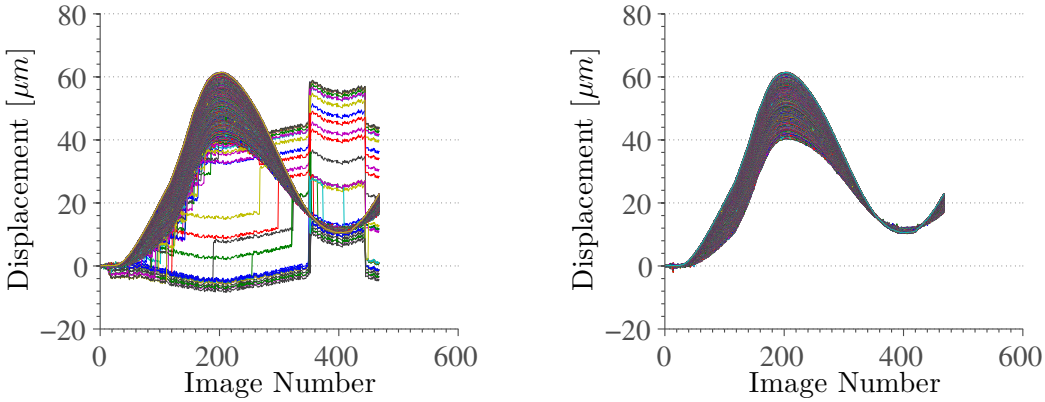


Figure 4.1: Force data from loading the CT specimen before, during and after a single overload cycle at 0.25 Hz.

4.1 DIC tracking of points

As explained in the previous chapter, DIC analysis was used to track a series of points located along, but with some distance from, the crack flanks. However, unlike during constant amplitude loading, in a number of cases during or directly after an overload cycle there a significant number of points that were tracked poorly. An example of points being track incorrectly with the DIC analysis during an overload cycle is shown with the displacement plots in Figure 4.2a. In this case, there are clearly a number of points for which the displacement is not close to the displacements of the majority of points. A filter was used that discarded points outside certain displacement and correlation limits of other points. Only the resulting displacements (Figure 4.2b) are used in further analysis, with the badly tracked points discarded. Figure 4.3 shows the analysed points around the crack tip before (a) and after (b) the poorly tracked points are removed. In most cases it was points very near the crack tip that needed to be removed. This was due to changes in surface features (appearing as darker areas) around the crack tip with the higher force applied from the overload cycle. Images of the crack tip during the maximum load of a regular cycle (2 kN) and the maximum

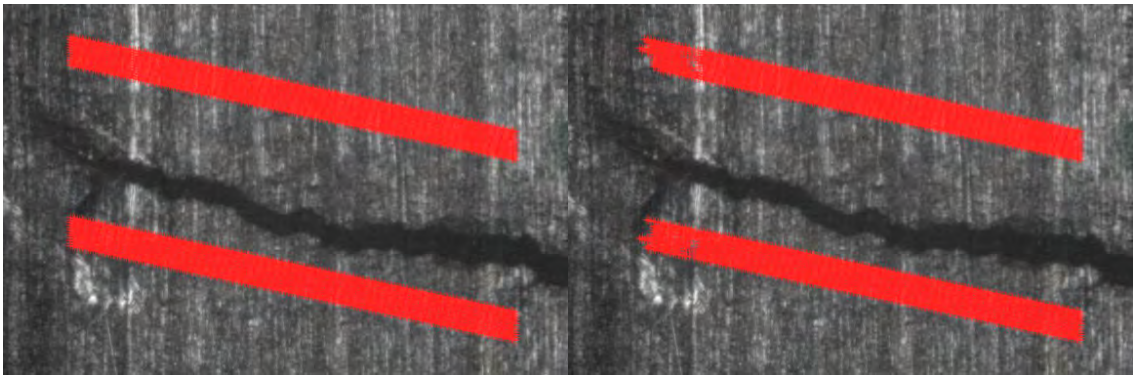
load of an overload cycle (3 kN) show these changing features around the crack tip in Figure 4.4. Removing these poorly tacked points was easily done, however, often there were significant gaps near the crack tip and therefore the closest points analysed near the crack tip were, in some cases, over 100 µm from the visually identified crack tip.



(a) Displacement of all points

(b) Badly tracked points removed

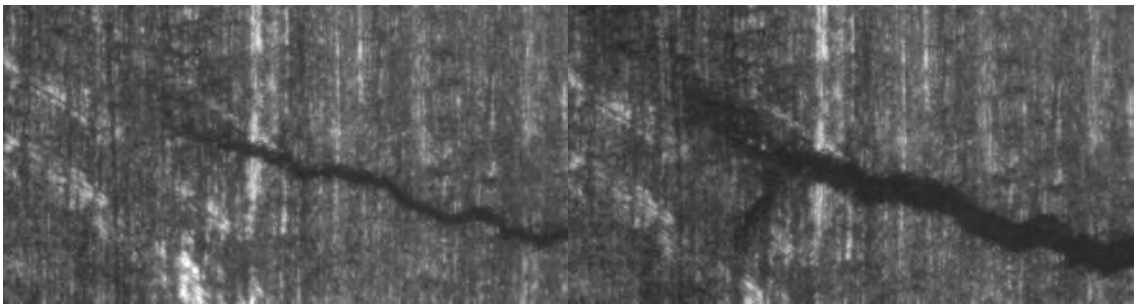
Figure 4.2: DIC calculated displacement data showing the badly tracked points (a) during an overload cycle. These points are removed from further analysis and the resulting points used (b).



(a) All points to be analysed

(b) Badly tracked points removed

Figure 4.3: Points to be tracked with DIC analysis (a) and points that remain after those that are poorly tracked have been removed (b).



(a) Loaded at 2kN (b) Loaded at 3kN

Figure 4.4: Close up images of the crack tip during the maximum load of a regular cycle (a) and the maximum load of an overload cycle (b).

4.2 Displacement Analysis

The displacement of points normal to the crack was analysed using the DIC calculated y direction displacement of points around the crack. The displacement of a point 250 µm from the crack tip before, during and after an overload cycle is displayed in Figure 4.5. The displacements of these cycles were calculated from the minimum load at the start of each respective cycle and therefore effectively zeroed at the start of each cycle. This clearly shows the various magnitudes of displacements around the crack tip and the effect of the overload. The displacement of the same point is shown plotted against the applied force in Figure 4.6, which shows how the force effects the displacement of a point around the crack tip when an overload is applied.

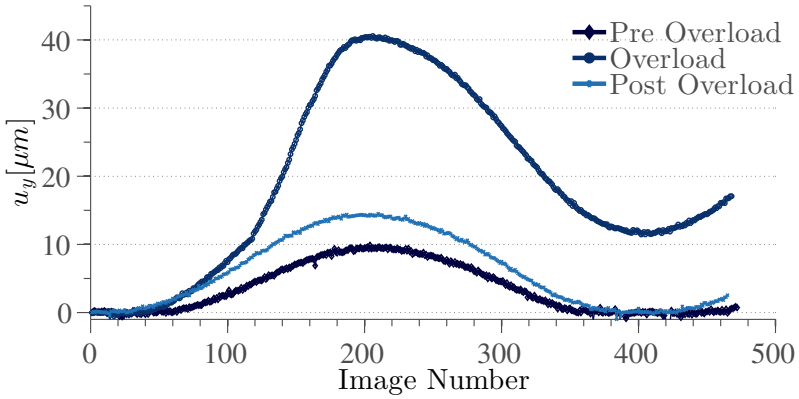


Figure 4.5: Displacement (u_y) vs Image Number for a point 250 µm from the crack tip directly before, during and after an overload cycle.

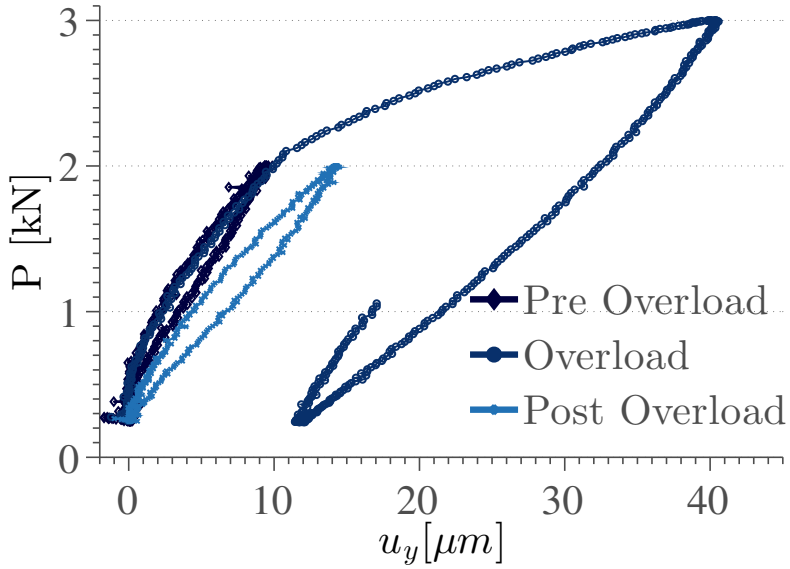


Figure 4.6: Applied Load (P) vs Displacement (u_y) for a point 250 µm from the crack tip directly before, during and after an overload cycle.

4.2.1 Overload Cycle

During an overload cycle of 3 kN, the displacement reaches significantly higher levels than during constant amplitude loading at 2 kN as shown in Figure 4.5. After the maximum load has been reached, the unloading profile is rather different than during constant amplitude loading, with the displacement never returning to the same level as it was when initially loaded. The displacement data of an overload cycle in Figure 4.2b shows that all points along the crack settle at a similar residual displacement value when unloaded after an overload cycle. The difference in loading and unloading during this cycle can be seen in Figure 4.7, where the displacements of points is compared with the load applied to the specimen. During the initial loading phase there appears to be a change in the displacement when $P > 0.75 \times P_{max}$, with the displacements increasing at a higher rate as the load approaches 3 kN. This is particularly noticeable near the tip (50 µm line on Figure 4.7). After the maximum load has been reached, the load starts reducing, but the points are much slower to reduce in displacement than they were to increase during loading. As the load reduced

back to the minimum in the loading cycle, a residual displacement remained along the whole crack and therefore crack closure no longer existed. The residual displacement after the overload is also seen in the crack mouth displacement readings, although the magnitude is significantly less than that seen near the crack tip. Figure 4.8 shows the displacement of all the analysed points along the crack once the load is reduced to a minimum of 0.25 kN after an overload of 3 kN. In constant amplitude loading this figure had all points very close to zero, and almost always less than 0.2 µm. This figure presents significantly higher displacements right along the crack, with the highest displacements of just over 14 µm near the crack tip. The displacement of points further from the tip is less than that at points near the tip. This explains why the readings from the CMOD gauge at the crack mouth do not show as much displacement after the overload as the points tracked on the specimen with DIC analysis. During the overload cycle, a large plastic zone develops around the crack tip and the significant residual stresses associated with this large increase in plasticity at the crack tip are what hold the crack open and prevent closure after the overload.

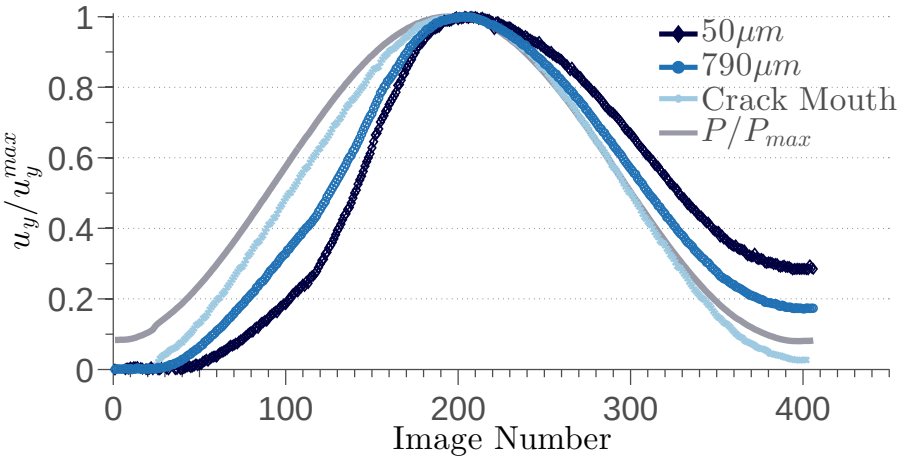


Figure 4.7: Typical variation of relative displacement at points 50 µm and 790 µm from the crack tip during an overload cycle with a maximum load of 3 kN. The sinusoidal applied load (P) and measurements from the CMOD gauge are plotted along with these displacements for comparison.

The change in displacement behaviour as the load is increased above the constant amplitude loading maximum of 2 kN is seen more clearly in Figure 4.9. After the

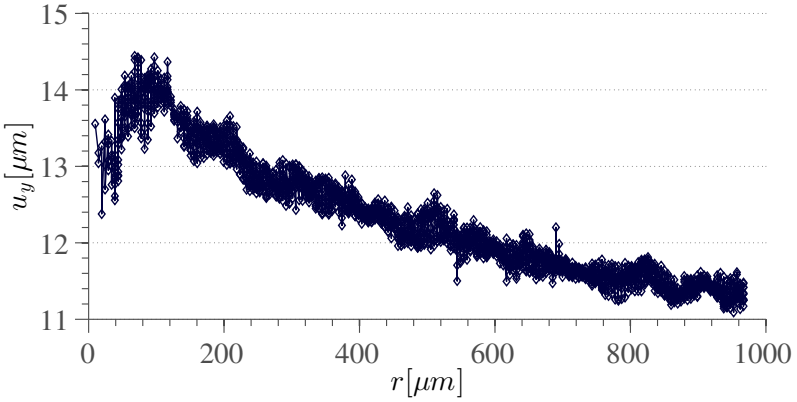


Figure 4.8: Typical residual displacements of points along a crack when the load is returned to a minimum (0.25 kN) after an overload of 3 kN.

opening load is reached, the displacement of all points increases with the load at a reasonably constant rate while $P < 0.75P_{max}$. When the load increases above this level, the displacement again increases at a steady rate, however this rate is considerably higher. This phase of plastic deformation, with large increases in the displacement along the crack, produces the resulting residual displacement when the load is reduced.

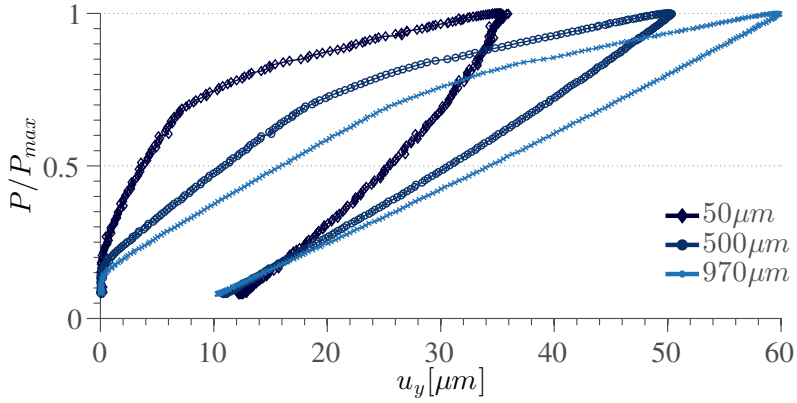
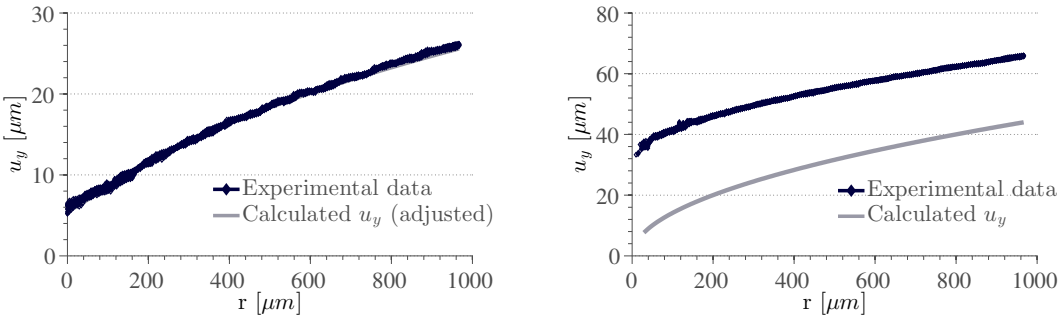


Figure 4.9: Relative load plotted against displacement, for three different sets of points located 50 µm, 500 µm and 790 µm from the crack tip. These displacements are from an overload cycle with a maximum load of 3 kN.

The analytical elastic crack calculations for displacement (Equation (3.4)) do not take into account the effects of plasticity, so when the experimental data is plotted alongside the calculated displacement there is a considerable difference at 3 kN (Fig-

ure 4.10b). In comparison, at 2 kN the same analysed points show a very good fit with the expected displacement (Figure 4.10a). In each case the calculated displacement has had the expected displacement at 0.25 kN subtracted to account for this being the base of the experimental measurements. This shows that the plasticity at the crack tip during the overload has a significant effect on the displacement of all points analysed around the crack flanks.



(a) Loaded at 2kN

(b) Loaded at 3kN

Figure 4.10: DIC measured displacement of points at 2 kN (a) and at an overload of 3 kN (b) plotted with calculated displacement at measured points according to Equation (3.4).

4.2.2 Post Overload

The cycle directly after an overload is applied is similar to those before the overload, but without the effects of crack closure. The loading and unloading phases are quite similar (certainly more so than during an overload) and there is little change in the displacement of points at the minimum load before and after the cycle (Figure 4.11). The differences in displacements of points around the crack tip for a loading cycle directly before and directly after an overload cycle are shown in Figure 4.12 (also shown in Figures 4.5 and 4.6). Figure 4.12 clearly shows the different behaviour during the initial loading and final unloading phase of a cycle. Before the overload there is a period of no change in displacement at low loads due to the crack being closed prior to the opening load being reached. After the overload, however, this feature is not present and the displacement increases right as the load begins to

increase. This results in higher overall displacements at the maximum load for all points analysed. It is no surprise then that the displacements of points are above the calculated values (Figure 4.13) that were very close to the experimental data points (Figure 4.10a) before the overload was applied.

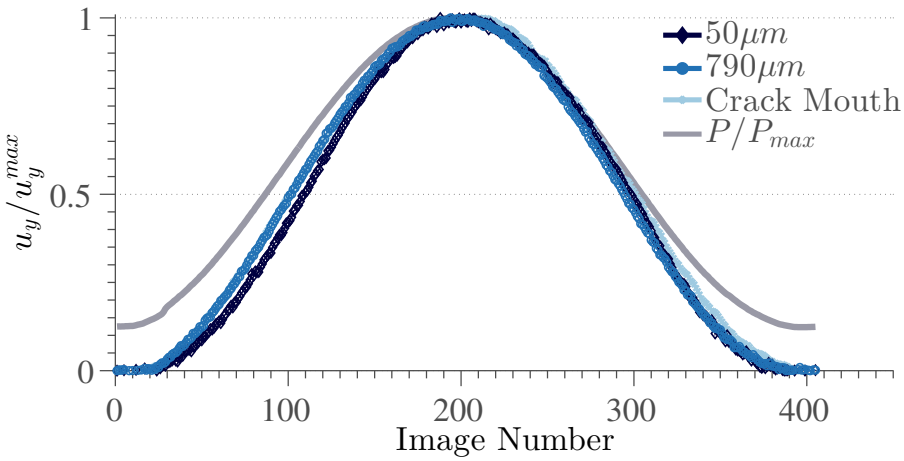
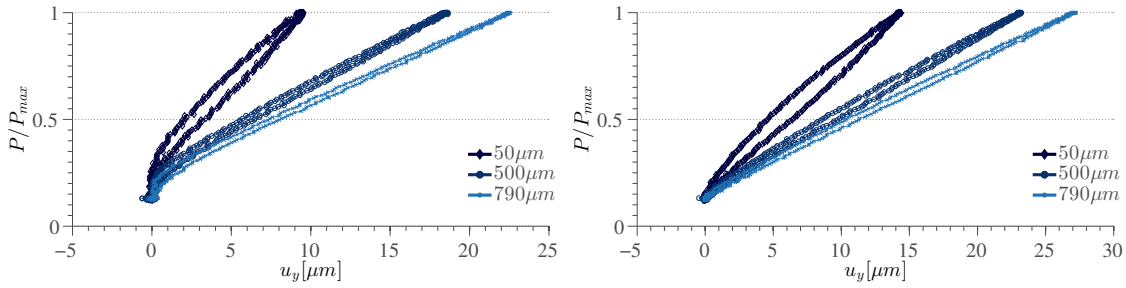


Figure 4.11: Typical variation of relative displacement at points 50 µm and 790 µm from the crack tip directly after an overload cycle with a maximum load of 3 kN. The sinusoidal applied load (P) and measurements from the CMOD gauge are plotted along with these displacements for comparison.



(a) Pre Overload (b) Post Overload

Figure 4.12: Relative load plotted against displacement, for three different sets of points located 50 µm, 500 µm and 790 µm from the crack tip. These displacements are analysed for the same points before an overload (a) and after an overload (b).

Looking further ahead after the overload, changes in the crack closure levels due to the overload become apparent. Figure 4.14 shows the displacement of points at various distances from the crack tip as the load is varied, captured from 1 to 8000 cycles after the overload has been applied. As mentioned before, there is no apparent crack closure immediately after the overload and the displacements increase right

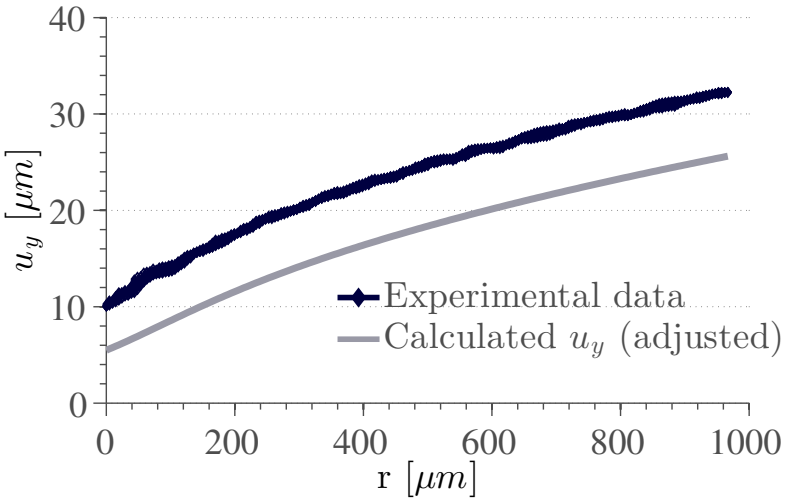


Figure 4.13: DIC measured displacement of points at 2 kN during constant amplitude loading directly after an overload plotted with calculated displacement at measured points according to Equation (3.4).

away as the load increases. In Figure 4.14b at 1000 cycles after the overload has been applied, the crack is growing through the large plastic zone created by the overload. The points near the crack reflect the displacements around the region of the crack grown after the overload cycle while the points closer to the mouth measure displacements of the crack region that was present when an overload was applied. This measurement of the crack with regions existing pre and post overload is repeated in Figures 4.14c to 4.14e, where the crack tip location during the overload cycle is still visible in the captured images. A crack tip image at 2000 cycles post overload shows this in Figure 4.15, with an arrow indicating the crack tip position during the overload cycle. These figures show that the newly growing crack has a significant amount of closure, with the displacements not increasing until the load rises to approximately $P/P_{max} > 0.5$. While this growing crack has large amounts of closure and requires high loads to increase the displacement, points analysed around the crack region that existed during (and prior to) the overload cycle continue to show no signs of crack closure. As the crack grows, the general shape of the plots become increasingly similar to those obtained prior to the overload cycle. After 7000

cycles post overload the closure levels are very near those recorded during constant amplitude loading prior to the overload.

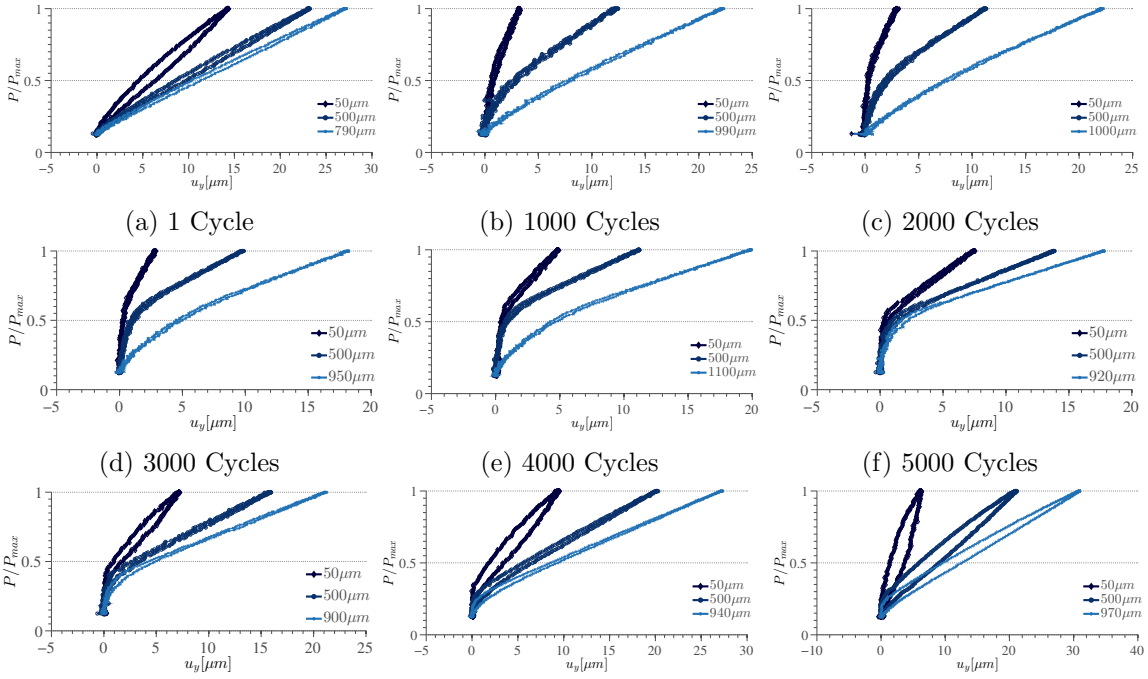


Figure 4.14: Relative load plotted against displacement, for three different sets of points located at various distances from the crack tip. These displacements are analysed between 1 and 8000 cycles after a single overload cycle.

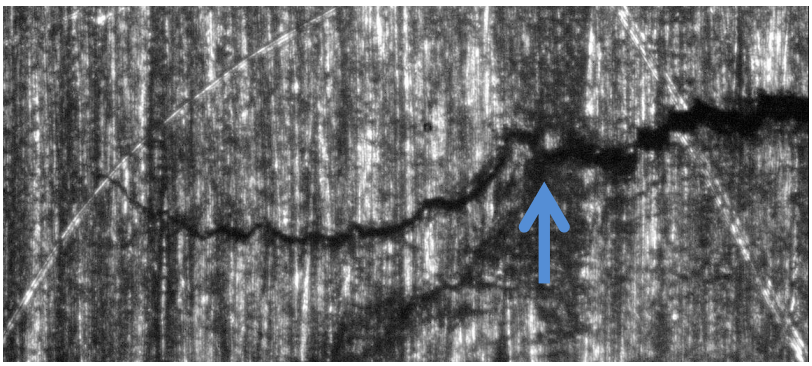
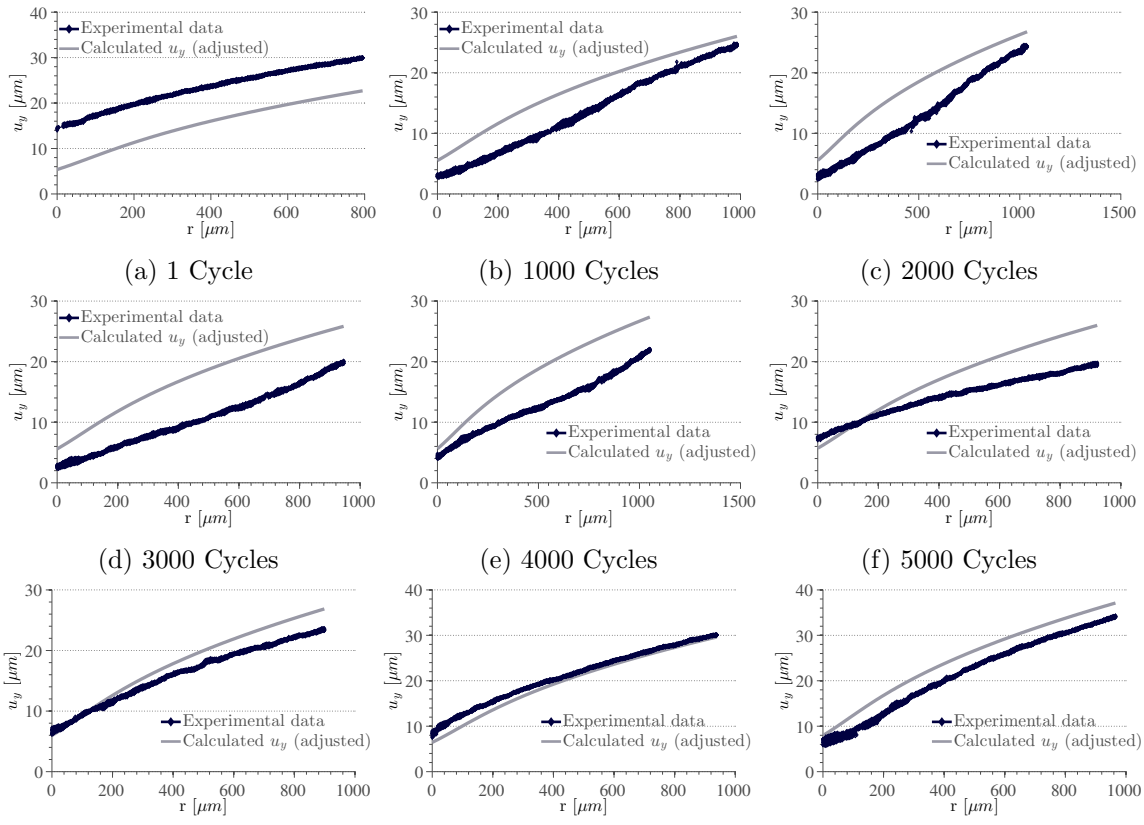


Figure 4.15: Image of crack tip at 2000 cycles post overload. The crack tip position at the overload cycle is shown with the blue arrow. The region that was present during (and prior to) the overload cycle (to the right of the blue arrow) was measured to have higher displacements and less closure.

Looking at the displacement at 2 kN of the DIC measured points compared to the calculated displacements (Figure 4.16), the effects of the changes in crack closure can be seen. As the crack starts to grow through the plastic zone, the displacement of

the growing crack is much lower than that calculated due to the displacement not increasing until the load has already increased to $P > 0.5P_{max}$. As the crack grows during the first 4000 cycles post overload, it is interesting to observe that the analysed points that have the greatest difference from the calculated values are positioned just after (further from the mouth) the crack tip position of the overload cycle. This point of largest difference is shown in Figures 4.16b to 4.16e moving to the right in each plot as the crack tip grows. When the crack grows further, after approximately 7000 cycles, the experimentally obtained displacement has a good fit with the calculated values, as it did before the overload was applied.



(a) 1 Cycle (b) 1000 Cycles (c) 2000 Cycles

(d) 3000 Cycles (e) 4000 Cycles (f) 5000 Cycles

(g) 6000 Cycles (h) 7000 Cycles (i) 8000 Cycles

Figure 4.16: DIC measured displacement of points at 2 kN during constant amplitude loading between 1 and 8000 cycles after a single overload cycle plotted with calculated displacement at measured points according to Equation (3.4).

The opening load can be examined by analysing the load at which the displacement of points begins to increase. By selecting a point at a distance from the crack tip and

defining the opening load as the load when this point has a displacement above 0.2 µm and the average of the next 10 displacement values of this point are above 0.5 µm, a plot of opening load vs crack length can be produced (Figure 4.17). This average value is used in an attempt to reduce to effects of noise or outlying points in the displacement data. A point at 250 µm from the crack tip is analysed in Figure 4.17, although similar shaped plots are produced when looking at points nearer and slightly further from the crack tip and also when adjusting slightly the determined opening distance criteria. At a larger distance from the crack tip, the closure levels remain low for a period after the overload due to the analysed point being located around the crack section that was present during the overload cycle. The dramatic drop in the opening load in Figure 4.17 occurs directly after the overload, before the opening load then rises to levels much higher than those seen previously in constant amplitude loading conditions. These results are consistent with those seen in Figure 4.14 showing the plots of relative load and displacement post overload. The opening load returns to levels similar to what it was prior to the overload after approximately 7000 cycles when the crack has grown 3.94 mm. It is likely that the opening load returned to similar levels that were present prior to the overload sometime between 6000 and 7000 cycles post overload (growth of 2.34 mm-3.94 mm), however points in between were not measured.

The crack was measured to be 24.47 mm long when the overload of 3 kN was applied giving a forward plane stress plastic zone size of 1.404 mm according to Equation (3.2). Irwin approximates the plastic zone to have a diameter of double that calculated by Equation (3.2), which would give a forward plastic zone size of 2.8 mm. This plastic zone size approximation is within the range of crack growth region where the opening load was significantly affected by the single overload cycle. The plastic zone size calculated in this way is shown over the plots of opening load in Figure 4.18. Examples from 3 specimens are shown in this figure, while others are not presented

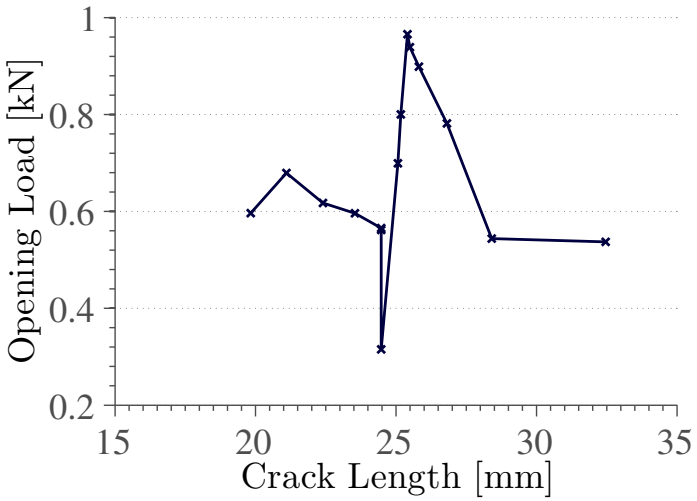
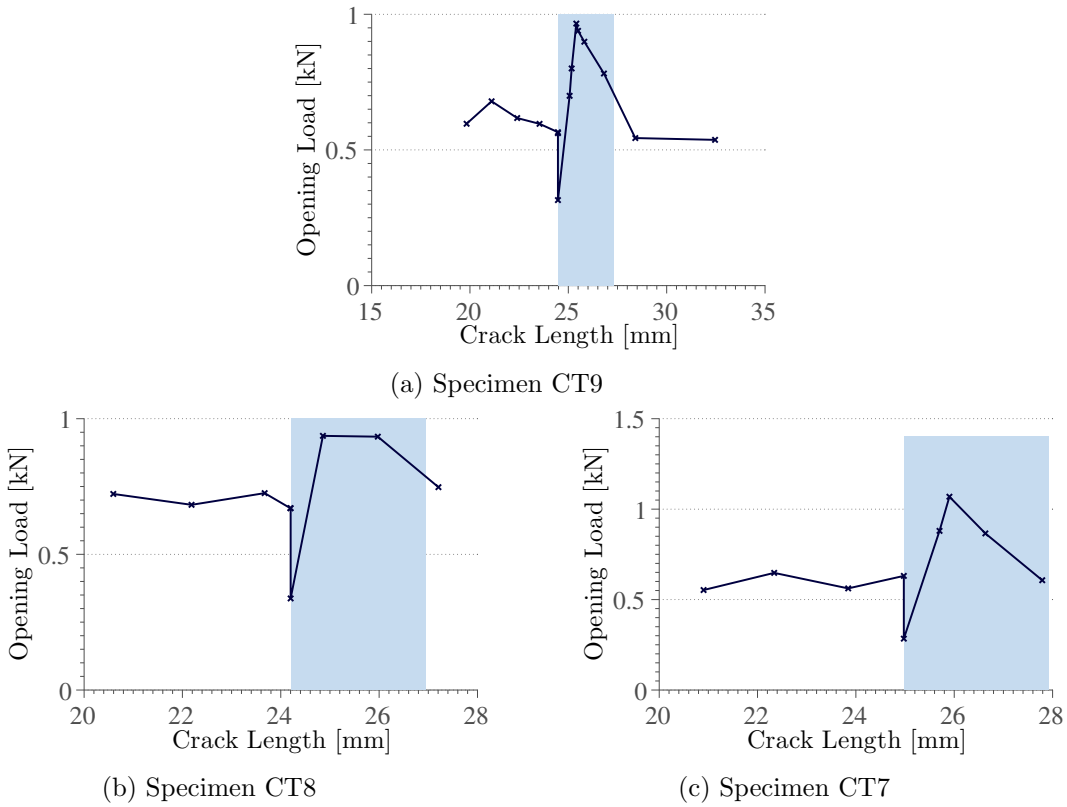


Figure 4.17: Opening Load vs Crack Length determined at a point 250 µm from the crack tip. The opening load is defined as the lowest load where the displacement is above 0.2 µm and displacement at the average of points at the next 10 load values is above 0.5 µm.

due to the low number of images collected before and after the overload cycle. In each case, the same general pattern of a large reduction in the opening load followed by an increase to levels not previously seen in constant amplitude loading is shown. The calculated plastic zone is roughly the size of the altered opening behaviour in each case. Of course, one might think it was the cyclic zone that had an influence on crack behaviour. In this case, the cyclic plastic zone size from the overload cycle is approximately the region from the overload crack length to the length where the maximum opening load is reached.



(a) Specimen CT9

(b) Specimen CT8

(c) Specimen CT7

Figure 4.18: Opening Load vs Crack Length for multiple specimen. The plane stress plastic zone size is calculated and doubled. This distance is added to the crack tip position during the overload cycle and shown in light blue shading on each figure.

4.3 Crack Growth

The overall crack length was calculated in the same way as previously (with images fitted together to create a full crack length image) and can be analysed to look at the effects of an overload cycle. Figure 4.19 shows the crack growth plotted against ΔK for periods before and after (red markers) a single overload. The ΔK value is calculated from the specimen geometry with $\Delta K = K_{max} - K_{min}$, and so the effects of crack closure are not taken into account. It is likely that the actual ΔK values at the crack tip will be less than those presented, especially when the level of crack closure is very high. The rate of crack growth (da/dN) is calculated numerically by dividing the distance grown between analysed points by the number cycles that had passed between measurements. Prior to the overload the crack growth forms a

straight line when plotted on a log-log plot, as expected from the Paris law. After the overload, however, there is a significant drop in the crack growth rate before eventually catching up to the rate expected from the plotted linear line. This drop in crack growth rate occurs during the same period that the crack closure levels are very high and the displacement of points around the crack is lower than expected at the maximum load, as described in the previous section. This shows that the crack closure levels, growth retardation and low displacements around the crack all occur together after an overload until the crack has grown a certain distance and normal constant amplitude loading behaviour is resumed.

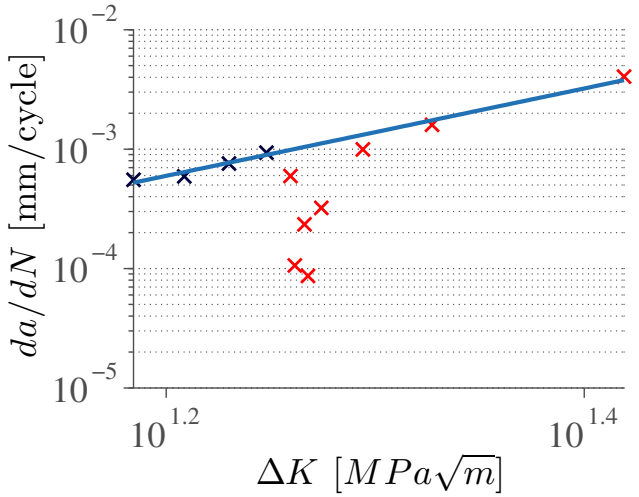


Figure 4.19: Rate of crack growth (per cycle) vs ΔK calculated from displacement data for a single specimen before (blue) and after (red) a single overload cycle plotted with a log scale.

4.4 Elastic Model Analysis

4.4.1 Single Overload Cycle

The single overload cycle displacement data can be analysed in the same way as the constant amplitude loading examples in the previous chapter. When loading up to 2 kN, the displacement data produces rather straight lines in a u_y vs $\sqrt{\frac{r}{2\pi}}\sin\frac{\theta}{2}\left(1+\sin^2\frac{\theta}{2}-\nu\cos^2\frac{\theta}{2}\right)$ plot with linear regression lines having R^2 values between $0.976 < R^2 < 0.998$ for loads $P/P_{max} > 0.4$. However, adding an offset to the crack tip of 100 µm improves this fit to $0.977 < R^2 < 0.999$ with an average of 0.995 for the same loads. This offset also provides a closer fit for the gradient of the plotted experimental K vs Load data (Figure 4.21) compared with the analytical calculation for K (gradient of 9.74 for experimental K vs 10.11 for the analytical value). Without any offset these gradients of K vs Load are 8.67 (experimental K) vs 10.11 (analytical K). This offset was therefore used in this analysis of the single overload cycle.

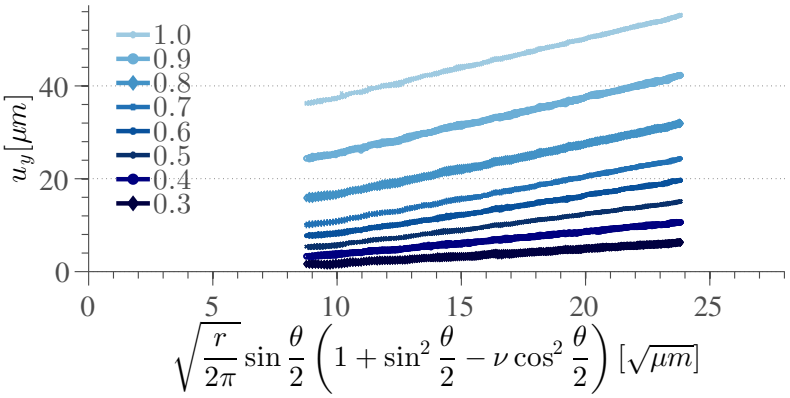


Figure 4.20: u_y vs $\sqrt{\frac{r}{2\pi}}\sin\frac{\theta}{2}\left(1+\sin^2\frac{\theta}{2}-\nu\cos^2\frac{\theta}{2}\right)$ plot for various loads (P/P_{max}) during a single overload cycle.

One of the prominent features of the u_y vs $\sqrt{\frac{r}{2\pi}}\sin\frac{\theta}{2}\left(1+\sin^2\frac{\theta}{2}-\nu\cos^2\frac{\theta}{2}\right)$ plot (Figure 4.20) is the spacing between plotted lines of each selected load as the load is increased. As the load approaches 3 kN, the spacing between the plotted values at each load increases due to the large increases in the displacement of analysed points

(as seen in Figure 4.9). If the behaviour at the crack tip was solely elastic, the plotted lines would be evenly spaced as the load is increased, with the linear regression lines having y intercepts of 0 and gradients increasing proportionally to the load increasing.

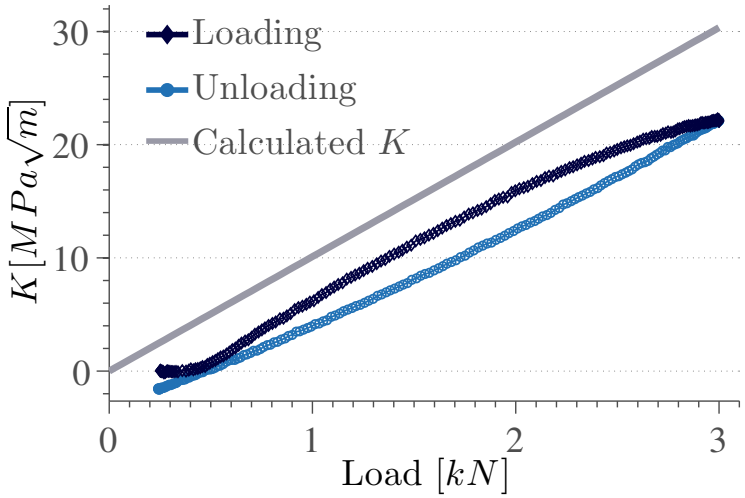


Figure 4.21: K vs Load plot calculated from linear regression lines fitted to data on u_y vs $\sqrt{\frac{r}{2\pi}}\sin\frac{\theta}{2}\left(1+\sin^2\frac{\theta}{2}-\nu\cos^2\frac{\theta}{2}\right)$ plots for a single overload cycle.

The K vs Load plot produced using the experimental displacement data is shown in Figure 4.21. The initial loading up to approximately 0.4 kN shows the period of crack closure before K increases at a very similar rate to that predicted from the specimen geometry. As the load increases higher, the rate of K increasing slows compared with the analytically calculated K value. The rate of growth of K continues to slow right up to the maximum load of the overload cycle. During unloading, the value of K changes linearly as the load is decreased, however, the rate of change is slower than the rate K changes in the analytical calculation. There is no crack closure after the overload cycle and therefore no period of very little change in K as the load approaches the minimum. Instead, the value of K calculated from the displacement data becomes negative. This is due to the plasticity at the crack tip preventing the crack from closing. Points close to the crack tip retain a higher displacement than points further from the crack tip as shown in Figure 4.8, and this produces a negative gradient on a u_y vs $\sqrt{\frac{r}{2\pi}}\sin\frac{\theta}{2}\left(1+\sin^2\frac{\theta}{2}-\nu\cos^2\frac{\theta}{2}\right)$ plot.

4.4.2 Post Overload Analysis

Directly after the overload, when constant amplitude loading is resumed there is no (or very little) crack closure observed. Once again plots of u_y vs $\sqrt{\frac{r}{2\pi}}\sin\frac{\theta}{2}\left(1+\sin^2\frac{\theta}{2}-\nu\cos^2\frac{\theta}{2}\right)$ produce good fitting linear regression lines, as shown in Figure 4.22. After the overload, the plotted points look to be spaced evenly as the load is increased, which is expected in an elastic model. With a crack tip offset of 100 µm the R^2 values of linear regression lines are $0.981 < R^2 < 0.999$ with an average of 0.997 for loads $P/P_{max} > 0.4$. However adding an additional offset of 100 µm (200 µm total offset) produces an improved fit with R^2 values of $0.981 < R^2 < 0.999$ and an average of 0.997. The gradient of the resulting K vs Load plot is also again much closer to that produced from the specimen geometry (9.76 vs 10.11) after this additional offset than before with an offset of only 100 µm (8.78 vs 10.11). This can be seen clearly in the plots of Figure 4.23 showing K vs Load with crack tip offsets of 100 µm and 200 µm. The additional offset seems reasonable as it is likely that there was some additional growth of the crack during the overload cycle and the exact same locations of analysed points were used for the cycles directly before, during and then immediately after the overload.

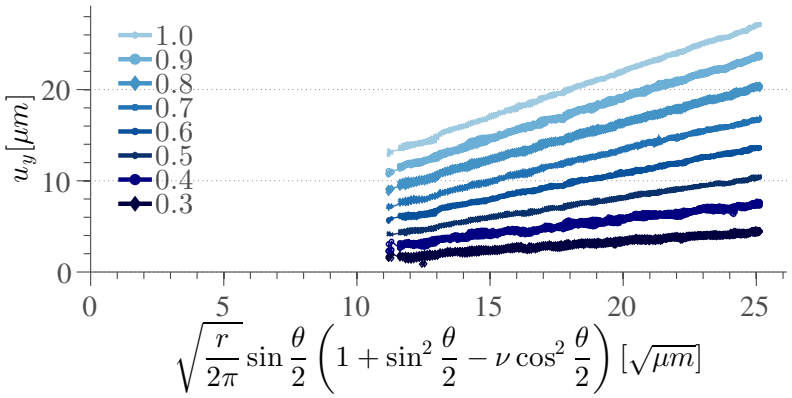
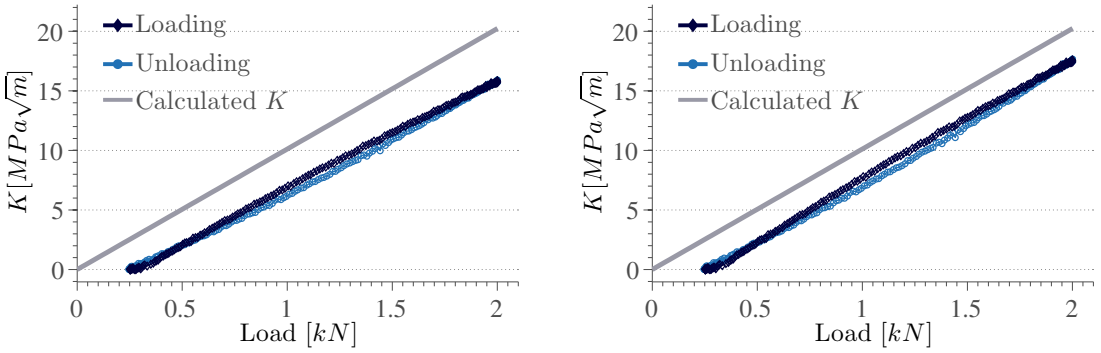


Figure 4.22: u_y vs $\sqrt{\frac{r}{2\pi}}\sin\frac{\theta}{2}\left(1+\sin^2\frac{\theta}{2}-\nu\cos^2\frac{\theta}{2}\right)$ plot for various loads (P/P_{max}) for a cycle directly after a single overload cycle.

Due to the reduction in crack closure effects after the overload, the plots of K



(a) Crack tip offset 100 µm

(b) Crack tip offset 200 µm

Figure 4.23: K vs Load plots calculated from linear regression lines fitted to data on u_y vs $\sqrt{\frac{r}{2\pi}}\sin\frac{\theta}{2}\left(1+\sin^2\frac{\theta}{2}-\nu\cos^2\frac{\theta}{2}\right)$ plots for a cycle directly after a single overload cycle.

vs Load (Figure 4.23) from the experimental displacement data have a close fit with the values determined from the specimen geometry. However, the offset that was seen previously in constant amplitude analysis is still present. It is likely that this offset is simply due to the displacement measurements around the crack tip being measured from the base image of the crack loaded at 0.25 kN. This gives a K value of 0 at this first image, even though the specimen has a load applied and there is displacement around the crack flanks. The analytical calculation does not take this into account and so the analytical value of K is reduced by the calculated value of K at 0.25 kN to compare the K vs Load plots. The result is a very good fit between the experimentally determined K vs Load plot and that produced from calculations based on the specimen geometry (Figure 4.24). The strong fit during a cycle with no closure suggests that prior to the overload the crack closure is solely responsible for the offset between the experimentally determined K and the K value calculated analytically.

As the crack grows, the crack growth rate is slowed and the images of the crack tip contain the crack tip position during the overload cycle. This region of the crack that was present during the overload cycle retains the large displacement levels seen immediately after the overload, as shown earlier in Figure 4.14. This affects the plots of u_y vs $\sqrt{\frac{r}{2\pi}}\sin\frac{\theta}{2}\left(1+\sin^2\frac{\theta}{2}-\nu\cos^2\frac{\theta}{2}\right)$, with linear regression lines no longer fitting

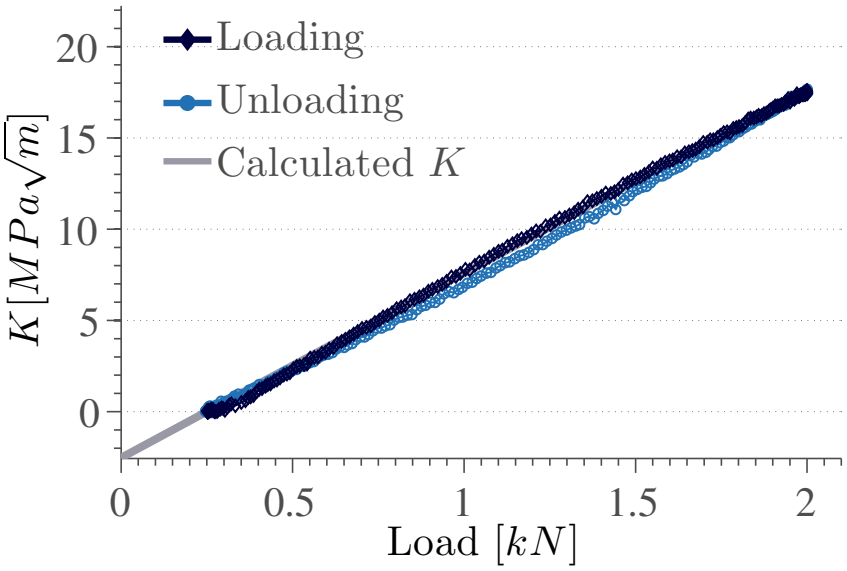
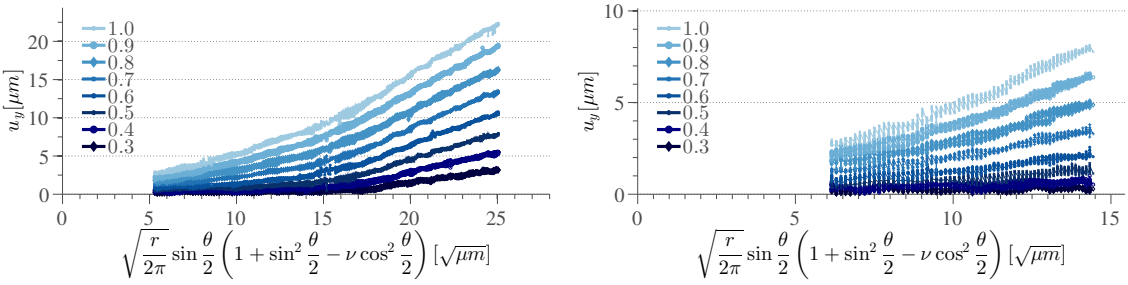


Figure 4.24: K vs Load plot calculated from linear regression lines fitted to data on u_y vs $\sqrt{\frac{r}{2\pi}}\sin\frac{\theta}{2}\left(1+\sin^2\frac{\theta}{2}-\nu\cos^2\frac{\theta}{2}\right)$ plots for a cycle directly after a single overload cycle. The K value calculated from the specimen geometry is adjusted by subtracting the value of K at a load of 0.25 kN.

well with all the displacement data (Figure 4.25a). The R^2 values of fitted lines are between $0.832 < R^2 < 0.977$ for loads $P/P_{max} > 0.4$, however if only the points within 300 µm of the crack tip are analysed, the displacments of points around the crack tip region that existed during the overload are discarded. This results in data with an improved fit for linear regression lines (Figure 4.25b) and this area near the crack tip is used to determine a value of K.



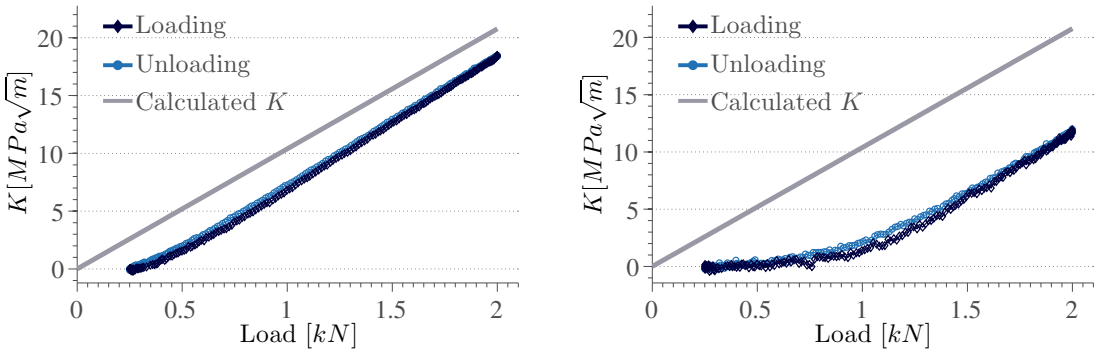
(a) All analysed points

(b) Points within 300 µm of the crack tip

Figure 4.25: u_y vs $\sqrt{\frac{r}{2\pi}}\sin\frac{\theta}{2}\left(1+\sin^2\frac{\theta}{2}-\nu\cos^2\frac{\theta}{2}\right)$ plot for various loads (P/P_{max}) of a cycle 1000 cycles after a single overload cycle.

The effects of the selection of points after an overload cycle on the calculation

of K can be seen in Figure 4.26. Without excluding the points around the crack area that existed during the overload cycle, the large displacement of these points produces a gradient on a linear regression line and masks the effects of the points near the crack having very little displacement at low loads. When only looking at points near the crack tip, the large period that the crack remains closed during initial loading is reflected with very little change in K during this phase.



(a) All analysed points

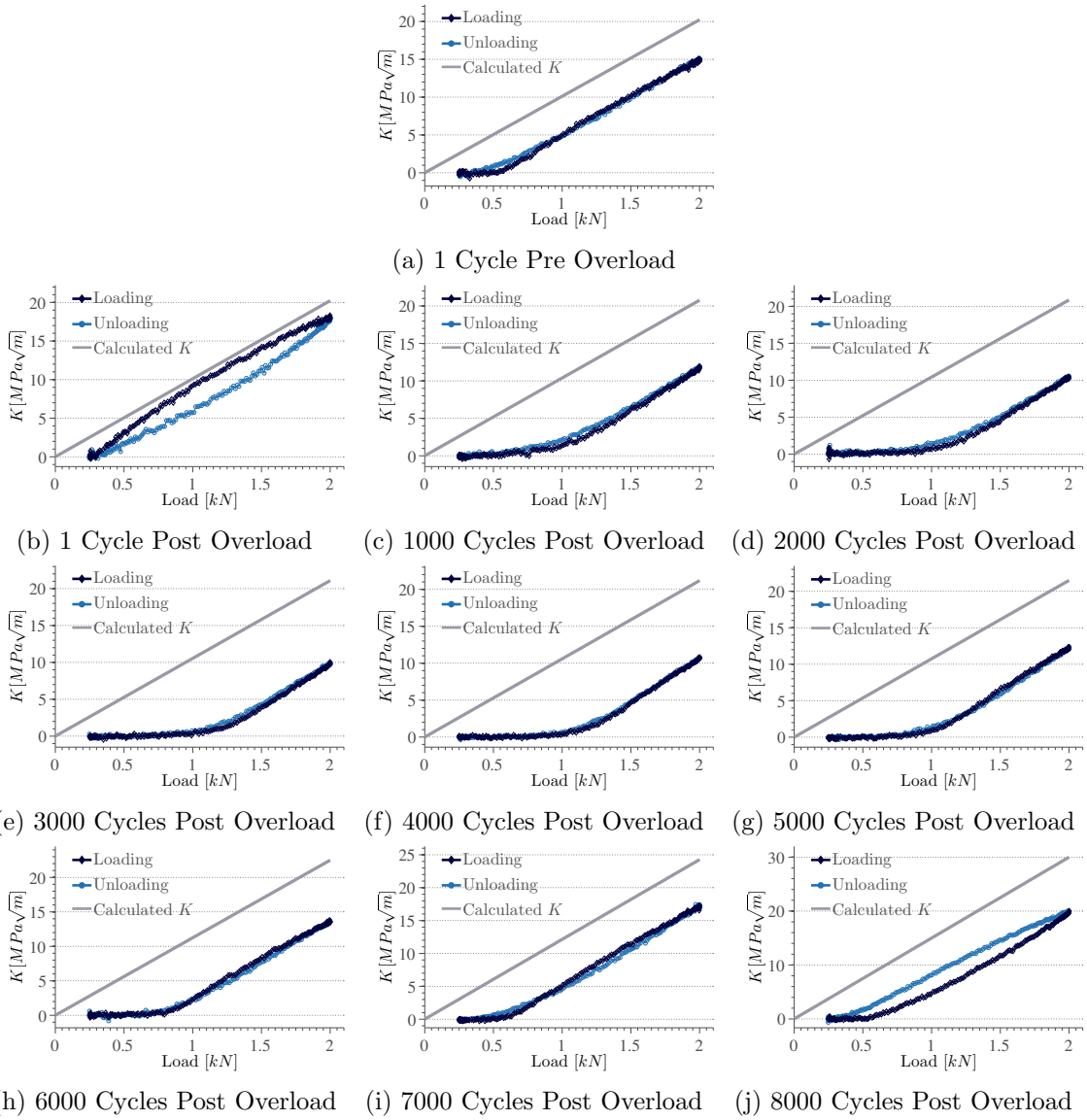
(b) Points within 500 µm of the crack tip

Figure 4.26: K vs Load plot calculated from linear regression lines fitted to data on u_y vs $\sqrt{\frac{r}{2\pi}}\sin\frac{\theta}{2}\left(1+\sin^2\frac{\theta}{2}-\nu\cos^2\frac{\theta}{2}\right)$ plots for a cycle 1000 cycles after a single overload cycle.

The change in K values at various stages after a single overload cycle are presented in Figure 4.27. The value of K based on the displacement data for the cycle before the overload was applied is shown in Figure 4.27a for comparison. This figure shows typical behaviour seen in constant amplitude loading. In most cases post overload, (the exception being directly after the overload) no offset was added to the crack tip position as there was a strong fit of linear regression lines to u_y vs $\sqrt{\frac{r}{2\pi}}\sin\frac{\theta}{2}\left(1+\sin^2\frac{\theta}{2}-\nu\cos^2\frac{\theta}{2}\right)$ plots and the gradient of the K vs Load plots was very similar, once the crack was open, to that of the analytically calculated K vs Load. The change in crack closure levels and opening loads can be seen in the periods of very little change in K during both initial loading and as the load approaches the minimum during unloading. The level of ΔK at the crack tip during a single cycle is greatly reduced during the period of 1000-6000 cycles post overload and therefore it is not surprising that the crack growth is retarded during this period. As the crack grows,

the K vs Load plots present similar features to those measured prior to the overload at 7000 cycles post overload (Figure 4.27i). At this stage the crack growth rate has returned to the level expected from calculations during constant amplitude loading and the experimentally determined ΔK has a similar (although slightly greater) offset to the analytical ΔK as that seen before the overload.

A value of ΔK_{eff} can be obtained from the experimentally determined K values shown in Figure 4.27. Unlike the analytical K values based on the specimen geometry, these values of ΔK_{eff} reduce after an overload, as a reflection of a period of increased crack closure. This is shown clearly in Figure 4.28. Using these values of ΔK_{eff}, a plot of the crack growth rate vs ΔK_{eff} can be produced to compare with Figure 4.19. Using the analytical value of ΔK, there is a clear deviation from a fitted regression line for a period just after the overload cycle due to decreased crack growth. However, with the experimentally determined ΔK_{eff} this feature is not present due to the decrease in ΔK_{eff} during the period of decreased crack growth. Therefore, all points have a reasonable fit with a linear regression line on a log scale plot, as predicted with the Paris Law. This suggests that the crack growth rate and ΔK are related and the analytical calculation deviates from the experimental results due to not taking into account the effects on ΔK from the overload.



(a) 1 Cycle Pre Overload

(b) 1 Cycle Post Overload

(c) 1000 Cycles Post Overload

(d) 2000 Cycles Post Overload

(e) 3000 Cycles Post Overload

(f) 4000 Cycles Post Overload

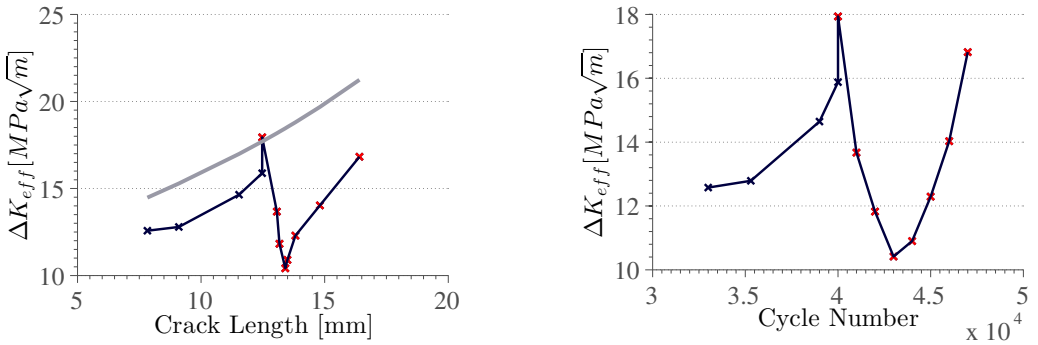
(g) 5000 Cycles Post Overload

(h) 6000 Cycles Post Overload

(i) 7000 Cycles Post Overload

(j) 8000 Cycles Post Overload

Figure 4.27: K vs Load plots at various stages before and after a single overload cycle for points within 300 µm of the crack tip position.



(a) ΔK_{eff} vs Crack Length

(b) ΔK_{eff} vs Cycles Applied

Figure 4.28: ΔK_{eff} vs (a) crack length and (b) number of cycles applied. Analytical calculation of K based on specimen geometry is plotted in (a)(grey). Calculated ΔK_{eff} based on experimental displacement data before (blue) and after (red) an overload cycle.

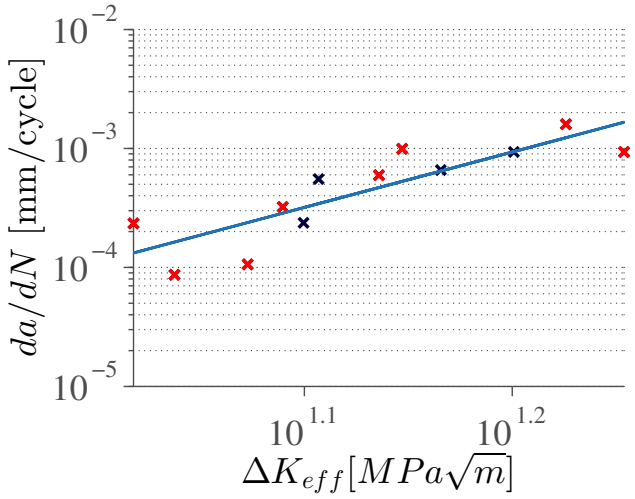


Figure 4.29: Rate of crack growth vs ΔK_{eff} plotted with a log scale. Data points are displayed from before (blue) and after (red) an overload cycle. ΔK_{eff} is calculated from the analysis of experimental displacement data presented in Figure 4.27

4.5 Elastic Plastic Model Analysis

Due to the large amount of plasticity during the overload cycle, it is not expected that the elastic model will completely account for the behaviour near the crack tip. The elastic plastic model proposed by Pommier [5] (see Section 2.2.4) can be used to analyse the variable amplitude period of loading to compare with constant amplitude loading conditions shown in the previous chapter. Equation (3.12) is used to analyse the displacement data with the gradient of linear regression lines fitted to a u_y vs $\sqrt{\frac{r}{2\pi}}\sin\frac{\theta}{2}\left(1+\sin^2\frac{\theta}{2}-\nu\cos^2\frac{\theta}{2}\right)$ plot giving the value of K (the same as in the previous section) and the y-intercept giving ρ, the plastic flow intensity factor.

$$u_y = 2\frac{K}{E}\sqrt{\frac{r}{2\pi}}\sin\frac{\theta}{2}\left(1+\sin^2\frac{\theta}{2}-\nu\cos^2\frac{\theta}{2}\right)+\rho \qquad \text{(3.12 revisited)}$$

4.5.1 Single Overload Cycle

During a single overload cycle (Figure 4.30), the change in ρ during the initial phases of loading are minor, as expected, during loading up to 2 kN. However, after this phase the value of ρ increases significantly with not much change in K. This is the same period that the growth of the experimentally determined value of K slows in comparison to the analytically calculated value as seen in Figure 4.21. It appears that over a certain load, the behaviour at the crack tip changes drastically with lower than expected values of K and significant levels of plasticity (ρ) giving much greater than expected levels of displacement around the crack. The phase of increasing ρ is very linear with the increase in K as the load approaches the maximum of 3 kN. During the initial unloading phase, K drops immediately with little change in ρ, as seen in most cases during constant amplitude loading. K and ρ continue to decrease as the load reduces to the minimum, but there is less change in ρ during the whole unloading phase as there was during loading. This leaves a residual ρ, which is a

reflection of the residual displacements around the crack as the load is returned to a minimum.

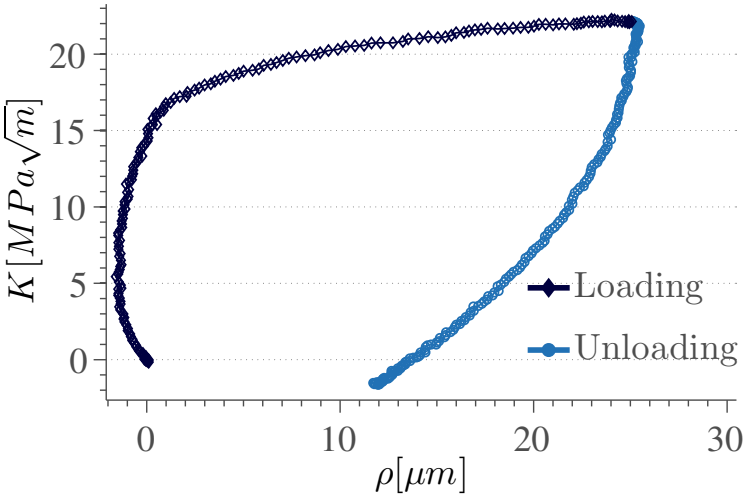
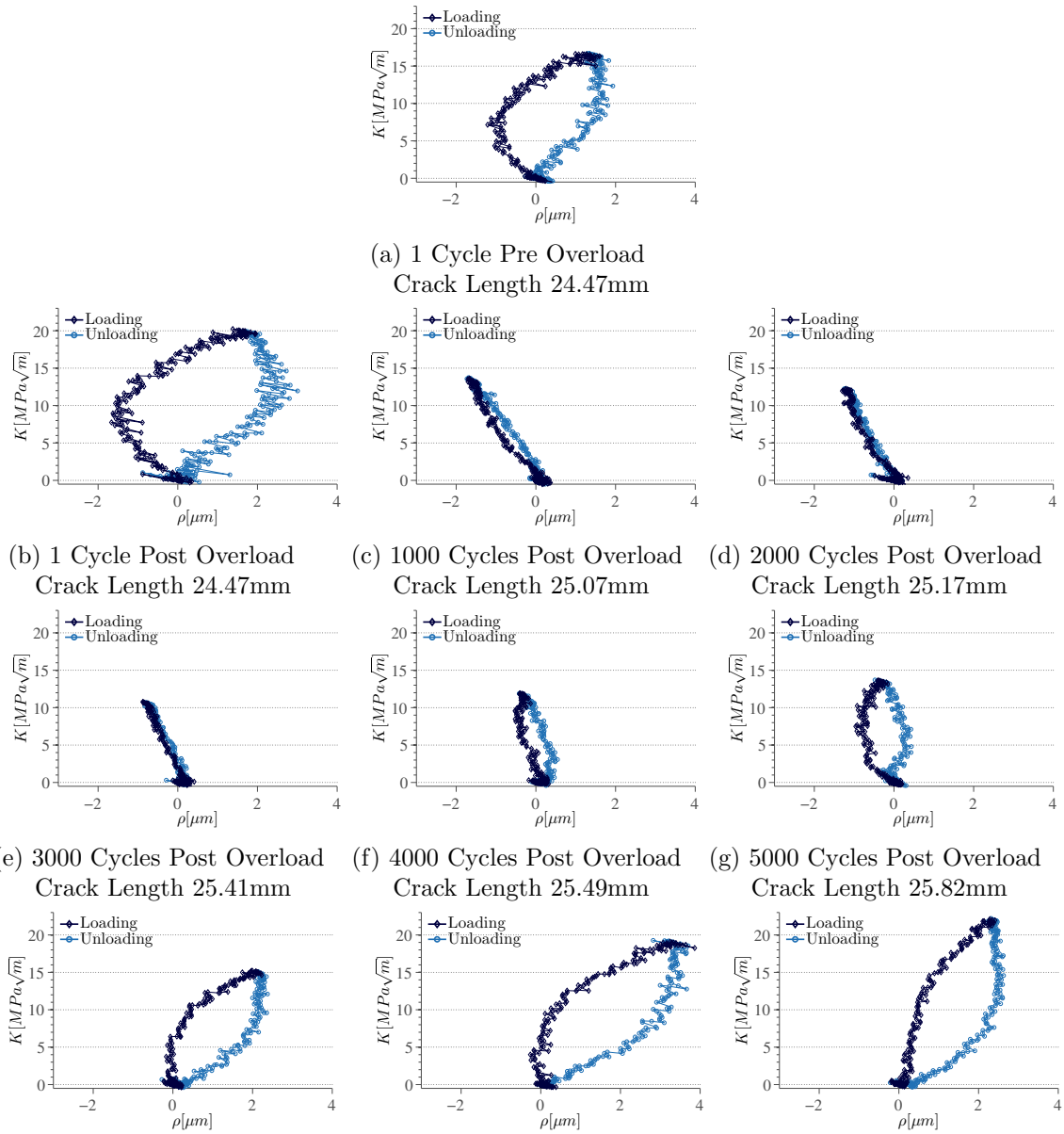


Figure 4.30: K vs ρ plot during a single overload cycle with maximum 3 kN.

4.5.2 Post Overload Analysis

Plots of K vs ρ that are calculated from the experimentally recorded displacement of points after an overload cycle are displayed in Figure 4.31. The cycle just prior to the overload is included for comparison, as this shows behaviour typical of constant amplitude loading. Initially after the overload, the K vs ρ behaviour is rather similar to before the overload. The main differences are that the $\Delta\rho$ during the cycle is larger and the level of ρ during unloading does not ever return to a value that existed during loading until the load is very close to the minimum. In comparison, during the unloading phase of a constant amplitude loading example, the value of ρ returns to a value that was present during initial loading at a low (but non zero) K value, as this is when crack closure begins. There are still negative ρ values obtained during initial loading, which are likely a reflection of the residual displacements after the overload rather than any crack closure. The residual displacement after the overload leaves points near the crack tip having a greater displacement than those nearer the crack

mouth (Figure 4.8) due to plasticity at the tip. By taking the image at minimum load post overload as the base image for DIC analysis, this residual displacement gradient is not accounted for and it is expected that the points further from the crack tip will initially have higher displacements relative to those near the crack tip that have a higher residual displacement from the overload.



(a) 1 Cycle Pre Overload Crack Length 24.47mm

(b) 1 Cycle Post Overload Crack Length 24.47mm

(c) 1000 Cycles Post Overload Crack Length 25.07mm

(d) 2000 Cycles Post Overload Crack Length 25.17mm

(e) 3000 Cycles Post Overload Crack Length 25.41mm

(f) 4000 Cycles Post Overload Crack Length 25.49mm

(g) 5000 Cycles Post Overload Crack Length 25.82mm

(h) 6000 Cycles Post Overload Crack Length 26.81mm

(i) 7000 Cycles Post Overload Crack Length 28.41mm

(j) 8000 Cycles Post Overload Crack Length 32.46mm

Figure 4.31: K vs ρ plots at various stages before (a) and after a single overload cycle for points within 300 µm of the crack tip. Crack length is a from the specimen geometry (Figure 3.7).

Cycles Applied	Crack Length	Calc. K	Exp. K	Calc. K - Exp. K	ρ_{min}	ρ_{max}	$\Delta\rho$
33000	19.83	16.55	13.96	2.59	0.38	-0.75	1.13
35300	21.10	17.47	13.90	3.57	0.24	-0.94	1.18
37500	22.40	18.48	15.58	2.90	2.07	-0.82	2.90
39000	23.54	19.41	16.78	2.64	0.34	-1.32	1.66
40000	24.47	20.23	17.23	3.00	1.40	-1.51	2.91
40000	**24.47**	**30.34**	**24.58**	**5.76**	**28.29**	**-1.38**	**29.67**
40000	24.47	20.23	19.95	0.28	2.84	-1.46	4.30
41000	25.07	20.77	13.74	7.04	0.77	-1.73	2.50
42000	25.17	20.87	12.27	8.60	0.35	-1.30	1.65
43000	25.41	21.10	10.98	10.12	0.30	-1.00	1.30
44000	25.49	21.18	12.02	9.17	0.44	-0.58	1.02
45000	25.82	21.49	13.81	7.68	0.21	-1.03	1.24
46000	26.81	22.50	15.41	7.09	2.21	-0.35	2.56
47000	28.41	24.28	19.27	5.02	-0.26	3.87	4.13
48000	32.46	29.99	24.81	5.18	-0.22	3.23	3.45

Table 4.1: K and ρ calculated from the specimen geometry (calc. K) and experimentally measured displacements (exp. K and ρ) before and after a single overload cycle. The overload cycle is highlighted in bold.

After this initial phase post overload, the shape of the K vs ρ plots change dramatically. Between 1000 and 3000 cycles post overload the change in ρ during loading is completely negative and there is very little difference in the values of ρ during loading and unloading. This is a large deviation from behaviour seen during constant amplitude loading, the overload cycle and just after the overload. In these cases values of ρ are significantly different during loading and unloading with a hysteresis type behaviour seen. The negative ρ values are a reflection of the very low displacement levels near the crack tip with points further from the tip (even within the 300 µm distance analysed) having larger displacements and causing the linear regression lines fitted to a u_y vs $\sqrt{\frac{r}{2\pi}}\sin\frac{\theta}{2}\left(1+\sin^2\frac{\theta}{2}-\nu\cos^2\frac{\theta}{2}\right)$ plot to have a negative y-intercept. This is a direct reflection of the increase in closure near the crack tip. This behaviour gradually ceases as the crack grows, with positive ρ values returning after 6000 cycles post overload (Figure 4.31h). From these results, it seems likely that the growth of the crack is related to the change in ρ over the loading cycle. In particular the dif-

ference in the loading and unloading values of ρ, that is displayed as hysteresis type behaviour during constant amplitude loading, appears to be related to both the level of crack closure and the growth rate of the crack.

The variation of $\Delta\rho$ with crack length is given in Figure 4.32 and shows similar behaviour to that of ΔK_{eff} (Figure 4.28) before and after an overload cycle. Before the overload cycle the value of $\Delta\rho$ is generally rising as crack length increases, as was shown in Figure 3.51 of the previous chapter. Directly after the overload a significant increase in $\Delta\rho$ can be seen, which coincides with a large increase in ΔK_{eff} and the absence of previously seen crack closure. The next phase post overload shows decreasing values of $\Delta\rho$ as crack growth is retarded and the opening load increases due to crack closure. As both opening loads and crack growth return to levels expected from pre overload behaviour, so does $\Delta\rho$ with the last point showing a value that could be expected for a crack of that length had an overload cycle not been applied. A plot of the crack growth vs $\Delta\rho$ (Figure 4.33) shows a rather weak linear relationship when plotted on a log scale. Compared with ΔK_{eff} (Figure 4.29) it appears to have less of a relationship with crack growth rate. However, as mentioned previously, the sensitivity of $\Delta\rho$ is very high and small changes in the determined crack tip position have a considerable effect. This is not so much the case with ΔK_{eff}, which is less affected by minor inaccuracies and adjustments to the crack tip position. Therefore, it is difficult to tell exactly the relationship between $\Delta\rho$ and other parameters in this experiment due to challenges in defining the crack tip position with very high accuracy.

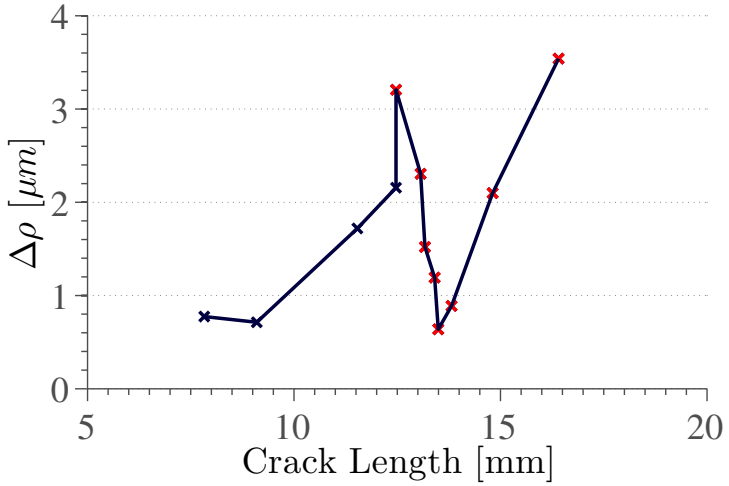


Figure 4.32: $\Delta\rho$ (as shown in Figure 4.31) vs Crack Length. Cycles before (blue) and after (red) an overload cycle are displayed.

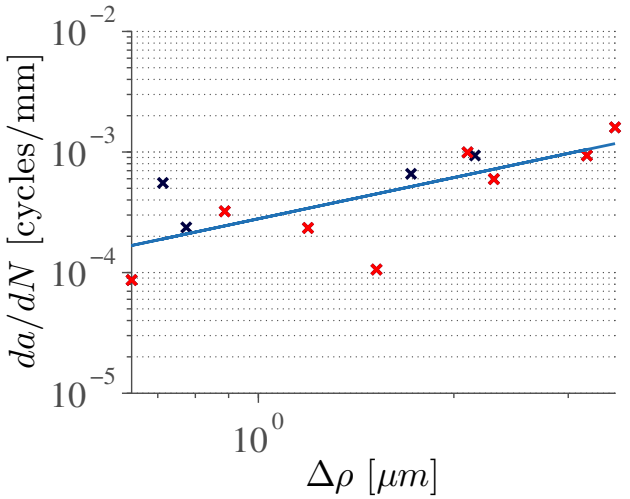


Figure 4.33: Crack growth rate vs $\Delta\rho$ (as shown in Figure 4.31) with a log scale and linear regression line. Cycles before (blue) and after (red) an overload cycle are displayed.

4.6 Conclusions

This chapter examined the behaviour around a crack tip during and after a single overload cycle is applied. A period of crack growth retardation followed the overload before the crack growth rate returned to similar levels to those predicted from constant amplitude loading before the overload was applied.

During the overload it was shown that the displacements around the crack tip displayed significant plastic deformation behaviour when the load increases above the constant amplitude levels. This resulted in above expected displacement levels around the crack and a residual displacement upon unloading. This residual displacement was larger closer to the crack tip where large plastic deformation occurred than at positions nearer the crack mouth. The result of this was a negative K value due to the residual stresses at the crack tip. A large change in ρ during the overload is a reflection of this plastic deformation and the residual ρ is a measure of the residual displacement at the crack tip after the overload.

Directly after the overload, there is no crack closure and the experimentally determined values of K fitted very well with those calculated from the specimen geometry. This suggests that the offset seen in constant amplitude loading was solely a reflection of crack closure, which results is a lower than expected ΔK for the loading cycle.

After applying constant amplitude loading post overload, the levels of displacement around the crack drop significantly lower than what is expected in an elastic model. At the same time crack closure near the tip increases and therefore ΔK decreases. In addition to this, the behaviour of ρ changes and is calculated to be negative with very little difference between loading and unloading. This behaviour continues until the crack grows further - to a distance approximately double the size of the plastic zone size calculated from the overload cycle. This suggests that it is likely to be the large plastic zone created by the overload that affects the growth, closure, ΔK and plasticity levels of the crack after an overload. Looking at the K

vs ρ behaviour and plots of $\Delta\rho$ vs both crack length and crack growth rate, a relationship (although rather weak) between $\Delta\rho$ and crack growth is shown. During periods of suppressed growth, there is very little change in ρ between the loading and unloading phases of a cycle and an overall negative ρ due to points very near the crack tip having low displacements.

Chapter 5

Imaging with a Scanning Electron Microscope

Similar analysis to that undertaken previously in Chapters 3 and 4 is repeated in this chapter, however images are captured using a Scanning Electron Microscope (SEM). This produces higher magnification images at a significantly increased resolution than those captured with a simple digital camera and telescopic lens. This allows analysis of an area much closer to the crack tip with improved accuracy. Images taken with the SEM in this experiment were slower to capture and therefore images were captured less frequently during a loading cycle. The specimen size was also altered in order to fit on a loading stage that applied loads to the specimen within the SEM chamber.

5.1 Testing Methodology

5.1.1 Experimental Set-up

Experiments were conducted in the Laboratory for In-situ Microscopy and Analysis (LIMA), which is part of the Solid Mechanics and Materials Engineering Group in the Department of Engineering Science at the University of Oxford. The imaging device used was a Carl Zeiss Evo LS15 VP-Scanning Electron Microscope and is shown in Figure 5.1. The chamber of the SEM was large enough so that in-situ testing could



Figure 5.1: Carl Zeiss Scanning Electron Microscope similar to that used at Oxford University [9]

be performed with a Deben testing stage, similar to that shown in Figure 5.2. A 5 kN load cell was attached to the testing stage and an extension rate of 1.25 mm/min (the maximum for the testing stage) was used for this testing. Computer software was used to set the drive parameters and collect live data on the force applied and extension from the testing stage during loading.

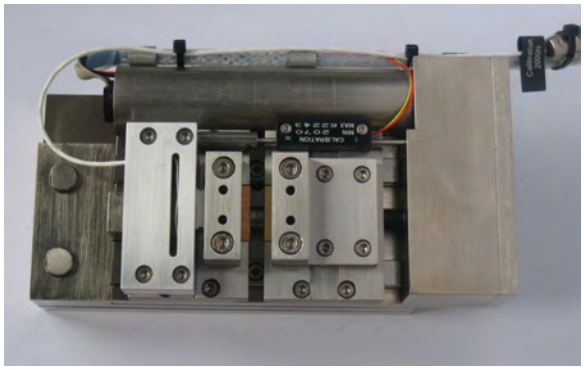


Figure 5.2: Deben In-Situ Microtest tensile & compression stage with a 2 kN load cell [10].

5.1.2 Specimen Loading

Specimens were made of the same material as that used in fatigue testing performed in Chapters 3 and 4 (Aluminium alloy 6082-T6), however the specimen size was altered to fit the Deben loading stage used. The specimen dimensions were designed to be as close as possible to complying with those recommended in ASTM E647-11 Standard Test Method for Measurement of Fatigue Crack Growth Rates [8] (Figure 5.4), although changes were required due to the constraints of the Deben stage size. The specimen dimensions are shown in Figure 5.3. The specimen shape is consistent with the recommended geometry presented in Figure 5.4. The overall size of the specimen and notch comply with the ASTM standard, while the loading holes are altered to be slightly smaller and further apart to fit on the loading stage. Loading is applied from the Deben stage to the specimen with small steel pins of 3 mm diameter. Although the geometry is slightly altered from the ASTM standard, the differences are minor and the calculation of K based on the geometry of the specimen (Equation (3.1) [8]) is still used in this in analysis.

The specimen was pre cracked before being loaded on the Deben stage with the same hydraulic testing rig used in Chapter 3. The hydraulic testing rig loaded the specimen at a frequency of 5 Hz, significantly faster than what could be achieved with the Deben testing stage. 17,000 cycles were applied to the specimen to grow the crack approximately 6.5 mm at the same loads to be used for later testing on the Deben stage. In order to utilise the same testing rig used previously, clevis adapters were constructed with dimensions to best comply with those specified in ASTM E647-11. Again, some changes were necessary to accommodate the modified specimen, although in this case the changes were only the size and shape of the holes that the loading pins passed through. The holes were small in order to fit the 3 mm loading pin and therefore the flat bottom of the hole in the clevis adapters was not included in order to simplify the machining process. The dimensions specified in ASTM E647-11 are

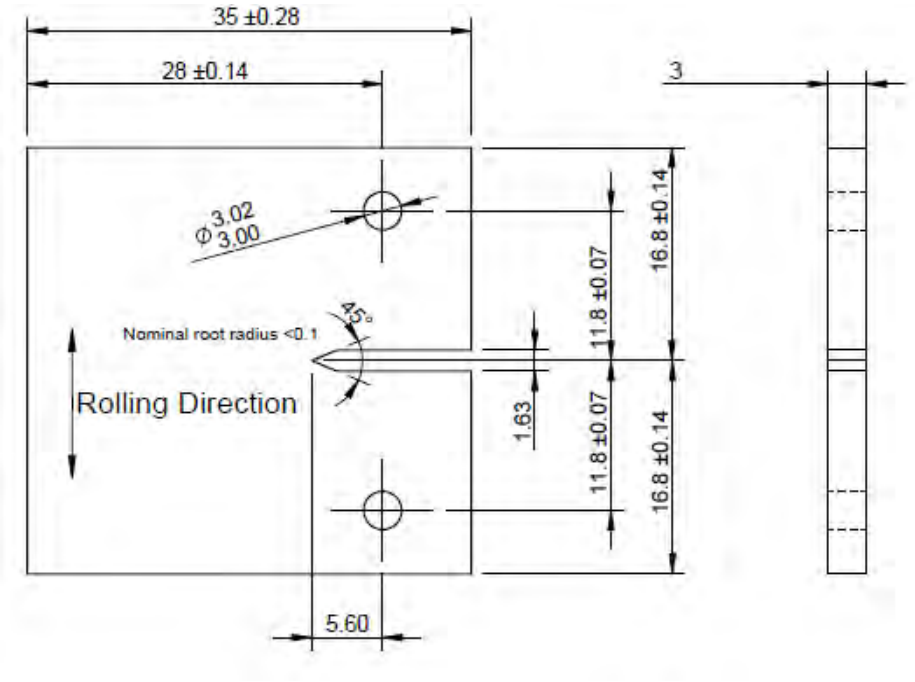


Figure 5.3: Dimensions (in mm) of specimens used for in-situ SEM testing. Specimens were cut from a sheet of aluminium alloy 6082-T6

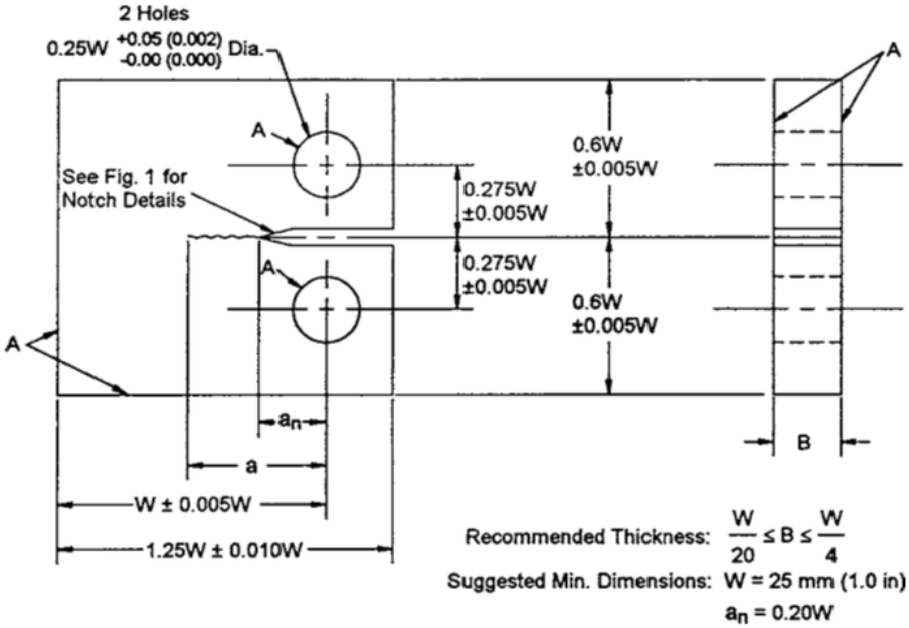


Figure 5.4: Recommended Compact Tension specimen dimensions from ASTM E647 - 11 Standard Test Method for Measurement of Fatigue Crack Growth Rates [8]. (repeated from page page 42)

displayed in Figure 5.5, while the clevis grip dimensions used in this experiment are given in Figure 5.6. A photo of the loading set-up including the CT specimen and

clevis grip, which fit inside the previously used clevis grips, is provided in Figure 5.7. After pre cracking, the specimen was unloaded, removed from the clevis grips and set-up on the Deben testing stage. The crack was grown further on the Deben stage to a length of approximately 6.9 mm before in-situ SEM images were captured.

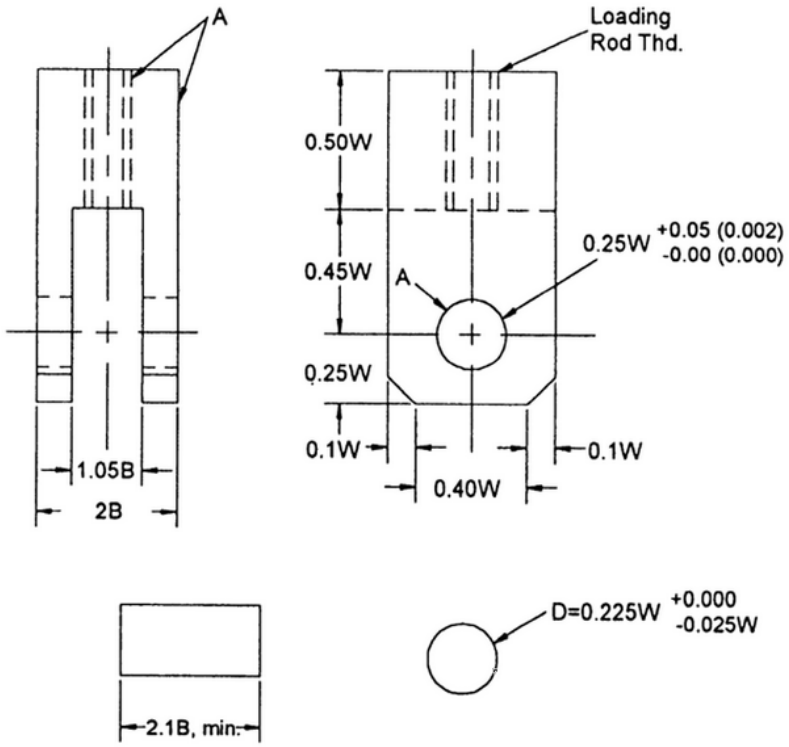


Figure 5.5: Recommended clevis and pin assembly geometry for gripping CT specimens [8]. Tolerance dimensions are in mm (inches).

Loading cycles applied to the specimen had a maximum force of 1.25 kN and minimum 0.125 kN, giving an R ratio of 0.1. With the motor speed of the tensile testing stage set a maximum speed of 1.25 mm/min, the time taken for a single cycle was approximately 140 seconds ($f = 0.0071$Hz). Some of this time was taken by the slow changes in motor direction when the force reached a maximum or minimum force value. A graph of the loading data obtained from the Deben software is shown in Figure 5.8.

In order to capture images with the SEM, the specimen loading needed to be paused during image capture. The loading process during and just after image cap-

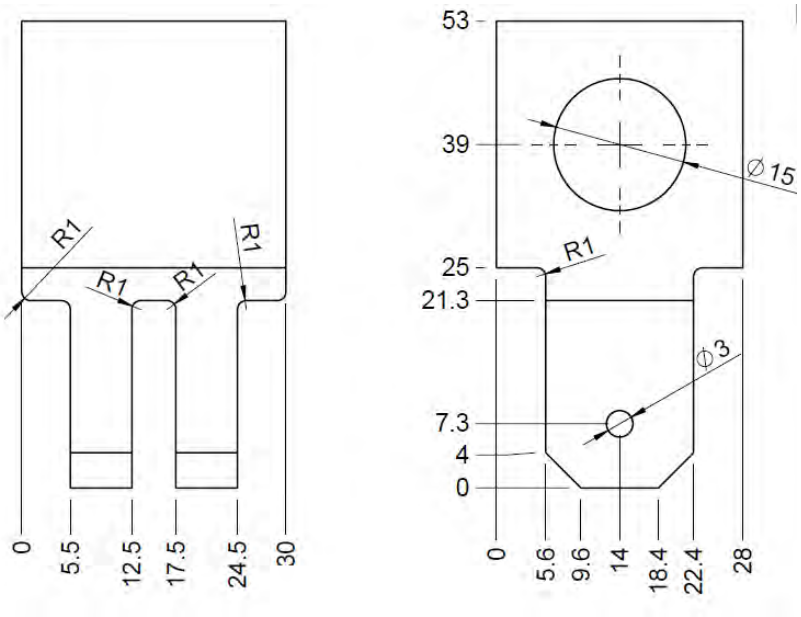


Figure 5.6: Dimensions of constructed clevis used to pre crack the CT specimen before loading in the SEM. Dimensions in mm.



Figure 5.7: Pre cracking the specimen before loading on the Deben testing stage. Adapters for the smaller specimen size are fitted to make use of the experimental set-up used in Chapter 3

turing is shown in Figure 5.9. This figure shows the pauses of approximately 2 minutes at each desired load to allow sufficient time to capture an image of the crack tip. This was done every 0.125 kN, giving 19 images for a complete cycle. After this image capture cycle, the load was raised to a maximum value and images were taken along the

crack in order to get a measure for the overall crack length just after the crack tip images were collected. Constant amplitude loading was then resumed as shown towards the end of the graph in Figure 5.9. The process of adjusting the load and capturing images for a single cycle during constant amplitude loading took approximately 40 minutes and then imaging the full crack length another 15 minutes.

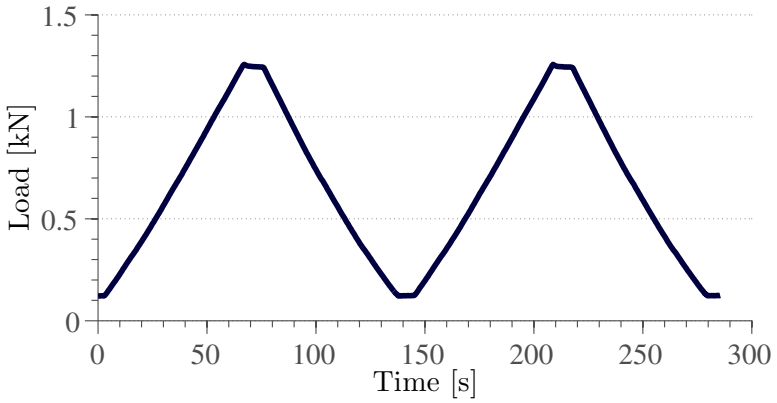


Figure 5.8: Force applied to the specimen during constant amplitude loading.

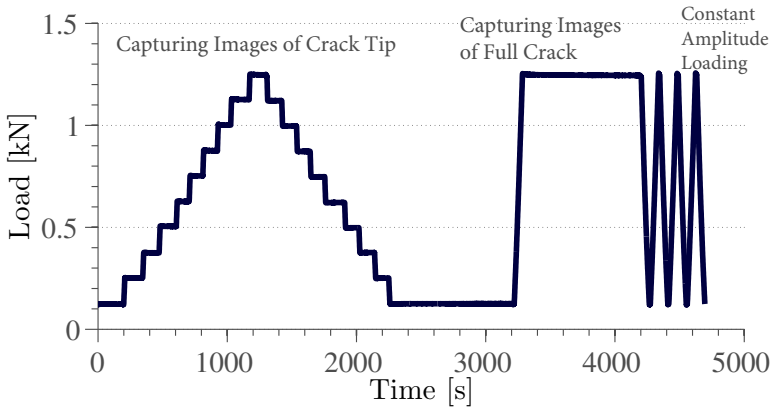


Figure 5.9: Force applied to the specimen during SEM image capture.

Analysis of variable amplitude loading was performed by applying a single overload cycle of 1.875 kN (150% of maximum) to the specimen. This cycle required more time to complete as a total of 29 images were captured at intervals of 0.125 kN. The loading profile (excluding pauses for image capture) is shown in Figure 5.10.

The timing of the image capture points is given in Table 5.1, with the number of loading cycles applied between each break in the constant amplitude loading given

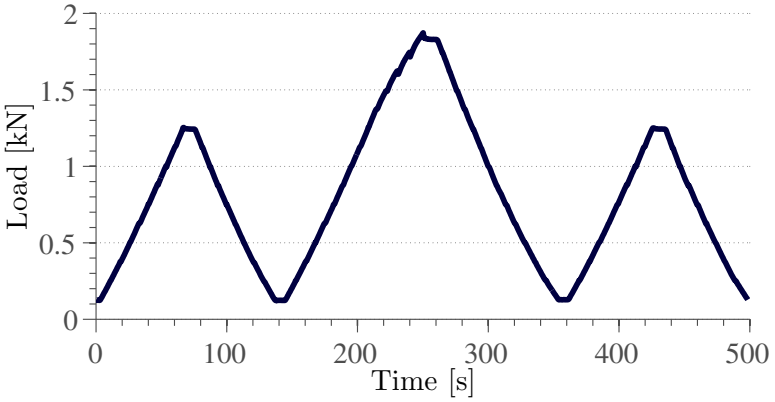


Figure 5.10: Loading applied to the specimen before, during and after an overload cycle.

in the left hand column. Sometimes images were collected for consecutive cycles, particularly at the overload, in order to examine the changes in K vs ρ behaviour from one cycle to the next.

Cycles Applied	Setup	Image Cycles	Reference Name	Crack Length [mm]	Notes
17000	Hydraulic testing rig	0	-	-	Pre Cracking Specimen
650	Deben Stage	1	Series1	6.99	-
110	Deben Stage	2	Series2	7.180	-
0	Deben Stage	4	Series3	7.180	Overload
50	Deben Stage	2	Series4	7.298	-
25	Deben Stage	1	Series5	7.375	-
50	Deben Stage	1	Series6	7.451	-

Table 5.1: Details of cycles applied to the specimen and points of image capture.

5.1.2.1 Plastic Zone Size

The forward plastic zone sizes for the specimen dimensions and load of 1.25 kN are given in Table 5.2. These are estimated by calculating the elastic stress field ahead of the crack tip to yield stress according to Equation (2.4). For the images collected in this experiment, $0.45 < a/W < 0.47$, so therefore the calculated forward plastic zone size was slightly below the values listed for $a/W = 0.5$. As mentioned previously, the

cyclic plastic zone size is calculated to be 1/4 of this forward plastic zone size.

		$r_y = \frac{1}{2\pi}\left(\frac{K}{\sigma_{yield}}\right)^2$[µm]		$r_y = \frac{1}{6\pi}\left(\frac{K}{\sigma_{yield}}\right)^2$[µm]	
t[mm]	P_{max}[kN]	$a/W = 0.25$	$a/W = 0.5$	$a/W = 0.25$	$a/W = 0.5$
3	2	229.4	882.5	76.5	294.2

Table 5.2: Size of the plane stress and plane strain plastic zones at $a/W = 0.25$ and $a/W = 0.5$ for the specimen used in SEM in situ testing. The corresponding crack lengths are 1.4 mm and 8.4 mm from the tip of the specimen notch.

5.2 Data Collection & Processing

Images were captured at a resolution of 3072 × 2304 pixels, giving an image area of approximately 215 µm × 161 µm. As the loading applied to the specimen was adjusted between images, translational displacement of the crack tip occurred. Due to the high magnification of the images, the crack tip location was often displaced out of the previous image frame and therefore the testing stage position was adjusted within the SEM to have the crack tip in approximately the same position for all images. Images were later aligned when processed using normalised 2-D cross-correlation with the MATLAB Image Processing Toolbox, so that the potential displacement of all points around the crack tip was minimized. This was done in an effort to improve DIC efficiency.

To analyse the captured images, the same MATLAB DIC code used in the previous experiments was utilised with some minor adjustments. A similar grid system was used as that explained in Chapter 3 except that only 2000 points were selected (rather than 2400) for each grid, with 200 in the x direction and 10 in the y direction normal to the crack. An example of the selected points to be tracked on an SEM image of the crack tip is shown in Figure 5.11.

Due to the high resolution of the images, displacements around the crack were

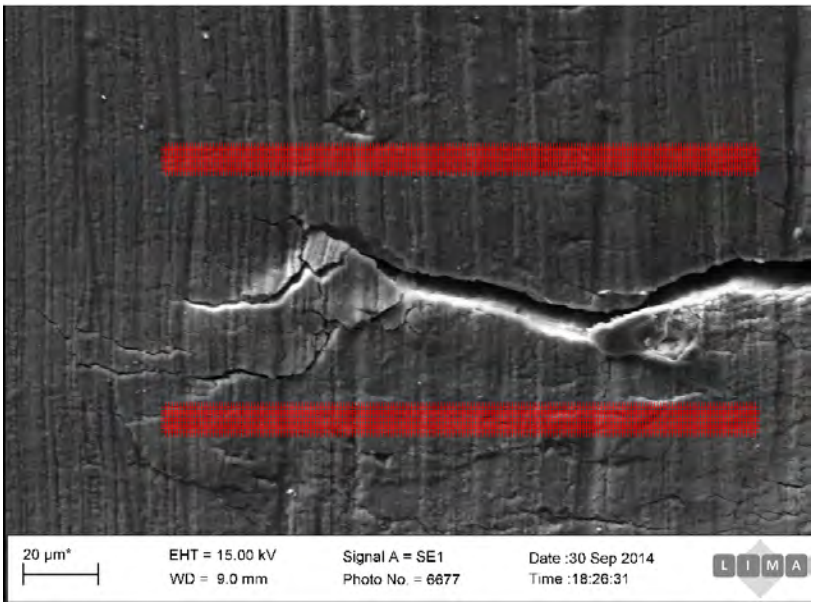


Figure 5.11: Typical image collected from the experiment at a load of 1.25 kN. Sets of points are selected on either side of the crack to measure displacements

quite large when the load was increased to the maximum. Therefore, in order to better track the points, the area surrounding each point that is used for image correlation was increased from a 31×31 pixel square that was used previously to a 201×201 pixel area. This significantly increased DIC processing time, although it also drastically improved the tracking of points within the images. The reduction in the number of points to be tracked was made in an effort to decrease this long processing time of the DIC analysis. During constant amplitude loading this proved to be an effective method of tracking points around the loaded crack, however, during and after an overload cycle there were still large sections near the crack tip that were unable to be tracked. This was due to visible changes picked up by the images on the surface of the specimen, particularly very near the crack tip.

In addition to the images taken to analyse displacements around the crack tip, images of the full crack were captured in order to measure crack length for calculations of K. These reduced magnification images were fitted together using normalised 2-D cross-correlation with the MATLAB Image Processing Toolbox to give an image of

the full crack length to measure from. An example is shown in Figure 5.12.

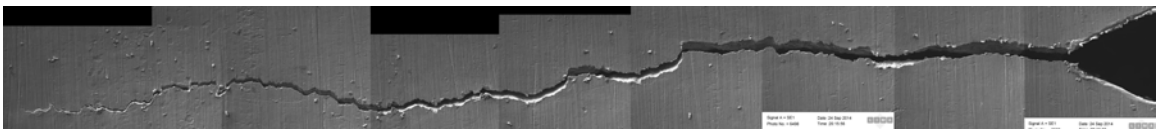


Figure 5.12: Series of images aligned to give an image of the full crack length at a load of 1.25 kN. Crack length is 7.123 mm.

5.3 Constant Amplitude Loading

This section provides analysis on the images collected prior to the overload (labelled 'Series2') after the specimen has been loaded with 17,760 cycles and the crack grown to 7.180 mm.

5.3.1 Displacement Along Crack Flanks

The displacement between sets of points was the basis for analysis around the crack tip. Displacements from the DIC analysis were given in pixels and therefore they were firstly converted into units of length using the scale included in each image. A graph of the relative displacement at various points along the crack tip plotted alongside the relative load (P/P_{max}) is shown in Figure 5.13. The differences in the loading and unloading phases of a cycle are noticeable in this plot and are more pronounced than in the constant amplitude loading of the previous experiment (Figure 3.20, page 55) . In particular, the initial loading and initial unloading phases involve the load changing and the displacements not responding at the same rate as they do during later stages of loading and unloading. This is more prominent at points very near the crack tip, which require a higher load before initial displacement and initially decrease in displacement slower than points further from the crack tip during unloading.

The higher opening load for points near the crack tip is reflected in the plot of relative load vs displacement (Figure 5.14) when looking at points 10 µm and 150 µm

from the crack tip. At points 10 µm from the crack tip, the displacement between the points only begins to noticeably increase when $P/P_{max} > 0.4$, while at 150 µm the required load is only $P/P_{max} > 0.3$. This is consistent with previous experiments and in this case improved resolution is provided for points close to the crack tip.

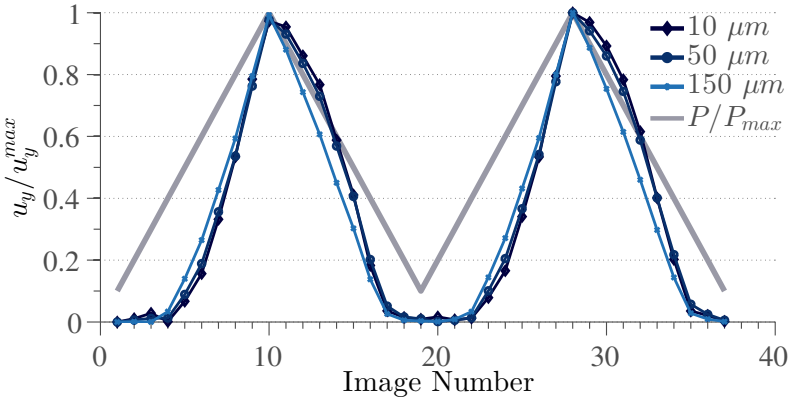


Figure 5.13: Typical variation of relative displacement u_y vs time (image number) compared to the applied load (P/P_{max}). Relative displacement between points located at 10 µm, 50 µm and 150 µm from the crack tip is shown.

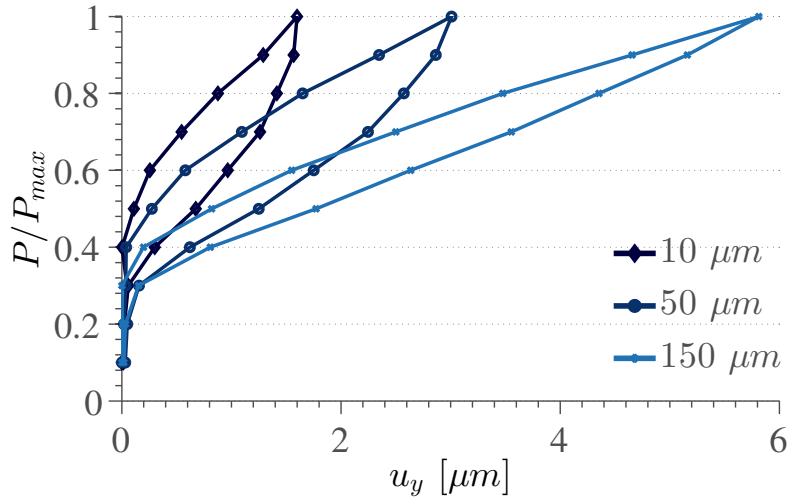


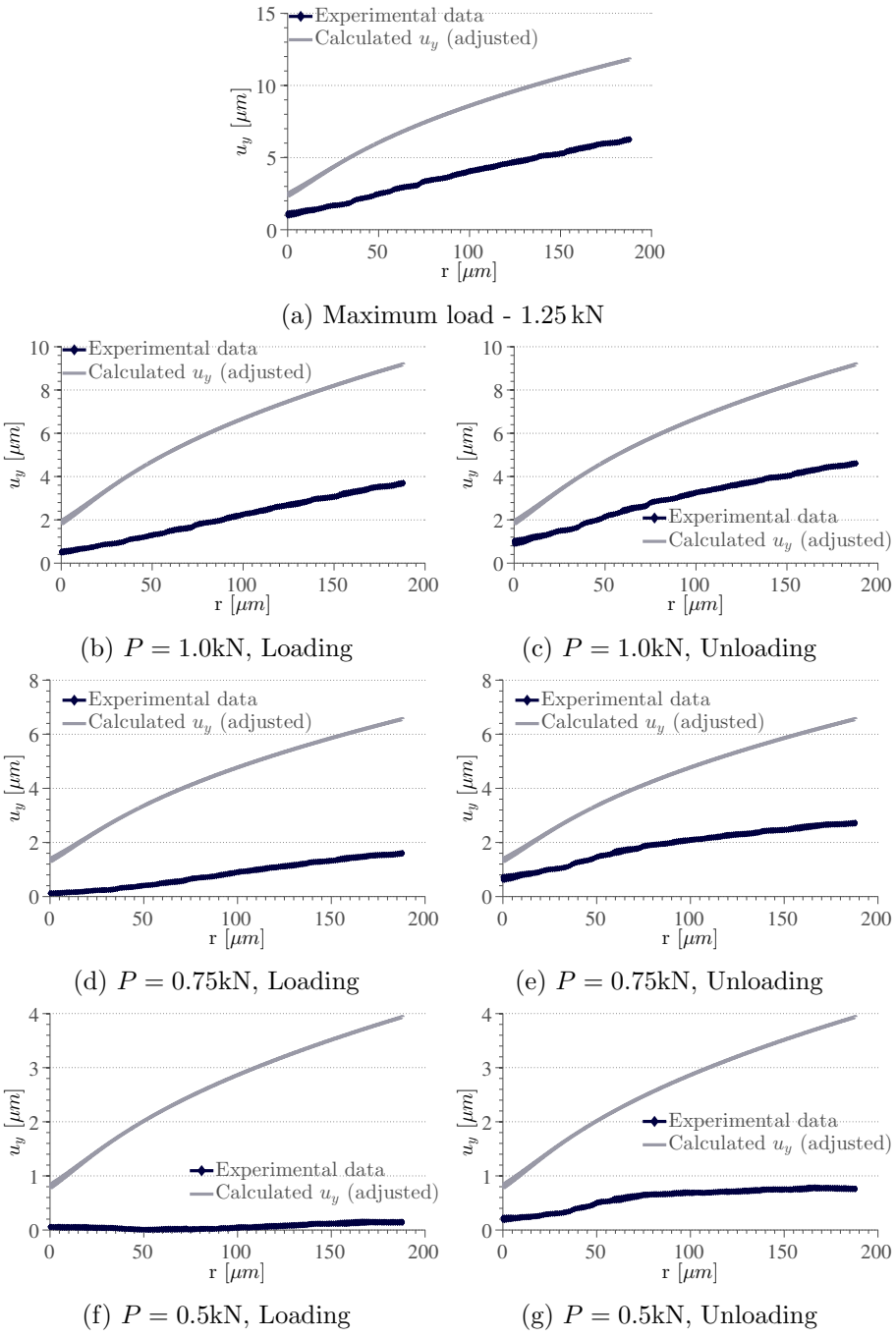
Figure 5.14: Relative load plotted against displacement, for three different sets of points located 10 µm, 50 µm and 150 µm from the crack tip.

The displacements of points along the crack flanks can be compared to those calculated from an elastic solution. As done in previous chapters, the calculated value (Equation (3.4)) is reduced by the value calculated at a minimum load to account for the experimental DIC procedure of using the loaded specimen as the

base image to measure displacements from. Figure 5.15 shows the displacements at various points in a loading cycle during both loading and unloading. In all cases, the experimentally obtained displacement values are significantly lower than those calculated. This is different from the previous experiment, where the calculated displacement had a good fit with that measured on the specimen. This could be due to the different loads applied to the specimen, with this smaller geometry having a lower maximum load. The larger specimen had lower than calculated displacements at loads below 2 kN, although at 1.2 kN the difference was not as substantial as that shown in the maximum load here (Figure 5.15a). Another possible reason for the occurrence of this difference is the presence of crack closure and high opening load that has a greater effect on points near the crack tip than those further along the crack flanks. In Figure 5.15f ($P/P_{max} = 0.4$) there is very little displacement along the whole section of crack examined, while the calculated displacement reaches approximately $u_y = 4$µm at 190 µm from the crack tip. This offset between the calculated displacements and those observed stays consistently near this value at higher loads. If the calculated displacement is again adjusted with the displacement at 0.5 kN subtracted to account for this difference, the experimental and analytical values have similar values (Figure 5.16).

5.3.2 Elastic Model Analysis

An elastic model can be used, as described previously, to analyse the crack tip displacements and obtain a value for K. This is done using Equation (3.4) and the gradients of linear regression lines fitted to u_y vs $\sqrt{\frac{r}{2\pi}}\sin\frac{\theta}{2}\left(1+\sin^2\frac{\theta}{2}-\nu\cos^2\frac{\theta}{2}\right)$ plots (Figure 5.17). The collected displacement data produces plots that have good fitting linear regression lines with R^2 values of $0.9345 < R^2 < 0.9989$ and mean $R^2_{mean} = 0.9836$ for loads $P/P_{max} > 0.4$. These values are very similar to those seen in the earlier experiments and once again increase when a small displacement is added



(a) Maximum load - 1.25 kN

(b) $P = 1.0$kN, Loading

(c) $P = 1.0$kN, Unloading

(d) $P = 0.75$kN, Loading

(e) $P = 0.75$kN, Unloading

(f) $P = 0.5$kN, Loading

(g) $P = 0.5$kN, Unloading

Figure 5.15: Measured displacement vs r for various stages in a loading cycle. The displacement calculated from the elastic displacement field (Equation (3.4)) is plotted for comparison.

to the crack tip location. The K vs Load plot produced from these regression lines displays the same features as those produced in Chapter 3, with a period of no increase in K when the crack is closed before increasing at a similar gradient to the K value calculated from the specimen geometry. Adding a displacement of 25 µm to the

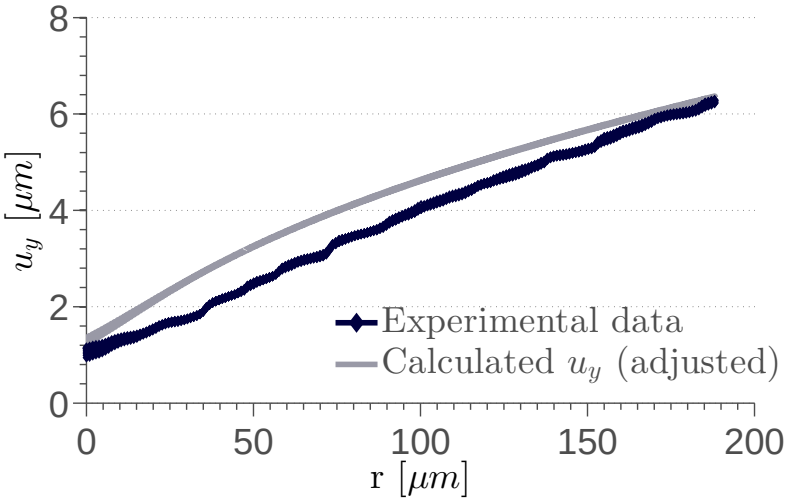


Figure 5.16: Measured displacement vs r at maximum load of 1.25 kN. The calculated displacement is reduced from Figure 5.15a by the calculated displacement at $P = 0.5$kN (Figure 5.15g) to account for crack closure.

crack tip location increases the experimental K values so that the K vs Load plot has a gradient closer to that of the calculated K vs Load (Figure 5.18b). This also slightly improves the fit of linear regressions lines used to determine K with R^2 values increasing to $0.9411 < R^2 < 0.9985$ and mean $R^2_{mean} = 0.9851$ for loads $P/P_{max} > 0.4$. With the high resolution and magnification of the images provided by the SEM, the visual crack tip location is easier to determine than in previous experiments and the accuracy of this is a less compelling reason to add an offset to the crack tip location. However, Irwin's theory of a 'virtual' crack tip location and the 3D nature of the crack tip arguments still apply. An image showing the crack tip with the visually determined location and the crack tip offset by 25 µm (the calculated cyclic plastic zone size approximately 45 µm) is provided (Figure 5.19) to display the visual crack tip location and how an offset justified by image resolution no longer applies.

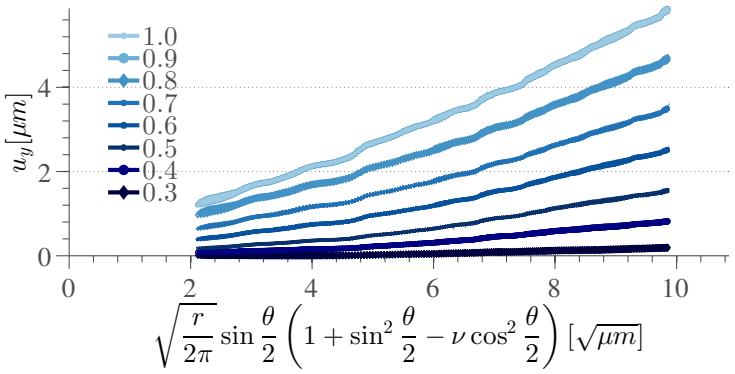
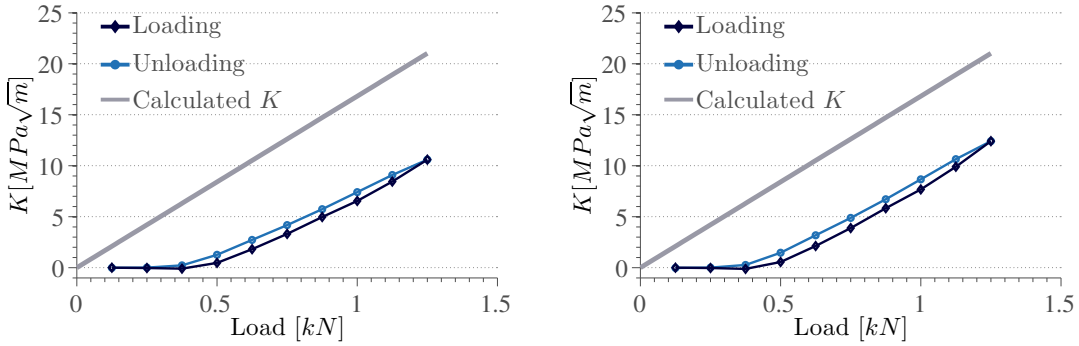


Figure 5.17: Variations of relative displacement (u_y) with distance from the crack tip (r) at eight different values of load (P/P_{max}) during the loading phase of a single cycle.



(a) No crack tip offset

(b) 25 µm offset added to crack tip location

Figure 5.18: Calculated K value at crack tip during loading cycle (Equation (3.1)) plotted with typical calculated K values from experimentally obtained displacement data.

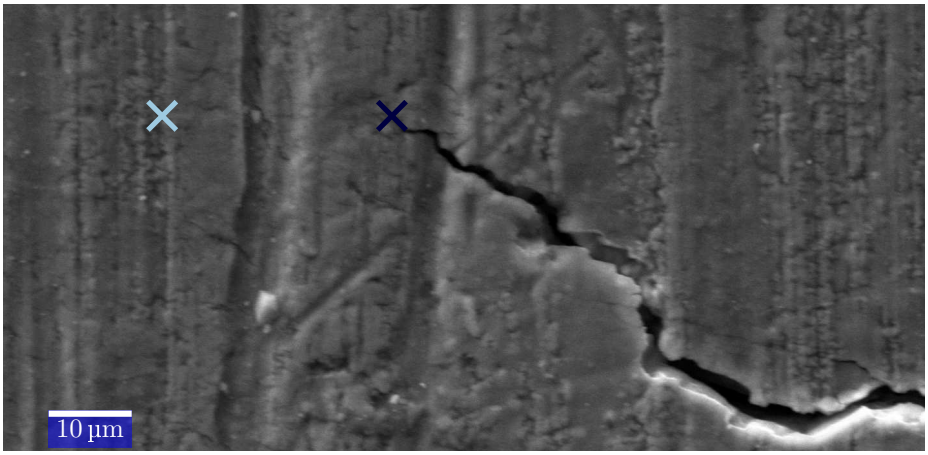


Figure 5.19: Image of the crack tip with the visually determined crack tip location marked (dark blue 'x') and the crack tip offset by 25 µm (light blue 'x').

5.3.3 Elastic-plastic Model

The elastic-plastic model is used to look at the plasticity during constant amplitude loading. A K vs ρ plot produced for two consecutive loading cycles is shown in Figure 5.20. This shows the typical hysteresis seen in previous examples, however one difference is that during loading all of the ρ values are negative, even at the maximum load. This is caused by the displacements of points further from the crack tip increasing faster than points near the crack tip during the loading phase. If points further than 50 µm from the crack tip are excluded from this analysis then the majority of the negative ρ values are removed (Figure 5.21a). When using only points within 10 µm the crack tip, the resulting K vs ρ plots exhibit similar features to those expected including a period of very little change in ρ during initial loading and initial unloading. Looking at 2 consecutive cycles is interesting and something not done in the experiments in Chapter 3. In each case, there is a slight change in ρ values from one cycle to the next. Most values of ρ increase and there is a slight increase in $\Delta\rho$, as expected in a growing crack.

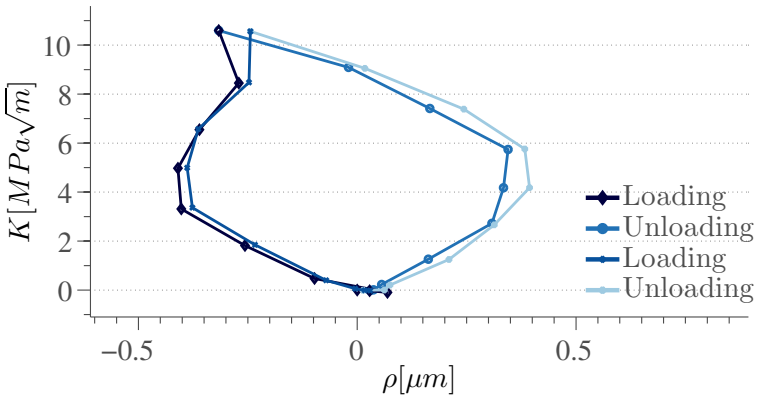
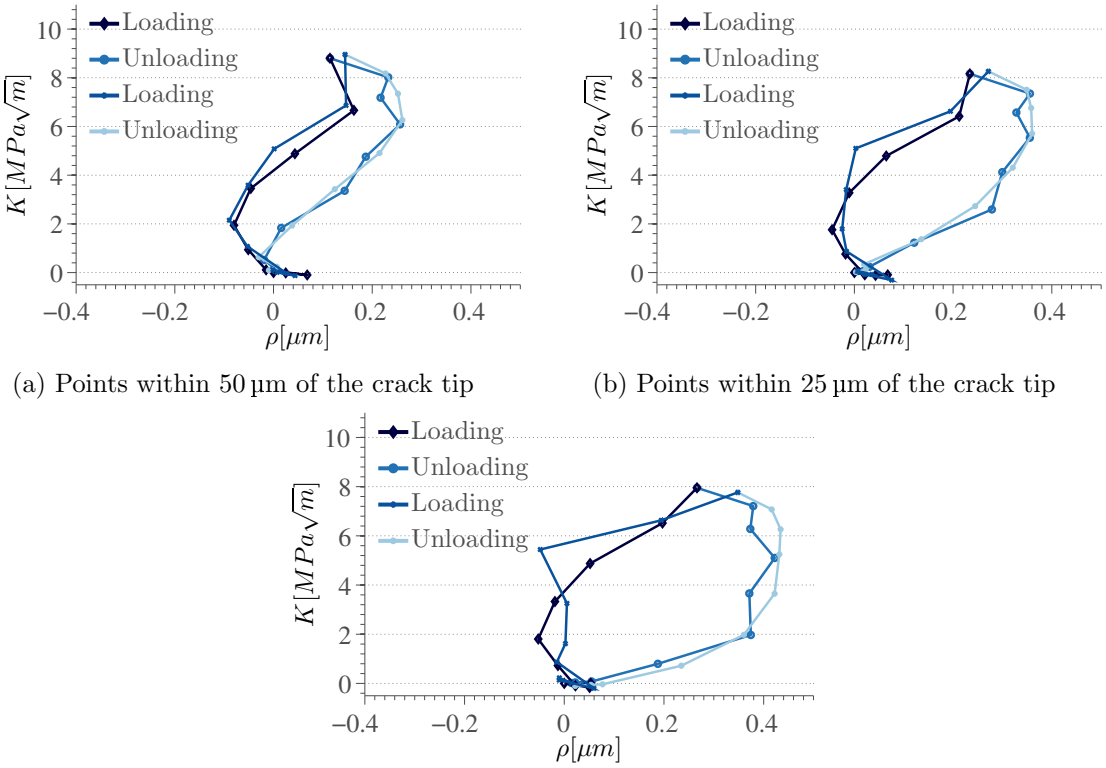


Figure 5.20: K vs ρ plot for 2 consecutive cycles during constant amplitude loading.



(a) Points within 50 µm of the crack tip

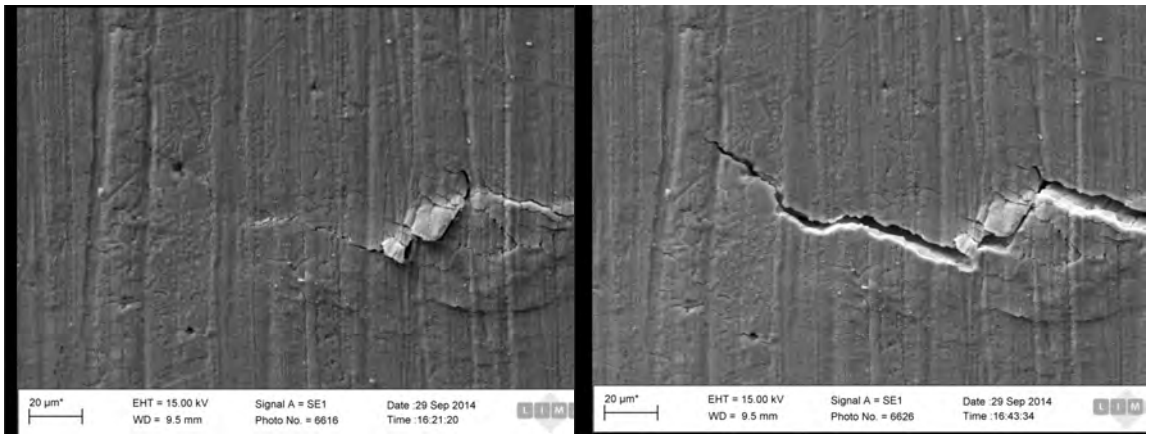
(b) Points within 25 µm of the crack tip

(c) Points within 10 µm of the crack tip

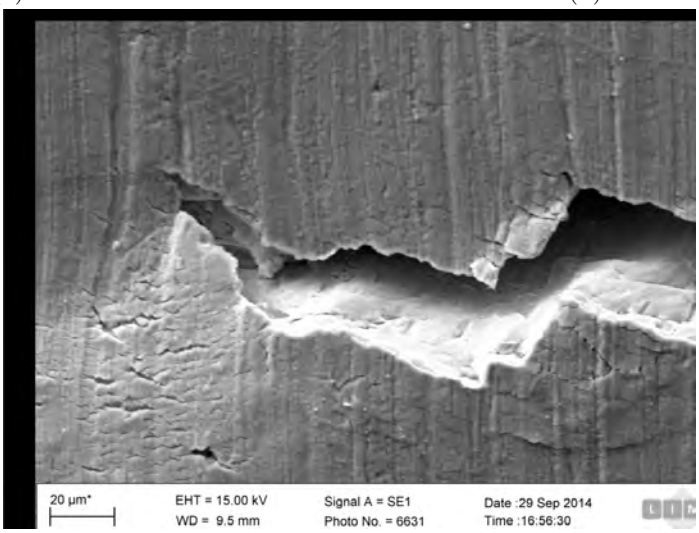
Figure 5.21: K vs ρ plots calculated using only specific ranges of points near the crack tip.

5.4 Variable Amplitude Loading

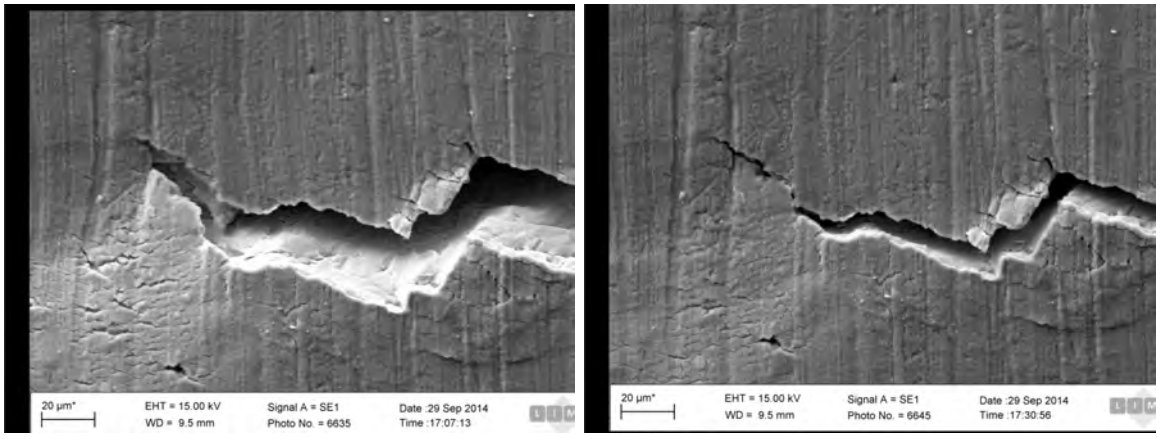
A single overload cycle was applied to the specimen after 17, 764 cycles of constant amplitude loading with the crack grown to 7.18 mm. It proved difficult to track points around the crack tip during this overload with the DIC method due to changes in the images when the load was increased to 150% (1.875 kN)of the maximum. A series of images showing the crack tip region during the overload cycle is shown in Figure 5.22. At the maximum load, the region just below the crack tip is where most of the DIC tracking issues occurred and the change to the surface features can be seen in Figure 5.22c. The displacement of points around the crack tip is displayed in Figure 5.23 and it is clear from this that some points needed to be removed from further analysis. The result of removing these points is a remaining selection of points without those within approximately 50 µm of the crack tip (Figure 5.24).



(a) 0.125 kN (b) 1.25 kN

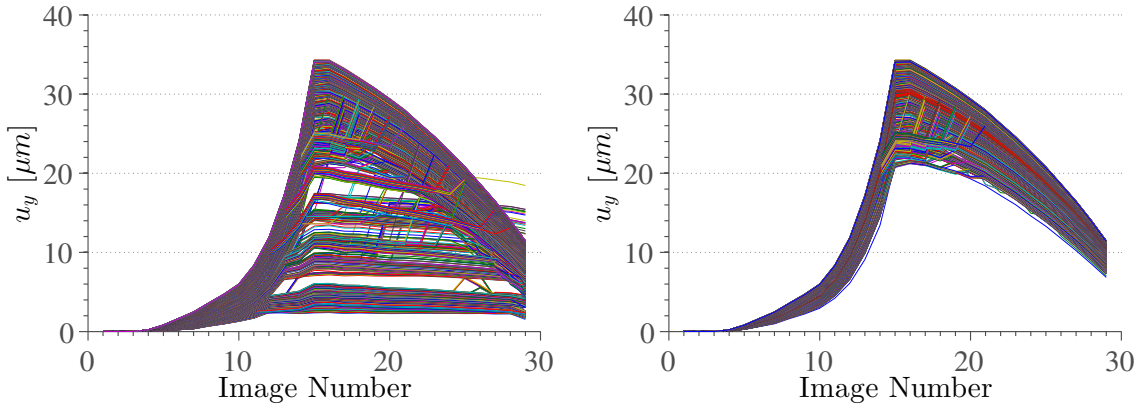


(c) 1.875 kN (overload)



(d) 1.25 kN (unloading) (e) 0.125 kN (unloading)

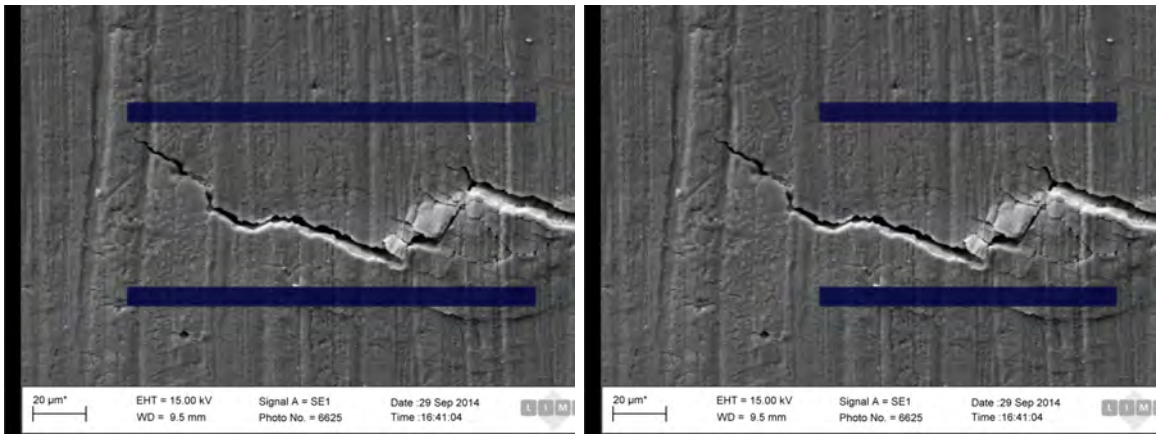
Figure 5.22: Series of images of a crack tip captured with the SEM during a single overload cycle



(a) Displacements of all points tracked for an overload cycle

(b) Displacements of points after removing those that were poorly tracked

Figure 5.23: u_y plots of points around the crack tip for an overload cycle. This shows the poorly tracked points and the remaining points after most of these were removed.



(a) Grid of points initially selected to be tracked

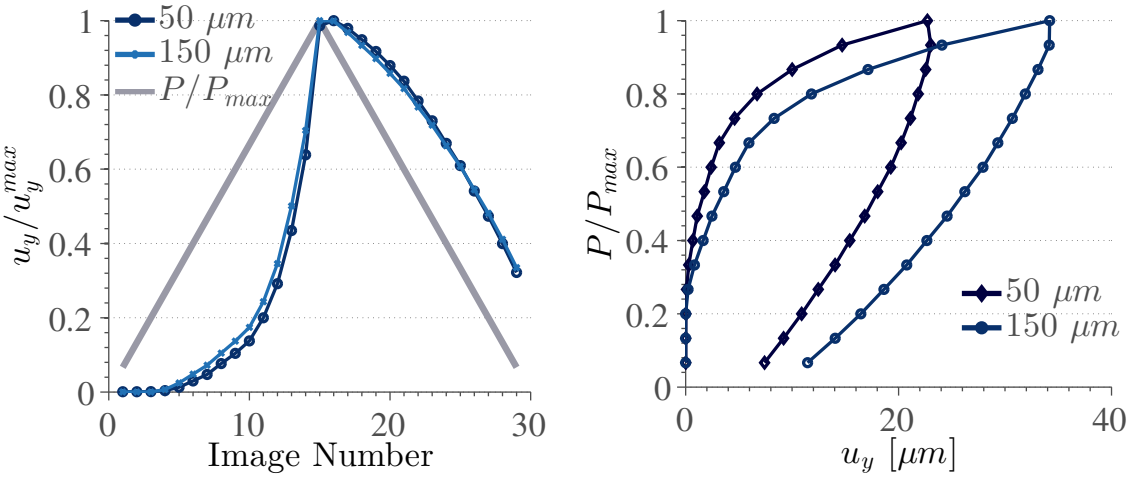
(b) Grid of points after removing those that were tracked poorly

Figure 5.24: Grids of points around the crack tip that were tracked using DIC. Figure (b) shows the remaining points after those that were poorly tracked (Figure 5.23) were removed from analysis.

5.4.1 Displacement Along Crack Flanks

5.4.1.1 Overload Cycle

During the overload cycle the crack opens significantly with large displacements around the crack flanks and a large amount of plastic deformation occurs at the crack tip. The images of the crack tip displayed in Figure 5.22 show the crack at various stages in this cycle and it is particularly noticeable how much wider the crack is at the overload position (Figure 5.22c) than at the maximum load during constant amplitude loading (Figure 5.22b). The relative displacements around the crack flanks are shown in Figure 5.25 where the magnitude of the increase in displacements can be seen as the load approaches the maximum overload value. In both the graphs and the crack tip images it can be seen that the majority of the crack opening occurs when $P/P_{max} > 0.66$ ($P > 1.25$kN). During loading up to $P/P_{max} = 0.66$, the displacement values increase linearly with the rising load (Figure 5.25b) before considerably increasing in the rate of displacement and large increments are seen in displacement values with little rise in the load. These features are characteristic of significant plastic deformation at the crack tip.



(a) Relative displacement of points with the relative load plotted for comparison

(b) Relative load vs displacement

Figure 5.25: Displacement of points around the crack flanks at various distances from the crack tip during a single overload cycle..

During unloading there is initially very little change in the displacement of the crack flanks. In fact, at 50 µm from the crack tip the measured displacement actually increases as the load is reduced from 1.875 kN to 1.75 kN. This is due to the large plastic deformation at the crack tip that prevents the crack from closing until the load is reduced further. When the load is reduced back to the minimum of 0.125 kN, a considerable residual displacement around the crack remains, which is clear in the visual images of Figure 5.22. These images show that the residual displacement of the crack flanks is actually greater after the overload, when the load has been returned to the minimum, than at the maximum load of a constant amplitude loading cycle (Figure 5.22b vs Figure 5.22e). A plot of the residual displacement values after the overload is shown in Figure 5.26, which shows the displacements increasing with distance away from the crack tip. This is consistent with measurements of points near the crack tip after an overload in the previous experiment (Figure 4.8 page 102), which then showed a decrease in displacements at distances further from the crack tip. In addition to the DIC measurements, the Deben testing stage recorded the extension of the stage during loading of the specimen, labelled as 'elongation'. From this data (Figure 5.27) the residual displacement after an overload is noticeable, although at a considerably smaller magnitude than at points near the tip where the residual displacement is greater than that when $P/P_{max} = 1$ prior to an overload.

5.4.1.2 Post Overload Cycles

The displacements of all points measured along the crack flanks during constant amplitude loading after a single overload were higher than prior to the overload cycle. The change in crack closure due to the residual stress at the crack tip is a significant factor in this. Plots of relative load vs displacement in Figure 5.29 show the initial reduction in crack closure (low opening load) directly after the overload cycle (Figure 5.29b). At this stage, crack closure does not exist as the crack is held open by

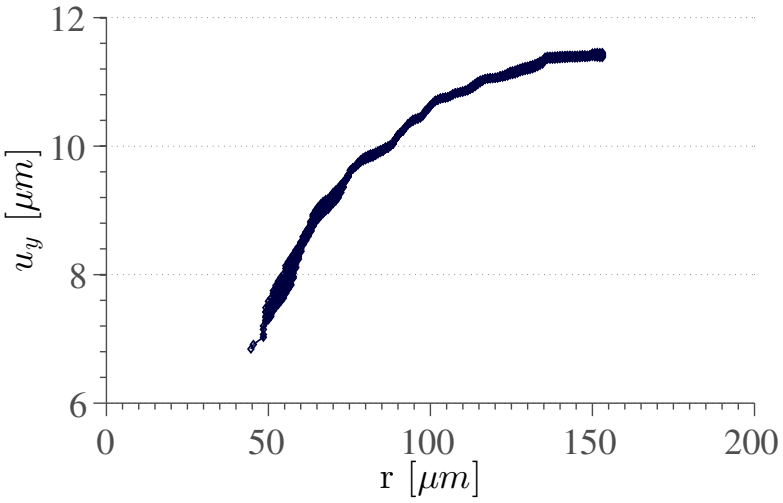


Figure 5.26: Residual displacement along the crack flanks once the load has been returned to the minimum (0.125 kN) at the end of a single overload cycle.

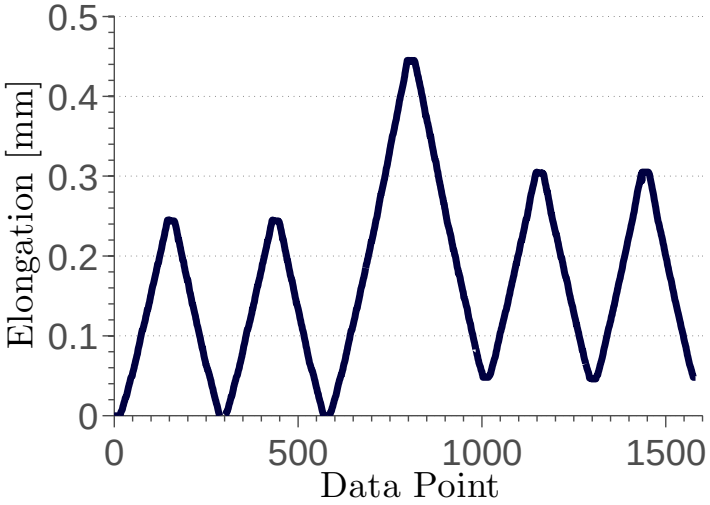


Figure 5.27: Extension data collected from the Deben testing stage before, during and after a single overload cycle is applied to the specimen.

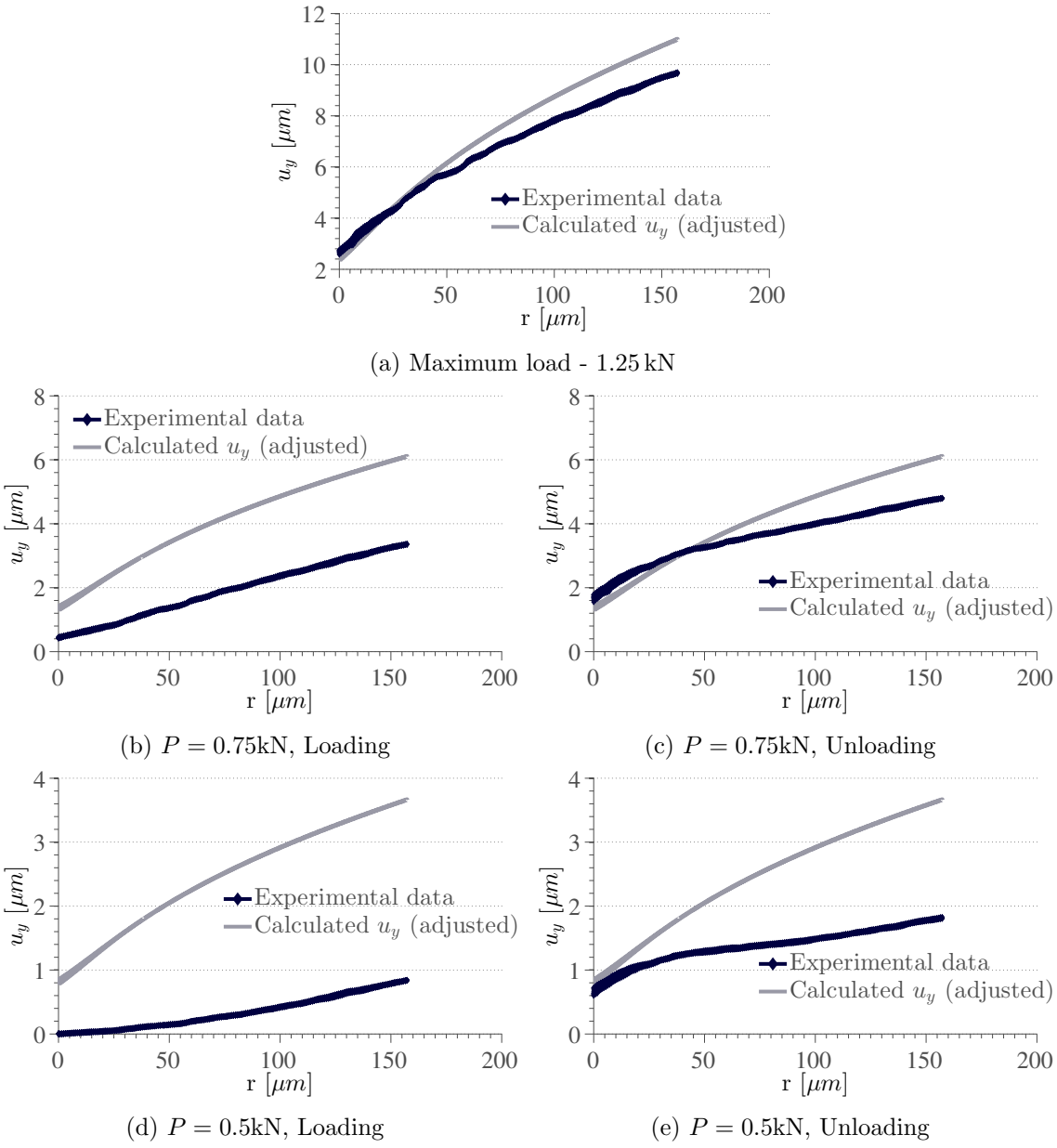
the residual displacement at the crack tip. Following this, once the crack has grown further, the opening load increases although it still remains low at points 150 µm from the crack tip. This behaviour is expected from analysis of the previous experiment and it is expected that high amounts of crack closure (identified by high opening loads) will exist for a period as the crack continues to grow after the overload cycle.

After 50 loading cycles are applied to the specimen post overload and the presence of crack closure returns, the displacements of points along the crack flanks are close to

those calculated from the specimen geometry (Figure 5.28a). This is a substantially different to displacements seen prior to the overload, which were far lower than the calculated values. Some of this difference can be accounted for by lower levels of crack closure, however there is only a minor amount of displacement seen at 0.5 kN (Figure 5.28d), where there was previously none and the calculated K was offset by its value at 0.5 kN to produce a close fit to the measured data. This suggests that the improved fit after the overload is more likely due to the effects of the residual stresses at the crack tip caused by the overload resulting in greater displacements. The increased plasticity at the crack tip produces different displacement behaviour during loading and unloading than seen prior to the overload. This can be seen with points near the crack tip initially being slower to increase in displacement during loading than those further from the crack tip and then also being slower to decrease in displacement during unloading.

5.4.2 Elastic Model Analysis

During the overload cycle, the plot of u_y vs $\sqrt{\frac{r}{2\pi}}\sin\frac{\theta}{2}\left(1+\sin^2\frac{\theta}{2}-\nu\cos^2\frac{\theta}{2}\right)$ (Figure 5.30) produces points that have a strong fit with linear regression lines. The resulting R^2 values for lines fitted when $P > P_{opening}$ is $0.9680 < R^2 < 0.9984$ with a mean of $R^2_{mean} = 0.9680$. The noticeable feature of this figure is the large displacements between points when $P/P_{max} > 0.7$ producing large gaps between the data points of different loads. The gradients of these lines are used to calculate K and the resulting K vs Load plot is shown in Section 5.4.2. This figure displays features seen in constant amplitude loading until the load rises above 1.25 kN and the value of K increases at a considerably higher rate. This continues until the maximum load is reached and K rises to a value much greater than that calculated for this load. During unloading, K reduces at a constant rate that is very similar to the rate of change of the calculated value and that seen during the initial loading. Once the



(a) Maximum load - 1.25 kN

(b) $P = 0.75$kN, Loading

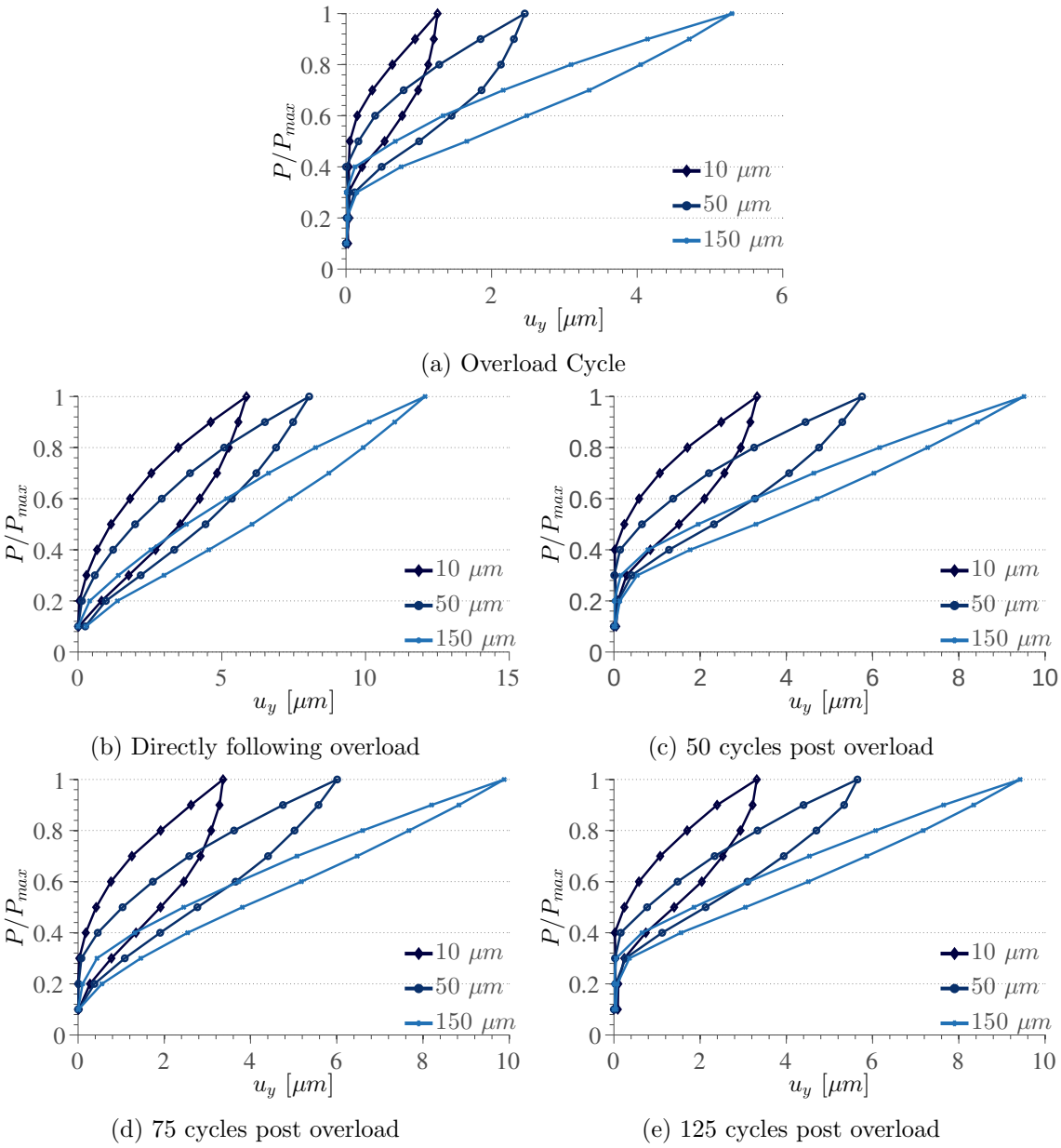
(c) $P = 0.75$kN, Unloading

(d) $P = 0.5$kN, Loading

(e) $P = 0.5$kN, Unloading

Figure 5.28: Measured displacement vs r for various stages in a loading cycle 50 cycles after a single overload cycle has been applied to the specimen. The displacement calculated from the elastic displacement field (Equation (3.4)) is plotted for comparison.

load returns to the minimum, a large residual K remains, as expected from looking at the residual displacements around the crack tip (Figure 5.26). This behaviour of K during the overload cycle is markedly different to that determined during an overload in the previous experiment in Chapter 4. In that case, the value of K was always below the calculated value and the rate of increase in K with load actually



(a) Overload Cycle

(b) Directly following overload

(c) 50 cycles post overload

(d) 75 cycles post overload

(e) 125 cycles post overload

Figure 5.29: Relative load vs displacement at various points along the crack flank. Graphs shown are for cycles during (a) and after (b-e) a single overload cycle.

dropped slightly as the load was close to the maximum. This difference in behaviour could be the result of analysing only points in close proximity of the crack tip and an improvement in the accuracy of measuring the displacement of these points.

After the overload cycle, the behaviour of K (Figure 5.31) is very similar to those expected from looking at the displacement data. The cycle after the overload exhibits no features associated with crack closure and therefore is very similar to the

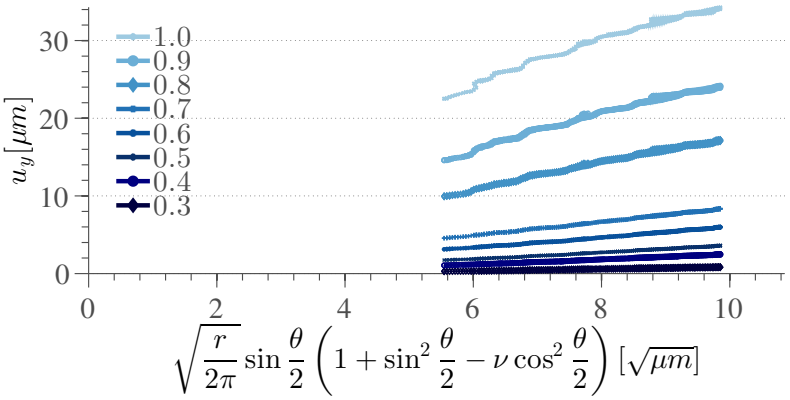
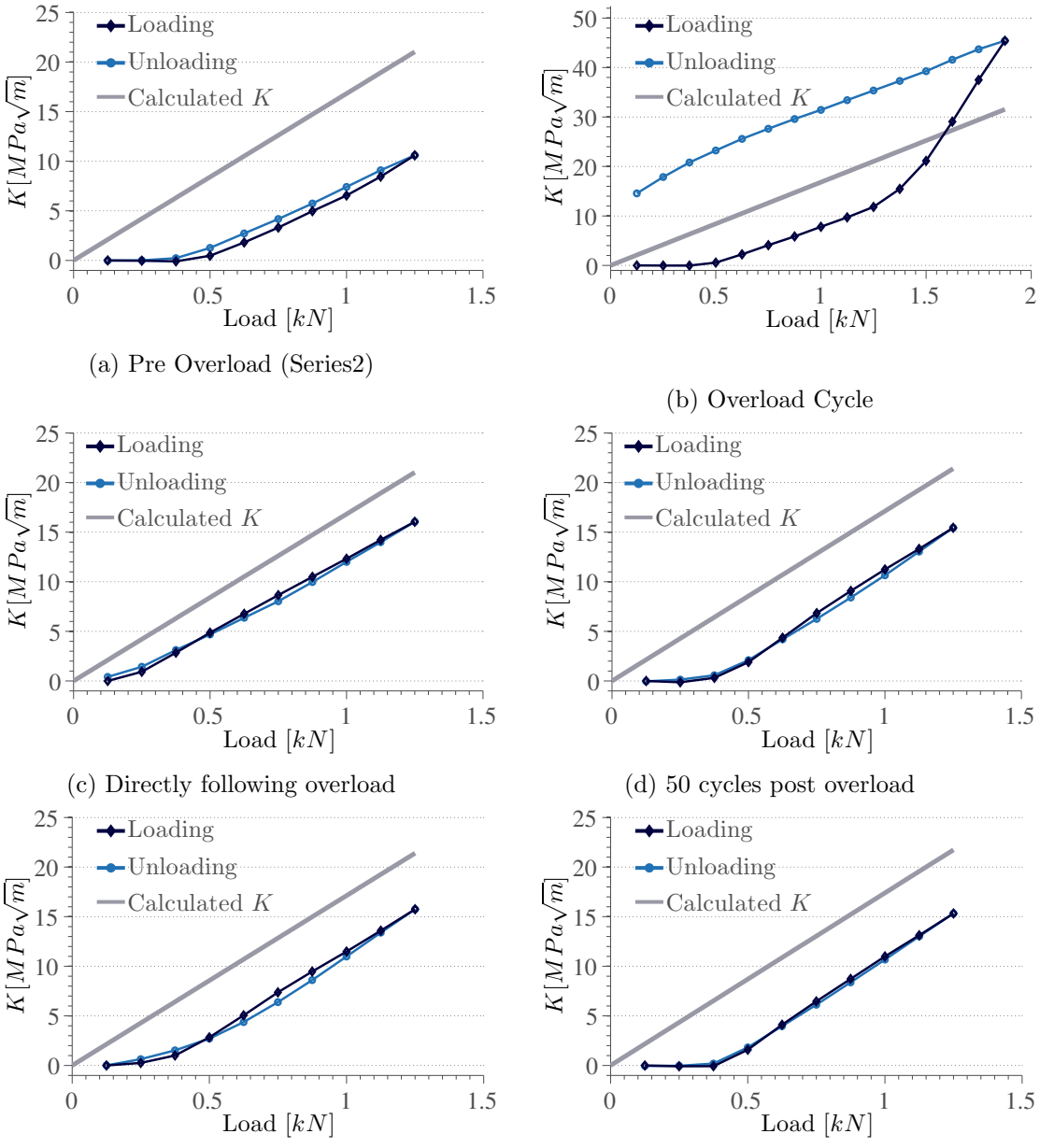


Figure 5.30: u_y vs $\sqrt{\frac{r}{2\pi}}\sin\frac{\theta}{2}\left(1+\sin^2\frac{\theta}{2}-\nu\cos^2\frac{\theta}{2}\right)$ during loading for a single overload cycle.

calculated value of K. With an offset of 25 µm added to the crack tip, which seems reasonable due to the slight increase in crack length from the overload cycle, and with the value of calculated K at 0.125 kN added to the experimentally determined value, the experimental value of K has a very good fit with the analytically calculated value for all loads (Figure 5.32). This addition of the calculated K at 0.125 kN is done to account for the DIC procedure of taking the image with loading 0.125 kN as the base image to measure displacements from.

With the crack grown further following the overload cycle, the gradient of the experimentally determined K vs load is consistently very similar to the calculated value without any displacements added to the crack tip position. The crack closure levels can be seen in these figures (Figure 5.31) and analysis from the previous experiment suggests that these images are captured in the period as the crack closure drops dramatically just after the overload and then begins to increase. This increase continues for a period when there is substantial crack closure that coincides with reduced ΔK values and the crack growth is retarded.



(a) Pre Overload (Series2)

(b) Overload Cycle

(c) Directly following overload

(d) 50 cycles post overload

(e) 75 cycles post overload

(f) 125 cycles post overload

Figure 5.31: K vs Load plots for calculated from the displacement around the crack flanks during cycles before (a), during (b) and after (c-e) a single overload cycle.

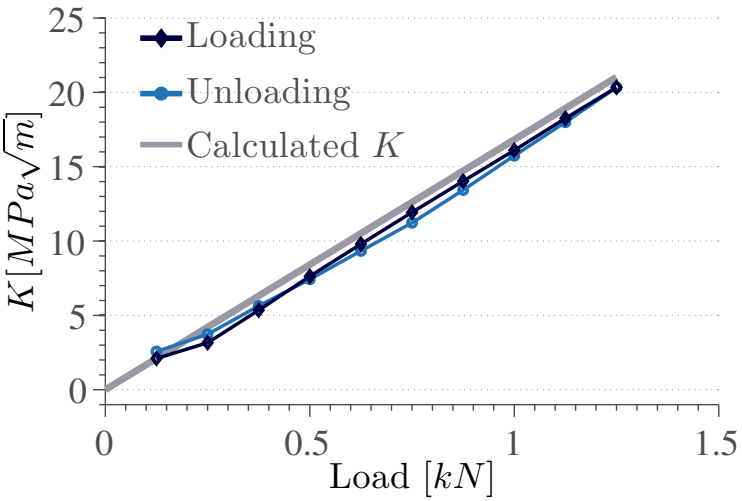


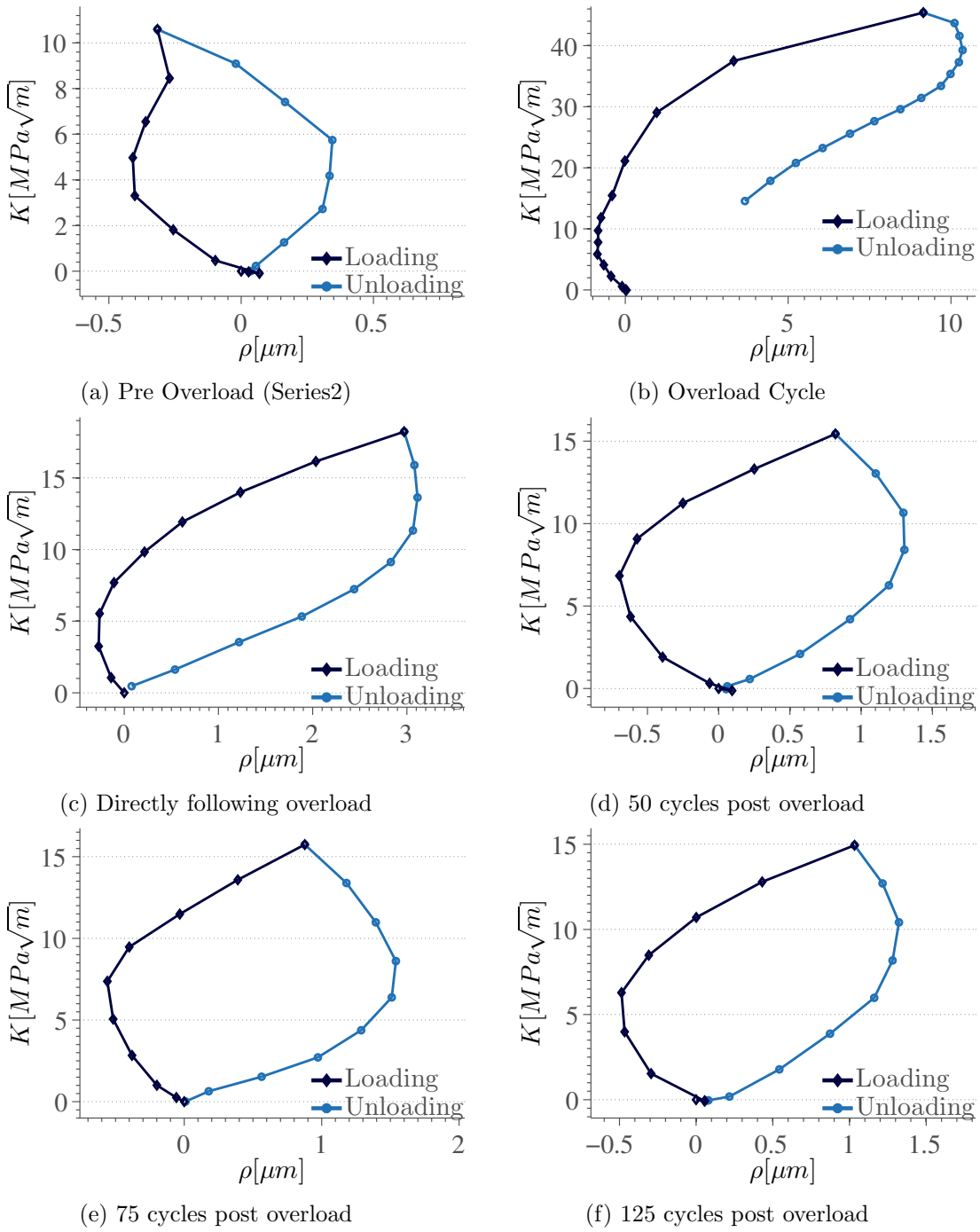
Figure 5.32: K vs Load plot for a cycle directly after a single overload cycle. The K value determined by displacement of points around the crack flanks is increased by the calculated K at 0.125 kN and the crack tip is offset by 25 µm.

5.4.3 Elastic-plastic Model

The large amount of plastic deformation during the overload cycle is reflected in a graph of K vs ρ, which shows large increases in ρ when $P > 1.25$kN (Figure 5.33b). After the maximum load is reached and the unloading phase begins, the determined value of ρ continues to increase for a period. This is a reflection of the displacements which, as commented on previously, are very slow to reduce in value as the load decreases, particularly near the crack tip. The large amount of the plasticity at the crack tip holds the crack open from the tip until the load is sufficiently reduced that the residual stresses are overcome. Below 1.25 kN, the values of ρ decrease linearly with K until the minimum load is reached with the residual ρ a reflection of the displacement at the crack tip.

After the overload cycle, the plots of K vs ρ (Figure 5.33) show features more similar to what is expected. Directly after the overload, the figure (Figure 5.33c) reflects a period of elastic loading (with very little change in ρ) during initial loading and unloading, which is predicted in Pommier's model. Following this is a phase of linearly increasing ρ with K. The $\Delta\rho$ during this cycle is much higher than that seen in other cycles prior to or after the overload cycle and is likely to be due to the larger ΔK.

The negative ρ values are a reflection of crack closure and points further from the crack tip displacing at a greater rate as the load initially increases than points near the crack tip. This is shown by the very little negative ρ directly after the overload when there is no crack closure and the predominantly high negative ρ values seen prior to the overload where the highest levels of crack closure in this experiment were observed. Adding an offset to the crack tip can significantly alter the shape of the K vs ρ plot, however to shift the ρ values positively, a negative offset is required. This in unrealistic as it is very unlikely that the crack tip position is closer to the crack mouth than where it is visually located.



(a) Pre Overload (Series2)

(b) Overload Cycle

(c) Directly following overload

(d) 50 cycles post overload

(e) 75 cycles post overload

(f) 125 cycles post overload

Figure 5.33: K vs ρ plots for calculated from the displacement around the crack flanks during cycles before (a), during (b) and after (c-e) a single overload cycle. All displacements are measured from the first image (at minimum load) in each cycle.

Analysing consecutive cycles gives a more complete picture of the $K - \rho$ space before, during and after the overload cycle. The same points were tracked on images of 4 consecutive cycles and the resulting K vs ρ plot is displayed in Figure 5.34. This

shows how each loading cycle produced noticeably different features and large changes in both K and ρ. The large residual ρ and K after the overload are features that are not identified when looking simply at the single cycle directly after the overload. This shows that while analysing each cycle with the method used in this experiment does provide information on the K and ρ behaviour of a loading cycle, it does not display in an obvious way any residual K or ρ that may be present.

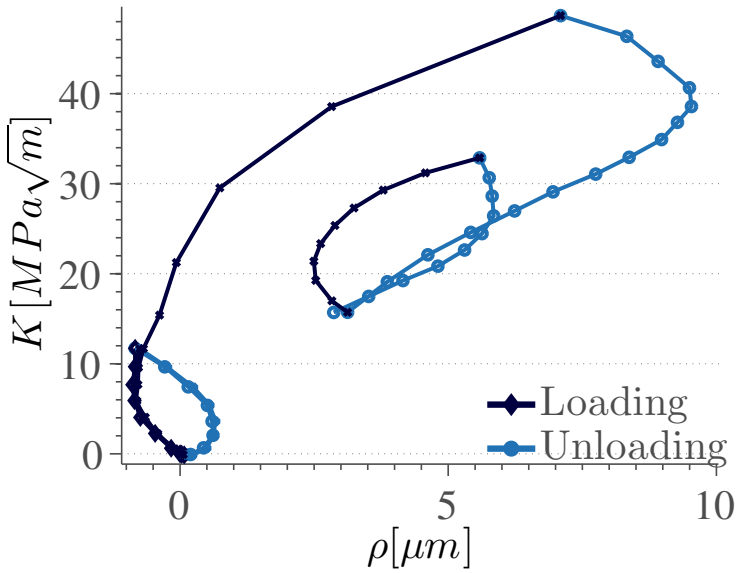


Figure 5.34: K vs ρ plot for cycles before, during and after an overload cycle. All displacements are based off the first image in the cycle before the overload.

5.5 Conclusions

Using the SEM produced images of higher resolution and higher magnification resulting in improved DIC tracking of points in positions very near the crack tip. The downside of this experimental method was greatly increased time and effort taken to capture the images and very slow loading with the Deben testing stage. Because of this, the specimen was pre cracked in a hydraulic testing rig and considerably fewer images were captured per loading cycle than with the camera and lens setup (19 images/loading cycle vs 400 images/loading cycle).

Analysing points near the crack tip with SEM obtained images produced similar results to those seen in Chapters 3 and 4. The elastic model provided a reasonable fit with the displacements along the crack flanks and determined K values once closure was accounted for. Large crack tip position offsets were not reasonable or necessary with these images due to the improved accuracy of visually determining the crack tip location. However, it was shown that a small offset did improve the fit of the experimentally determined K value with that calculated from the specimen geometry prior to the overload cycle.

Using an elastic-plastic model to analyse the displacement data showed noticeable changes in the plasticity at the crack tip when a single overload cycle was applied to the specimen and the residual effects following this overload. The improved resolution of the displacement data allowed analysis of consecutive cycles to show the changes of increasing ρ values from one cycle to the next that are likely to have not been visible in the previous experiment. It also showed that even when analysing points within 150 µm of the crack tip, the crack closure and residual stress around the crack tip affect the determined ρ values in ways not predicted by the model during initial loading and unloading.

This method of imaging the crack during an overload cycle proved to be effective and further study of displacements around the crack tip following an overload cycle,

particularly for longer periods after the overload where large amounts of crack closure are likely to be observed, is worthy of future investigation.

Chapter 6

Conclusions and Future Work

6.1 Conclusions

The work described in this thesis includes reference to analytical and experimental techniques for crack closure investigation. The experimental methods involve analysing the displacements along crack flanks using DIC during constant and variable loading conditions. The main conclusions are as follows:

1. DIC methods provided consistent results of point displacements during constant amplitude loading. This technique relies on the quality of the images collected with higher resolution images allowing increased accuracy in displacement measurements. During an overload cycle, features on the surface of the specimen around the crack tip were altered, making it very difficult to track points in this region with DIC analysis. However, generally most points were tracked sufficiently and rarely were poorly tracked points required to be removed. While increasing computational time, selecting a large number of points to be tracked between images reduced the error associated with tracking points that displace by very small amounts, especially in the lower resolution images captured with the USB camera.

2. DIC methods were simple to implement using open source MATLAB scripts and the Digital Image Processing Toolbox. This method provided a quick and non invasive method of measuring displacements of points near the crack tip. This technique can also be adjusted in terms of correlation area size and number of points to be tracked after an experiment has been performed in order to improve measurement accuracy.

3. The crack tip location was difficult to determine visually on the specimen surface, particularly with the lower resolution images captured by the USB camera and lens. In some cases, an offset to the crack tip location produced an improved fit with the calculated K values. This seemed reasonable due to the difficulty in determining the crack tip location from the images and the likelihood that the crack tip was actually further ahead of where it could be visually seen. The higher resolution and magnification of the SEM images provided a good fit with analytical models with little or no offset added to the crack tip location. This was due to the considerable improvement in visually locating the crack tip accurately.

4. Crack closure was observed by analysing the displacement of points along the crack flanks near the crack tip. The effects of a single overload on closure levels were shown, along with the changes in crack growth rate. Significantly increased levels of crack closure (higher opening loads) and reduced ΔK were determined from the reduction in displacements normal to the crack (to values far below those predicted in an elastic model) following an overload. These occurred during the a period of crack growth retardation and followed a brief period of no closure, high ΔK and large displacements directly after the overload cycle.

5. An elastic model proved to be reasonably good in predicting the rate of K increasing with load during constant amplitude loading. An offset between the

experimentally determined K value and the analytically calculated value was observed and determined to be the result of crack closure. During the cycle directly after an overload, crack closure was not observed and an elastic model proved to fit very well with that determined by the DIC measured displacements.

6. A single overload cycle produced large amounts of plastic deformation at the crack tip and therefore large displacements that, unsurprisingly, did not produce a strong fit with an elastic model. The plastic deformation was accounted for in an elastic-plastic model with the factor ρ. This model showed how ρ changed during individual cycles during constant amplitude loading and how it was affected by an overload cycle.

7. The plasticity factor at the crack tip, quantified by ρ, was observed to be related to ΔK_{eff}, crack closure and crack growth. This was seen most prominently during post overload analysis.

8. In-situ SEM imaging of the crack tip proved to be an excellent method of producing high resolution image of the crack tip during a loading cycle. Considerably more time was required to capture the images and load the specimen than using a hydraulic testing rig and USB digital camera. However, the improved resolution and magnification of the images allowed for greater accuracy in DIC measurements at locations very near the crack tip.

The present investigation was based on previous work performed by de Matos and Nowell [50] but extended the experimental work and analysis by capturing more images, tracking and analysing a significantly higher number of points with DIC and performing experiments with in-situ SEM imaging. This provided data that could be compared with elastic and elastic-plastic models during constant and variable amplitude loading.

6.2 Future Work

During the course of this work, the following items were found to be worthy of further investigation:

1. The in-situ SEM testing in this investigation was limited and was mainly aimed at analysing some cycles before, during and just after a single overload cycle. More work could be done to capture images after the crack has grown further following an overload to investigate the period of high crack growth retardation and large levels of crack closure. A limitation of the in-situ testing in this experiment was the time required to capture images and perform DIC analysis on the high resolution SEM images. Work could be performed to make this process more efficient allowing analysis to be performed on more images over a greater number of cycles.

2. This work only involved comparison between experimentally obtained displacement data and basic models. A comparison with more sophisticated crack tip models (eg using measured displacements with finite element analysis) would be useful to compare results and extend the investigation.

3. These experiments were limited in terms of the testing environment and the material used. It would be interesting to do similar analysis with different environmental conditions and other materials.

4. Further analysis using Digital Image correlation methods could be used to investigate the crack tip location and methods for best determining this. The DIC analysis could also be extended to analysing stains around the crack tip during constant and variable amplitude loading rather than only displacements.

References

[1] Ted L Anderson. *Fracture mechanics: fundamentals and applications*. CRC press, 2005.

[2] Michael Janssen, Jan Zuidema, and Russell Wanhill. *Chapter 3: Crack Tip Plasticity*, pages 61–82. Fracture Mechanics, Second Edition: Fundamentals and Applications. Spon Press, Oxfordshire, 2 edition, 2004.

[3] P.F.P de Matos. D.phil. thesis. *University of Oxford, UK*, 2008.

[4] M. Janssen, J. Zuidema, and R. Wanhill. *Fracture Mechanics, Second Edition: Fundamentals and Applications*. ISBN 9780203596869.

[5] S. Pommier and R. Hamam. Incremental model for fatigue crack growth based on a displacement partitioning hypothesis of mode i elastic plastic displacement fields. *Fatigue and Fracture of Engineering Materials and Structures*, 30(7): 582–598, 2007.

[6] William N. Sharpe Jr, Jr Sharpe, and N. William. *Springer handbook of experimental solid mechanics*. Springer, 2008.

[7] D. S. Gianola and The Johns Hopkins University. *Deformation Mechanisms in Nanocrystalline Aluminum Thin Films: An Experimental Investigation*. Johns Hopkins University, 2007. ISBN 9781109996135.

[8] ASTM Standard. E647-11: standard test method for measurement of fatigue crack growth rates. *ASTM International, West Conshohocken, PA (USA)*, 2003.

[9] n8 Research Partnership. Carl zeiss evo ma15 vp-sem. URL `http://www.n8equipment.org.uk/id/1_10101111/t/Carl-Zeiss-EVO-MA15-VP-SEM/`.

[10] Deben. 2kn & 5kn tensile compression and horizontal bending stage. URL `http://deben.co.uk/products/mini-tensile-tester-testing/2kn-5kn-tensile-compression-and-horizontal-bending-stage/`.

[11] Elber Wolf. Fatigue crack closure under cyclic tension. *Engineering Fracture Mechanics*, 2(1):37–45, 1970.

[12] George R. Irwin. Analysis of stresses and strains near the end of a crack traversing a plate. *J.appl.Mech.*, 1957.

[13] DS Dugdale. Yielding of steel sheets containing slits. *Journal of the Mechanics and Physics of Solids*, 8(2):100–104, 1960.

[14] Grigory Isaakovich Barenblatt. The mathematical theory of equilibrium cracks in brittle fracture. *Advances in applied mechanics*, 7(1):55–129, 1962.

[15] Calvin Rans, René Alderliesten, and Rinze Benedictus. Misinterpreting the results: How similitude can improve our understanding of fatigue delamination growth. *Composites Science and Technology*, 71(2):230–238, 2011.

[16] Jo C. Newman Jr. A crack-closure model for predicting fatigue crack growth under aircraft spectrum loading. *ASTM STP*, 748:53–84, 1981.

[17] JC Newman Jr and PR Edwards. *Short-crack growth behaviour in an aluminum alloy-an AGARD cooperative test programme*, 1988.

[18] CS Lee, CG Park, and YW Chang. Precise determination of fatigue crack closure in al alloys. *Materials Science and Engineering: A*, 216(1):131–138, 1996.

[19] John Codrington and Andrei Kotousov. Investigation of plasticity-induced fatigue crack closure. In *5th Australasian Congress on Applied Mechanics (ACAM 2007)*, volume 1, pages 127–132. Engineers Australia, 2007.

[20] J. Schijve. Four lectures on fatigue crack growth. *Engineering Fracture Mechanics*, 11(1):167–168, 1979.

[21] R. Pippan, O. Kolednik, M. Lang, and HP Stuwe. A new model for the plasticity-induced closure under plane strain condition. In *ECF10, Berlin 1994*, 2013.

[22] HL Ewalds and RT Furnee. Crack closure measurement along the fatigue crack front of center cracked specimens. *International Journal of Fracture*, 14(2): R53–R55, 1978.

[23] FJ Pitoniak, AF Grandt, LT Montulli, and PF Packman. Fatigue crack retardation and closure in polymethylmethacrylate. *Engineering Fracture Mechanics*, 6(4):663–666, 1974.

[24] RC McClung, BH Thacker, and S. Roy. Finite element visualization of fatigue crack closure in plane stress and plane strain. *International Journal of Fracture*, 50(1):27–49, 1991.

[25] Huseyin Sehitoglu and Wei Sun. Modeling of plane strain fatigue crack closure. *ASME, Transactions, Journal of Engineering Materials and Technology*, 113: 31–40, 1991.

[26] William N. Sharpe Jr, Bin Yuan, Ranji Vaidyanathan, and Richard L. Edwards. Measurements of youngs modulus, poissons ratio, and tensile strength of polysilicon. In *Micro Electro Mechanical Systems, 1997. MEMS97, Proceedings, IEEE., Tenth Annual International Workshop on*, pages 424–429. IEEE, 1997.

[27] Marc Zupan and KJ Hemker. Application of fourier analysis to the laser based interferometric strain/displacement gage. *Experimental Mechanics*, 42(2): 214–220, 2002.

[28] K. Li. Interferometric strain/slope rosette for static and dynamic measurements. *Experimental Mechanics*, 37(2):111–118, 1997.

[29] Colin A. Walker. A historical review of moiré interferometry. *Experimental Mechanics*, 34(4):281–299, 1994.

[30] John Guild. *The interference systems of crossed diffraction gratings: theory of moiré fringes*, volume 15. Clarendon Press Oxford, 1956.

[31] Kazunori KATO, Tadao MUROTA, and Yukio KUMAMOTO. Improvement of the method of measuring shear strain using interferometry of diffraction beams. *Bulletin of the JSME*, 27(224):165–171, 1984.

[32] Daniel Post. New optical methods of moiré fringe multiplication. *Experimental Mechanics*, 8(2):63–68, 1968.

[33] Daniel Post. Isochromatic fringe sharpening and fringe multiplication in photoelasticity. *proc.SESA*, 12(2):143–156, 1955.

[34] Cesar A. Sciammarella. The moiré method review. *Experimental Mechanics*, 22 (11):418–433, 1982.

[35] CA Walker and J. McKelvie. A practical multiplied-moiré system. *Experimental Mechanics*, 18(8):316–320, 1978.

[36] WH Peters and WF Ranson. Digital imaging techniques in experimental stress analysis. *Optical Engineering*, 21(3):213427–213427–, 1982.

[37] MA Sutton, WJ Wolters, WH Peters, WF Ranson, and SR McNeill. Determination of displacements using an improved digital correlation method. *Image and Vision Computing*, 1(3):133–139, 1983.

[38] TC Chu, WF Ranson, and MA Sutton. Applications of digital-image-correlation techniques to experimental mechanics. *Experimental Mechanics*, 25(3):232–244, 1985.

[39] HA Bruck, SR McNeill, M. Ae Sutton, and WH Peters Iii. Digital image correlation using newton-raphson method of partial differential correction. *Experimental Mechanics*, 29(3):261–267, 1989.

[40] Michael A. Sutton, Stephen R. McNeill, Jeffrey D. Helm, and Yuh J. Chao. *Advances in two-dimensional and three-dimensional computer vision*, pages 323–372. Photomechanics. Springer, 2000.

[41] MR James, WL Morris, and BN Cox. A high accuracy automated strain-field mapper. *Experimental Mechanics*, 30(1):60–67, 1990.

[42] BW Smith, M. Li, and W. Tong. Error assessment for strain mapping by digital image correlation. *Experimental Techniques*, 22(4):19–21, 1998.

[43] Vikrant Tiwari, MA Sutton, and SR McNeill. Assessment of high speed imaging systems for 2d and 3d deformation measurements: methodology development and validation. *Experimental Mechanics*, 47(4):561–579, 2007.

[44] Vikrant Tiwari, Michael A. Sutton, SR McNeill, Shaowen Xu, Xiaomin Deng, William L. Fourney, and Damien Bretall. Application of 3d image correlation for full-field transient plate deformation measurements during blast loading. *International Journal of Impact Engineering*, 36(6):862–874, 2009.

[45] CW Smith and AS Kobayashi. Experimental fracture mechanics. *VCH Publishers, Inc., Handbook on Experimental Mechanics.Second Revised Edition(USA), 1993,*, pages 905–968, 1993.

[46] MA Sutton. Digital image correlation for shape and deformation measurements. *Handbook of experimental solid mechanics.Springer, New York*, pages 565–600, 2008.

[47] H. Jin, WY Lu, and J. Korellis. Micro-scale deformation measurement using the digital image correlation technique and scanning electron microscope imaging. *The Journal of Strain Analysis for Engineering Design*, 43(8):719–728, 2008.

[48] Christoph Eberl, R. Thompson, D. Gianola, W. Sharpe Jr, and K. Hemker. Digital image correlation and tracking. *MatLabCentral, Mathworks file exchange server, FileID*, 12413, 2006.

[49] Aluminium alloy 6082 - t6 t651 plate. URL `http://www.aalco.co.uk/datasheets/Aluminium-Alloy-6082-T6T651-Plate_148.ashx/`.

[50] D. Nowell, ME Kartal, and PFP De Matos. Digital image correlation measurement of near tip fatigue crack displacement fields: constant amplitude loading and load history effects. *Fatigue and Fracture of Engineering Materials and Structures*, 36(1):3–13, 2013.